

**IN-SITU MONITORED GROWTH OF
SEMICONDUCTOR NANOCCLUSERS AND
NANOPARTICLES**

**DOCTORAL THESIS
(DISSERTATION)**

Accepted by the Bayreuth Graduate School of Natural and Mathematical Sciences (BayNAT) /
University of Bayreuth (Germany) in consideration of the academic grade of
Doctor rerum naturalium (Dr. rer. Nat.)
and The University of Melbourne (Australia) in fulfilments of the requirements of the degree of
Doctor of Philosophy (PhD)
in agreement with a joint-degree-agreement

submitted by

Maria Ritter, M.Sc.

born in Waischenfeld, Germany

ORCID 0000-0002-9777-9932

May 2018

Approval

This doctoral thesis was prepared at the department of Physical Chemistry I at the University of Bayreuth and the School of Chemistry at the University of Melbourne from June 2014 until May 2018 and was supervised by Prof. Dr. Stephan Förster and Prof. Dr. Paul Mulvaney within the DAAD Bayreuth-Melbourne Polymer/Colloid Network.

This is a full reprint of the dissertation submitted to obtain the academic degree of Doctor of Natural Sciences (Dr. rer. nat.) / Doctor of Philosophy (PhD) and approved by the Bayreuth Graduate School of Mathematical and Natural Science (BayNAT) of the University of Bayreuth and the University of Melbourne (Australia).

Date of submission:	04/05/2018
Date of defence:	11/09/2018
Acting director:	Prof. Dr. Dirk Schüler (University of Bayreuth)
Doctoral committee:	Prof. Dr. Stephan Förster (reviewer)
	Prof. Dr. Josef Breu (reviewer)
	Prof. Dr. Paul Mulvaney (additional reviewer)
	Prof. Dr. Peter Strohmriegl (chairman)
	JProf. Dr. Mirijam Zobel

Abstract

The formation processes of semiconductor nanomaterials and their size-controlled wet-chemical synthesis remain poorly understood, despite their importance. To realise the full potential of nanomaterials and to guarantee their successful implementation for cutting edge industrial applications, better insight into nanomaterial growth and assembly is essential. In this thesis, different semiconductor nanomaterial systems were chosen to highlight size-related properties arising from nano-confinement effects and to demonstrate the formation process in real-time. A range of formation regimes are studied, starting with the nucleation and growth of nanoclusters and nanocrystals, to their successful stabilization via inorganic and organic materials in the reaction mixture.

In a first study, in-situ methodologies in combination with ex-situ characterization techniques were used to study the formation of methylammonium-based perovskites. The successful adaption of the diffusion-controlled soft-template method to microfluidic devices allows the in-situ detection of highly crystalline superstructures through oriented attachment of nanocrystals. The structural evolution of the growth stages of the perovskite nanocrystals were confirmed by ex-situ electron microscopy. In a second study, a novel, room temperature synthetic route to diverse colloidal metal chalcogenide and metal halide nanocrystals was developed in organic solvents. The systematic variation of reaction parameter (e.g. reaction temperature, ligand system, precursor ratio and injection order) together with monitoring of the size-related optical properties enabled cluster growth to be followed, highlighting the quantum confined nature of the structures. The composition was analysed by X-ray diffraction and advanced electron microscopy techniques. In a final study, nanoclay-stabilized CdTe quantum dots were synthesized via hot-injection method in aqueous media. Large areas of well-separated quantum dot arrays along an inorganic material framework were studied through the detection of size-related absorption features and complementary characterization methods, such as atomic force microscopy, fluorescence microscopy and transmission electron microscopy.

These novel syntheses of inorganic/organic hybrid nanomaterials, as well as the novel methodologies developed to study their growth process, adds to growing pool of fundamental knowledge in the field of nanotechnology. This knowledge has the potential to augment the function of a variety of optoelectronic devices in the future.

This is to certify that:

- (i) This thesis comprises only my original work toward the PhD except where indicated
- (ii) due acknowledgement has been made in the text to all other material used
- (iii) the thesis is less than 100.000 words in lengths, exclusive of tables, figures, bibliographies and appendices.

.....

Maria Ritter

Acknowledgements/Danksagung

Ich möchte hier die Gelegenheit nutzen, um mich bei einigen Personen zu bedanken. Durch euren professionellen und freundschaftlichen Beistand ist die Anfertigung dieser Arbeit überhaupt möglich gewesen.

Mein größter Dank gilt meinen Doktorvätern/Supervisoren Prof. Dr. Stephan Förster und Prof. Dr. Paul Mulvaney für die Betreuung während der letzten Jahre. Ihr habt mir die Möglichkeit gegeben im Rahmen eines Double-Degree Programms zu promovieren und die wissenschaftlichen Arbeiten an den Lehrstühlen in Bayreuth und Melbourne durchzuführen. Vielen Dank für die stets offene Tür, die anregenden Diskussionen und die professionelle Begleitung während des gesamten Forschungsprojektes, was maßgeblich zum Gelingen dieser Arbeit beitrug.

Mein Dank gilt auch den Organisatoren, die beim Austausch im Rahmen des Bayreuth-Melbourne Polymer/Colloid Network mitgewirkt haben Dr. Arnim Heinemann, Dr. Murali Sukumaran, Dr. Melanie Pöhlmann, Sylvia Sprödhuber und Alex Strich. Dankbar anerkennen will ich ihre immer freundliche und uneingeschränkte Bereitschaft interkontinentale Herausforderungen zu meistern.

Herzlichen Dank an meine Mentoren in Deutschland und Australien Prof. Dr. Andreas Fery, Prof. Dr. Peter Strohriegel, Prof. Dr. Ken Ghigginio und Dr. Wallace Wong.

Ein großer Dank geht an Elisabeth Düngfelder, Jennifer Hennessy, Johanna Monk, Sarah Mulvey und Kathy Palmer. Ihr konntet mir so einige bürokratische Fragen beantworten. Eure organisatorische Unterstützung und euer Engagement hat mir mehr Zeit zum Forschen gelassen. Die warmherzigen und freundschaftlichen Gespräche haben dem Lehrstuhl familiären Flair verliehen.

Ich bedanke mich bei Dr. Stephan Hauschild für deine geduldige und auch aufopfernde Hilfe im IT-Bereich und deine kreative Problemlösung bei technischen Fragen. Deine Doppelkekse haben mich immer wieder zum Fußballtraining angespornt.

Vielen Dank an die technischen Angestellten Karlheinz und Julia, die den Laborbetrieb aufrecht gehalten haben. Die vielen kleinen Tätigkeiten, sei es Abfallentsorgung oder Sicherheitsbelehrungen, haben die Laborarbeit um einiges erleichtert. Karlheinz deine Geschichten bleiben unvergessen und ich hoffe du trägst deinen Akubra voller Stolz.

Ein besonderer Dank gebührt Dr. Sabine Rosenfeldt und Dr. Martin Dulle für die netten und beratenden Gespräche, die auch über den fachlichen Rat hinausgingen. Dankeschön an Vanessa, Maria und Susi die den Arbeitsalltag erleichtert haben. Besonders erwähnt sei die Unterstützung, wenn es um die Auswertung von Streudaten ging.

Ich möchte mich bei allen ehemaligen und gegenwärtigen Förstis bedanken, die mich seit meiner Bachelor-Arbeit begleitet und unterstützt haben: Nonio, Alex, Caro, Corinna, Eddie, Miriam, Matze, Jan, Misha, Sara, Corinna, Kilian, Tobias J., Sylvia und Xuelian. Ebenso bedanke ich mich bei der buntgemixten Arbeitsgruppe in Australien, wodurch ich einen Einblick in die verschiedenen Küchen und Kulturen erfahren konnte. Dadurch sind schöne Freundschaften entstanden die hoffentlich weiter anhalten. I thank my fellows Aruni, Calum, Cameroni, Christian, Heyou, Yue, Gangcheng, Pegah, Weijie G., Weijie N. Jiancaho, Xuying, Marc, Fabio, Sonam und Maja. I am so thankful James for the sleepless nights before the submission and all the fun we have had in the last time. You went through the draft of the thesis and corrected English grammar and usage.

Neben den Förstis und den Mulvanys möchte ich mich noch bei den Arbeitsgruppen von Matthias Karg, Markus Retsch und Anna Schenk bedanken: Tobi H., Julian, Astrid, Kirsten, Kristina, Arne, Patrick, Alex, Pia, Bernd, Anna und Johannes.

Herzlichen Dank an meine Praktikanten, die ich im Laufe der Jahre betreut habe und mit denen ich weiter dazulernen durfte.

Tobi G., Daniela und Sascha haben mich als Büro- und Laborkollegen super unterstützt und meine Launen ertragen. Ihr habt geduldig meine Millionen Fragen beantwortet und ihr habt jederzeit tatkräftig geholfen. Danke für die lustigen Abende, wodurch oftmals der Arbeitstag beschlossen wurde. Ich hoffe, dass der Kontakt weiterhin bestehen bleibt.

Danke an meine langjährigen Wegbegleiter Christian, Fadabi und David. Weit über die Arbeit hinaus habe ich von euch wertvolle Unterstützung und Beistand von Gleichgesinnten erfahren. Eure offenen und ehrlichen Worte weiß ich sehr zu schätzen. Ich hoffe, dass wir weiterhin in Kontakt stehen werden.

Zu guter Letzt möchte ich mich bei meiner großen Familie bedanken. Der größte Dank davon geht an Andreas, Sabine, Baptist, Stefan, Sophie, Basti, Julia, Frederik, Anna und Maxl. Danke für eure stetige Unterstützung, egal was ich mir in den Kopf setze oder wie stressig die Zeiten sind. Danke für euren Rückhalt und das Ertragen meiner Gemütslagen. Ich kann immer auf euch bauen und bin so unendlich dankbar dafür. Ihr seid die wichtigsten Personen – danke, dass es euch gibt!

Table of Contents

Abstract	v
Acknowledgements/Danksagung	vii
Table of Contents	ix
List of Tables	xii
List of Figure	xiii
Chapter 1	1
Introduction and Motivation	1
Chapter 2	3
Fundamentals	3
2.1 Fundamental Concepts of Colloidal Nanocrystals	3
2.1.1 LaMer Theory.....	3
2.1.2 Classical Nucleation	4
2.1.3 Classical Growth	6
2.1.4 Growth Mechanism of Nanoparticles.....	7
2.2 Semiconductor Clusters and Regular Quantum Dots	8
2.2.1 Regular Quantum Dots	8
2.2.2 Magic-sized (Nano-)clusters.....	11
2.3 General Aspects of Wet-chemical Colloid Synthesis	13
2.3.1 Strategy to Synthesize Semiconductor Materials at High Temperature	14
2.3.2 Strategy to Synthesize Semiconductor Materials at Room Temperature	15
2.4 Fundamentals of Microfluidics.....	16
2.5 Fundamentals of X-ray Scattering Experiments.....	18
2.6 Fluorescence and Confocal Microscopy	21
2.7 Cathodoluminescence in Scanning Electron Microscopy	24
2.8 Thesis Outline.....	27
References	28
Chapter 3	36
Experimental Methods and Instrumentation	36
3.1 Introduction	36
3.2 Chemicals	36
3.2.1 Materials for the CdTe/Nanoclay Nanocomposite Synthesis	36
3.2.2 Materials for CH ₃ NH ₃ PbBr ₃ Perovskite Synthesis	36
3.2.3 Materials for Metal Halide and Metal Chalcogenide Nanocluster Synthesis	37

3.3 CdTe/Nanoclay Nanocomposite Synthesis	37
3.4 Synthesis of Perovskite Nanocrystals.....	38
3.5 Synthesis of Semiconductor Nanoclusters	41
3.6 Instrumentation.....	45
3.6.1 Small Angle X-ray Scattering.....	45
3.6.2 UV-Vis Absorbance Spectroscopy and Analysis	46
3.6.3 Confocal Laser Scanning Microscopy.....	47
3.6.4 Transmission Electron Microscopy	47
3.6.5 Scanning Electron Microscope.....	47
3.6.6 Atomic Force Microscopy	48
3.6.7 Fluorescence Microscopy	48
3.6.8 Fluorescence Spectroscopy.....	48
3.6.9 X-ray Diffraction.....	49
References.....	47
Chapter 4.....	51
In-situ Growth of CdTe Quantum Dots on Hectorite Nanoclays in Aqueous Medium	51
4.1 Introduction and Motivation.....	51
4.2 Colloidal Materials: Combination of Nanoclay Minerals and Quantum Dots	53
4.2.1 Nanoclay Minerals.....	53
4.2.2 Formation of Semiconductor/Nanoclay Composites.....	56
4.2.3 Heat-up Synthesis CdTe	58
4.3 Experimental Section.....	59
4.4 Results and Discussion.....	62
4.4.1 Detection of Optical Properties	62
4.4.2 Fluorescence Microscopy	65
4.4.3 Atomic Force Microscopy	67
4.4.4 Transmission Electron Microscopy	71
4.5 Conclusion.....	76
Appendix 1	77
References	79
Chapter 5.....	84
Study of Nucleation and Growth Kinetics of Perovskite Nanocrystals	84
5.1 Introduction and Motivation.....	84
5.2 Structural Evolution of Perovskite Nanocrystals.....	85
5.2.1 AMX ₃ Organohalide Lead Perovskites	85
5.2.2 Kinetic Studies of Nanoparticle Formation with Microfluidic Systems.....	87
5.3 Experimental Section.....	88
5.4 Results and Discussion.....	89

5.4.1 Perovskite Large Scale Synthesis	89
5.4.2 Ex-situ Electron Microscopy	93
5.4.3 Microfluidic Experiments.....	104
5.4.4 Capillary Interdiffusion Experiment.....	111
5.5 Conclusion.....	123
References	124
Chapter 6.....	129
Novel Scalable Synthesis of Semiconducting Magic-sized Clusters and Nanocrystals	129
6.1 Introduction and Motivation.....	129
6.2 Semiconducting Clusters and Quantum Dots.....	131
6.2.1 Living-Metal Polymer Concept.....	131
6.2.2 Surfactant-Controlled Synthesis of Semiconductor MSC and QD.....	132
6.3 Experimental Section.....	134
6.3.1 Novel Scalable Synthesis	134
6.3.2 Metal Precursor	134
6.3.3 Anionic Precursor	135
6.4 Results and Discussion.....	140
6.4.1 Metal Chalcogenide.....	140
6.4.2 Silver Halides	184
6.5 Conclusion.....	203
Appendix 2	204
References	205
Summary.....	215
Zusammenfassung.....	218
Declaration/(Eidesstattliche) Versicherungen und Erklärung.....	222

List of Tables

Table 1: Perovskite large scale synthesis with different compositions of MABr, OABr and PbBr ₂	39
Table 2: Flow composition and the corresponding flow rates for the perovskite synthesis in the microfluidic chip.....	40
Table 3: Amounts of substances in mmol and g for the preparation of metal oleate precursor.....	41
Table 4: Amount of substance in mmol, mg and mL for the preparation of metal halide nanoclusters.....	43
Table 5: Amount of substance in mmol, mg and mL for the preparation of metal chalcogenide nanoclusters.....	44
Table 6: Synthetic conditions and optoelectronic information of nanoclay-based composites.....	65
Table 7: Characteristics of CdTe quantum dots attached on nanoclay edges at different reaction times.....	74
Table 8: Summary of experimental and standard diffraction patterns of lead nanocrystals.....	96
Table 9: Data of experimental and standard diffraction pattern of perovskite nanoplatelets.....	98
Table 10: Data of experimental and standard diffraction patterns of perovskite cubic bulk-like nanocrystals.....	100
Table 11: Comparison of the PL peaks during the formation process of large-scale synthesis and reported PL-signals.....	110
Table 12: Calculated parameters for the emission detection after the time Δt with respect to the channel position Δd_{x2} and the beginning of the interdiffusion process.....	111
Table 13: Comparison of the absorption peaks during the formation process in capillary, large-scale synthesis and reported absorption signals.....	116
Table 14: Structural information for CdS clusters including the calculated diameter D of the given nanocrystal sample with respect to the wavelength λ of the first excitonic absorption peak in the UV-Vis spectrum.....	145
Table 15: The structural information regarding ZnS clusters, including the calculated diameter D of the given nanocrystal sample with respect to the band gap of the cluster material.....	173
Table S1: 2θ values of the phases are stable at room temperature RT and after the phase transition into the α -AgI phase which are in good coincidence with the literature.....	204

List of Figures

Figure 1: Schematic representation of the LaMer model. The qualitative plotted curve describes the monomer concentration as a function of time.	4
Figure 2: Free energy ΔG diagram of the surface ΔG_S , bulk ΔG_B , and total free energy ΔG_T contributions as function of the particle radius r . The critical radius r_c describes the energy barrier for the smallest stable particle during the nucleation according the classical nucleation theory.....	5
Figure 3: Comparison of electronic energy states and bandgap of different types of semiconductor materials. Starting with inorganic bulk semiconductors with separated energy bands (left), different sizes of inorganic nanocrystals (quantum dots, middle) and molecular semiconductors with discrete energy levels (right) explain the origin of the nanoscale size effects.....	9
Figure 4: Schematic illustration of the reduced dimensionality of semiconductor nanocrystals. Bulk semiconductor, quantum well (2D), quantum rod (1D) and quantum dot (0D).....	10
Figure 5: Characteristic formation of magic-sized clusters (MSC) during the synthesis of regular quantum dots (QD). Different families of MSC can be observed within a series of growth steps. One cluster family arises at the expense of a smaller clusters sizes.....	12
Figure 6: Mercaptopropionic acid (MPA) is used as capping ligand for the controlled synthesis CdTe quantum dots of various sizes covering the emission window from 500 nm to 800 nm.....	15
Figure 7: Schematic representation of two incident X-rays (blue) on three atomic layers of a crystal, e.g. atoms are separated by the distance d . The X-rays are reflected (red) from the adjacent planes with the path difference between two X-rays of $2d \sin\theta$	19
Figure 8: Jablonski diagram displaying schematically the details of the absorption and emission process of a molecule (left) and the basic setup of a fluorescence microscope with light source, excitation filter, dichroic mirror, objective, emission filter and detector or eyepiece (right).....	22
Figure 9: Schematic setup of the confocal laser scanning microscope with the optical pathway and the principal components: the focused laser light, the pinholes, dichroic mirror and detector/photomultiplier (PMT).....	23
Figure 10: Schematic drawing of the teardrop-shaped interaction volume of the incident electron beam and the specimen. The origin of secondary electrons (SE), backscatter electrons (BE), Auger electrons (AE), X-rays and cathodoluminescence (CL) can be found in these electron-specimen interaction.....	25
Figure 11: Schematic representation of an experimental setup. The collimated X-ray beam hits the vertical sample. The scattered X-rays are detected by the SAXS detector in a vacuum tube which leads to the characteristic 2D scattering pattern. The sample-to-detector distance is responsible for the detected q -values of the scattered X-rays.....	46

Figure 12: Schematic representation of the use of nanoclays as support material for the selective adsorption of targeted pollutants in aqueous systems (e.g. heavy metals ions).....	52
Figure 13: General schematic structure of the layered $[\text{Na}_{0.5}]^{\text{inter}}[\text{Mg}_{2.5}\text{Li}_{0.5}]^{\text{octr}}[\text{Si}_4]^{\text{tetr}}\text{O}_{10}\text{F}_2$ hectorite. The sodium hectorite consists of parallel stacked tetrahedral-octahedral-tetrahedral aluminosilicate TOT lamellae ($\text{SiO}_2/\text{AlO}_2(\text{OH})_4/\text{SiO}_2$) which is separated by exchangeable Na^+ counterions.....	54
Figure 14: Side projection of exterior hydroxyl ions of TOT minerals which can be deprotonated under basic conditions.....	55
Figure 15: Simplified model after the osmotic swelling of nanoclay material. After mixing with Cd^{2+} ions at room temperature and an incubation time of 8 h the ions are adsorbed on the nanoclay edges due to electrostatic forces.....	60
Figure 16: Illustration of the in-situ growth process of CdTe quantum dots onto the negatively charged edges of nanoclays. After the adsorption of Cd^{2+} cations the pH value was adjusted to 12 followed by the injection of the TeH^- precursor with the exclusion of oxygen.....	61
Figure 17: Normalized absorption spectra of CdTe nanocrystals synthesized using cadmium acetate and sodium telluride hydride as precursor salt. Due to variation of the reflux time ($t = 1-35$ min) nanocrystals with various sizes can be obtained.....	62
Figure 18: TEM image of CdTe quantum dots after 35 min (drop casting) and the corresponding size distribution with $4.0 \text{ nm} \pm 0.9 \text{ nm}$ in diameter.....	63
Figure 19: UV-vis spectra of the nanocomposite dispersion synthesized using cadmium acetate and sodium telluride hydride as precursor salt in the presence of $\text{Na}_{0.5}$ -hectorite. Due to variation of the reflux time ($t = 5-120$ min) nanocrystals with various size can be obtained.....	64
Figure 20: Photograph of a series of CdTe-nanoclay composite materials taken after different reaction times demonstrating their size-related optical properties covering the visible and near-infrared region.....	64
Figure 21: Fluorescence image of CdTe/nanoclay nanocomposites (QDN-60), synthesized according to the hot injection route at 100°C for 60 min in water (1 wt% in water), showing quantum dot-labeled edges.....	66
Figure 22: Fluorescence image of CdTe/nanoclay nanocomposites, synthesized a by the hot injection route at 100°C for 60 min in water (1 wt% in water, QDN-60) showing quantum dots along the edges of stacked nanoclay lamellae.....	67
Figure 23: Topographical AFM images of a $\text{Na}_{0.5}$ -hectorite after the synthesis. (a) 2D image and b) 3D image nanoclays surrounded by CdTe quantum dots after 60 min reaction time (QDN-60). (c) and d) show sample QDN-75 with partially stacked nanoplatelets because of drying effects. (e) and (f) show 2D and 3D images of CdTe/nanoclay nanocomposite after 2 h (QDN-120).....	68

Figure 24: Topographical AFM images (a) and the corresponding cross section (b) of QDN-60 gives QD height of 2.03 nm. (c) and (d) height profile of CdTe/nanoclay composites with QD diameter of 2.85 nm (QDN-75). (e) and (f) show sample QDN-120 with mean diameter of 5.8 nm. The height of delaminated nanoclays is in the range 1.08 nm to 1.16 nm.....69

Figure 25: Phase AFM images (a) of nanocomposites QDN-60 and the corresponding cross section (b) after 60 min synthesis gave QD with 32.18° phase difference. After 75 min reaction time (QDN-75) the phase profile of 37.9° difference (c) and (d) show delaminated nanoclay composites a phase lag of 34.6° could be detected for QDN-120 after 120 min (e) and (f).....70

Figure 26: TEM images after the in-situ growth process (QDN-75: T=100 °C, 75 min) illustrate the size distribution of the well-separated nanocrystals as well as the nearly monodisperse morphology of the highly emissive CdTe quantum dots with an average size of 4.1 nm ± 0.9 nm (1 wt% in water, (a) scale bar 200 nm (b) scale bar 100 nm (c) scale bar 100 nm).....72

Figure 27: TEM images after the in-situ growth process (QDN-120: T=100 °C, 120 min) illustrate the size distribution of the well-separated nanocrystals as well as the nearly monodisperse morphology of the highly emissive CdTe quantum dots with an average size of 6.9 nm ± 1.5 nm (1 wt% in water, (a) scale bar 200 nm (b) scale bar 100 nm (c) scale bar 50 nm).....73

Figure S1: Additional data of AFM (left) and TEM (right) analysis of $[\text{Na}_{0.5}]^{\text{inter}} [\text{Mg}_{2.5}\text{Li}_{0.5}]^{\text{octr}} [\text{Si}_4]^{\text{tet}} \text{O}_{10}\text{F}_2$ hectorite to prove the delamination into single lamellae with lateral dimensions reaching from 0.5 to 10 μm and the typical height of the lamellae is found to be around 1.2 nm.....77

Figure S2: Additional data of AFM analysis of CdTe quantum dots synthesized via hot-injection method at 100 °C in aqueous medium.....78

Figure S3: AFM image to study the surface modification of $[\text{Na}_{0.5}]^{\text{inter}} [\text{Mg}_{2.5}\text{Li}_{0.5}]^{\text{octr}} [\text{Si}_4]^{\text{tet}} \text{O}_{10}\text{F}_2$ nanoclays after the in-situ growth of CdTe nanocrystals. The 7-fold amount of cadmium precursor (resp. $\text{Na}_{0.5}$ -hectorite, 14.8 g $\text{Cd}^{2+}/100$ g clay and 35 g $\text{Cd}(\text{acetate}) \times 2\text{H}_2\text{O}/100$ g clay) results in fully covered nanoclay lamellae.....78

Figure 28: Classification of AMX_3 -type perovskites into the alkali-halide perovskites and halide perovskites with monovalent (A), divalent (M) cations and a monovalent halide anion (X).....85

Figure 29: Schematic illustration of a cubic halide perovskites $\text{CH}_3\text{NH}_3\text{PbBr}_3$ unit cell (left) and perovskite nanocube surrounded by organic stabilizing ligands (right).....86

Figure 30: TEM images ((a)–(c)) show the formation of nanocrystal islands prepared with ratio $\text{PbBr}_2:\text{OAmBr}:\text{MAMBr}$ 0.1:0.3:0.1 (P03) in toluene (5.3 nm ± 1.0 nm in diameter).....89

Figure 31: TEM images ((a)–(c)) show the formation of ultra-thin nanoplatelets of various size prepared with ratio $\text{PbBr}_2:\text{OAmBr}:\text{MAMBr}$ 0.1:0.1:0.3 (P02) in toluene.....90

Figure 32: TEM images ((a)–(c)) show the formation of three-dimensional nanocubes prepared with ratio $\text{PbBr}_2:\text{OAmBr}:\text{MAMBr}$ 0.3:0.1:0.1 (P01) in toluene.....90

Figure 33: UV-Vis (left) and photoluminescence spectra (right) of $\text{CH}_3\text{NH}_3\text{PbBr}_3$ perovskites with ratio $\text{PbBr}_2:\text{OAmBr}:\text{MAMBr}$ 0.1:0.16:0.24 (P04) in toluene ($\lambda_{\text{exc}}=350$ nm) over 2 days.....	91
Figure 34: TEM images during the formation of smaller nanocrystals ((a)–(c)) in the early growth stages ($4.6 \text{ nm} \pm 1.7 \text{ nm}$ in diameter) prepared with the ratio $\text{PbBr}_2:\text{OAmBr}:\text{MAMBr}$ 0.1:0.16:0.24 (P04) in toluene.....	92
Figure 35: TEM images during the formation of nanocrystals and nanosheets, and smaller nanocrystals prepared with the ratio $\text{PbBr}_2:\text{OAmBr}:\text{MAMBr}$ 0.1:0.16:0.24 (P04) in toluene after one day.....	92
Figure 36: TEM results of perovskite nanocrystals: a) TEM image of the formation of nanocrystals and nanosheets (scale bar: 50 nm), b) selected area for the diffraction pattern (scale bar: 100 nm), d) SAED pattern (scale bar: 2 1/nm) of the marked area in (b) and the size distribution of the Pb^0 seeds ($6.1 \pm 2.1 \text{ nm}$ in diameter).....	95
Figure 37: TEM results of perovskite nanoplatelets: (a), (b) TEM image of the selected area for the diffraction pattern (scale bar: 500 nm and 100 nm), (c) SAED pattern (scale bar: 2 1/nm) of the marked area in (a) and (b), (d) the magnified image shows the crystal lattice of the perovskite grains (scale bar: 10 nm).....	97
Figure 38: TEM results of perovskite nanocubes: (a), (b) TEM image of the selected area for the diffraction pattern (scale bar: 200 nm and 10 nm), (c) the magnified image shows the expansion of the monocrystalline surface (scale bar: 10 nm), (d) SAED pattern of the marked area (scale bar: 2 1/nm) in (a)(c).....	99
Figure 39: SEM surface images of $\text{CH}_3\text{NH}_3\text{PbBr}_3$ nanocrystals synthesized via large scale synthesis result in cube-like morphologies of various sizes in the nm to μm region (P01: $\text{PbBr}_2:\text{OAmBr}:\text{MAMBr}$ 0.3:0.1:0.1). The images were taken with different detector combinations ((a-d) SE2 detector and (e, f) CL together with Inlens detector).....	101
Figure 40: SEM images of $\text{CH}_3\text{NH}_3\text{PbBr}_3$ nanocrystals synthesized at room temperature according to the large scale synthesis (P04: $\text{PbBr}_2:\text{OAmBr}:\text{MAMBr}$ 0.10:0.16:0.24). Ultrathin nanoplatelets stacked together to form superstructures were detected with ((a-d) SE2 detectors, (e, f) Inlens detectors).....	102
Figure 41: SEM images of colloidal $\text{CH}_3\text{NH}_3\text{PbBr}_3$ nanocrystals synthesized via large scale synthesis to adapt the reaction conditions on the capillary diffusion approach. The images ((a), (b), (e) SE2 detector and (c), (d), (f) Inlens detector) show ultrathin plate-like nanosheets and narrow distributed spherical nanocrystals ($6.5 \text{ nm} \pm 1.0 \text{ nm}$ in diameter).....	103
Figure 42: Photograph of the microfluidic chip mounted on the translational stage of the CLSM (right). Schematic PDMS-PPXn-based 3D double focusing hybrid chip connected to a 2-mm quartz capillary for photoluminescence detection during nanocrystal formation. Inlet 3 acts as the main channel and the inlets 1, 2, 4, 5 as side channels for buffer and precursor solutions (left).	104

Figure 43: Simplified overview of the microfluidic device after the second mixing cross. Fluorescence detection with Confocal Laser Scanning Microscopy (CLSM) along the channel gives information about the solvent-induced precipitation of perovskites.....	105
Figure 44: Brightfield images of the microfluidic channel. Image (a) was taken without solutions showing the first x1 and second channel cross x2 and the dimensions in μm . Image (b) shows the zoom-in of x1 and x2 with 3D focused streams A and B and the sheathing stream C.....	106
Figure 45: CLSM image of the EH09 chip during the perovskite formation along the microfluidic channel. Emission scans ($\lambda_{\text{exc}}=405\text{ nm}$) were taken along the channel ($\Delta d_{x2}=0.4\text{--}2.2\text{ mm}$).....	107
Figure 46: Multiplex emission spectra along the microfluidic channel ($\lambda_{\text{exc}}=405\text{ nm}$). A series of PL peaks could be detected which implies various numbers of corner-sharing PbBr_6 octahedra (attached unit cells) between 450 nm and 501 nm. The dominant emission peak shows a red-shift from 527 nm to 533 nm.....	108
Figure 47: Schematic representation of the diffusion process in a quartz capillary. The reaction components consist of the precursor salt (PbBr_2 , MAmBr) and the organic ligand (OAmBr) dissolved in DMF, buffer layer (DMF: Toluene 1:1), toluene.....	112
Figure 48: The perovskite nucleation and growth visualized by the instantaneous color change which can be monitored with in-situ UV-vis experiments (left: under normal light, right: under the UV-lamp $\lambda=365\text{ nm}$).....	113
Figure 49: UV-vis spectra: nucleation and growth of spheroidal $\text{CH}_3\text{NH}_3\text{PbBr}_3$ nanocrystals through interdiffusion in the capillary process. Increase of the intensity (a) and a red-shift from 437 nm to 451 nm (b) within $t = 26\text{ sec}$ implies the attachment of unit cells.....	114
Figure 50: UV-vis spectra: transformation of spheroidal $\text{CH}_3\text{NH}_3\text{PbBr}_3$ nanocrystals into nanosheets occurs with arising of the absorbance edge around 501 nm (c) due to attachment of corner-sharing PbBr_6 octahedra after 60 sec and absorbance edge at 522 nm (d) after 16 min....	115
Figure 51: Kinetic studies of the perovskite nucleation and growth monitored with in-situ UV-vis experiments.....	115
Figure 52: The time evolution of the ligand-assisted synthesis over the entire growth period. The stacks are formed from the 0-dimensional spheroidal nanocrystals via self-assembly processes over 2-dimensional precursor nanosheets into highly ordered stacks.....	116
Figure 53: Photograph of the setup used to monitor the perovskite nucleation and growth process with in-situ SAXS experiments (left: under normal light, right: UV-lamp $\lambda=365\text{ nm}$).....	117
Figure 54: SAXS measurement with 2.54 m sample-to-detector distance for sample P04. The scattering profile (left) shows the development of the structured peak at higher q-values within 100 sec and (right) the temporal structural evolution for the following minutes.....	118
Figure 55: Six representative SAXS patterns showing significant features for understanding the structural evolution after 9 sec, 11.5 sec, 25 sec, 50 sec, 500 sec and 1200 sec.....	118

Figure 56: Six representative SAXS patterns showing close agreement between experimental SAXS data (data points) and the corresponding fits (solid lines) for (left) $t=9$ sec, 11.5 sec, 25 sec and (right) $t=50$ sec, 500 sec and 1200 sec.....	119
Figure 57: SAXS patterns showing the development of the structure factor peak around 1.89 nm^{-1} after $t=11.5$ sec (left). The structural evolution of the structure factor peak can be detected after 1200 sec in the 2D scattering pattern (right).....	120
Figure 58: Intensity (left) of the structure factor peak and FWHM (right) vs. reaction time. The intensity remains constant and the FWHM becomes narrower from $t=400$ sec to $t=20$ min.....	121
Figure 59: SAXS measurement with 1.66 m sample-to-detector distance of sample P04. Scattering profile (left) shows the development of the structure peak at higher q -values within 100 sec and (right) the temporal structure evolution for the following minutes.....	122
Figure 60: Semiconducting material CdS, resulting in regular quantum dots. Ligand-stabilized Cd and sulfur precursors act as source materials in an organic solvent and the heterogeneous formation includes the nucleation and growth periods.....	130
Figure 61: Illustration of the two-step nucleation mechanism for the quantum dot growth starting with molecular precursor and magic-sized clusters as key intermediates.....	132
Figure 62: General approach for the synthesis of metal halide and metal chalcogenide magic-sized clusters at room temperature (RT) in organic solvents. A^+ represents the metal ion, B^- the halide or sulfur ion. Organic ligands act as stabilizing agents during the synthesis.....	134
Figure 63: Metal oleate reacts with primary amines to form metal oleate-amine complexes to achieve complete solubility of the metal precursor.....	135
Figure 64: General approach for the Finkelstein reaction for the conversion of tetraoctylammonium bromide to tetraoctylammonium iodide in presence of sodium iodide.....	136
Figure 65: Illustration of the liquid-liquid phase transfer of polysulfide anions into the organic phase with the help of the phase transfer agent tetraoctylammonium bromide (left). The photograph was taken directly after starting the phase transfer reaction (right).....	137
Figure 66: Absorbance spectra directly after the conversion of S/Na ₂ S in water. The main peaks are around 225 nm, 298 nm, 369 nm representing the coexistence of polyanions (left). After the phase transfer (S:TOABr 1:1) into the chloroform phase, the absorbance signal around 339 nm increases within 24 h. The phase transfer agent TOABr shows absorbance $\lambda < 250$ nm.....	138
Figure 67: In-situ UV-Vis detection showing the temporal evolution of CdS clusters with stoichiometric ratio of S: Cd 1:1 in cyclohexane at room temperature. The sulfur precursor (black curve) decomposes directly after injecting amine and cadmium oleate and induces the CdS cluster growth (green curves).....	140
Figure 68: Absorption spectra of CdS nanoclusters demonstrating heterogeneous growth with discrete steps at 259 nm, 285 nm, 311 nm, 348 nm and 380 nm (left). The sulfur precursor	

(dashed line) decomposes after the injection of amine and cadmium oleate and induces the CdS cluster growth (right).....	141
Figure 69: Synthesis of CdS clusters differing in their amounts of Cd(oleate) ₂ . The metal oleate was quickly injected into the sulfide-rich organic solvent at room temperature. Cd(oleate) ₂ increases the yield of the 285 nm- and 311 nm-species, whereas a higher sulfur content favours larger CdS clusters.....	143
Figure 70: TEM images of 1.6 nm CdS nanoclusters synthesized in cyclohexane (ratio S: Cd 1:2). The standard deviation could be calculated to 0.3 nm.....	144
Figure 71: TEM image of CdS clusters synthesized with ratio Cd:S 1:0.5 in cyclohexane. The corresponding diameter of 4.0 ± 0.7 nm and 1.7 ± 0.4 nm could be detected.....	146
Figure 72: Synthesis of CdS clusters differing in the initial ratio of sulfide precursor. The sulfur precursor was quickly injected into the metal-rich organic solvent at room temperature. Cd(oleate) ₂ increases the yield of the 285 nm- and 311 nm-species, whereas a higher sulfur content favours larger CdS clusters.....	147
Figure 73: Synthesis of CdS nanostructures with the initial ratio of S: Cd: R-NH ₂ 1:2:0. The metal oleate was quickly injected into the sulfur-rich organic solvent at room temperature. The 285 nm- and 311 nm-MSCs were not formed without the coordinating agents R-NH ₂	148
Figure 74: Synthesis of CdS nanostructures with the initial ratio of sulfide and Cd(oleate) ₂ precursor of 1:2. The metal oleate was quickly injected into sulfur-rich organic solvent at room temperature. Various amine amounts demonstrate the necessity of coordinating agent R-NH ₂	149
Figure 75: Synthesis of CdS nanostructures with the initial ratio of sulfide and Cd(oleate) ₂ precursor of 1:2. The metal oleate was quickly injected into the sulfur-rich organic solvent at room temperature. Various amounts of oleic acid demonstrate the influence of the coordinating agent R-COOH.....	151
Figure 76: Synthesis of CdS nanostructures with the initial ratio of sulfide and Cd(oleate) ₂ precursor of 1:2. The metal oleate was quickly injected into the sulfur-rich organic solvent at room temperature. In presence of oleic acid the equilibrium between 285 nm and 311 nm MSCs could be influenced towards the formation of the smaller species.....	152
Figure 77: Synthesis of CdS clusters with fix initial ratio of sulfide precursor and Cd(oleate) ₂ of 1:2 at three different temperatures (T=10 °C, 20 °C and 40 °C). The metal oleate was quickly injected into the sulfide-rich organic solvent. Lower temperatures favour the yield of the 285 nm- and 311 nm-species, whereas a higher temperatures favour the growth of regular CdS QD \geq 350 nm.....	153
Figure 78: Kinetic data demonstrate the absorbance at 311 nm and 285 nm as a function of time during the CdS clusters synthesis with sulfide precursor and Cd(oleate) ₂ ratio of 1:2 at T=40 °C	

(left). Semi-logarithmic plots were used for the calculation of the rate constants $k_1=0.050 \text{ min}^{-1}$, $k_2=0.00254 \text{ min}^{-1}$, $k_3=0.226 \text{ min}^{-1}$ and $k_4=0.00212 \text{ min}^{-1}$ (right).....	154
Figure 79: Kinetic plots demonstrate the absorbance at 311 nm and 285 nm as a function of time during the CdS cluster synthesis at three different temperatures ($T=10 \text{ }^\circ\text{C}$, $20 \text{ }^\circ\text{C}$ and $40 \text{ }^\circ\text{C}$)...	156
Figure 80: Synthesis of CdS clusters with fixed initial ratio of sulfide precursor and Cd(oleate)_2 1:2 and four different precursor concentrations at room temperature. The metal oleate was quickly injected into the sulfide-rich organic solvent and the absorbance values are proportional to the precursor concentration during the synthesis (Inset).....	157
Figure 81: Kinetic data from the growth of 285 nm and 311 nm CdS cluster of different concentrations. The time-dependent absorbance was detected at four different concentrations of 0.18 mM, 0.25 mM, 0.35 mM and 0.75 mM.....	158
Figure 82: Synthesis of CdS clusters with fixed initial ratio of sulfide precursor and Cd(oleate)_2 of 1:2 in solvents of different polarity. The metal oleate was quickly injected into the sulfide-rich organic solvent and the temporal evolution monitored by UV-Vis spectra.....	159
Figure 83: Absorbance spectra of CdS nanoclusters formed in octadecene ODE. A considerable amount of stabilizing ligands helped to maintain the colloid stability of clusters at higher temperatures.....	160
Figure 84: CdS MSCs in cyclohexane show the characteristic yellow fluorescence under the UV lamp ($\lambda=365 \text{ nm}$) (left) before and after the extraction with methanol in a two-phase system...	161
Figure 85: Time evolution of the absorbance spectra of CdS clusters for the sample containing the ratio Cd:S of 1:1 at $T=20 \text{ }^\circ\text{C}$. The sulfur precursor was quickly injected into the metal-rich organic solvent at room temperature. The yellow fluorescence is clearly visible under the UV lamp ($\lambda=365 \text{ nm}$) after 1 day (right).....	162
Figure 86: Time evolution of the corresponding fluorescence spectra of CdS clusters ($\lambda_{\text{exc}}=285 \text{ nm}$ and 300 nm) for the sample containing the ratio of Cd:S 1:1 at $T=20 \text{ }^\circ\text{C}$	163
Figure 87: Emission and excitation spectra of CdS clusters at room temperature. The excitation was performed at 285 nm for the sample containing the ratio Cd:S of 1:1. The sulfur precursor was quickly injected into the metal-rich organic solvent at room temperature.....	164
Figure 88: Absorption (left) and emission spectra (right) of CdS nanoclusters shows a strong dependency on the initial ratios of Cd(oleate)_2 and the sulfur precursor. The heterogeneous growth shows a set of magic-sized clusters at 259 nm, 285 nm, 311 nm, 348 nm and 380 nm...	165
Figure 89: Photograph of Teflon-based y-mixer connected to a 1-mm quartz capillary for spectroscopic detection during nanocluster synthesis. The precursor solutions are pumped through the Inlet A and Inlet B to the inlet junction. The structural evolution was monitored via an Ocean Optics spectrometer.....	166

Figure 90: In-situ UV-Vis detection within a microfluidic setup to investigate the temporal evolution of CdS clusters with stoichiometric ratio S:Cd of 1:2 in cyclohexane. The sulfur precursor (black curve) decomposes directly after injecting amine and cadmium oleate and induces the CdS cluster growth (green curves).....167

Figure 91: In-situ UV-Vis detection showing the temporal evolution of ZnS clusters with stoichiometric ratio S:Zn of 1:1 in cyclohexane at room temperature. The sulfur precursor (black curve) decomposes directly after injecting amine and zinc oleate and induces the ZnS cluster growth (blue curves).....169

Figure 92: Absorption spectra of ZnS nanoclusters with discrete absorbance signals at 230 nm, 264 nm and 282 nm (left). The synthesis of ZnS clusters with different ratios of sulfide precursor and Zn(oleate)₂ reaching from 1:0.5 to 1:2. The metastable ZnS products shown after one week (right) and the corresponding luminescence spectra with the emission maximum at $\lambda_{\text{max}}=380$ nm (bottom).....170

Figure 93: Absorption spectra of ZnS nanoclusters with discrete absorbance signals at 230 nm, 264 nm, 282 nm and 325 nm (left). The synthesis of ZnS clusters with the Zn(oleate)₂ and sulfide precursor ratio of 1:0.5 and 1:1 show metastable ZnS products which convert to smaller cluster species after one week (right). The corresponding luminescence spectra shows emission maxima at $\lambda_{\text{max}}=380$ nm and 450 nm (bottom).....171

Figure 94: TEM images of ZnS nanoclusters synthesized in cyclohexane S:Zn 1:0.5 (a, b, e) and Zn:S 1:0.5 (c, d, f). The well-separated nanoclusters show average sizes of $2.0 \text{ nm} \pm 0.6 \text{ nm}$ for S:Zn 1:0.5 and two fractions with $1.7 \text{ nm} \pm 0.7 \text{ nm}$ and $4.0 \text{ nm} \pm 0.6 \text{ nm}$ for Zn:S 1:0.5.....172

Figure 95: In-situ UV-Vis detection showing the temporal evolution of PbS clusters with stoichiometric ratio S:Pb of 1:1 in cyclohexane at room temperature. The sulfur precursor (black curve) decomposes directly after injecting amine and lead oleate and induces the PbS cluster growth (red curves).....175

Figure 96: Absorption spectra of PbS nanoclusters showing weak but pronounced absorbance signals at 253 nm, 293 nm and 336 nm (left) according to their synthesis with different ratios of sulfide precursor and Pb(oleate)₂ (S:Pb 1:0.5 to 1:2). Changing the injection order lead to pronounced absorbance signals at 266 nm, 310 nm, 360 nm and 450 nm (right) after one day..176

Figure 97: The observable band gaps determined by the experimental data. Extrapolating the linear parts of $[\hbar\omega\sigma(\omega)]^2$ against the energy axis $\hbar\omega$ gives $E_g=3.80 \text{ eV}$, 4.05 eV and 4.10 eV for Pb:S 1:0.5, 1:1 and 1:2.....177

Figure 98: TEM images of PbS nanostructures synthesized in cyclohexane S:Pb 1:0.5 (a, b, e) and Pb:S 2:1 (c, d, f). The well-separated nanoclusters show average sizes of $2.5 \text{ nm} \pm 0.9 \text{ nm}$ for S:Pb 1:0.5 and $2.4 \text{ nm} \pm 0.7 \text{ nm}$ for Pb:S 1:2.....178

Figure 99: The corresponding luminescence spectra show emission maxima around $\lambda_{\max}=409$ nm and 568 nm.....	179
Figure 100: In-situ UV-Vis detection showing the temporal evolution of Ag_2S clusters with stoichiometric ratio S:Ag of 1:1 in cyclohexane at room temperature. The sulfur precursor (black curve) decomposes directly after injecting amine and silver oleate and induces the Ag_2S cluster growth (grey curves).....	180
Figure 101: Absorption spectra of Ag_2S nanocluster samples showing weak but pronounced absorbance signals at 246 nm, 261 nm, 299 nm and 355 nm (left) depending on their synthesis with different ratios of sulfide precursor and Ag(oleate) (S:Ag1:0.25 to 1:2). Changing the injection order leads to pronounced absorbance signals at 246 nm, 299 nm, and 353 nm (right) after one day.....	181
Figure 102: TEM images of Ag_2S nanostructure synthesized in cyclohexane with S:Ag 1:0.5 (a, b, e) and S:Ag 1:2 (c, d, f). The well-separated nanoclusters show average sizes of $5.8 \text{ nm} \pm 0.8 \text{ nm}$ for S:Ag 1:0.5 and $3.0 \text{ nm} \pm 0.7 \text{ nm}$ for S:Ag 1:2.....	182
Figure 103: The corresponding photoluminescence spectra show emission maxima around $\lambda_{\max}=380$ nm and 401 nm.....	183
Figure 104: The UV-vis spectra of energetically favored AgBr clusters show their absorbance peaks around 240 nm, 255 nm, 273 nm in cyclohexane and CHCl_3 as co-solvent. 179	
Figure 105: Absorption spectra of AgBr nanoclusters with absorbance signals at 240 nm, 255 nm, 273 nm. Nanoclusters were prepared with different ratios of bromide precursor and Ag(oleate) (Br:Ag1:0.10 to 1:55).....	186
Figure 106: Absorbance spectra of AgBr clusters and regular quantum dots with ratios Ag:Br 1:6 to 1:1.0. Pronounced absorbance signals could be detected at 273 nm and 304 nm (left). The absorbance spectra (right) gives an overview of stable AgBr clusters synthesized by the two approaches.....	187
Figure 107: TEM images of AgBr nanostructures synthesized in cyclohexane Br:Ag 1:0.30 (a, b, e) and Br:Ag 1:0.55 (c, d, f). The well-separated nanoclusters show average sizes of $1.2 \text{ nm} \pm 0.4 \text{ nm}$ for Br:Ag 1:0.30 and $1.6 \text{ nm} \pm 0.3 \text{ nm}$ for Br:Ag 1:0.55.....	188
Figure 108: TEM images of AgBr nanocrystals synthesized in cyclohexane Ag:Br 1:1.0 show average sizes of $21.0 \text{ nm} \pm 3.0 \text{ nm}$	189
Figure 109: UV-vis spectra showing the cluster formation at three different temperatures ($T=10$ °C, $T=20$ °C and $T=40$ °C) and four different ratios Br:Ag 1:20 to 1:0.55. At higher temperature, the absorption decreases due to peak broadening (FWHM at ratio Br:Ag 1:0.55: $T=10$ °C: 14 nm, $T=20$ °C: 15 nm, $T=40$ °C: 25 nm).....	190

Figure 110: UV-vis spectra showing the cluster formation at three amine ratios Br:Ag:R-NH₂ 1:0.55:25 to 1:0.55:80. A higher amine content leads to the formation of red-shifted and broadened AgBr cluster species.....191

Figure 111: The UV-vis spectra of energetically favored AgI clusters show their decomposition of the iodide precursor (265 nm and 293 nm) and absorbance peaks around 274 nm, 295 nm in cyclohexane and CHCl₃ as co-solvent.....193

Figure 112: The UV-vis spectra of energetically favored AgI clusters shows the decomposition of the iodide precursor (265 nm and 293 nm) and absorbance peaks around 274 nm, 295 nm in cyclohexane and CHCl₃ as co-solvent. Nanoclusters were prepared with different ratios of iodide precursor and Ag(oleate) (I:Ag 1:0 to 1:55).....194

Figure 113: Absorbance spectra of AgI clusters and regular quantum dots with ratios Ag:I 1:10 to 1:0.50. Pronounced absorbance signals could be detected at 274 nm, 300 nm, 325 nm and 422 nm (left). The absorbance spectra (right) gives an overview of stable AgI clusters synthesis by the two approaches.....195

Figure 114: TEM images of AgI nanostructures synthesized in cyclohexane I:Ag 1:0.10 (a, b, e) and I:Ag 1:0.55 (c, d, f). The well-separated nanoclusters show average sizes of 1.1 nm ± 0.3 nm for I:Ag 1:0.10 and 1.8 nm ± 0.5 nm for I:Ag 1:0.55.....196

Figure 115: TEM images of AgBr nanocrystals synthesized in cyclohexane Ag:I 1:0.50 showing average sizes of 38.0 nm ± 8.6 nm.....197

Figure 116: Absorbance spectra of AgI clusters and regular quantum dots with ratios of I:Ag 1:0.55 and Ag:I 1:0.50. The AgI dispersion can be influenced by the addition of solvents CHCl₃ and EtOH with higher polarity resulting in red-shifts of the absorption signals.....198

Figure 117: Emission spectra of AgI clusters and regular quantum dots with ratios of Br:Ag 1:0.55 and I:Ag 1:0.55. Silver rich clusters for AgI and AgBr at 360 and 370 are formed along with pure silver rich clusters.....199

Figure 118: XRD spectrum of β- and γ-AgI nanocrystals at room temperature synthesized via our novel approach in organic solvent at room temperature.....200

Figure 119: XRD spectrum of AgI nanocrystals synthesized via our novel approach in organic solvent at room temperature. The β- and γ-phases are stable at room temperature and undergo phase transition to the α-AgI phase at higher temperatures.....201

Figure 120: STEM-EDS analysis for studying the composition of AgBr nanocrystals (10 nm, STEM (a)). Elemental mapping (b) and line profiling (c) evidence the presence of bromide (blue) in AgBr nanocrystals202

Figure S1: Absorbance spectra showing the characteristic signals of the sulfur precursor after the reaction with oleic acid and amine as well as the CdS cluster.....204

Chapter 1

Introduction and Motivation

Nanomaterials deal with small particles with at least one dimension in the size range from 1 nm to 100 nm. Their structures range from atoms to bulk materials and their properties are determined by their size and morphology.^[1] The extreme spatial confinement leads to the so-called 'quantum confinement effect'. The most illustrative examples are semiconducting nanomaterials and scientists have shown great interest and ingenuity in exploring their material properties over the last decades.^{[2][3][4]}

Beside the quantum confinement effect the large effective surface area is also responsible for essential and outstanding features of colloid nanomaterials which are beneficial and attractive for further technologies.^{[5][6][7]}

Inorganic nanocrystals show novel and unique size and shape dependent magnetic^{[8][9]} electronic^{[9][10]}, catalytic^[6] and optical^{[9][10]} properties based on these aforementioned nano effects^[1]. They have received considerable attention and show potential application in fields such as magnetic data storage^[11], solar cells^[12], catalysis^[5]. Therefore, the research field of colloid chemistry is a rapid evolving area in view of the development of synthetic techniques to generate nanocrystals which are uniform in shape, size and stoichiometry. Recent synthetic advances demonstrate the production of high-quality nanocrystals with novel functionalities.^{[13][14][15]} The focus lies in methods which are easy to upscale, highly versatile for varying compositions, and a good size, shape and surface control. Essential studies^{[2][16][17][18]} over the last two decades investigated the size- and shape-tunability of nanoparticles and their structure-related properties to gain a better understanding and insight in the field of colloid chemistry.

Current research is also focused on the development and successful implementation of nanomaterials for technological applications.^[1] The combination of ease of fabrication and processing of nanomaterials while maintaining their outstanding properties requires intensive research efforts which are the subject of on-going studies.^{[19][20]}

The grand challenge lies in the fundamental understanding of the nucleation and growth process of nanocrystals, because the ability to control their size and shape is important for the development of synthetic routes to prepare high-quality semiconductor nanocrystals. Organometal halide perovskites show remarkable optoelectronic properties and hold a vast potential for new photovoltaic applications. Therefore, structure-related studies should open up opportunities for

fundamental research on the controlled synthesis and characterization of the hybrid perovskite family.

Much attention has been paid to the regular quantum dot growth of III-V or II-VI semiconductors, whereas the experimentally observed formation of their magic-sized cluster (MSC) intermediates is still poorly understood. Their significance in fundamental studies, mainly due to their size-dependent properties of molecule-like precursors with discrete numbers of atoms should be addressed for an enhanced understanding of the colloidal synthesis.^{[25][26]}

Recent studies using the combination of ex-situ and in-situ characterization techniques such as X-ray scattering^{[21][22]}, transmission electron microscopy (TEM) and UV-Vis spectroscopy^{[23][24]} have given a better insight into the growth process of nanocrystals in solution. Such methods should be useful to monitor the nucleation and growth process of nanomaterials showing confinement effects.

Chapter 2

Fundamentals

2.1 Fundamental Concepts of Colloidal Nanocrystals

The grand challenge in synthesizing nanocrystals of high quality (crystallinity, monodispersity etc.) is to understand the interplay of the reaction factors (e.g. precursor reactivity, precursor concentration and reaction temperature) and the growth process in detail. For many years, the formation process of colloidal systems was described by basic theoretical models which are explained in the following paragraphs.

2.1.1 LaMer Theory

The formation process of inorganic nanocrystals according to the model of LaMer and Dinegar^[27] has been known since 1950 and can be divided in three parts which are illustrated in figure 1:

I) The free monomer concentration in solution increases rapidly with proceeding reaction time. After reaching the supersaturation level C_s , homogenous nucleation is possible but effectively infinite.

II) After exceeding a critical nucleation concentration C_{min} level the system has to surpass a high energy barrier for the self-nucleation. The burst nucleation reduces the free monomer concentration which drops below the critical level and no additional nucleation occurs.

III) Nanocrystals grow under the control of monomer diffusion towards pre-existing nuclei in solution. The reaction on stable nuclei surfaces results in discrete particles under the consumption of monomers. For the preparation of monodisperse nanoparticles the separation of nucleation and growth processes is essential and a high nucleation rate is followed by a slow growth process.^[18]

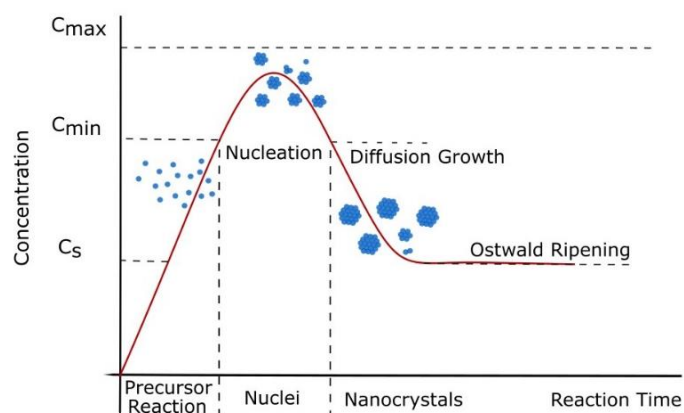


Figure 1: Schematic representation of the LaMer model. The qualitative plotted curve describes the monomer concentration as a function of time.

2.1.2 Classical Nucleation

The basic idea of the separation of nucleation and growth^[18] can be interpreted as the division into a homogenous and heterogeneous phase. The energy barrier for the generation of nuclei from solution (homogenous nucleation) compared to the growth process at the expense of monomers onto existing stable nucleating surfaces (heterogeneous nucleation) is much higher. The classical nucleation^[28] theory is the expression for the thermodynamically driven formation process which is depicted in figure 2.

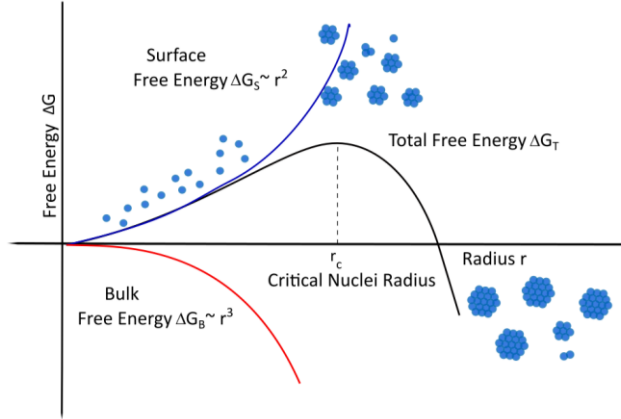


Figure 2: Free energy ΔG diagram of the surface ΔG_S , bulk ΔG_B , and total free energy ΔG_T contributions as function of the particle radius r . The critical radius r_c describes the energy barrier for the smallest stable particle during the nucleation according to the classical nucleation theory.

The homogeneous nucleation is described by summing the total free energy of a system ΔG_T of spherical particles with radius r . The principal aim of the model is to estimate the formation of a stable nucleus in which the total free energy of ΔG_T is in general expressed as the sum of the surface free energy ΔG_S with surface energy γ and bulk free energy ΔG_B , which is dependent upon temperature T , Boltzmann's constant k_B , supersaturation of the solution S and molar volume v of the system.

$$\Delta G_T = 4\pi r^2 \gamma + \frac{4}{3} \pi r^3 \Delta G_B \quad (2.1)$$

$$\Delta G_B = -k_B T \ln(S)/v \quad (2.2)$$

Changing the experimental parameters like temperature T , supersaturation S and surface free energy ΔG_S due to variation of stabilizing ligands has strong effects on the system.^[18] The contribution from the bulk free energy term ΔG_B is always negative and favours nuclei formation in a supersaturated system. The positive term of the surface free energy ΔG_S describes the unfavourable formation of new surfaces. The total free energy ΔG_T as a function of radius r represents a maximum free energy which a nucleus needs to become stable, without getting redissolved.

$$\Delta G_C = 4/3 \pi \gamma r_c^2 \quad (2.3)$$

This energy barrier is called the critical free energy ΔG_C which is required to obtain stable particles with the critical radius r_C .

$$r_C = \frac{-2\gamma}{\Delta G_B} \quad (2.4)$$

The critical particle radius corresponds to the minimum size particles which persist in solution before growing further.

2.1.3 Classical Growth

According to the classical nucleation model^[28], nuclei are formed which act as templates for further crystal growth. Each growing particle can be treated as a spherical and independent particle which is surrounded by a concentration gradient with spherical symmetry.^[29] The growth process can be described according the classical growth theory^{[18][30]} and consists of monomer diffusion to the surface and then reaction at the surface. Both the number of nuclei and free monomers control the growth process.

The diffusion mechanism can be described according Fick's first law^[29], where the monomer transport J is proportional to the diffusion coefficient D and x is the distance to the centre of the particle. The monomer concentration gradient $\frac{dC}{dx}$ is the driving force and is also proportional to the flux of the monomers to the particles J .

$$J = -4\pi x^2 D \frac{dC}{dx} \quad (2.5)$$

For particles in solution, where δ is the distance from the particle surface to the bulk monomer concentration C_B and C_I the monomer concentration at the solid/liquid interface, Fick's first law can be rewritten as

$$J = -\frac{4\pi D r(r+\delta)}{\delta} (C_B - C_I) \quad (2.6)$$

For nanosized particles, the particle radius r is smaller than the diffusion layer δ ($r \ll \delta$) and can be neglected. After the diffusion to the particle, the surface reaction can be written as

$$J = -4\pi r^2 k(C_B - C_R) \quad (2.7)$$

Where the rate of the surface reaction, k , is independent of the particle size, and C_R is the concentration at the surface of the particle. For the classical growth model, either the monomer diffusion to the particle surface or the monomer reaction at the surface is the limiting factor. If the monomer-surface reaction is faster than the diffusion step, it can be ascribed as a diffusion controlled ($D \ll k_r$, k_r : rate of surface reaction) process. The opposite case describes a surface reaction rate controlled ($D \gg k_r$) process, where the diffusion rate is much higher than the reaction rate.

2.1.4 Growth Mechanism of Nanoparticles

Different existing models describe the growth mechanisms that produce nanocrystals and which dictate the final morphology of nanoparticles. Modern in-situ characterization techniques^[31] allow the evaluation of the growth process based on new concepts of non-classical growth of inorganic nanoparticles.^[32]

Monomer attachment describes the initial growth process after the nucleation stage.^[32] The mechanism includes two similar processes: coalescence^[33] and orientated attachment^{[34][35]} which differ in the orientation of the crystal lattice. The coalescence describes the non-preference for grain attachment among neighbouring grains which leads to randomly orientated lattices planes.^[31] The orientated attachment, also known as the grain rotation-induced grain coalescence mechanism (GRIGC), is the perfect crystallographic alignment of the lattice planes and coalescence of neighbouring grains, eliminating a common grain boundary. The rotation of grains during the attachment is driven by low energy configurations.^[36]

In 1950 the widely used nucleation and growth model of LaMer was described the first time and it is also interpreted for the synthesis of nanocrystals. According to this model, the diffusion and the consumption of monomers result in particle growth. Oriented attachment is a new approach to explain the growth process of nanocrystals and does not match with the classical model by LaMer. The approach was increasingly described in the last twenty years and explains the self-assembly into single-crystalline nanostructures from individual particles.^{[34][35]} There is no current model for quantifying this growth process and modelling the growth kinetics.

Ostwald ripening occurs in the later growth stages.^[31] The thermodynamic driven mechanism describes the growth process of larger particles at the expense of smaller particles in solution.^[37] The atoms from smaller particles undergo dissolution because of high solubility and surface energy, resulting in larger particles. Digestive ripening^[38] can be explained as the inverse Ostwald ripening process. Colloidal particles are transformed in smaller particles at the expense of large ones by the reduction of the interfacial free energy.^[39]

The controlled synthesis of high quality semiconductor nanocrystals has been an important material chemistry research topic. The shape control of CdSe nanocrystals was described by Peng and co-workers as interparticle growth process.^[40] The interplay of chemical potential of the bulk solution and the surface energy of the particle facets is responsible for the diffusion-controlled growth process of the monomer along the nanocrystal surface.

2.2 Semiconductor Clusters and Regular Quantum Dots

Nanomaterials are attracting increasing attention due to their novel, tunable and fascinating electronic and optical properties. The following chapter addresses semiconducting materials and the impact of size reduction within the nanometer region. Two main effects related to reduced size of nanomaterials are investigated: the quantum confinement effect and a large volume-to-surface ratio which are explained in more detail.

2.2.1 Regular Quantum Dots

Regular quantum dots (QD) are semiconductor nanocrystals composed of periodic group III-V or II-VI semiconductor materials such as ZnS^[41], PbS^[42], CdS^[43], CdSe^{[43][44][45]}, CdTe^{[43][46]} They consist typically of 100–100,000 atoms per QD and have sizes between 2-50 nm depending on the material.^[47] They have been studied because of their novel optoelectronic functionalities resulting from their unique size- and shape-dependent properties due to nanoscale size effects.^{[1][2][45]} The size effects find their origin in the quantum confinement and surface effect which are defined below.

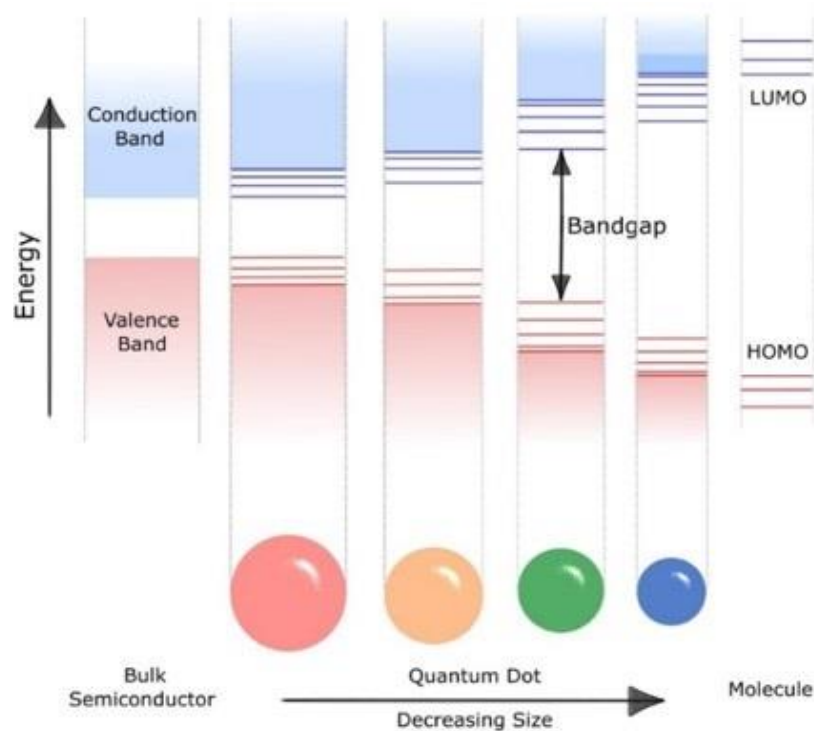


Figure 3: Comparison of electronic energy states and bandgap of different types of semiconductor materials. Starting with inorganic bulk semiconductors with separated energy bands (left), different sizes of inorganic nanocrystals (quantum dots, middle) and molecular semiconductors with discrete energy levels (right) explain the origin of the nanoscale size effects.

Calculations according to the Linear Combination of Atomic Orbitals (LCAO) theory^[48] provide more information about the energy band structure in crystalline materials of different sizes.^{[47][49]} In principle, the combination of atomic orbitals leads to the evolution of bonding and anti-bonding molecular orbitals (energy states).^[47] The electrons from the individual atoms occupy the bonding molecular orbitals (highest occupied molecular orbital, HOMO). The first unoccupied antibonding orbital is termed the lowest unoccupied molecular orbital (LUMO). The HOMO and LUMO levels are separated by a forbidden energy bandgap E_g where no orbitals exist. For crystalline bulk materials the number of atoms increases ($\sim 10^{23}$ atoms) and the electronic structure changes from a discrete energy level structure to continuous energy bands.^[47] The total number of energy levels increases with the number of atoms in the molecule and becomes a continuous energy band. The conduction band is equivalent to the LUMO level and the valence band consists of bonding molecular orbitals (formerly HOMO). For semiconductor materials the energy bands are split into

two, separated by the bandgap making them different to the parent metal band structure. Nanosized QDs can be considered as large molecules and show the formation of a quantized electronic band structure.^{[48][49]} With the absorption of photons, excitons can be generated which are the bound state of electrons and electron holes driven by electrostatic Coulomb forces.^{[47][49]} The Coulomb forces in semiconductor nanocrystals is much higher compared to bulk material. Due to the size restriction in nanocrystals the spatial extension of the exciton wave function is confined.^{[45][47][48]} The spatial restriction of the exciton wave function and also the density of electronic states and the bandgap separation E_g .

The degree of the quantum confinement^{[16][48][49]} depends on the nanocrystal shape and is useful for the classification of nanomaterials (Figure 4). Nanoparticles can be synthesized with confinement in all directions (0D). For anisotropic nanocrystals, like quantum rods, wires or tubes, the excitons are confined in only one direction (1D). Nanoplatelets or thin films have the confinement only in their thickness (2D). Due to the ongoing restriction in their dimensions, the density of energy states changes from bulk material (3D) to discrete quantized energy levels for 2-, 1- and 0-dimensional structures.

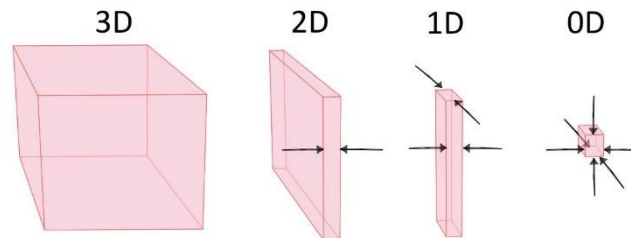


Figure 4: Schematic illustration of the reduced dimensionality of semiconductor nanocrystals. Bulk semiconductor, quantum well (2D), quantum rod (1D) and quantum dot (0D).

The impact of the quantum confinement effect on the quantum dot properties can be evaluated by the size restriction of the QD and the corresponding Bohr radius r_B .^[48] One can distinguish between the weak confinement regime and the strong confinement regime depending on the semiconductor nanostructure.^{[17][48]} The confinement phenomena lead to massive changes in the optoelectronic properties of semiconductor nanocrystals and the QD becomes strongly size- and shape-dependent.^{[1][16][17]} By implication, the examination of the light absorbance together with empirical calculations^{[48][50][51][52]} and the photoluminescence/quantum yield detection^{[17][41][53]} give

information about electronic and optical material properties including the bandgap of semiconducting materials and their elemental composition.^{[2][17][48]}

The second finite size effect is the increased surface-to-volume ratio and important consequences of this are surface-related phenomena.^{[6][13][45][48][54]} The relative proportion of surface atoms in small quantum dots increases with smaller particle sizes, while the total number of atoms gradually decreases. Due to the exceptionally large surface-to-volume ratio, the surface becomes the dominant player in many chemical and physical processes. Surface effects, and particularly surface defects for charge carriers,^{[48][55]} lead to quenching of the radiative recombination of excitons in QDs and to a reduced emission and quantum yield. These so-called surface traps are caused by lattice defects and dangling orbitals. Passivating agents (i.e. ligand molecules) can be used to coat the surface of colloidal nanocrystals to prevent nonradiative recombination of excitons at these traps.^{[9][18][48][56]} The surface modification is very important to lower the surface trap energy and to achieve photostable QDs. Additionally, the organic surfactants are able to control size and shape during preparation but also post preparative ligand exchange^{[13][18]} affect the colloid stability and the electronic/optical properties.

2.2.2 Magic-sized (Nano-)clusters

Over the last few years numerous research groups^{[4][25][26][52][57][58][59][60]} observed the synthesis of II-IV metal chalcogenide nanoparticles yielding some findings concerning the reaction kinetics. The synthesis of regular quantum dots based on a series of increasing size nanoclusters occurs according the 'living-metal polymer concept'.^[25] In the early stages of the reaction the creation and degradation of discrete nanoclusters could be observed by spectroscopic methods.^{[4][52][57][60][61][62]} The detection of narrow absorbance peaks during the growth of these products indicate the existence of small nanocluster species.

Magic-sized clusters (MSC) describe clusters of particularly high stability with a core diameter between $0.5 < d < 2$ nm.^{[52][57][61]} The MSCs consist of discrete numbers of atoms and show a high monodispersity in size and specific stoichiometry.^{[57][63]} Each cluster size refers to a stable atomic configuration which can be explained by the absence of regular quantum dots and ripening processes.^{[4][58]} A Gaussian fit can be used to characterize the absorbance signals with typical Full Width Half Maximum (FWHM) around 10-30 nm.^{[60][64]}

Peng et al.^[62] were able to synthesize CdSe at 250 °C and to monitor a sequential cluster formation in real-time during the reaction. The particle size 4 ms after the injection was calculated to be 1.75 nm. Kudera et al.^[53] observed different families of clusters during the synthesis of CdSe quantum dots by the consumption of more metal precursor. According to these studies, the result indicates that sharp absorption signals of highly stable nanocluster intermediates arise at lower temperatures, whereas at higher temperatures the life-span decreases significantly and the conversion into regular quantum dots could be monitored. The general mechanism describes that relatively mild reaction temperatures slow down the reaction rate and facilitate the study of magic-sized clusters. The formation process depicted in figure 5 involves the appearance of ultra-small cluster peaks in the early growth stages, followed by the diminishing of the cluster peaks and the evolution of new nanocluster sizes (small MSC).^[53] A high temperature is favourable for the transformation into regular quantum dots.

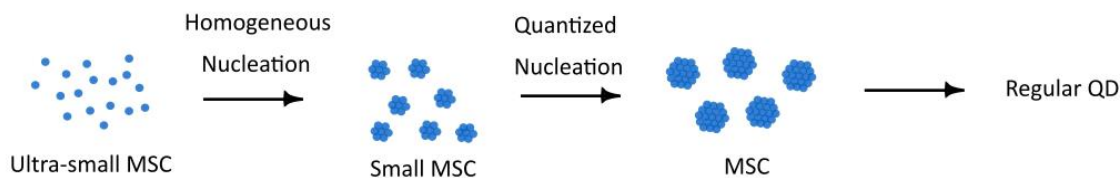


Figure 5: Characteristic formation of magic-sized clusters (MSC) during the synthesis of regular quantum dots (QDs). Different families of MSC can be observed within a series of growth steps. One cluster family arises at the expense of smaller cluster sizes.^[53]

The stepwise red-shift of individual absorbance peaks from various MSCs underline the sequential series of magic-sized clusters. After recording the UV-vis spectra over many hours, the average size of a family remains constant and grew only in size with sufficient stabilization through organic ligands. Dance et al.^[65] synthesized in 1984 the first chalcogenide molecular clusters and claimed that the presence of the ligands lead to stable molecular clusters. During the synthesis of MSCs the (co-)existence of cluster families can be detected which can be assigned to a heterogeneous growth process.^[57]

In contrast to this observation, the formation of conventional nanoclusters is termed a homogeneous growth process.^[57] The formation of polydisperse ensembles and the gradual shift of the bandgap

absorbance peak with time during synthesis are characteristic for the formation of ultra-small nanocrystals.^[60]

The unique behaviour of MSC is an interplay of the synthetic parameters like the temperature^{[58][61]}, the prepared starting material, the monomer concentration^{[52][60][61]} and nature of the ligands (ligand/QD surface chemistry)^{[58][60]}, the supersaturation caused by the monomer concentration, the solvent, the affinity of ligands and the ratio of monomers in the system.^{[57][64]} The formation and also the synthesis of stable semiconductor nanoclusters is more challenging compared to metal nanoclusters but all these different approaches gain better access to investigations of early growth stages. The isolation of MSC, their sensitivity to chemical treatments and their insufficient characterization with common methods are the reason that nanoclusters and their resultant properties are only transiently observed.

2.3 General Aspects of Wet-chemical Colloid Synthesis

Various methods are used for the preparation of nanocrystals and classified in two wide-ranging categories termed as 'Top-down' and 'Bottom-up' processes.^{[16][18]}

The 'Top-down' approach, describes the generation of nanostructures from larger initial objects. Typical physical based methods are lithography through etching^[66] or electron-beam lithography^[67]. Another way to produce nanoparticles is the application of ball mills^[68] where shear forces are necessary to break microparticles in nanoscaled particles. The advantage of these approaches is the production of large quantities of nanocrystals but it is challenging to fabricate uniform-sized nanocrystals with good size control.

The 'Bottom up' strategy uses building blocks like atoms and molecules which form larger structures through wet-chemical processes.^{[18][30]} In contrast to the 'Top-down' approach, homogenous nanocrystals in only sub-gram quantities can be produced. Semiconductor nanocrystals have been synthesized by solution-phase synthesis including the most popular synthetic procedures involving the 'hot-injection' method^{[2][18][43]} and the 'heat-up' synthesis^[30] of precursors.

2.3.1 Strategy to Synthesize Semiconductor Materials at High Temperature

The most common wet-chemical colloid methods are based on the formation of nanocrystals inside confining structures. The basic concept of the 'heat-up' synthesis is mixing the precursor at low temperature and doing the precursor reaction at higher temperatures. The first stage (according LaMer model, Chapter 2.1.1) is the precursor decomposition which occurs sufficiently quickly and results in supersaturation of the system. The supersaturation leads to burst nucleation (stage II) at controlled temperature followed by a seed-mediated growth process with the assistance of organic surfactants (stage III).^{[30][69]}

The alternative 'hot-injection' approach, consists of precursors which act as an initial monomer source in high boiling point organic solvents. For the solubilization and stabilization organic surfactants are present. For the synthesis in aqueous medium the precursor and stabilizing ligands show good solubility in water. The decomposition of the precursor at elevated temperatures and the injection of further components lead to a controlled nucleation event followed by the growth process to nanocrystals.^{[30][40][69]}

The ultrafast nanocrystal synthesis of CdE (E=S, Se, Te) in aqueous solution in presence of water soluble ligands could be prepared with NaHE and CdCl₂ as precursor (Figure 6).^[2] Zou et al. outlined the drastic impact of the monomer ratio, the stabilizing ligand, and the pH value of the reaction mixture. According to this method, quantum dots of high quality (i.e. crystallinity and optical properties) can be synthesized but the drawback is the high sensitivity of precursor and the production of toxic by-products. Chapter 4 in this thesis describes the important preparation of 'hot-injection'-prepared nanocomposites by monitoring the in-situ growth process.

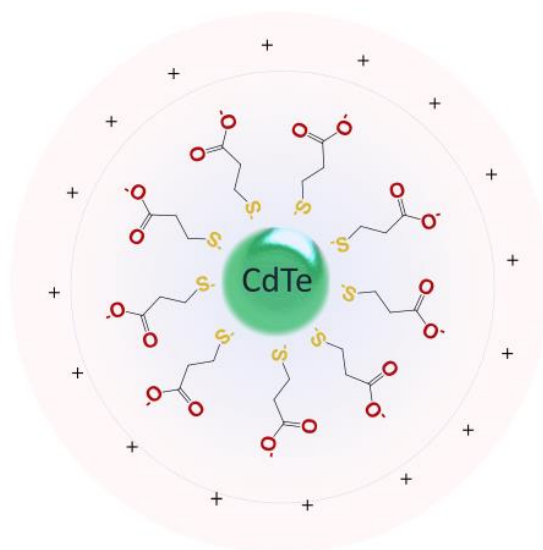


Figure 6: Mercaptopropionic acid (MPA) is used as capping ligand for the controlled synthesis CdTe quantum dots of various sizes covering the emission window from 500 nm to 800 nm.

For the formation of colloidal nanocrystals, the reaction parameters, such as reaction temperature and time, precursor decomposition, monomer concentration and solubility and diffusion and solvent play a crucial role. The choice of capping ligands is also essential because they act as mediator to control of the crystalline phase, and the size and morphology of the nanomaterials.^[56] For designing novel syntheses (see Chapter 6) appropriate reaction components should be carefully chosen by inspecting the decomposition and formation mechanism and the complex interplay of each reagent, which is still poorly understood.

2.3.2 Strategy to Synthesize Semiconductor Materials at Room Temperature

Beside the mentioned procedure, involving high-temperature thermolysis of precursors, the 'Bottom up' approach also includes the production of nanoparticles by 'Chemical Precipitation' at moderate temperature.^{[70][71]}

For instance, the preparation of high quality perovskite nanocrystals based on this concept^{[72][73]} can overcome the problem of thermal, moisture and photo-instability. The precursor of

methylammonium based perovskites (methylammonium lead perovskite, MAPbBr₃) were mixed in a suitable solvent which exhibit a good solvency for the solids. The subsequent addition of an anti-solvent induced crystallization because of the reduced solubility of the precursor ionic building blocks. Through the addition of anti-solvent, the supersaturation of the reaction system can be realized which leads to seed formation. Additionally, the growth process can be controlled through the addition of organic stabilizing ligands. In Chapter 5 more information is provided about the investigation of the nucleation and growth process of organic CH₃NH₃PbBr₃ perovskites based on the 'anti-solvent induced precipitation concept'.

An alternative procedure is based on a 'Lewis acid-base reaction' at room-temperature to synthesize II-VI semiconductor nanoclusters in absence of nanocrystals.^[58] For this synthesis, a metal, highly reactive halide-amine complexes, and octylammonium selenocarbamate, react in *n*-octylamine, the latter acting as both ligand and solvent. The reaction of the precursor according to the HSAB concept^[74] lead to the formation of *n*-octylamine-passivated nanoclusters in absence of larger nanocrystals. Characteristic absorption features clearly indicate the presence of alloy nanoclusters. A subsequent heating step results in the formation of larger nanocrystals. Chapter 6 uses a similar approach for the development of inorganic clusters and nanocrystals.

2.4 Fundamentals of Microfluidics

The introduction of microfluidic systems-based downscaling of conventional flask-based systems and laboratory-based analysis systems provides a new class of devices.^{[75][76]} For our interest, this approach is used for chemical transport and nanoparticle formation within microfluidic channels.^[77] The systems deals with small volumes of fluids, typically 10⁻⁹-10⁻¹⁸ litres, channels of tens to hundreds of micrometers and diffusion is the mass transport phenomenon which plays the major role.^[78] The aim of microfluidic systems is to enhance the mixing efficiencies and increase throughput.^[79] Micrometer-scale chips allow the integration of data analysis^{[21][24]} for in-situ detection of experimental conditions, and their combination with high-precision syringe pumps for the liquid transport through the channels. Detection techniques include UV-Vis and fluorescence measurements^[24], X-ray scattering experiments^{[21][80]}, and confocal laser scanning microscopy^{[77][80]} with high temporal and spatial resolution sensitivity. The systems are highly attractive because of their low sample consumption through the confined fluid flow, low fabrication costs, short time for

analysis and upscaling to industrial scales.^[78] The microfluidic approach for nanoparticle formation allows the separation and a precise study of nucleation and growth of crystals within the channel.

The fluid behaviour and the fluid dynamics of Newtonian fluids in confined microfluidic systems differ from those in macroscopic systems. In a micrometer-scale channel, capillary forces dictate the flow of the fluid and the stream is largely influenced by the surface energy of the channel walls and the surface tension of fluid itself.^{[81][82]} The fluid dynamics of Newtonian fluids is described by the Navier-Stokes equation, where ρ is the fluid density, u is the fluid velocity, f_{ext} is the external force acting on fluid, p the pressure of the fluid, and μ is the kinematic viscosity of the fluid.

$$\rho \left(\frac{\partial u}{\partial t} + ((u\nabla)u) \right) = f_{ext} - \nabla p + \mu \nabla^2 u \quad (2.8)$$

From the Navier-Stokes equation follows the Reynolds number, which is a dimensionless parameter used in studying fluids with the fluid velocity u , the dynamic viscosity and L , the length of the channel.

$$Re = \frac{\rho u L}{\nu} \quad (2.9)$$

These fundamental equations describe physical and chemical processes of well-defined flow conditions. For flows in long and straight channels, with radius/height of 1-100 μm and velocities not greater than the cm/s range, the Reynolds number for flow will be so low that all flow will be laminar.^[83] Under these conditions, diffusion is the important mass transport phenomenon which plays the major role in microfluidic devices.

The liquid flow inside microchannels is laminar, meaning that multiple liquid streams can flow side-by-side without turbulent mixing, allowing good spatial control.^[81] In laminar flow, the velocity of a particle is not a random function of time. The streamlines are all straight and parallel, and the magnitude of the velocity is constant. The ratio of inertial to viscous forces on fluids is characterized by the Reynolds number

$$Re = \frac{F_{inertial}}{F_{viscous}} \quad (2.10)$$

Pressure driven flow occurs in microfluidic devices in which the fluid is pumped through the device. The fluid dynamics in this case are assumed to have no-slip boundary conditions, meaning the velocity vector of a flowing fluid is assumed to be zero at the wall.

Within the channel a parabolic-flow profile is observed at any cross sectional view with the highest velocity along central streamline.^[82]

The Stokes flow region with very low Reynolds numbers ($Re \ll 1$) poses a challenge for mixing. Mixing along the channel occurs via diffusion when there is a concentration gradient of one kind of molecule within a fluid. The Péclet number, a dimensionless quantity, describes the transport phenomena defined as the ratio between the system length and the diffusion length.

$$Pe = \frac{Lu}{D} \quad (2.11)$$

Where L is the characteristic length, u is the average fluid velocity and D the diffusion coefficient. Furthermore, the Péclet number determines the required channel length for each component to diffuse across the channel width. For $Pe \gg 1$, the diffusion length is much shorter than system size and concentration gradients form within system. For $Pe \ll 1$, the diffusion length is much longer than the system size which describes a linear concentration profile.

Precise microfluidic design control^[78] enables fabrication of reproducible microfluidic channels. Fluids streams come together in the microfluidic channel and diffusion of molecules occurs across the interface between fluids (anti-solvent precipitation).

2.5 Fundamentals of X-ray Scattering Experiments

Optoelectronic properties of nanoparticles depend on the chemistry of the material and on the dimensionality, which includes the size and shape of nanomaterials ranging from 0D spherical objects, 1D nanorods and 2D nanosheets to 3D superstructures. In-situ small-angle (SAXS) and wide-angle X-ray scattering (WAXS) measurements are relatively non-destructive analytical methods and provide structural information about the nucleation and growth of nanomaterials.^[21] This chapter gives an overview of X-ray scattering and a basic account of the analysis method. X-rays are electromagnetic waves with wavelength from 0.1 nm to 10 nm and can be used for the study of objects with very small dimensions, including atoms, molecules and nanocrystals.^{[84][85]} In a typical scattering experiment, a collimated X-ray beam collides with a sample, where three interactions can be described. One fraction of X-rays will be absorbed, another fraction will pass through and a fraction will be scattered on the scattering objects.^[84] Scattering can be divided into

Compton scattering (inelastic scattering) and Thomson scattering (elastic scattering). Whereas Compton scattering does not carry structural information, Thomson scattering is interesting for fundamental structural studies. In this scattering event, the incoming photons hit the sample and scatter without energy transfer. The X-rays collide with the bound electrons of the scattering object and induce the oscillation of these electrons with the same frequency. This causes the emission of radiation with the same frequency of the incident wave. In case of an aperiodic scatterer, the emitted secondary waves are scattered in all directions.

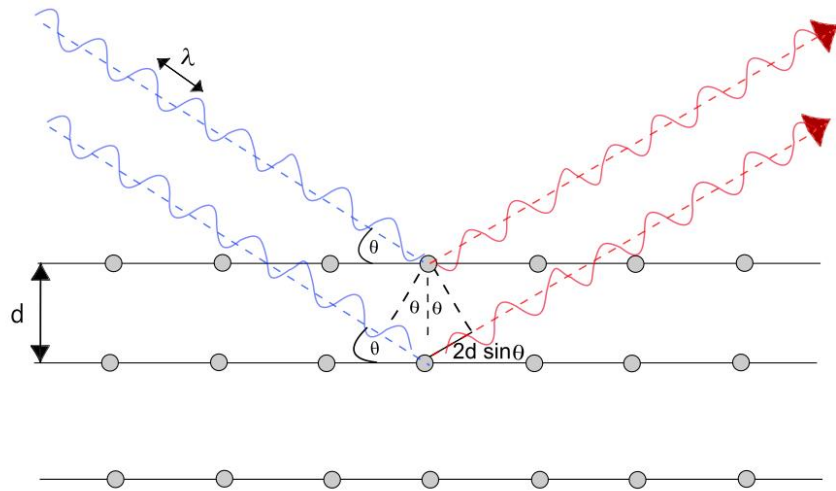


Figure 7: Schematic representation of two incident X-rays (blue) on three atomic layers of a crystal, e.g. atoms are separated by the distance d . The X-rays are reflected (red) from the adjacent planes with the path difference between two X-rays of $2d \sin \theta$.

For a periodic scatterer (figure 7), coherent waves of neighbouring atoms can interfere and scatter in precise directions. The scattered X-rays are detected and the information is summarized in an interference pattern caused by constructive (bright spots) and destructive interference.^[86] Bragg formulated a fundamental equation for the interference of X-rays which is defined as

$$n\lambda = 2d \sin \theta \quad (2.12)$$

The interplay of the scattering angle θ , the distance d of the periodic planes and the wavelength λ of the X-rays are described by Bragg's law. For constructive interference, the secondary X-rays are in phase and the phase difference $2d \sin \theta$ must be an integer number n of the wavelength λ . The conditions for Bragg's law are met. The destructive interference occurs when the equation is not

satisfied and this leads to dark spots in the interference pattern. The scattered X-rays are detected and lead to a 2D scattering pattern with structural information about the scatterer.

In the Fourier space, the Bragg's law is rewritten as

$$q = \frac{2\pi}{d} = \frac{4\pi}{\lambda} \sin\theta \quad (2.13)$$

and shows the reciprocal relation between the size of the particle d and the scattering angle θ . In contrast to the scattering angle θ , the 'length of the scattering vector' q is independent of the applied wavelength and the resulting scattering profile shows gives structural information as function of the q -value. The dimension of q -values is one over length [1/nm] and therefore small objects scatter at large angles (q -values) and large objects scatterer at small angles (q -values).^[84]

As mentioned above, the interference of secondary waves emitted from a certain object produce 2D scattering patterns in the plane of the detector. The amount of data can be reduced by producing a 1D scattering pattern which contains all the necessary information about the scatterer. This SAXS pattern consists of three regimes^[87], the Guinier, Fourier and Porod regions.

The Guinier regime is located at very low q -values, and gives information about larger objects in real space. Analysis of this regime allows the direct estimation of the radius of gyration R_g . The Guinier plot is the line fit to the natural logarithm of the intensity as a function of q^2 ($\ln I(q)$ vs. q^2). The structure of the particles can be determined, by calculating the volume and molecular weight of the scattering object.^[84]

The Fourier region gives significant information about the particle shape and the size distribution. The decay at large scattering angles is directly related to the particle shape. The Porod regime describes the interface and fractal dimensions of scattering objects. The inter-particle interference has no effect at large angles and the surface-to-volume ratio can be determined.

The particle size, volume, and electron density can be described as a function of the form factor $F(q)$.^[87] The scattering of the intra-particle structure in an ideal monodisperse and diluted solution is collected and no position or orientational correlation between single particles contribute to the experimental scattering curves. The particles are well-separated and the total intensity of the scattering profile is then the sum of each particle intensity for monodisperse particles. The scattering is produced by the atoms of the particle and those of all identical particles is summed up

and the scattering pattern is the result of the form factor multiplied by the number of the detected particles.

At higher concentrations, stronger interaction between particles cannot be neglected and a densely packed particle system leads to rearrangement of particles and a long-range order (Van-der-Waals interaction, Coulomb interaction, hard-sphere interaction).^[84] The Structure factor $S(q)$ becomes important and provides information about these interactions.^[85] The corresponding scattering curve shows Bragg peaks for periodic components and the degree of order of the particles (peak intensity), and the spatial extent of the ordered domain (peak width), give more information. The multiplication of the Form factor $F(q)$ and the Structure factor $S(q)$ contribute to the SAXS pattern and together contain the information about the internal density of the particles and interactions.

$$I(q) = F(q)S(q) \quad (2.14)$$

The sample-to-detector distance, and the beam collimation will greatly influence the scattering profile. For the generation of high intensity X-rays (keV) a synchrotron radiation source is necessary where the X-rays are produced accelerated, collected and collimated into an intense X-ray beam (beamline).^[88] With a shorter sample-to-detector distance, diffraction patterns at larger scattering angles can be observed. The method is therefore called wide-angle X-ray scattering (WAXS) and the crystallinity (crystal structure) on the atomic scale can be detected. WAXS is based on the same theoretical background as SAXS and requires analysis of scattering patterns caused by Bragg peaks.

2.6 Fluorescence and Confocal Microscopy

Organic or inorganic specimens are able to absorb light of appropriate wavelength and emit light at a longer wavelength. The wavelength of excitation and emission is material-dependent with the energy shift to longer wavelength known as the Stokes shift.^[89] The excitation and emission process (figure 8) can be described as follows: Molecules are, at ambient temperatures, in their ground electronic state S_0 (lowest energy state). Through the absorption of photons, the energy of the electron increases and it goes in to a higher energetic level (S_1 and S_2). Collision with surrounding molecules ($\leq 10^{-8}$ sec) and spontaneous emission lowers the energy of the molecules by emitting photons and the electron drops from the higher energy level back to a lower energy level. Either the subsequent emission can be nearly simultaneous with absorption, known as fluorescence or the

emission persists for a longer time after excitation, known as phosphorescence (due to intersystem crossing).^{[89][90]}

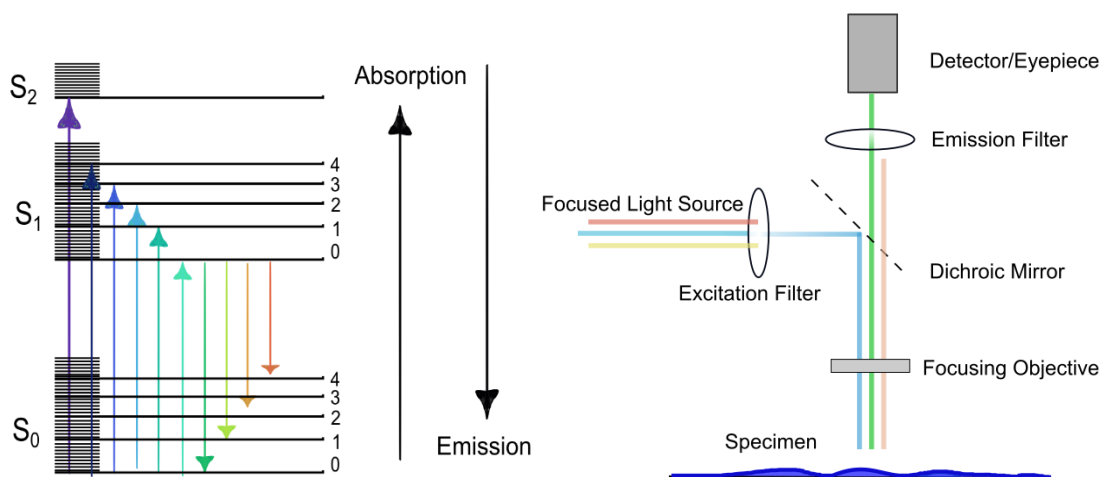


Figure 8: Jablonski diagram displaying schematically the details of the absorption and emission process of a molecule (left) and the basic setup of a fluorescence microscope with light source, excitation filter, dichroic mirror, objective, emission filter and detector or eyepiece (right).

Based on this phenomenon, standard fluorescence microscopy and Confocal Laser Scanning Microscopy (CLSM) have become important techniques in material science (e.g. semiconducting quantum dots).^{[90][91][92]} The basic principle of fluorescence microscopy is, to form images from objects which fluoresce (within a few nanoseconds).^[89] Light is coming from the light source (e.g. mercury arc lamp) and travels through collector lenses and apertures to the excitation filter, where the desired wavelength can pass the filter and the undesired wavelengths are blocked. The excitation wavelength reaches the dichroic beam splitting mirror, which is oriented at a 45° angle to the incoming light. Light of shorter wavelength reflects at this interference filter while light of longer wavelength is transmitted. The excitation light passes through the objective and to the sample. The emitted fluorescent light is gathered by the objective and passes back through the dichroic mirror, because the emitted light consists of longer wavelengths. With the help of an emission filter undesired emission is suppressed and the fluorescent light of interest can reach the detector or eyepiece.^{[90][93]}

Typically, the emission intensity is 10^5 to 10^6 times lower than the excitation light.^[90] Therefore, powerful lamps, a high specimen extinction coefficient and quantum yield and the fluorescence

lifetime are all important factors which contribute to the intensity of the fluorescence emission. For instance, a high intensity mercury lamp generates light in the near UV spectrum, which covers the excitation wavelength region for CdTe quantum dots.^{[90][94]} Modern microscopes combine a lot of technical improvements like digital acquisition or electronic imaging to detect low light level and/or visually undetectable radiation.

Confocal microscopy, also known as Confocal Laser Scanning Microscopy (CLSM) is a specialized form of standard fluorescence microscopy. The basic concept was developed in 1955 by M. Minsky^[95] at Harvard University with the key elements of the instrument, the pinhole apertures and the point-by-point illumination of the specimen (figure 9).

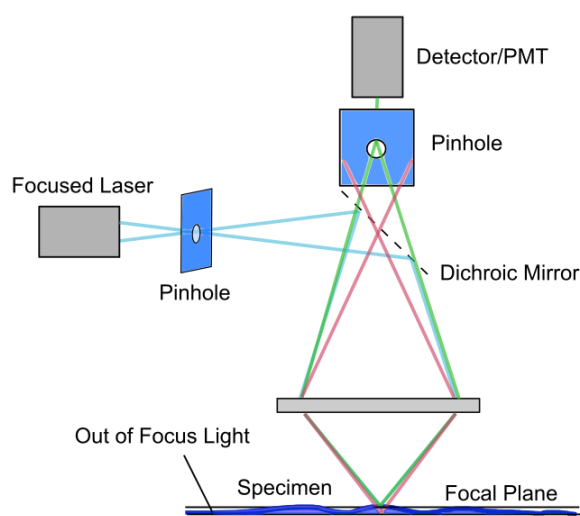


Figure 9: Schematic setup of the confocal laser scanning microscope with the optical pathway and the principal components: the focused laser light, the pinholes, dichroic mirror and detector/photomultiplier (PMT).

The principal ideas of the pinholes apertures are to eliminate out-of-focus light. The first pinhole aperture is placed in front of the light source. The coherent laser light passes through the aperture which is in a conjugate plane with the scanning point on the fluorescent specimen. The exciting light is directed by a dichroic mirror, focused by the objective, and excites the specimen. The emitted light returns through the objective, the dichroic mirror and the detector pinhole aperture. The detector pinhole aperture is situated in front of the detector and a small fraction of fluorescence emission passes through it. In that case, the pinhole aperture lies in the optically conjugate focal

plane of the returning light from the specimen, hence the term 'confocal'. This fraction of emitted light is focused as a confocal point at the pinhole. A significant amount of out-of-focus fluorescence emission is not detected and does not contribute to image. This emission is above and below the objective focal planes and not confocal with the pinhole. The directed light is measured by photomultiplier (PMT) tube detectors and upon scanning the sample creates two dimensional images of the specimen which are precise and have a better contrast and since background emission is reduced.^[96]

The point-by-point image construction can be realized by focusing each point of the specimen sequentially. The emitted light has a very low intensity, hence the image point is illuminated for a longer time and the light source works with high intensity. Serial scanning of specimen sections occurs by moving the specimen on the stage in the vertical and horizontal direction and keeping the optical setup stationary. The scanning unit is responsible for the excitation scans and collecting the returning photons from the specimen. For visualization the detector is connected to a computer which builds up the 3D image.^[97]

Over the last few years several parameters have been optimized and modern instruments consist of advanced computational techniques for data acquisition and processing. Laser systems with high stability and intensity and sensitive optoelectronic detectors, are able to reconstruct the high quality three dimensional structures.^[96] Confocal microscopy is an essential technique in combination with microfluidic devices.^[98]

2.7 Cathodoluminescence in Scanning Electron Microscopy

Electron microscopy based on the electron-specimen interaction of employs high energetic electrons with acceleration energies from 0.1–50 keV.^[99] These interactions lead to a variety of important processes, such as inelastic and elastic scattering, and absorption and transmission of electrons through the specimen, making electron microscopy and luminescence detection possible and giving information about the surface topography, the chemical composition and the crystalline structure of the specimen. In case of Scanning Electron Microscopy (SEM), the electron beam (primary electrons) is focused on the specimen and penetrate the sample in a teardrop-shaped volume.^[100] The volume depends on the energy of the electron beam, the incidence angle and the

material of the specimen. The most important electron-specimen interaction processes are shown in figure 10.

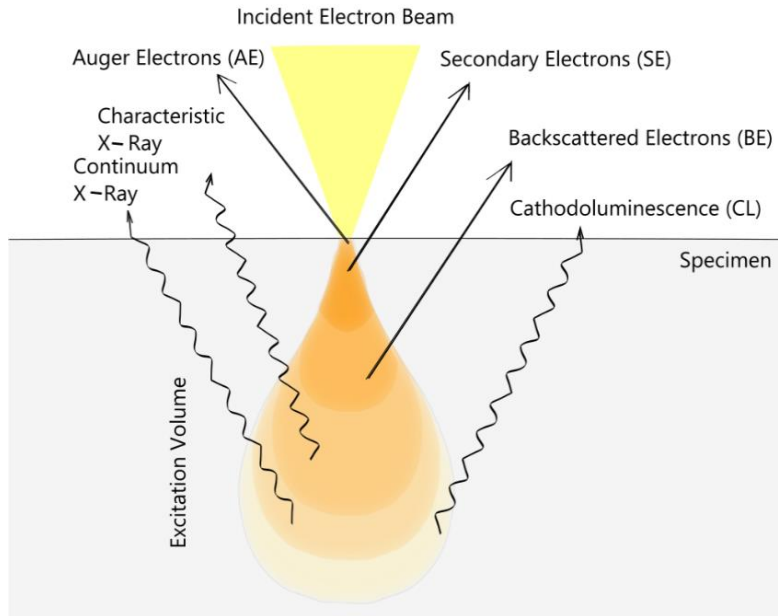


Figure 10: Schematic drawing of the teardrop-shaped interaction volume of the incident electron beam and the specimen. The origin of secondary electrons (SE), backscatter electrons (BE), Auger electrons (AE), X-rays and cathodoluminescence (CL) can be found in these electron-specimen interaction.

The contribution of secondary and backscattered electrons (SE, BE), X-rays, Auger electrons (AE) and photons are the basis for the final signals and the image information. The majority will be secondary electrons, which are generated by ejection from the specimen surface due to inelastic collision with the highly energetic electron beam. This leads to excited electrons with most probable energies of 2-50 eV escaping from near-surface layers (< 10 nm) of the specimen. The collected SE primarily give information about changes in topography.^[99] Backscattered electrons are responsible for a broad energy spectrum between the energy of the incident electron beam and 50 eV, caused by multiple inelastic scattering processes. The primary electrons are scattered through a larger angle and provide information about the specimen composition and the crystallography of the material. The production of BE depends on the atomic number of elements involved. Elements of higher atomic number appear brighter and give a brighter contrast in the resulting SEM image. The incident electron beam generates electron-hole pairs in luminescent materials and the subsequent recombination causes the emission of photons and the relaxation of

the system into an unexcited state. The wavelength of the emitting light depends on the bandgap of the material and gives therefore information about the composition. The emitted photons cover the ultraviolet (UV, < 400 nm), the visible (400 nm–700 nm) and infrared (IR, > 700 nm) spectrum and the process is termed Cathodoluminescence (CL). Furthermore, we can distinguish between the recombination of electron-hole pairs in an intrinsic semiconductor or in an extrinsic semiconductor.^{[101][102]} Structural imperfections cause intrinsic luminescence whereas extrinsic luminescence has its origin in impurities in the structure. The latter ones are responsible for contrast from different phases, visualization of defects and trace elements.

The working principal of conventional SEM techniques includes the generation of primary electrons by electron sources (e.g. Schottky field emission cathode) and the subsequent acceleration towards the anode under high potentials. In the following steps, the electron beam is focused by various lenses to a spot size in the nm to μm region and passes scanning coils in the electron column.^[99] The directed electron beam reaches the final lens where the beam is deflected to raster scan the specimen surface. The specimen resides in a high vacuum chamber and should be electrically conductive to avoid building up a static charge. SEM can be used for the detection of bulkier specimens where the electron beam is scanned across the sample. The different types of emitted electrons and photons are detected inside the specimen chamber with the help of attached sensitive detectors. Digital images were recorded with very high resolutions.^[99] The resolution shows a strong instrumentation dependency and is influenced by factors such as the diameter of the electron beam, the scattering of the specimen or the signal to noise ratio.

2.8 Thesis Outline

The aim of this thesis is the evaluation of the in-situ monitored growth process of semiconducting clusters and nanocrystals. An outline of the methods and instrumentation used within this work is provided in Chapter 3 and the thesis is composed of three experimental parts presented in Chapter 4 to 6. In principle, the presented research deals with colloidal semiconducting systems, starting from the precursor synthesis and subsequent investigation of nucleation and growth processes under real time conditions. Information about the formation process of different quantized systems is highlighted.

Chapter 4 describes the important linkage and the preparation of nanocomposites by monitoring the in-situ growth process of quantum dots on a clay matrix while maintaining their unique optical properties. Spherical and well-separated CdTe quantum dots attached on nanoclay edges were obtained as proven by imaging microscopes, based on different measurement principles.

In Chapter 5 the investigation of the nucleation and growth process of organic-inorganic $\text{CH}_3\text{NH}_3\text{PbBr}_3$ perovskite nanocrystals and their further self-assembly into two-dimensional oriented nanosheets and 3D superstructures is presented. The lead-based perovskite synthesis was adapted to diffusion controlled microfluidic and capillary approaches and for detailed analysis of the structure property relationship, X-ray scattering experiments and spectroscopic studies were used.

This is followed in Chapter 6 by the development and examination of the room temperature ionic reaction of a metal-based precursor and ligand-stabilized halide and chalcogenide counter ions in an organic medium to form inorganic clusters and nanocrystals. To design a novel method that yields information about the formation process, the reaction components and their interplay needs to be investigated. The synthetic technique has been used to prepare a multitude of clusters with a focus on silver halide and metal sulfide systems.

References

- [1] G. Schmid, *Nanoparticles: From Theory to Application*, Weinheim, FRG: Wiley-VCH Verlag GmbH & Co. KGaA, 2004.
- [2] L. Zou *et al.*, ‘Ultrafast synthesis of highly luminescent green- to near infrared-emitting CdTe nanocrystals in aqueous phase’, *Journal of Materials Chemistry*, vol. 18, p. 2807, 2008.
- [3] A. R. B. M. Yusoff and M. K. Nazeeruddin, ‘Organohalide Lead Perovskites for Photovoltaic Applications’, *Journal of Physical Chemistry Letters*, vol. 7, no. 5, pp. 851–866, 2016.
- [4] B. M. Cossairt and J. S. Owen, ‘CdSe clusters: At the interface of small molecules and quantum dots’, *Chemistry of Materials*, vol. 23, no. 12, pp. 3114–3119, 2011.
- [5] D. T. Thompson, ‘Using gold nanoparticles for catalysis’, *Nano Today*, vol. 2, no. 4, pp. 40–43, 2007.
- [6] R. Narayanan and M. A. El-Sayed, ‘Catalysis with transition metal nanoparticles in colloidal solution: Nanoparticle shape dependence and stability’, *Journal of Physical Chemistry B*, vol. 109, no. 26, pp. 12663–12676, 2005.
- [7] H. A. Patel, R. S. Somani, H. C. Bajaj, and R. V. Jasra, ‘Nanoclays for polymer nanocomposites, paints, inks, greases and cosmetics formulations, drug delivery vehicle and waste water treatment’, *Bulletin of Materials Science*, vol. 29, no. 2, pp. 133–145, 2006.
- [8] A. Akbarzadeh, M. Samiei, and S. Davaran, ‘Magnetic nanoparticles: Preparation, physical properties, and applications in biomedicine’, *Nanoscale Research Letters*, vol. 7, no. 1, p. 144, 2012.
- [9] F. E. Kruis, H. Fissan, and A. Peled, ‘Synthesis of nanoparticles in the gas phase for electronic, optical and magnetic applications—a review’, *Journal of Aerosol Science*, vol. 29, no. 5–6, pp. 511–535, 1998.
- [10] I. W. Andrew N. Shipway Eugenio Katz, ‘Nanoparticle Arrays on Surfaces for Electronic, Optical, and Sensor Applications’, *ChemPhysChem*, vol. 1, no. 15, pp. 18–52, 2000.
- [11] T. Hyeon, ‘Chemical synthesis of magnetic nanoparticles’, *Chemical Communications*, no. 8, pp. 927–934, 2003.
- [12] H. A. Atwater and A. Polman, ‘Plasmonics for improved photovoltaic devices’, *Nature Materials*, vol. 9, no. 3, pp. 205–213, 2010.
- [13] C. de M. Donegá, ‘Synthesis and properties of colloidal heteronanocrystals’, *Chem. Soc. Rev.*, vol. 40, no. 3, pp. 1512–1546, 2011.
- [14] S. O’Brien, L. Brus, and C. B. Murray, ‘Synthesis of monodisperse nanoparticles of barium

- titanate: Toward a generalized strategy of oxide nanoparticle synthesis', *Journal of the American Chemical Society*, vol. 123, no. 48, pp. 12085–12086, 2001.
- [15] J. Pérez-Juste, I. Pastoriza-Santos, L. M. Liz-Marzán, and P. Mulvaney, 'Gold nanorods: Synthesis, characterization and applications', *Coordination Chemistry Reviews*, vol. 249, no. 17–18 SPEC. ISS., pp. 1870–1901, 2005.
- [16] C. de Mello Donegá, Ed., *Nanoparticles*. Berlin, Heidelberg: Springer Berlin Heidelberg, 2014.
- [17] X. Zhong and Y. Feng, 'New strategy for band-gap tuning in semiconductor nanocrystals', *Research on Chemical Intermediates*, vol. 34, no. 2–3, pp. 287–298, 2008.
- [18] J. Park, J. Joo, G. K. Soon, Y. Jang, and T. Hyeon, 'Synthesis of monodisperse spherical nanocrystals', *Angewandte Chemie - International Edition*, vol. 46, no. 25, pp. 4630–4660, 2007.
- [19] I. Aziz, M. Sirajuddin, M. H. Khan, S. Nadeem, S. A. Tirmizi, and R. A. Khan, 'Investigation of adsorption of lead(II) onto a montmorillonite clay modified by humic acid', *Journal of the Chemical Society of Pakistan*, vol. 37, no. 5, 2015.
- [20] T. Wang and J. L. Keddie, 'Design and fabrication of colloidal polymer nanocomposites', *Advances in Colloid and Interface Science*, vol. 147–148, no. C, pp. 319–332, 2009.
- [21] X. Chen, J. Schröder, S. Hauschild, S. Rosenfeldt, M. Dulle, and S. Förster, 'Simultaneous SAXS/WAXS/UV-Vis Study of the Nucleation and Growth of Nanoparticles: A Test of Classical Nucleation Theory', *Langmuir*, vol. 31, no. 42, pp. 11678–11691, 2015.
- [22] Y. Bekenstein, B. A. Koscher, S. W. Eaton, P. Yang, and A. P. Alivisatos, 'Highly Luminescent Colloidal Nanoplates of Perovskite Cesium Lead Halide and Their Oriented Assemblies', *Journal of the American Chemical Society*, vol. 137, no. 51, pp. 16008–16011, 2015.
- [23] X. Peng, J. Wickham, and A. P. Alivisatos, 'Kinetics of II-VI and III-V colloidal semiconductor nanocrystal growth: "Focusing" of size distributions [15]', *Journal of the American Chemical Society*, vol. 120, no. 21, pp. 5343–5344, 1998.
- [24] I. Lignos, S. Stavrakis, A. Kilaj, and A. J. deMello, 'Millisecond-Timescale Monitoring of PbS Nanoparticle Nucleation and Growth Using Droplet-Based Microfluidics', *Small*, vol. 11, no. 32, pp. 4009–4017, 2015.
- [25] M. A. Watzky and R. G. Finke, 'Nanocluster Size-Control and "Magic Number" Investigations. Experimental Tests of the "Living-Metal Polymer" Concept and of Mechanism-Based Size-Control Predictions Leading to the Syntheses of Iridium(0) Nanoclusters Centering about Four Sequential Magic ', *Chemistry of Materials*, vol. 9, no.
-

- 12, pp. 3083–3095, 1997.
- [26] J. Y. Rempel, M. G. Bawendi, and K. F. Jensen, ‘Insights into the kinetics of semiconductor nanocrystal nucleation and growth’, *Journal of the American Chemical Society*, vol. 131, no. 12, pp. 4479–4489, 2009.
- [27] V. K. Lamer and R. H. Dinegar, ‘Theory, Production and Mechanism of Formation of Monodispersed Hydrosols’, *Journal of the American Chemical Society*, vol. 72, no. 11, pp. 4847–4854, 1950.
- [28] S. Karthika, T. K. Radhakrishnan, and P. Kalaichelvi, ‘A Review of Classical and Nonclassical Nucleation Theories’, *Crystal Growth and Design*, vol. 16, no. 11, pp. 6663–6681, 2016.
- [29] F. Zhang, *Photon Upconversion Nanomaterials*. Berlin, Heidelberg: Springer Berlin Heidelberg, 2015.
- [30] J. van Embden, A. S. R. Chesman, and J. J. Jasieniak, ‘The Heat-Up Synthesis of Colloidal Nanocrystals’, *Chemistry of Materials*, vol. 27, no. 7, pp. 2246–2285, 2015.
- [31] E. R. Leite and C. Ribeiro, *Crystallization and Growth of Colloidal Nanocrystals*. New York, NY: Springer New York, 2012.
- [32] J. E. Evans, K. L. Jungjohann, N. D. Browning, and I. Arslan, ‘Controlled growth of nanoparticles from solution with in situ liquid transmission electron microscopy’, *Nano Letters*, vol. 11, no. 7, pp. 2809–2813, 2011.
- [33] H. Zheng, R. K. Smith, Y. W. Jun, C. Kisielowski, U. Dahmen, and A. Paul Alivisatos, ‘Observation of single colloidal platinum nanocrystal growth trajectories’, *Science*, vol. 324, no. 5932, pp. 1309–1312, 2009.
- [34] C. Schliehe *et al.*, ‘Ultrathin PbS sheets by two-dimensional oriented attachment’, *Science (New York, N.Y.)*, vol. 329, pp. 550–553, 2010.
- [35] W. K. Koh, A. C. Bartnik, F. W. Wise, and C. B. Murray, ‘Synthesis of monodisperse PbSe nanorods: A case for oriented attachment’, *Journal of the American Chemical Society*, vol. 132, no. 11, pp. 3909–3913, 2010.
- [36] C. Ribeiro, E. J. H. Lee, T. R. Giraldo, R. Aguiar, E. Longo, and E. R. Leite, ‘In situ oriented crystal growth in a ceramic nanostructured system’, *Journal of Applied Physics*, vol. 97, no. 2, 2005.
- [37] A. Baldan, ‘Progress in Ostwald ripening theories and their applications to nickel-base superalloys. Part I: Ostwald ripening theories’, *Journal of Materials Science*, vol. 37, no. 11, pp. 2171–2202, 2002.
- [38] W. R. Lee *et al.*, ‘Redox-transmetalation process as a generalized synthetic strategy for
-

- core-shell magnetic nanoparticles’, *Journal of the American Chemical Society*, vol. 127, no. 46, pp. 16090–16097, 2005.
- [39] D. K. Lee, S. Il Park, J. K. Lee, and N. M. Hwang, ‘A theoretical model for digestive ripening’, *Acta Materialia*, vol. 55, no. 15, pp. 5281–5288, 2007.
- [40] X. Peng *et al.*, ‘Shape control of CdSe nanocrystals’, *Nature*, vol. 404, no. 6773, pp. 59–61, 2000.
- [41] H. Labiadh and S. Hidouri, ‘ZnS quantum dots and their derivatives: Overview on identity, synthesis and challenge into surface modifications for restricted applications ZnS quantum dots and their derivatives’, *Journal of King Saud University - Science*, vol. 29, no. 4, pp. 444–450, 2017.
- [42] S. H. Choi, K. An, E. G. Kim, J. H. Yu, J. H. Kim, and T. Hyeon, ‘Simple and generalized synthesis of semiconducting metal sulfide nanocrystals’, *Advanced Functional Materials*, vol. 19, no. 10, pp. 1645–1649, 2009.
- [43] C. B. Murray, D. J. Norris, and M. G. Bawendi, ‘Synthesis and Characterization of Nearly Monodisperse CdE (E = S, Se, Te) Semiconductor Nanocrystallites’, *Journal of the American Chemical Society*, vol. 115, no. 19, pp. 8706–8715, 1993.
- [44] L. Qu and X. Peng, ‘Control of photoluminescence properties of CdSe nanocrystals in growth’, *Journal of the American Chemical Society*, vol. 124, no. 9, pp. 2049–2055, 2002.
- [45] A. M. Smith and S. Nie, ‘Semiconductor Nanocrystals: Structure, Properties, and Band Gap Engineering’, *Acc Chem Res.*, vol. 43, no. 2, pp. 190–200, 2010.
- [46] S. F. Wuister, I. Swart, F. van Driel, S. G. Hickey, and C. de Mello Donegá, ‘Highly luminescent water-soluble CdTe quantum dots’, *Nano Letters*, vol. 3, no. 4, pp. 503–507, 2003.
- [47] A. P. Alivisatos, ‘Perspectives on the physical chemistry of semiconductor nanocrystals’, *Journal of Physical Chemistry*, vol. 100, no. 31, pp. 13226–13239, 1996.
- [48] V. A. Singh, V. Ranjan, and M. Kapoor, ‘Semiconductor quantum dots: theory and phenomenology’, *Bulletin of Materials Science*, vol. 22, no. 3, pp. 563–569, 1999.
- [49] F. T. Rabouw and C. de Mello Donega, ‘Excited-State Dynamics in Colloidal Semiconductor Nanocrystals’, *Topics in Current Chemistry*, vol. 374, no. 5, pp. 1–30, 2016.
- [50] J. Jasieniak, L. Smith, J. Van Embden, P. Mulvaney, and M. Califano, ‘Re-examination of the size-dependent absorption properties of CdSe quantum dots’, *Journal of Physical Chemistry C*, vol. 113, no. 45, pp. 19468–19474, 2009.
- [51] W. W. Yu, L. Qu, W. Guo, and X. Peng, ‘Experimental determination of the extinction coefficient of CdTe, CdSe, and CdS nanocrystals’, *Chemistry of Materials*, vol. 15, no. 14,
-

- pp. 2854–2860, 2003.
- [52] Y. Park *et al.*, ‘Aqueous Phase Synthesized CdSe Nanoparticles with Well-Defined Numbers of Constituent Atoms’, *J. Phys. Chem. C*, vol. 114, no. 44, pp. 18834–18840, 2010.
- [53] S. Kudera *et al.*, ‘Sequential growth of magic-size CdSe nanocrystals’, *Advanced Materials*, vol. 19, no. 4, pp. 548–552, 2007.
- [54] S. Link and M. A. El-Sayed, ‘Shape and size dependence of radiative, non-radiative and photothermal properties of gold nanocrystals’, *International Reviews in Physical Chemistry*, vol. 19, no. 3, pp. 409–453, 2000.
- [55] K. W. Böer, *Handbook of the Physics of Thin-Film Solar Cells*, Berlin Heidelberg, Springer, 2013.
- [56] R. A. Sperling and W. J. Parak, ‘Surface modification, functionalization and bioconjugation of colloidal inorganic nanoparticles’, *Philosophical Transactions of the Royal Society A: Mathematical, Physical and Engineering Sciences*, vol. 368, no. 1915, pp. 1333–1383, 2010.
- [57] S. M. Harrell, J. R. McBride, and S. J. Rosenthal, ‘Synthesis of ultrasmall and magic-sized CdSe nanocrystals’, *Chemistry of Materials*, vol. 25, no. 8, pp. 1199–1210, 2013.
- [58] J. Yang *et al.*, ‘Chemical Synthesis, Doping, and Transformation of Magic-Sized Semiconductor Alloy Nanoclusters’, *Journal of the American Chemical Society*, vol. 139, no. 19, pp. 6761–6770, 2017.
- [59] A. Smith, S. Nie, ‘Semiconductor Nanocrystals: Structure, Properties and Band Gap Engineering’, *Acc. Chem. Res.*, vol. 43, no. 2, pp. 190–200, 2010.
- [60] K. Yu *et al.*, ‘Thermodynamic equilibrium-driven formation of single-sized nanocrystals: Reaction media tuning CdSe magic-sized versus regular quantum dots’, *Journal of Physical Chemistry C*, vol. 114, no. 8, pp. 3329–3339, 2010.
- [61] T. Vossmeier *et al.*, ‘CdS nanoclusters: Synthesis, characterization, size dependent oscillator strength, temperature shift of the excitonic transition energy, and reversible absorbance shift’, *Journal of Physical Chemistry*, vol. 98, no. 31, pp. 7665–7673, 1994.
- [62] L. Qu, W. W. Yu, and X. Peng, ‘In situ observation of the nucleation and growth of CdSe nanocrystals’, *Nano Letters*, vol. 4, no. 3, pp. 465–469, 2004.
- [63] A. Kasuya *et al.*, ‘Ultra-stable nanoparticles of CdSe revealed from mass spectrometry’, *Nature Materials*, vol. 3, no. 2, pp. 99–102, 2004.
- [64] D. R. Nevers, C. B. Williamson, T. Hanrath, and R. D. Robinson, ‘Surface chemistry of cadmium sulfide magic-sized clusters: a window into ligand-nanoparticle interactions’,
-

- Chem. Commun.*, vol. 53, no. 19, pp. 2866–2869, 2017.
- [65] I. G. Dance, A. Choy, and M. L. Scudder, ‘Syntheses, properties, and molecular and crystal structures of (Me₄N)₄[E₄M₁₀(SPh)₁₆] (E = sulfur or selenium; M = zinc or cadmium): molecular supertetrahedral fragments of the cubic metal chalcogenide lattice’, *Journal of the American Chemical Society*, vol. 106, no. 21, pp. 6285–6295, 1984.
- [66] F. S. Chien, C. Wu, Y. Chou, T. T. Chen, and S. Gwo, ‘Nanomachining of (110)-oriented silicon by scanning probe lithography and anisotropic wet etching and anisotropic wet etching’, *Appl. Phys. Lett.*, vol. 75, no. 16, pp. 2429–2431, 1999
- [67] J. H. Park, D. A. Steingart, S. Kodambaka, and F. M. Ross, ‘Electrochemical electron beam lithography: Write, read, and erase metallic nanocrystals on demand’, *Science Advances*, no. July, pp. 1–8, 2017.
- [68] Y. Wang, Y. Li, C. Rong, and J. P. Liu, ‘Sm-Co hard magnetic nanoparticles prepared by surfactant-assisted ball milling’, *Nanotechnology*, vol. 18, no. 46, 2007.
- [69] J. V. I. Timonen, E. T. Seppälä, O. Ikkala, and R. H. A. Ras, ‘From hot-injection synthesis to heating-up synthesis of cobalt nanoparticles: Observation of kinetically controllable nucleation’, *Angewandte Chemie - International Edition*, vol. 50, no. 9, pp. 2080–2084, 2011.
- [70] L. C. Schmidt *et al.*, ‘Nontemplate synthesis of CH₃NH₃PbBr₃ perovskite nanoparticles’, *Journal of the American Chemical Society*, vol. 136, no. 3, pp. 850–853, 2014.
- [71] S. Sepeur, *Nanotechnology: Technical Basics and Applications*, Hannover, Vincentz Network, 2008.
- [72] M. Konstantakou, D. Perganti, P. Falaras, and T. Stergiopoulos, ‘Anti-Solvent Crystallization Strategies for Highly Efficient Perovskite Solar Cells’, *Crystals*, vol. 7, no. 10, p. 291, 2017.
- [73] S. Paek *et al.*, ‘From Nano- to Micrometer Scale: The Role of Antisolvent Treatment on High Performance Perovskite Solar Cells’, *Chemistry of Materials*, vol. 29, no. 8, pp. 3490–3498, 2017.
- [74] R. G. Pearson, ‘Hard and soft acids and bases, HSAB part II: Underlying theories’, *J. Chem. Educ.*, vol. 45, no. 10, pp. 643–648, 1968.
- [75] J. Zhang *et al.*, ‘Fundamentals and applications of inertial microfluidics: a review’, *Lab Chip*, vol. 16, no. 1, pp. 10–34, 2016.
- [76] R. M. MacEiczyk, K. Dümbgen, I. Lignos, L. Protesescu, M. V. Kovalenko, and A. J. Demello, ‘Microfluidic reactors provide preparative and mechanistic insights into the synthesis of formamidinium lead halide perovskite nanocrystals’, *Chemistry of Materials*,
-

- vol. 29, no. 19, pp. 8433–8439, 2017.
- [77] T. L. Sounart *et al.*, ‘Spatially-resolved analysis of nanoparticle nucleation and growth in a microfluidic reactor’, *Lab on a Chip*, vol. 7, no. 7, p. 908, 2007.
- [78] G. M. Whitesides, ‘The origins and the future of microfluidics’, *Nature*, vol. 442, no. 7101, pp. 368–373, 2006.
- [79] Y. Gambin, C. Simonnet, V. VanDelinder, A. Deniz, and A. Groisman, ‘Ultrafast microfluidic mixer with three-dimensional flow focusing for studies of biochemical kinetics’, *Lab Chip*, vol. 10, no. 5, pp. 598–609, 2010.
- [80] C. Fürst, P. Zhang, S. V. Roth, M. Drechsler, and S. Förster, ‘Self-assembly of block copolymers via micellar intermediate states into vesicles on time scales from milliseconds to days’, *Polymer (United Kingdom)*, vol. 107, pp. 434–444, 2016.
- [81] T. M. Squires, ‘Microfluidics Fluid physics at the nanoliter scale’, *Reviews of modern Physics*, vol. 77, no.3, pp. 997-1026, 2005.
- [82] T. A. Franke and A. Wixforth, ‘Microfluidics for miniaturized laboratories on a chip’, *ChemPhysChem*, vol. 9, no. 15, pp. 2140–2156, 2008.
- [83] N.-T. Nguyen, S. T. Wereley, *Fundamentals and Applications of Microfluidics*, Boston, London, Artech House, 2002.
- [84] H. Schnablegger and Y. Singh, *The SAXS guide: getting acquainted with the principles*, Austria, Anton Paar GmbH, 2013.
- [85] B. R. Pauw, ‘Corrigendum: Everything SAXS: small-angle scattering pattern collection and correction’, *Journal of Physics: Condensed Matter*, vol. 26, no. 23, p. 239501, 2014.
- [86] C. G. Pope, ‘X-ray Diffraction and the Bragg Equation’, *Journal of Chemical Education*, vol. 74, no. 1, p. 129, 1997.
- [87] L. Boldon, F. Laliberte, and L. Liu, ‘Review of the fundamental theories behind small angle X-ray scattering, molecular dynamics simulation, and relevant integrated application’, *Nano Reviews*, vol. 6, no. 1. p. 25661, 2015.
- [88] Deutsches Elektronen-Synchrotron, Germany, 2018,
Retrieved from http://photon-science.desy.de/research/students__teaching/primers/storage_rings__beamlines/index_eng.html.
- [89] J. W. Lichtman and J. A. Conchello, ‘Fluorescence microscopy’, *Nature Methods*, vol. 2, no. 12, pp. 910–919, 2005.
- [90] R.G. Driggers, *Encyclopedia of Optical Engineering*, Boca Raton, Florida, CRC Press 2003.
- [91] T. Lundy, ‘Advanced Confocal Microscope: An essential technique for microfluidics development’, *Microscopy Today*, 8-12.
-

- [92] D. Semwogerere and E. R. Weeks, *Confocal Microscopy, Encyclopedia of Biomaterials and Biomedical Engineering*, London UK, Taylor & Francis, 2005
- [93] Carl Zeiss Microscopy GmbH, Germany, 2018,
Retrieved from <http://zeiss-campus.magnet.fsu.edu/articles/lightsources/mercuryarc.html>.
- [94] F. Gao *et al.*, ‘CdTe-montmorillonite nanocomposites: Control synthesis, UV radiation-dependent photoluminescence, and enhanced latent fingerprint deTectiön’, *Journal of Physical Chemistry C*, vol. 115, no. 44, pp. 21574–21583, 2011.
- [95] M. Minsky, ‘Memoir on inventing the confocal scanning microscope’, *Scanning*, vol. 10, no. 4, pp. 128–138, 1988.
- [96] N. S. Claxton, T. J. Fellers, and M. W. Davidson, ‘Confocal Microscopy’, *Encyclopedia of Medical Devices and Instrumentation*, vol. 1979, no. 21, pp. 1–37, 2006.
- [97] V. Prasad, D. Semwogerere, and E. R. Weeks, ‘Confocal microscopy of colloids’, *Journal of Physics Condensed Matter*, vol. 19, no. 11, 2007.
- [98] A. Jahn, J. E. Reiner, W. N. Vreeland, D. L. DeVoe, L. E. Locascio, and M. Gaitan, ‘Preparation of nanoparticles by continuous-flow microfluidics’, *Journal of Nanoparticle Research*, vol. 10, no. 6, pp. 925–934, 2008.
- [99] L. Reimer, *Scanning Electron Microscopy*, vol. 45. Berlin, Heidelberg: Springer Berlin Heidelberg, 1998.
- [100] K. D. Vernon-Parry, ‘Scanning electron microscopy: an introduction’, *III-Vs Review*, vol. 13, no. 4, pp. 40–44, 2000.
- [101] S. Boggs and D. Krinsley, *Application of Cathodoluminescence Imaging to the Study of Sedimentary Rocks*. Cambridge: Cambridge University Press, 2006.
- [102] J. Götze, M. Plötze, and D. Habermann, ‘Origin, spectral characteristics and practical applications of the cathodoluminescence (CL) of quartz - A review’, *Mineralogy and Petrology*, vol. 71, no. 3–4, pp. 225–250, 2001.

Chapter 3

Experimental Methods and Instrumentation

3.1 Introduction

The purpose of this chapter is to provide an overview of the chemicals, syntheses, and the instrumentation employed during the course of this work at the University of Bayreuth and the University of Melbourne. Relevant experimental setups will be reported in each experimental chapter.

3.2 Chemicals

3.2.1 Materials for the CdTe/Nanoclay Nanocomposite Synthesis

Tellurium powder (Te, -30 mesh, 99.997%), Sodium borohydride (NaBH_4 , $\geq 96\%$), Cadmium acetate dihydrate ($\text{Cd}(\text{CH}_3\text{COO})_2 \times 2\text{H}_2\text{O}$, 98%), 3-mercaptopropionic acid ($\text{HSCH}_2\text{CH}_2\text{CO}_2\text{H}$, $\geq 99\%$) and hydrogen peroxide solution (H_2O_2 , 30% in H_2O) were purchased from Sigma-Aldrich and used as delivered. The solvents isopropanol and acetone (AppliChem, tech.) for RCA cleaning (Radio Corporation of America) and ammonium hydroxide solution (NH_4OH , 25% in H_2O , Merck Millipore) were used as received. Exfoliated nanoclays $[\text{Na}_{0.96}]^{\text{inter}}[\text{Mg}_{5.14}\text{Li}_{0.94}]^{\text{oct}}[\text{Si}_8]\text{O}_{20}\text{F}_4$ (dispersed in an aqueous solution 1 wt%) with interlayer distance of $99 \text{ nm} \pm 12 \text{ nm}$ according earlier experimental studies^[1] and the typical cation exchange capacity (CEC) of 126 mequiv./100 g clay were synthesized by melt synthesis and fully characterized by Breu et al.^[2] Solution pH was adjusted with sodium hydroxide solution (NaOH , $c=1 \text{ mol/L}$, Sigma-Aldrich).

3.2.2 Materials for $\text{CH}_3\text{NH}_3\text{PbBr}_3$ Perovskite Synthesis

Methylamine solution (33 wt% in absolute ethanol, Sigma Aldrich), octylamine (99%, Sigma Aldrich), hydrobromic acid (HBr , 48 wt%, Sigma Aldrich) and lead(II)bromide (PbBr_2 , 99.999%, Sigma Aldrich) were used for the precursor synthesis in N,N-dimethylformamide (DMF, $\geq 99.8\%$,

Fisher Scientific). Toluene ($\geq 99.7\%$, Sigma Aldrich) acts as anti-solvent and tetrahydrofuran (THF, Sigma-Aldrich, 99.9%) was used to redisperse the perovskite samples.

3.2.3 Materials for Metal Halide and Metal Chalcogenide Nanocluster Synthesis

Tetraoctylammonium bromide (TOABr, 98%, Sigma-Aldrich) was used as both bromide source and phase transfer agent. Sodium sulfide nonahydrate ($\text{Na}_2\text{S} \times 9 \text{H}_2\text{O}$, 99.99%, Sigma Aldrich) and pure sulfur (S, 99.998%, Sigma-Aldrich) were used as precursors for the chalcogenide clusters. Sodium iodide (NaI, 99.999%) and *n*-octylamine ($\geq 99\%$) were used as received. Sodium oleate ($>97.0\%$, TCI Europe) as precursor was reacted with silver nitrate (AgNO_3 , $\geq 99.9\%$, Sigma Aldrich), cadmium acetate dihydrate ($\text{Cd}(\text{CH}_3\text{COO})_2 \times 2\text{H}_2\text{O}$, 98%), zinc chloride (ZnCl_2 , $\geq 98\%$, Sigma Aldrich) and lead(II) chloride (PbCl_2 , $\geq 98\%$, Sigma Aldrich). The solvents cyclohexane (CH, $\geq 99.9\%$, Sigma Aldrich), chloroform (CHCl_3 , $\geq 99.9\%$, Sigma Aldrich), toluene ($\geq 99.7\%$, Sigma Aldrich) and ethanol (EtOH, AppliChem, tech) were used as delivered.

3.3 CdTe/Nanoclay Nanocomposite Synthesis

The synthesis of CdTe/Nanoclay composites consists of two steps. These steps include the fixation of cadmium ions on the nanoclays^{[3][4]} and the subsequent nanoparticle growth modified to our needs.^[5]

Cd^{2+} Adsorption onto Charged Nanoclays

We used a melt-synthesized sodium hectorite with unit cell a composition of $[\text{Na}_{0.5}]^{\text{inter}} [\text{Mg}_{2.5}\text{Li}_{0.5}]^{\text{oct}} [\text{Si}_4]^{\text{tet}} \text{O}_{10}\text{F}_2$ (abbreviated as $\text{Na}_{0.5}$ -hectorite) by Breu et al.^[2], which shows a homogeneous intracrystalline reactivity. The preparation of highly diluted dispersions induced complete delamination of the $\text{Na}_{0.5}$ -hectorite tactoids. A few drops of the diluted dispersion (0.5 wt%) were spin coated and dried on a pre-cleaned glass wafer and analysed with Atomic Force Microscopy (AFM) experiments to prove this. Individual platelets with a typical height of 1 nm and a size between 0.5 and 10 μm were detected. The first step of our two-step approach is the selective attachment of Cd^{2+} ions on the nanoclay edges. The metal precursor salt Cd acetate dihydrate (0.02 g, 0.075 mmol, 1 eq) was mixed together with 0.2 g $\text{Na}_{0.5}$ -hectorite in 20 mL MilliQ

water (10 eq $w_{\text{Na}_{0.5}\text{-Hectorite}}/w_{\text{Cd}}$). The pH value of the dispersion was around 8. After an incubation time of 8 h and stirring at 200 rpm, the supernatant was carefully removed by decanting and the dispersion was diluted to the desired volume.

NaHTe Precursor (NaBH₄:Te 2.5:1 eq)

To prepare the NaHTe precursor stock solution, 25.4 mg telluride powder (0.2 mmol), 18.4 mg NaBH₄ (0.5 mmol) and 5 mL MilliQ water were stirred under inert gas atmosphere.^[5] The reaction mixture turned slowly to a purple colour within 30 min of heating at 80 °C.

CdTe Quantum Dots Synthesis on Nanoclay Matrix

The pH value of Na_{0.5}-hectorite solutions after the addition of mercaptopropionic acid (11.9 mg, 9.95 µL, 0.1125 mmol, 1.5 eq) was around 6 and before the injection of the telluride precursor it was adjusted to 12 with the addition of NaOH (1 mol/L). The final step involves the injection of 0.19 mL (0.0076 mmol) from the purple NaHTe precursor solution into 20 mL reaction mixture at 100 °C. After defined reaction times of 5 min, 30 min, 60 min, 75 min and 120 min, aliquots were taken and the reaction was quenched by the addition of water. For purification the reaction mixture was centrifuged (3000 rpm, 5 min). The colorful Na_{0.5}-hectorite composites showed a good settling and the desired concentration was reached by adjusting the volume with MilliQ water.

3.4 Synthesis of Perovskite Nanocrystals

The precursor methylammonium bromide (MAMBr) and octylammonium bromide (OAMBr) were synthesized according to a previously reported method with slight modifications.^[6] Typically, 14.9 mL methylamine (33 wt% in absolute EtOH, 0.1 mol) was placed in a 50 mL round-bottom flask. The flask was allowed to cool in an ice bath and 11.3 mL HBr (48 wt% in water, 0.1 mol) was added via a dropping funnel. Hydrobromic acid was slowly added to the corresponding amine with the temperature held below 10 °C. After constant stirring for 2 h at room temperature, the excess of unreacted precursor was removed by washing the product methylammonium bromide with diethyl ether (three times). The product was then stirred for 1 h at 60 °C and after precipitating with

diethyl ether the resulting white, crystalline solid was filtered, dried and stored in the vacuum oven at room temperature.

Octylammonium bromide was synthesized by a similar procedure. Methanol (5 mL) was added to 19.8 mL pure octylamine (99%, 0.1 mol). The diluted amine was placed in a 50 mL round-bottom flask and allowed to cool in an ice bath. A dropping funnel was filled with 11.3 mL HBr (0.1 mol) and placed on the top of the reaction vessel. After the slow addition (< 10 °C) of HBr the product was washed with diethyl ether three times, filtered and dried in the vacuum oven at room temperature.

Synthesis Perovskite Nanocrystals

The conventional large scale synthesis was based on a literature report^[7] with modifications to suit our needs. The precursor MAmBr (26.4 mg 0.24 mmol), OAmBr (33.5 mg 0.16 mmol) and PbBr₂ (36.7 mg 0.10 mmol) were dissolved in 3.5 mL N,N-dimethylformamide (DMF) and heated to 70 °C for complete dissolution (table 1). Subsequently, the clear solution was slowly added to 17 mL toluene. The dispersion was cooled after 2 min in an ice bath. The yellow dispersion produced was immediately centrifuged (4500 rpm, 10 min) and redispersed in toluene.

Table 1: Perovskite large scale synthesis with different compositions of MABr, OABr and PbBr₂.

Sample Precursor	P01 [mmol]	P02 [mmol]	P03 [mmol]	P04 [mmol]
MABr	0.1	0.3	0.1	0.24
OABr	0.1	0.1	0.3	0.16
PbBr ₂	0.3	0.1	0.1	0.10

Microfluidic Synthesis

The precursor MAmBr (132.0 mg, 1.2 mmol), OAmBr (167.5 mg, 0.8 mmol) and PbBr₂ (183.5 mg, 0.5 mmol) were dissolved in 5 mL DMF at 70 °C. The 3D double focusing hybrid microfluidic chip employed consists of five inlets. The connected syringes were filled according table 2. The corresponding flow rate Q was adjusted between 125 $\mu\text{L/h}$ and 3000 $\mu\text{L/h}$ for the precursor solutions in DMF, and Toluene:DMF mixtures of 1:1 ratio and 2:1. The photoluminescence detection commenced after reaching steady state conditions.

Table 2: Flow composition and the corresponding flow rates for the perovskite synthesis in the microfluidic chip.

Channel	Inlet 1	Inlet 2	Inlet 3	Inlet 4	Inlet 5
Flow rate Q in [$\mu\text{L/h}$]	3000	250	125	250	3000
Solvent Composition	Toluene	Toluene/DMF 2:1	Precursor in Toluene/DMF 1:1	Toluene/DMF 2:1	Toluene

Capillary Interdiffusion Synthesis

The precursor MAmBr (132.0 mg, 1.2 mmol), OAmBr (167.5 mg, 0.80 mmol) and PbBr₂ (183.5 mg, 0.5 mmol) were dissolved in 1.5 mL DMF at 70 °C. A volume of 83.5 μL toluene was loaded in a 1 mm diameter quartz capillary with the syringe pump. A mixture of 1:1 DMF/Toluene acts as buffer layer (10 μL). The double layer was coated with 16.5 μL of this DMF solution. The UV-Vis detection commenced with the addition of the precursor solution.

In-situ UV-Vis/SAXS Experiments

The setup can vary the distance between the sample and SAXS detector. Each experiment was performed at 2 different detector-to-sample distances. The scattering range from

$0.1 \text{ nm}^{-1} \leq q \leq 3.0 \text{ nm}^{-1}$ could be detected to capture scattering from the beginnings of the growth process (form factor, small q region) and the formation of hierarchical stacked structures of lamellar sheets (structure factor, large q region). The detector-sample distance was 1.6 m to detect the $0.1 \text{ nm}^{-1} \leq q \leq 1.0 \text{ nm}^{-1}$ region.

3.5 Synthesis of Semiconductor Nanoclusters

The preparation of the metal(oleate) precursor was based on the conversion of sodium oleate with the corresponding metal salt. To a solution of 3.957 g sodium oleate (13.0 mmol) in 50 mL water was added a solution of metal salt in 10 mL water at 50 °C with vigorous stirring (table 3). After 2 h stirring, the resulting white precipitate was filtered and washed with water. The metal(oleate) was dried and stored in the dark until use.

Table 3: Amounts of substances in mmol and g for the preparation of metal oleate precursor.

Oleate precursor	Metal salt	n in [mmol]	m in [g]
Ag(oleate)	AgNO ₃	13.0	2.208
Cd(oleate) ₂	Cd(CH ₃ COO) ₂ x 2H ₂ O	6.5	1.732
Pb(oleate) ₂	PbCl ₂	6.5	1.807
Zn(oleate) ₂	ZnCl ₂	6.5	0.886

The phase transfer technique was used to yield tetraoctylammonium sulfide (TOA₂S₂) and tetraoctylammonium iodide (TOAI) as anion sources for the cluster synthesis. Typically, 50 mL aqueous solution of 102.4 mg NaI (0.68 mmol) was mixed with 50 mL of toluene containing a stoichiometric amount of 373.57 mg tetraoctylammonium bromide (TOABr). The two-phase mixture was continuously stirred for 24 h. The phase transfer can be monitored with a color change from colorless to yellow. The purity was determined with melting point determination.^[8] As a result, the relative error was calculated to be 1.55 %, indicating a high phase transfer efficiency within one day.

The tetraoctylammonium sulfide precursor (TOA₂S₂) was prepared according to a modified version of the liquid-liquid phase transfer method of Li et al.^[9] A mixture of 0.16 g sulfur (5.0 mmol) and 1.907 g Na₂S in 50 mL water were stirred at 50 °C for 1 h. After the complete dissolution, the generated sodium sulfide mixture (Step I, stock solution) was purged with nitrogen and stored in the dark at +4 °C. An excess of sulfur avoids the incomplete conversion of TOABr during the subsequent phase transfer (Step II). The phase transfer agent TOABr (273.41 mg, 0.5 mmol) was dissolved in 9 mL dry chloroform and 2.5 mL of the sulfide mixture Na₂S_{2x} (Step I) was added under Schlenk conditions. The polysulfide anions tend to move into the organic phase with the help of the phase transfer agent TOABr. The subsequent reaction between polyanions and the phase transfer agent TOABr leads to the replacement of bromide which can be monitored by UV-Vis spectroscopy. A control experiment monitoring the remaining water phase indicates a high transfer efficiency within 24 h.

Synthesis of Silver Halide Nanoclusters

In a first approach, 5.81 mg Ag(oleate) (0.0164 mmol) and a minimum volume of 30 µL *n*-octylamine was added to a volume of 17.5 mL cyclohexane. After complete solution 1.75 mL aliquots were taken and placed in a cuvette. TOAI (9.73 mg, 0.0164 mmol) and 8.97 mg TOABr (0.0164 mmol) were dissolved in 10 mL cyclohexane and 500 µL CHCl₃ were added to guarantee the complete dissolution of the halide precursor. For the nanocluster formation, different aliquots of the halide solution were added to the silver solution. In a second approach, 1 mL of the prepared stock solution of TOAI and TOABr were placed in a cuvette and different aliquots of the silver stock solution added. The cluster growth was monitored via UV-Vis spectroscopy.

Table 4: Amount of substance in mmol, mg and mL for the preparation of metal halide nanoclusters.

	TOABr	TOAI	Ag(oleate)
Amount of Substance in [mg]	8.97	9.73	5.81
Volume of Cyclohexane in [mL]	10	10	17.5
n in [mmol]	0.0164	0.0164	0.0164
Aliquots for Ratio 1:1 in [mL]	1	1	1.75

Synthesis of Metal Chalcogenide Nanoclusters

For the first approach, the metal(oleate) stock solutions were prepared by adding a certain amount of the metal precursor (0.0109 mmol, 7.36 mg Cd(oleate)₂, 8.39 mg Pb(oleate)₂, 6.85 mg Zn(oleate)₂) to a volume of 20 mL cyclohexane (CH).

For the first approach, 40 µl from the sulfur stock solution (Step II, table 5, 0.00109 mmol) was mixed with 1.5 mL cyclohexane and 7 µL *n*-octylamine was added to each solution. In a second step, different aliquots of metal solution were quickly injected to the sulfur solution and the cluster growth was monitored via UV-Vis spectroscopy.

For the second approach, a volume of 2 mL metal precursor (0.00109 mmol) was placed in a cuvette and 7 µL *n*-octylamine was added to each solution. In a second step, 80 µL from the sulfur stock solution (Step II) was mixed with 3 mL cyclohexane in a cuvette. Different volumes from the sulfur solution (table 5) were quickly injected into the metal precursor solution in the cuvette and the cluster growth was monitored via UV-Vis spectroscopy.

Table 5: Amount of substance in mmol, mg and mL for the preparation of metal chalcogenide nanoclusters.

Approach 1		Approach 1		Approach 2		Approach 2	
Sulfur Precursor in CH		Metal(oleate) in CH		Metal(oleate) in CH		Sulfur Precursor in CH	
[mL]	[mmol]	[mL]	[mmol]	[mL]	[mmol]	[mL]	[mmol]
1.5	0.00109	4	0.00218	2	0.00109	3	0.00218
1.5	0.00109	3	0.00164	2	0.00109	1.5	0.00109
1.5	0.00109	2	0.00109	2	0.00109	0.75	0.00054
1.5	0.00109	0.5	0.00054				

Cleaning of Glass and Silicon Wafer

RCA cleaning^[10] was used for removing contamination from silicon wafers. For the cleaning procedure, the general recipe consists of 5 parts water, 1 part ammonium hydroxide (25 %) and 1 part 30 % hydrogen peroxide. Water (80 mL) was placed in a beaker and 16 mL of NH₄OH and 16 mL of H₂O₂ added. The solution with the wafer was heated at 70 °C under stirring for 15 min. After cleaning, the wafer was extensively rinsed with water and stored in water until use. The glass slides were cleaned in isopropanol and acetone in an ultrasonic bath. They were stored in isopropanol and treated with O₂ plasma to achieve a hydrophilic surface.

TEM Grid Preparation

For TEM measurements, the final products were prepared by drop-casting of the solution/dispersion onto a carbon film-coated Cu grid (300 mesh, Plano GmbH). The excess liquid was removed by blotting using filter paper and the solvent was allowed to evaporate at room temperature prior to imaging.

AFM Sample Preparation

AFM imaging requires that the objects of interest are rigidly adhered to a substrate with very low surface roughness. The well-dispersed colloidal samples (100 μL , 1 wt%) in water were spin coated onto hydrophilic AFM glass wafers (Thermo Scientific) and dried in air. The samples were kept in a dust-free environment.

Fluorescence Microscopy Sample Preparation

For fluorescence imaging, the well-dispersed colloidal samples (100 μL , 0.5 wt%) in water were placed on hydrophilic glass wafers by drop casting. The samples were dried in air and stored in dust-free environment.

SEM Sample Preparation

For standard sample preparation, 50 μL of the perovskite dispersions was placed on a pre-cleaned silicon wafer and dried under ambient conditions. The wafer was mounted on the holder with double-sided tape.

XRD

For standard sample preparation, the metal chalcogenide dispersions in cyclohexane were dried on pre-cleaned silicon wafers under ambient conditions. The metal halide dispersion in cyclohexane was freeze-dried and the powder was placed on a pre-cleaned silicon wafer.

3.6 Instrumentation

3.6.1 Small Angle X-ray Scattering

SAXS measurements for the kinetic study of perovskites were performed at the Deutsches Elektron-Synchrotron (DESY) in Hamburg, Germany. All experiments were carried out at the P03, Micro- and Nanofocus X-ray Scattering (MiNaXS) beamline at the PETRA III storage ring. For

our setup, the sample was loaded in a quartz capillary and mounted in a holder in front of the SAXS vacuum tube which includes the SAXS detector. The setup for the SAXS detection is depicted in figure 11 where the sample-to-detector distance is variable.

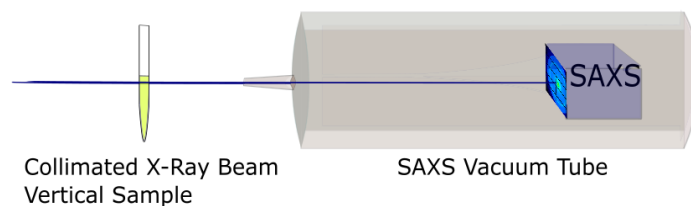


Figure 11: Schematic representation of an experimental setup. The collimated X-ray beam hits the vertical sample. The scattered X-rays are detected by the SAXS detector in a vacuum tube which leads to the characteristic 2D scattering pattern. The sample-to-detector distance is responsible for the detected q -values of the scattered X-rays.

The sample-to-detector distance was set to be 1.66 m and 2.54 m, leading to a q -range from $0.01 \text{ nm}^{-1} \leq q \leq 3.0 \text{ nm}^{-1}$. The measurements were performed with a beam size of $320 \text{ nm} \times 250 \text{ nm}$ and radiation of wavelength 0.0954 nm . The photon energy was 13 keV and the scattering data was collected with a Pilatus 1M detector. Silver behenate with a d -spacing of 58.38 \AA was used as standard for the calibration. A quartz capillary ($\text{\O} = 1 \text{ mm}$, Hildenberg GmbH) with wall thickness of 10 \mu m was used as the analysis cell. The 2 dimensional scattering patterns were acquired at an interval of 0.5 sec for 20 min. The background correction for the one dimensional SAXS profiles was made using toluene.

3.6.2 UV-Vis Absorbance Spectroscopy and Analysis

UV-Vis absorbance spectra were recorded on Agilent 8453 UV-Vis spectrophotometer. The instrument is equipped with a deuterium and tungsten light source covering the wavelength range of 190 nm to 1100 nm. The collimated beam passes the samples in the quartz cuvette and is dispersed onto a photodiode array detector. The UV-Visible ChemStation software was used for spectral analysis.

Time-dependent UV-Vis absorption spectra were recorded on a USB 2000+ XR1-ES detector ($\lambda = 200 \text{ nm}$ to 1100 nm) equipped with a deuterium-halogen light source (DH-2000-BAL, Ocean Optics, Germany) and connected with fiber optic cables. A quartz capillary ($\text{\O} = 1 \text{ mm}$, Hildenberg

GmbH) with wall thickness of 10 μm was used as the analysis cell. Ocean View Software was used for the real-time acquisition and analysis. The acquisition time was set to 0.5 min for perovskite and CdS nanocluster growth.

3.6.3 Confocal Laser Scanning Microscopy

The Confocal Laser Scanning Microscope (CLSM) Leica TCS SP8, equipped with an inverse DMI 6000B Microscope (Leica) was used for fluorescence imaging of perovskites in the microfluidic chip EH09. The specimen was mounted on a precise x-, y-, z-stage. The emission (region of interest scan, ROI) along the microfluidic channel was recorded within the wavelength region 415 nm to 780 nm and a laser excitation of $\lambda_{\text{exc}} = 405$ nm. The high-precision syringe pump (NEMESYS, Cetoni GmbH) guarantees laminar flows within the EH09 microfluidic chip. The inlets and outlets of the microfluidic device were connected via PE tubings (Scientific Commodities Inc.) and PE luer locks (Braun Melsungen AG) to gas-tight syringes (Hamilton Company).

3.6.4 Transmission Electron Microscopy

The colloidal samples were analyzed with three different Transmission Electron Microscopes (TEM). TEM images were obtained by a Zeiss CEM 902 electron microscope (Zeiss Microscopy GmbH). The TEM was equipped with a tungsten cathode and the acceleration voltage was 80 kV. For data imaging, the Gatan CCD Camera (Orios) with GMX 2.3 was used. Furthermore, the Zeiss LEO EM 922 Omega TEM with LaB₆ cathode operating at 200 keV in combination with the Gatan CCD Camera (Ultrascan 1000) with GMS 1.9 was used. The high resolution Tecnai F20 instrument, running at 200 kV equipped with STEM and EDS detectors was used.

3.6.5 Scanning Electron Microscope

Scanning Electron Microscope (SEM) images were taken at the Zeiss Leo 1530 high resolution FE-SEM with Schottky Field Emission Gun (FEG) as the electron source, with high efficiency SE inlens and SE detector (Everhardt Thornley) for secondary electron images and the MiniCL cathodoluminescence detector (Oxford Instruments) for cathodoluminescence images. The operating voltage was set to 5 keV and the working distance was 7.4 mm.

The high resolution Zeiss Ultra plus field emission was equipped with Schottky Field Emission electron source (FEG), SE inlens and SE detector (Everhardt Thornley) with acceleration voltage of 3.00 keV and a working distance from 3.5 nm to 3.8 mm.

3.6.6 Atomic Force Microscopy

Topographical and phase measurements were performed on the commercial Dimension 3100 Atomic Force Microscope (AFM, Veeco Instruments Inc., USA) equipped with a NanoScope V SPM controller and a hybrid XYZ closed-loop scanner (Bruker). Scanning of surface features was acquired in tapping mode under ambient conditions using aluminium-coated cantilevers (OTESPA-R3, Bruker). Image processing and data analysis were conducted with the Software Nanoscope Analysis v1.40 (Bruker).

3.6.7 Fluorescence Microscopy

The Olympus IX71 inverted microscope includes a light source (100 W mercury burner, U-LH100HG, Olympus), the Olympus microscope objective LCACHN 40x/0.55 Ph2 and the IX2-RFAC fluorescence filter cube with orange filter U-MWIGA3 (ET CY3, Olympus). The excitation light was passed through a band pass filter BP 530-550 nm, a dichroic mirror DM 570 nm and long pass emission filter BA 575-625 nm ensured only yellow-orange emission was detected. The Olympus U-CMAD3 model was used as microscope camera.

3.6.8 Fluorescence Spectroscopy

Fluorescence emission measurements were made on diluted solutions in quartz cuvettes (pathlength: 1 cm) on a Horiba Jobin Yvon Fluorolog-3 spectrometer. The PMT detector was corrected or wavelength dependent response and using the in-built correction function provided by Horiba Jobin Yvon.

Furthermore, the spectrofluorometer FP-6500 (Jasco Deutschland GmbH) with 150 W Xenon lamp was used to detect the wavelength reaching from 200 nm to 900 nm. Spectroscopy Software Spectra Manager was used for evaluating the measurements.

3.6.9 X-ray Diffraction

The X'Pert MPD Pro (PANalytical, Almeo, Netherland) X-ray diffractometer was used to obtain diffraction data. As an X-ray source a Cu-K α anode was used. The reaction chamber for studies of solids and gas reactions up to 900 °C and 10 bar was the XRK-900 (Anton Paar GmbH, Graz, Austria) for in-situ X-ray diffraction measurements.

References

- [1] S. Rosenfeldt, 'SAXS measurements on sodium hectorite', unpublished manuscript 2014.
- [2] M. Stöter *et al.*, 'Nanoplatelets of sodium hectorite showing aspect ratios of $\approx 20\ 000$ and superior purity', *Langmuir*, vol. 29, no. 4, pp. 1280–1285, 2013.
- [3] F. Ciesielczyk, P. Bartczak, and T. Jesionowski, 'Removal of cadmium(II) and lead(II) ions from model aqueous solutions using sol–gel-derived inorganic oxide adsorbent', *Adsorption*, vol. 22, no. 4–6, pp. 445–458, 2016.
- [4] M. Elmuntasir Ibrahim Ahmed, 'Selective Adsorption of Cadmium Species onto Organic Clay Using Experimental and Geochemical Speciation Modeling Data', *International Journal of Engineering and Technology*, vol. 8, no. 2, pp. 128–131, 2016.
- [5] L. Zou *et al.*, 'Ultrafast synthesis of highly luminescent green- to near infrared-emitting CdTe nanocrystals in aqueous phase', *Journal of Materials Chemistry*, vol. 18, p. 2807, 2008.
- [6] S. Zhuo, J. Zhang, Y. Shi, Y. Huang, and B. Zhang, 'Self-template-directed synthesis of porous perovskite nanowires at room temperature for high-performance visible-light photodetectors', *Angewandte Chemie - International Edition*, vol. 54, no. 19, pp. 5693–5696, 2015.
- [7] S. Gonzalez-Carrero, R. E. Galian, and J. Pérez-Prieto, 'Maximizing the emissive properties of $\text{CH}_3\text{NH}_3\text{PbBr}_3$ perovskite nanoparticles', *J. Mater. Chem. A*, vol. 3, no. 17, pp. 9187–9193, 2015.
- [8] G. Merck KGaA, Darmstadt, 2018.
Retrieved from <https://www.sigmaaldrich.com/catalog/product/aldrich/294136?lang=en®ion=AU>.
- [9] D. Li *et al.*, 'Efficient synthesis of functional long-chain alkyl disulfides under liquid-liquid phase-transfer catalysis: The analysis of chemical equilibrium and phase-transfer mechanism', *Catalysis Communications*, vol. 89, pp. 9–13, 2017.
- [10] Kevin M. Walsh, University of Louisville Standard Operating Procedures, 2013,
Retrieved from <http://mitghmr.spd.Louisville.edu/lutz/resources/sops/>

Chapter 4

In-situ Growth of CdTe Quantum Dots on Hectorite Nanoclays in Aqueous Medium

4.1 Introduction and Motivation

Nanocomposites comprise a widespread and highly active research area merging different constructions and architectures of colloid particles with microscopic elements.^{[1][2][3][4][5]} In order to tailor this new generation of nanodevices, we must focus on synthetic methods for constructing organized nanoparticle arrays on flat substrates while maintaining their unique optical properties. For the fabrication of such 'smart materials', various self-assembly techniques exist, based on the specific adsorption of nanoparticles on surfaces.^{[6][7][8]} The production includes the clear separation of nanoparticles syntheses and their subsequent ordered immobilization on substrates. The organization on a solid matrix requires the surface modification of substrates and the adsorption of nanoparticles through covalent or electrostatic interactions. Assemblies of gold monolayers can be prepared on nonconductive glass substrates according this approach. The hydrophilic surface allows the polymerization of trialkylsilane on the substrate surface to achieve new functionality capable of binding nanoparticles.^{[6][9][10]} In a following step, the silanized substrate was dipped in solution containing gold nanoparticles at different period times. An alternative method is the formation of monolayers by the Langmuir-Blodgett technique.^[11] The transparency of the substrate allows characterization with spectroscopic methods. Similar approaches use the attachment of citrate-stabilized gold nanoparticles on solid supports through amine- and thiol-functionalized ITO glass surfaces.^[12] Considerable attention was received by Wang and co-workers^[13] for the in-situ growth of gold nanoparticles on positively charged substrate surfaces. The procedure requires the preparation of patterned polymer substrates to provide a limited area for the in-situ growth of nanoparticles and the polymer surfaces need to be modified with positive charges to capture the ionic precursor AuCl_4^- . The fabrication of nanoparticles could be promoted with the addition of a growth solution and this leads to average sizes reaching from 180 nm to 300 nm. The in-situ growth of silver nanoparticles could be realized on dopamine pre-treated graphene oxide surfaces in the presence of stabilizing agents.^[14] This work provides a strategy to synthesize monolayers of 80 nm silver nanoparticles.

Further, efforts have already been made to avoid the substrate surface functionalization step using natural clay materials.^{[1][15]} This class of materials are used as adsorbing agents due to their layered

structure of silica and alumina sheets and their surface chemistry.^{[16][17]} A glance at the literature shows the combination of the outstanding features of nanoclays with the excellent properties of adjacent branches, such as the polymer chemistry.^{[4][18][19]} Another widespread method is the combination of nanoclays with organophilic ions to become hydrophobic nanocomposites (organoclays).^{[5][20][21]} The intercalation of ammonium ions into the inorganic matrix is quite common and leads to an expansion of the interlayer distance between the silica and alumina sheets such that they can finally act as a lipophilic modifier in their composites. Concomitantly, an increase in the surface area as well as a maximization of the adsorption capacity towards targeted pollutants could be achieved.^[3] The latter application utilizes nanoclays as a support material to remove heavy metals ions in water (figure 12). Diverse techniques were used to remove toxic metals from industrial waste water and their adsorption on clay materials is one of the most effective methods. As a logical next step the idea emerged to use the well-defined and selective ion absorption ability of nanoclays and couple it with post-treatments in the form of nanoparticle growth.

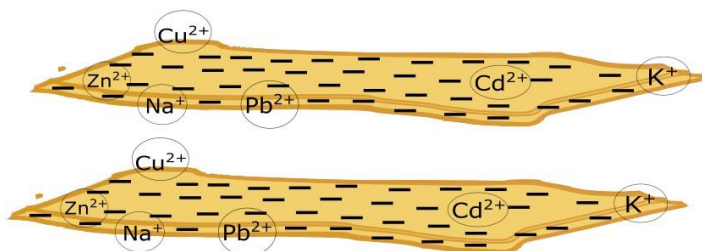


Figure 12: Schematic representation of the use of nanoclays as support material for the selective adsorption of targeted pollutants in aqueous systems (e.g. heavy metals ions).

The in-situ intercalation of CdTe/nanoclay materials and the in-situ reduction of nanostructured Pt-nanoclay materials is already described in the literature.^{[1][15]} Both methods rely on the adsorption of an ionic metal precursor on natural clay materials on the basal facets in aqueous solutions. The subsequent one-pot in-situ method for the preparation of nanostructured hybrid materials lead to embedded CdTe quantum dots and randomly distributed Pt nanoparticles under moderate synthetic conditions.

Beside the nature-inspired in-situ growth process of nanoparticles, nanoclay-based composite materials are used in significant areas of current and emerging interest,^{[3][17]} for applications in nanoscale filling, reinforcement,^{[22][23]} or adsorbent material^{[5][24][25]}, due to their high surface area, their mechanical properties and their high cation exchange capacity (CEC).^{[20][26][27]}

The aim of this chapter is the in-situ synthesis of nanocomposites which include the combination of semiconductor QD and nanoclays. Furthermore, the surface-bound nanoparticles should be well-organized on the natural material. The preparation method consists of two steps: the specific ion absorption on the surface edges, and the time-controlled nanoparticle growth via hot injection method.

4.2 Colloidal Materials: Combination of Nanoclay Minerals and Quantum Dots

4.2.1 Nanoclay Minerals

Clay and clay composite materials are used as cheap and effective absorbent materials.^[5] They have various advantages over other absorbent materials, such as the abundant availability, their swelling behaviour^[28], their high surface area^[26], their high pore volume and their cation exchange capacity (CEC).^[27] For these reasons they have received much attention in diverse research fields. Clay materials have many similarities concerning their chemical and structural composition which are briefly summarized next.

The majority of the layered family of oxhydroxides consist of stacked layers of silica and alumina sheets and can be divided according the electrical charge of their layer and also their layer structure.^[17] One representative is the sodium hectorite type which belongs to the smectite group clays which are also known as 2:1 phyllosilicates (anionic clay material) and has the chemical formula $[\text{Na}_{0.5}]^{\text{inter}} [\text{Mg}_{2.5}\text{Li}_{0.5}]^{\text{octr}} [\text{Si}_4]^{\text{tetr}} \text{O}_{10}\text{F}_2$.^[28] The structure of these sodium nanoclays is depicted in figure 13. The schematic structure of the 2:1 silicate includes two-dimensional and 1.0-2.0 nm thick parallel stacked layers of two tetrahedral silica layer (T, SiO_2) and one central octahedral alumina layer (O, $\text{AlO}_2(\text{OH})_4$).^[28] The three layers are connected via oxygen bonding where the anion belongs to the octahedral and also to the tetrahedral layers.

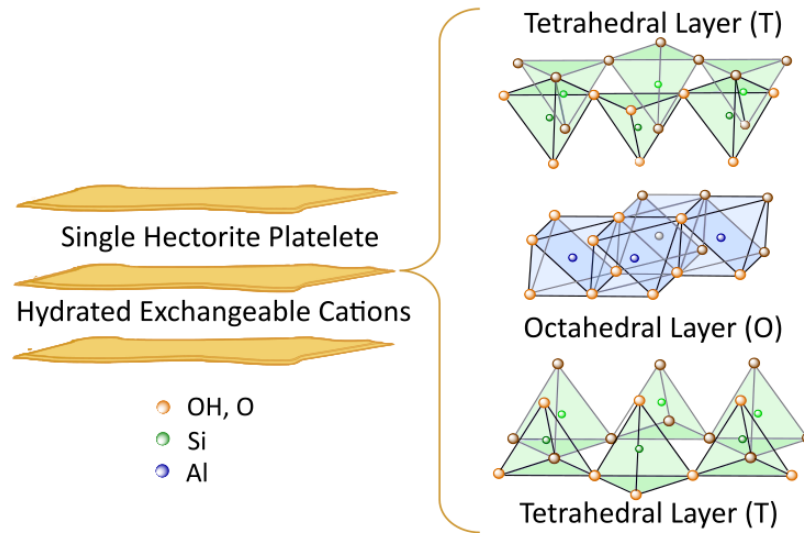


Figure 13: General schematic structure of the layered $[\text{Na}_{0.5}]^{\text{inter}}[\text{Mg}_{2.5}\text{Li}_{0.5}]^{\text{octr}}[\text{Si}_4]^{\text{tr}}\text{O}_{10}\text{F}_2$ hectorite. The sodium hectorite consists of parallel stacked tetrahedral-octahedral-tetrahedral aluminosilicate TOT lamellae ($\text{SiO}_2/\text{AlO}_2(\text{OH})_4/\text{SiO}_2$) which is separated by exchangeable Na^+ counterions.

The lateral dimensions can vary within the nm to μm range.^{[26][28]} In the case of naturally occurring hectorite nanoclays, mainly the Al^{3+} ion of the octahedral site is isomorphically substituted ($\text{Li}^{1+}/\text{Mg}^{2+}$) which results in a net negative charge on the surfaces of the tetrahedral layer.^[29] The creation of negative charges is counterbalanced with alkali or earth alkali cations, typically Na^+ counterions between each TOT layer. The extent of charge deficiency of smectites ranges from $0.2 < x < 0.8$ equivalents per Si_4O_{10} unit.^[30] Weak interlayer forces act between the sandwich-like TOT units which are responsible for the crystalline feature of the clay material. The hierarchical stacking of the TOT layer creates a lamellar structure with a 'Van der Waals gap' which represents the hydrated cation interlayer.^{[28][30]}

Post processing methods like exfoliation leads to delamination of the TOT building block and to single silicate layers and a higher aspect ratio. Shearing forces overcome the interaction (100 kJ/mol)^[28] between the layers and well-separated nanoplatelets are present in the aqueous solution. The layer separation through delamination caused by hydration of the interlamellar cation is also responsible for the high and homogeneous charge densities (osmotic delamination)^{[26][28][30]}, whereby the swelling behavior depends on the relative humidity (RH) in different surroundings.

Concerning the chemical properties, clay materials have a hydrophilic character because of the high ionic charge densities on the clay surface due to isomorphous substitution.^[30] Furthermore, external charges from broken edges and therefore exposed OH-groups enhance the hydrophilic character. These two kinds of electrical charges contribute to the cation exchange capacity (CEC) of hectorite nanoclays.^{[30][31][32]} The latter one shows an amphoteric charge which results from the pH-dependent proton adsorption-desorption process of the hydroxyl groups. Due to an increasing solution pH the functional groups on the clay edges are in an ionized state. The existing silanol (SiOH) and aluminol (AlOH) groups are free from protonation (figure 14).

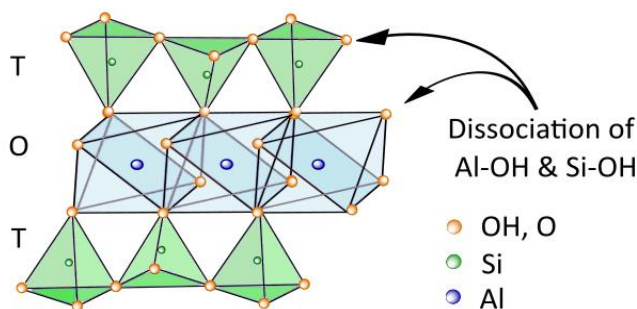


Figure 14: Side projection of exterior hydroxyl ions of TOT minerals which can be deprotonated under basic conditions.

Within the acidic/neutral pH region (pH=3-6) the permanently charged basal and interlayer surfaces are responsible for the cation exchange of heavy metal cations like Cd(II). With increasing pH value, the surface complexation on variably-charged edge surfaces plays the major role in the adsorption process.^[25] Different studies of nanoclays provide evidence that the surfaces-edges show an amphoteric character in aqueous solution.^{[25][33]} The large lamellar surfaces of nanoclays can be modified with the addition of hydroxyl ions favoring cation exchange reactions on the surface-edges.^[34] By adjusting the permanent and variable interactions of external surfaces of the TOT layer,^[30] or exceeding the critical salt concentration,^[16] the edge-basal plain interaction may lead to coagulation (cardhouse structure) and flocculation of the lamellae system. This restricts the application of nanoclay materials in acidic conditions.

4.2.2 Formation of Semiconductor/Nanoclay Composites

Nanoclays as an adsorbent material are supposed to have three adsorption sites for cations. The first possible site is the high surface area external planar surface where the electrostatic adsorbed cations are exchangeable. Another possibility is adsorption on the clay edges which can be also followed by the penetration into the octahedral sheets.^{[33][35]}

The solution pH, the initial metal concentration, the ionic strength, the contact time and the temperature have an enormous influence on the adsorption behavior.^{[34][36]} The pH value is the most critical factor and several research groups have proven that the pH dependent maximum of adsorption does not follow a simple model as outlined above. With the adjustment of the pH values to 6–9^[25], the irreversibility of the exchange process at the surface edges increases. In the deprotonated form, the concentration of hydrogen ions on the active edge sites is reduced, leading to a decreased competition of H⁺ with present metal ions and an increase in the adsorption capacity.^[37]

Various research groups^{[37][38][39][40]} showed that the absorption efficiency increases within the first minutes and reaches an equilibrium (effectiveness ≤ 90 %) and is less efficient in the later stages of the contact time. Jesionowski et al.^[41] has shown that for an ion concentration of 25 mg/L to 100 mg/L, just 0.5 g to 3 g of the adsorbate was necessary to remove all ions from solution. These results also showed dependence of the adsorption efficiency on the protonation of surface functional groups. Considering these results, and the CEC the experimental conditions were carefully chosen.

A lower ion concentration affects the very strong adsorption mechanism in a positive way.^[35] In the beginning, a low heavy metal concentration leads to preferred edge coverage while a higher concentration of the Cd ions results in a further adsorption on the clay basal surface.^{[15][36][37]} Full coverage of the nanoclays is also possible, however in this case the high energy edge sites are likely filled in the beginning. The predominant edge adsorption of Cd(II) on coated minerals indicates the great affinity for these kinds of heavy metals ions. Additionally, a high concentration of adsorbent material ensures 100% effective removal of the ions in solution whereas increasing metal concentration caused a significant decrease.^[36]

Beside the contributing factors of concentration, pH value and reaction time, the surface complexation depends on the ion source. In the last decades, the successful surface complexation of Ni(II), Zn(II), Cd(II), Fe(II) on 2:1 phyllosilicate has been reported.^[17] In view of its outstanding optical properties the adsorption behaviour of cadmium is our focus. In aqueous solution, the Cd(II) ion is hydrolyzed and this results in the formation of various species. The pH range plays an

important role and within the solution pH of 5–7 the hydrolyzed species appears in the form of $\text{Cd}(\text{OH})^+$, $\text{Cd}(\text{OH})_2$, and $\text{Cd}(\text{OH})_3^-$.^[37] With increasing pH value the fraction of the negatively charged hydrolyzed product increases.^[36] Among all ionic products the Cd^{2+} is the predominant species in the solution at the pH value of 6, the adsorption on the negative charged edges is favored.^[37] Simulations by Zhang et al.^{[33][42]} showed (SPNESC/CE modeling) recently that 2:1-type edge surface of clay materials show a very high binding affinity for divalent heavy metal cations. In diverse clay materials (e.g. Kaolinite, Montmorillonite) the immobilization predominantly takes place in form of different cation specific complexing mechanisms. In 2017, Zhang and co-workers discussed simulations showing that the preferred tetradentate complex of Ni(II) is on the octahedral vacancies of the inorganic oxide adsorbent material.^[33] The cation is embedded into lattice because it fits like a lattice cation into the vacancy of on the (110) edge. The complex formation may require the involvement of two or more complexing groups on the nanoclay edges (SiO^- , AlO^-) and Ni(II) shows a minor favorable monodentate complex on the Si-site and the bidentate complex on the Al-site. The common substitution of Mg for Al reduces the complexation ability. The complexing structure varies with the metal ion which can be underlined with free energy simulations and in contrast to Ni(II), Cd(II) shows a different complexing structure.^[42] Cadmium is not able to occupy the lattice position because of its much larger radius R (e.g. for aqua-cations, $R(\text{Cd-O})=2.29 \text{ \AA}$).^[43] Instead, Cd(II) forms highly stable tetradentate complexes at the octahedral vacancies and the values for complexing the Si- and Al-sites are lower compared to the octahedral vacant site. This complex predominant adsorption on the vacant sites of (010) interfaces of 2:1 phyllosilicates.^[42] Cd(II) shows a complexing structure and is not embedded into the lattice position which allows the access of reactive counterions. The presence of stabilizing ligands should lead to a controlled quantum dot growth. All the above mentioned factors are able to influence the adsorption kinetics but the well-defined and favorable ion adsorption on nanoclay edges should allow the controlled deposition of ordered quantum dots on nanoclay edges.

The in-situ synthesis of nanocomposites allows the generation of quantum dots with outstanding optical properties attached on solid supports. Well-organized, highly stable and luminescent nanocrystals are of great importance for the subsequent formation of optoelectronic devices. Each component of the new construct has outstanding functionalities which are combined in one 'smart material' to make a multifunctional nanocomposite. The size-dependent photoluminescence of CdTe quantum dots can be controlled by the reaction time and nanoclay additives show effective mechanical and thermal properties.

4.2.3 Heat-up Synthesis CdTe

According to previous literature^{[44][45]} highly luminescent CdTe quantum dots at 100 °C were synthesized in aqueous solution. The experimental section^[44] gives insight into the quantum dot synthesis and highlights the influence of different factors. This includes the variation of the pH value, $\text{Te}^{2-}:\text{Cd}^{2+}:\text{Mercaptopropionic acid (MPA)}$ ratio and the precursor concentration. We prepared thiol stabilized nanocrystals with $\text{Te}^{2-}:\text{Cd}^{2+}:\text{MPA}$ ratio of 0.1:1:1.5 at a pH value of 12 to confirm the results of the previous studies in section 4.4.1.

4.3 Experimental Section

Simple mixing of pre-synthesized quantum dots with delaminated Na_{0.5}-hectorite at pH=6 was considered before the in-situ hot-injection as major control. The results show entrapped QDs between stacked nanoplatelets or the coexistence of both colloidal ingredients due to missing attractive forces between organic ligands and neutral charged nanoclays (Appendix). The new approach via hot-injection synthesis was chosen to build up the organized quantum dot array along the inorganic support material. The Na_{0.5}-hectorite was immersed in a cadmium rich aqueous solution. Therefore, exfoliated clay platelets were dispersed in an aqueous solution to 1 wt%. The interlayer distance was around 99 nm ± 12 nm according to earlier experimental studies^[46] and the typical cation exchange capacity CEC of ~125 mequiv./100 g clay, synthesized and determined by Breu et al.^[26] To this nanoclay dispersion, cadmium acetate was added which acts as ion source. The adhesive ability arising from the deprotonated hydroxyl groups under slightly basic conditions (pH=8) provides a good anchoring group for Cd²⁺ ions. The divalent cadmium ions show a strong complexing ability^{[25][36]} and a preferred coverage can be found on the edges (figure 15). Moreover, the large surface-edge to volume ratio favors the deposition of metal ions along the favored anchoring group. The 10-fold weight excess of Na_{0.5}-hectorite (resp. the cadmium precursor) exceeds the Cd-ion concentration of 37.5 mmol per 100 g of clay material. Therefore, the amount of Cd²⁺ lies (4.2 g Cd²⁺/100 g clay and 10 g Cd(acetate)x2H₂O/100 g clay) far below the high values of the total sorption capacity^{[26][36][47]} of the clay material, favoring the absorption on the exterior clay edges (Appendix). The pH value of pH=8 favors the formation of free Cd²⁺ instead of hydroxyl species and the interaction with the inorganic adsorbent.^[37] In contrast, the extreme in-situ approach with the 7-fold excess amount of cadmium precursor (resp. Na_{0.5}-hectorite, 14.8 g Cd²⁺/100 g clay and 35 g Cd(acetate)x2H₂O/100 g clay) results in fully covered nanoclay platelets (Appendix) according to AFM measurements. With the lower cadmium content, replacement of existing Na⁺ ions in the inner layers should be avoided, unless the edges are saturated with counter ions. The incubation time was around 8 h, increasing the effectiveness and homogenous cation coverage along the edges of the support material.^[25] A subsequent washing step was carried out with water to avoid desorption of the cadmium ions.^[36]

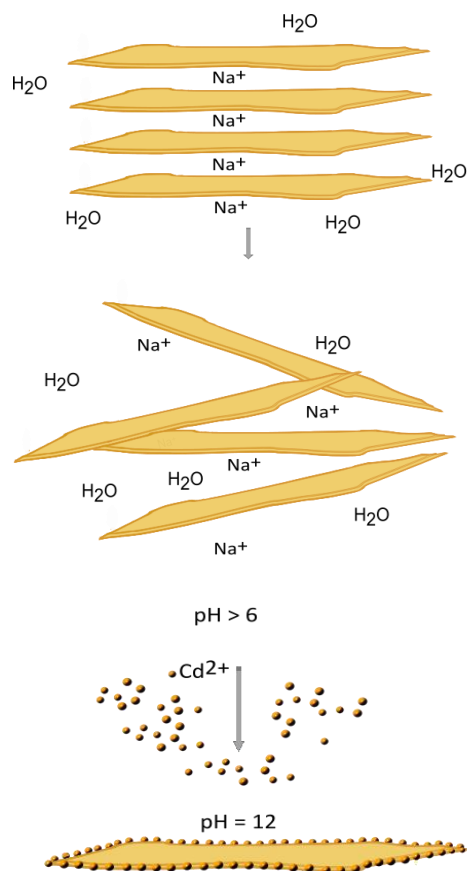


Figure 15: Simplified model after the osmotic swelling of nanoclay material. After mixing with Cd^{2+} ions at room temperature and an incubation time of 8 h the ions are adsorbed on the nanoclay edges due to electrostatic forces.

As discussed in previous literature, the ratio of $\text{Te}^{2-}:\text{Cd}^{2+}$ and the stabilizing ligand mercaptopropionic acid (MPA) plays an important role during the growth process and shows a strong influence on the growth time.^{[44][48]} A 1.5-fold excess of MPA in relation to the Cd precursor was added. The addition step should be subsequent to the diffusion controlled adsorption process to avoid the competing mechanism of forming single quantum dots in presence of nanoclays.^[35] The mono- and dithiol cation complexes $(-\text{S}^-\text{Cd}^{2+}\text{-S}^-)^{[44]}$ are formed under basic conditions. They exist in water in a molecular state, promote the growth rate, provide a good size distribution and maintain the confinement effect. As a consequence of the cadmium attachment, only a restricted spatial attack of thiol ligands is possible. With the assumption of single and well-separated attached

Cd^{2+} mono/dithiol monomer complexes, various clusters could be formed which acts as seeds for a heterogeneous nucleation process (figure 18).

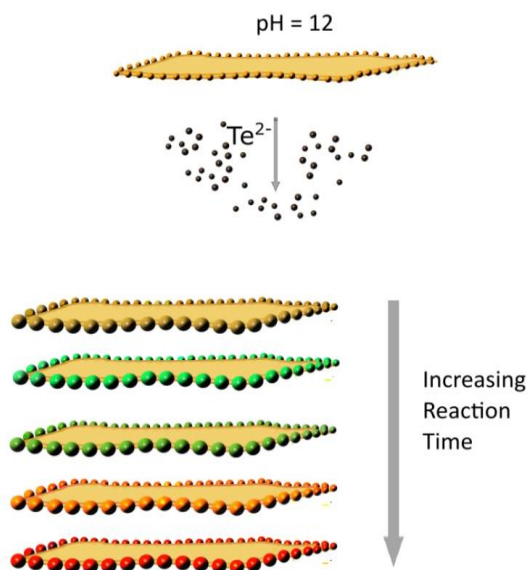


Figure 16: Illustration of the in-situ growth process of CdTe quantum dots onto the negatively charged edges of nanoclays. After the adsorption of Cd^{2+} cations the pH value was adjusted to 12 followed by the injection of the TeH^- precursor with the exclusion of oxygen.

After the generation of a large number of well-separated Cd^{2+} seeds and the addition of stabilizing agents, the ionic growth reaction could be achieved at elevated temperatures in form of ionic primary clusters with TeH^- ions.^[44] The injection of the NaHTe precursor at 100 °C under Schlenk conditions lead to quantum dot growth according the ionic reaction of Te^{2-} -ions on Cd^{2+} -seeds. The consumption of the Te^{2-} -ions is controlled by the presence of deprotonated MPA and hydroxyl ions. The electrostatic repulsive and reactive Cd^{2+} ions on specific sites on the nanoclays prevent the quantum dots from post growth processes and agglomeration. To monitor the size-dependent properties, aliquots were taken at different reaction times (figure 16). For the purification the reaction mixture was centrifuged wherein the colourful sodium hectorite shows a good settlement. The supernatant was carefully removed and the nanocomposite samples redispersed.

4.4 Results and Discussion

4.4.1 Detection of Optical Properties

The previous literature^{[44][45]} describes the formation of highly luminescent CdTe quantum dots at 100 °C in water. The controlled growth process of CdTe quantum dots under oxygen free conditions shows unique size-dependent optical properties. The organic compound mercaptopropionic acid was used to stabilize the quantum dots during the growth process. The nanocrystals were prepared with $\text{Te}^{2-}:\text{Cd}^{2+}:\text{MPA}$ ratio of 0.1:1:1.5 at a pH value of 12 to confirm the results of the previous studies. Figure 17 (left) shows the normalized UV-vis spectra with the absorption window from 450 nm to 610 nm and the shift of the peak maximum with proceeding reaction time ($t=1-35$ min) (right).

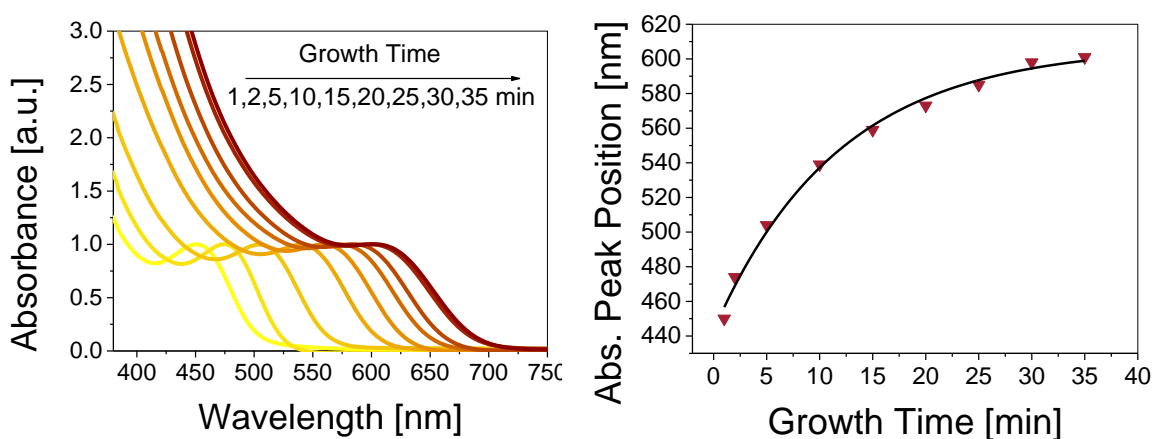


Figure 17: Normalized absorption spectra of CdTe nanocrystals synthesized using cadmium acetate and sodium telluride hydride as precursor salt. Due to variation of the reflux time ($t=1-35$ min) nanocrystals with various sizes can be obtained.

To ensure the spherical morphology (figure 18) and a narrow size distribution, transmission electron microscope (TEM) and AFM (Appendix) were used. The CdTe quantum dots are well-separated with a mean diameter of 4.0 nm and standard deviation of 0.9 nm, based on 100 particles ($N=100$).

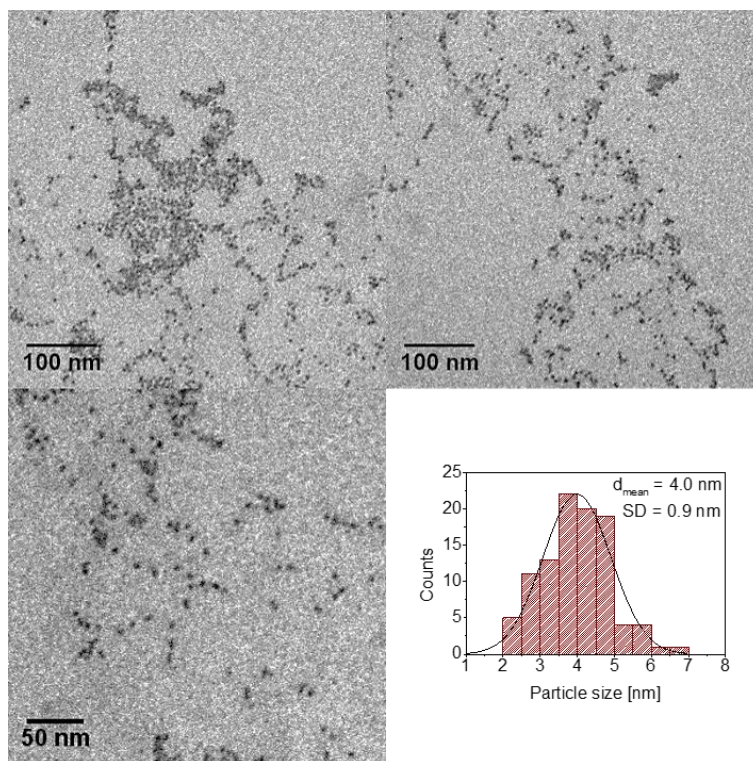


Figure 18: TEM image of CdTe quantum dots after 35 min (drop casting) and the corresponding size distribution with $4.0 \text{ nm} \pm 0.9 \text{ nm}$ in diameter.

The controlled growth process of nanocomposites under oxygen free conditions can yield uniform quantum dots with unique size-dependent optical properties. Therefore, the clay absorbent material acts in concert with the organic ligand as an outstanding stabilizer to suppress the agglomeration, ripening process, and precipitation of the grown quantum dots. Both stabilizers, nanoclays and mercaptopropionic acid, prevent the tunable highly efficient radiation-dependent photoluminescence of CdTe quantum dots.

After the successful adsorption of cadmium ions on hectorite edges, the QD/nanoclay dispersion was heated to $80 \text{ }^\circ\text{C}$. Directly after the addition of the NaHTe precursor, the color of the reaction mixture changes instantly to yellow. At this stage, no luminescence could be observed. With raising the reaction to $100 \text{ }^\circ\text{C}$ for a longer period of time the reaction mixture changed color from yellow, to greenish, to orange, then to dark red. Aliquots were taken after different reaction times according table 4 and quenched with water. The samples were centrifuged to remove unreacted side products and transferred to a quartz cuvette to obtain the UV-Vis spectra shown in figure 19.

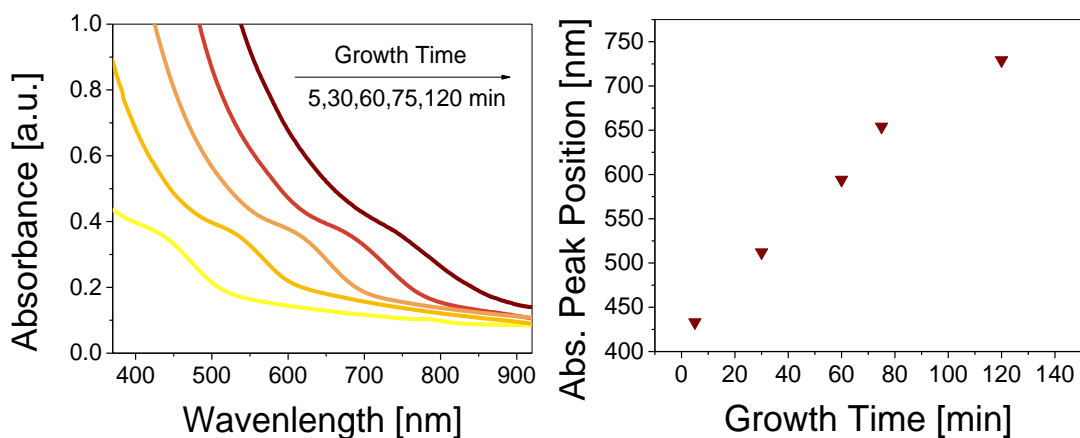


Figure 19: UV-vis spectra of the nanocomposite dispersion synthesized using cadmium acetate and sodium telluride hydride as precursor salt in the presence of $\text{Na}_{0.5}$ -hectorite. Due to variation of the reflux time ($t=5$ -120 min) nanocrystals with various size can be obtained.

The absorbance band gap shifts from the visible wavelength range ($\lambda=433$ nm) to the near infrared range ($\lambda=729$ nm). As discussed in Chapter 2, quantum dot size is directly related to the observed absorbance edge due to the spatial confinement and its influence on the electronic structure. The long absorption tail on the low energy side indicates the presence of nanoclay material. The corresponding photograph of taken aliquots is depicted in figure 20.

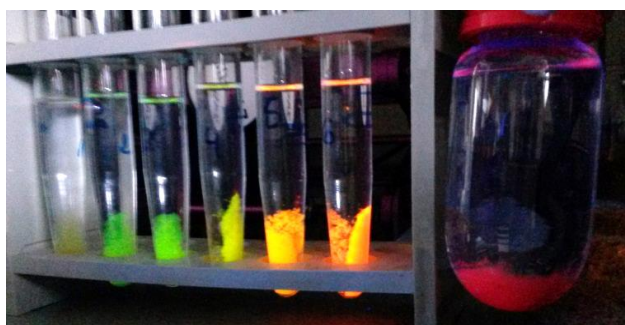


Figure 20: Photograph of a series of CdTe-nanoclay composite materials taken after different reaction times demonstrating their size-related optical properties covering the visible and near-infrared region.

The 10-fold weight percentage of $\text{Na}_{0.5}$ -hectorite (resp. Cd precursor) and the presence of stabilizing ligands significantly slow down the ionic reaction during the formation of quantum dots.

Compared to free solutions, these factors affect the effective ion diffusion within the reaction mixture.^[49] Spatial restriction was also generated by the selective attachment of cadmium ions along the nanoclay edges, and the complexation through stabilizing ligands. The following shows the synthetic parameters of the hot-injection synthesis and summarizes optical information about the nanocomposites.

Table 6: Synthetic conditions and optoelectronic information of nanoclay-based composites.

Sample	Reflux time [min]	Temperature [°C]	Abs. max [nm]
QDN-05	5	100	433
QDN-30	30	100	512
QDN-60	60	100	594
QDN-75	75	100	654
QDN-120	120	100	729

4.4.2 Fluorescence Microscopy

Fluorescence microscopy is an effective technique to visualize and localize quantum dots after their preparation in the presence of nanoclays. The microscope is equipped with a mercury lamp as light source and an orange filter for emission detection between 575–625 nm. The optimized excitation wavelength filter for CdTe QD is around 500–550 nm. The fluorescence of the QD/nanoclay after QD synthesis for 1 h at 100 °C was detected under the microscope at (x40) magnification. The following figure 21 shows the nanocomposites prepared according to the previously described hot injection method.

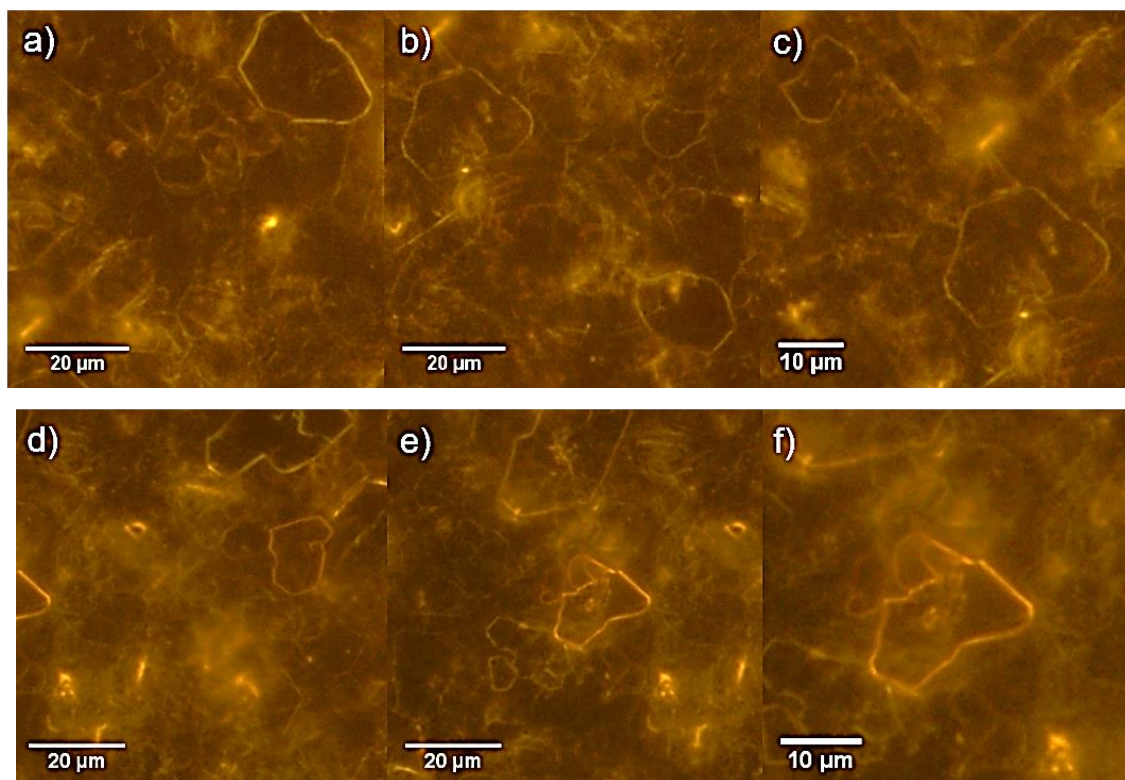


Figure 21: Fluorescence image of CdTe/nanoclay nanocomposites (QDN-60), synthesized according to the hot injection route at 100 °C for 60 min in water (1 wt% in water), showing quantum dot-labeled edges.

The studies indicate clearly the presence of QDs in the hybrid nanomaterial. The selective adsorption of cadmium ions at the edges and the subsequent injection of telluride-based precursor in the presence of thiol-containing ligands allow the growth of water-stable and strongly fluorescent QDs. Regarding the distribution, the QDs showed preferred attachment on the nanoclay edges instead of a random distribution on the drop-cast nanocomposite film. In contrast to earlier studies, the contours of the single lamellae are visible, whereas no emission signal is detected at the basal surfaces.

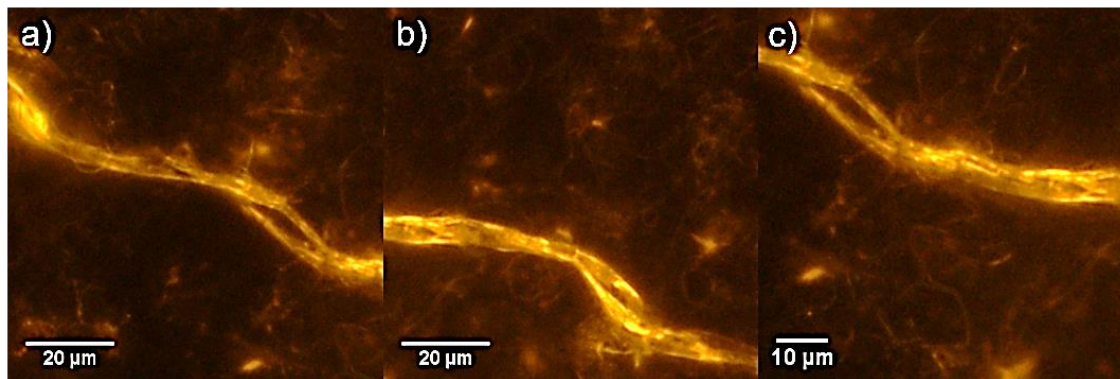


Figure 22: Fluorescence image of CdTe/nanoclay nanocomposites, synthesized a by the hot injection route at 100 °C for 60 min in water (1 wt% in water, QDN-60) showing quantum dots along the edges of stacked nanoclay lamellae.

The top-down view in figure 22 (a)-(c) shows the edge of stacked lamellae sheets. Insufficiently delaminated clays assist the nanoclays to stay upright at the edges as consequence of the preparation method. Fluorescence microscopic images display the size-related emission of immobilized QDs, but for more information about the detailed localization of the semiconductor nanocrystals, the combination with high resolution transmission electron microscopy and topographical AFM measurements is required.

4.4.3 Atomic Force Microscopy

Atomic force microscopy (AFM) is a useful technique for analyzing the surface morphology of thicker structures. The advantage of AFM over fluorescence microscopy is, that horizontal dimensions (x- and y-dimensions) of the sample within the nm to μm region and the vertical dimensions (height and depth profile, z-direction) can be determined. When the AFM technique operates in a vibrating mode, the cantilever vertically scans the sample surface and inter-atomic forces between sample surface and tip cause changes in the amplitude of the tip vibration. For topographical mapping, changes in the vibrational amplitude are transformed into a height image which provides information about the surface roughness. Additionally, the tapping mode allows the simultaneous detection of the phase image which provide information about surface features. Phase imaging enables one to identify different materials and differentiate between regions of

distinct surface hardness.^[50] For this AFM technique, the phase lag between the signal that drives the cantilever to oscillate and the cantilever oscillation output signal are monitored. The surface properties cause the phase lag while the topographic image is taken and a direct correlation between surface and topographic features exists during the detection of the three dimensions with high magnification.

Different aliquots from the aqueous QD/nanoclay reaction mixture after the reaction times of 60 min, 75 min and 120 min were taken and quenched with water. The highly diluted dispersions were spin-coated on pre-cleaned glass wafers. The tapping mode was chosen for AFM analysis and the recorded surface profiles are shown in figure 23.

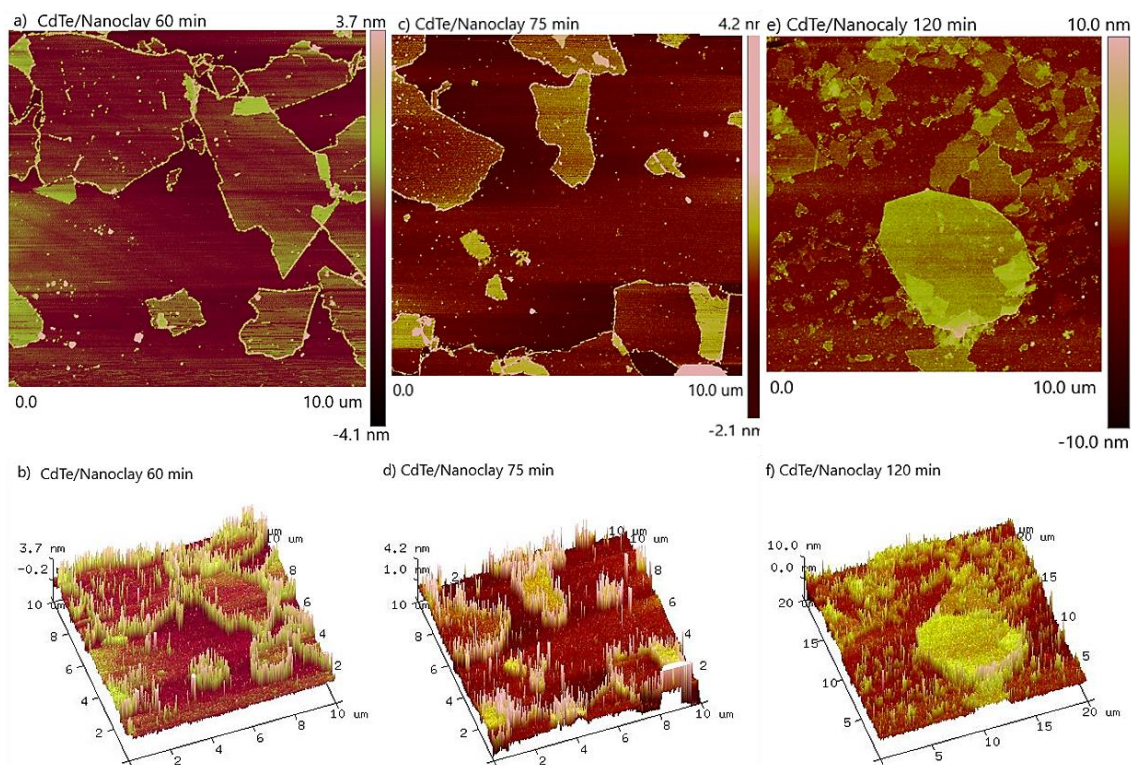


Figure 23: Topographical AFM images of a $\text{Na}_{0.5}$ -hectorite after the synthesis. (a) 2D image and (b) 3D image nanoclays surrounded by CdTe quantum dots after 60 min reaction time (QDN-60). (c) and (d) show sample QDN-75 with partially stacked nanoplatelets because of drying effects. (e) and (f) show 2D and 3D images of CdTe/nanoclay nanocomposite after 2 h (QDN-120).

According to the 2D and 3D topographical images, the darker regions correspond to the nanoclays which exhibit a uniform contrast on the glass substrate, representing a smooth surface. The $\text{Na}_{0.5}$ -hectorite was delaminated into single lamellae with lateral dimensions reaching from 0.5 to 10 μm .

Brighter areas label the support material which can be assigned as the QD around the nanoclay edges. The CdTe quantum dot show a selective attachment on the nanoplatelets. The large hectorite platelets as well as the QDs show some contrast in the 10-20 μm scanned regions. Zooming in on regions of interest which show CdTe surrounded nanoclays and a corresponding cross-section analysis can give more information about the dimensions (figure 22). The typical 2D line profiles show discrete steps between the nanoclay monolayers and substrate. The typical height of the lamellae is found to be around 1.2 nm. Under higher magnification remarkable differences between the nanoclay height and the QD around the edges could be detected. The height data gives information about the precise dimensions of the nanocrystals. Figure 24 (a) and (b) show the results after 60 min reaction time with QD height around $2.03 \text{ nm} \pm 0.4 \text{ nm}$. After 75 min reaction time (c) and (d) the lateral dimensions of measured CdTe reaches $2.85 \text{ nm} \pm 0.4 \text{ nm}$ for 2 h synthesis $5.8 \text{ nm} \pm 0.5 \text{ nm}$.

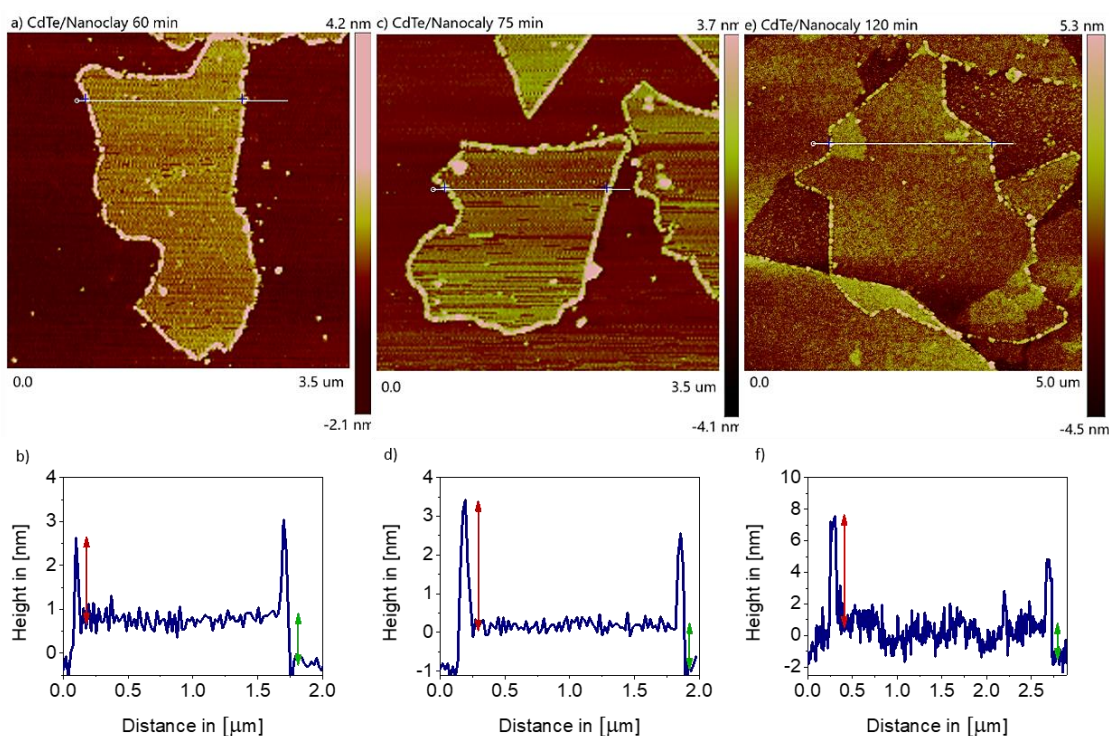


Figure 24: Topographical AFM images (a) and the corresponding cross section (b) of QDN-60 gives QD height of 2.03 nm. (c) and (d) height profile of CdTe/nanoclay composites with quantum dot diameter of 2.85 nm (QDN-75). (e) and (f) show sample QDN-120 with mean diameter of 5.8 nm. The height of the delaminated nanoclays is in the range 1.08 nm to 1.16 nm.

Beside topographical imaging, operating in the AFM tapping mode allows the detection of phase images and the distinction between different surface features. The AFM cantilever is also sensitive enough to detect phase shifts which can be attributed to the substrate materials. The phase lag is induced by several factors, such as material stiffness, adhesion, and dissipated energy, making the interpretation of the data more complicated.^[51] For our needs, phase imaging is sufficient for the detection of heterogeneities and in consideration of the height profile a distinction of the multicomponent sample is possible.

The different contrasts in the AFM phase images (figure 25) defines the composition of the hybrid material. The phase shift and therefore the material stiffness is highlighted with different colors. According to the mapping of components, the bright domains represent larger phase shifts which can be attributed to the ligand-covered CdTe quantum dots. The darker nanoclay regions correspond to the delaminated clay material.

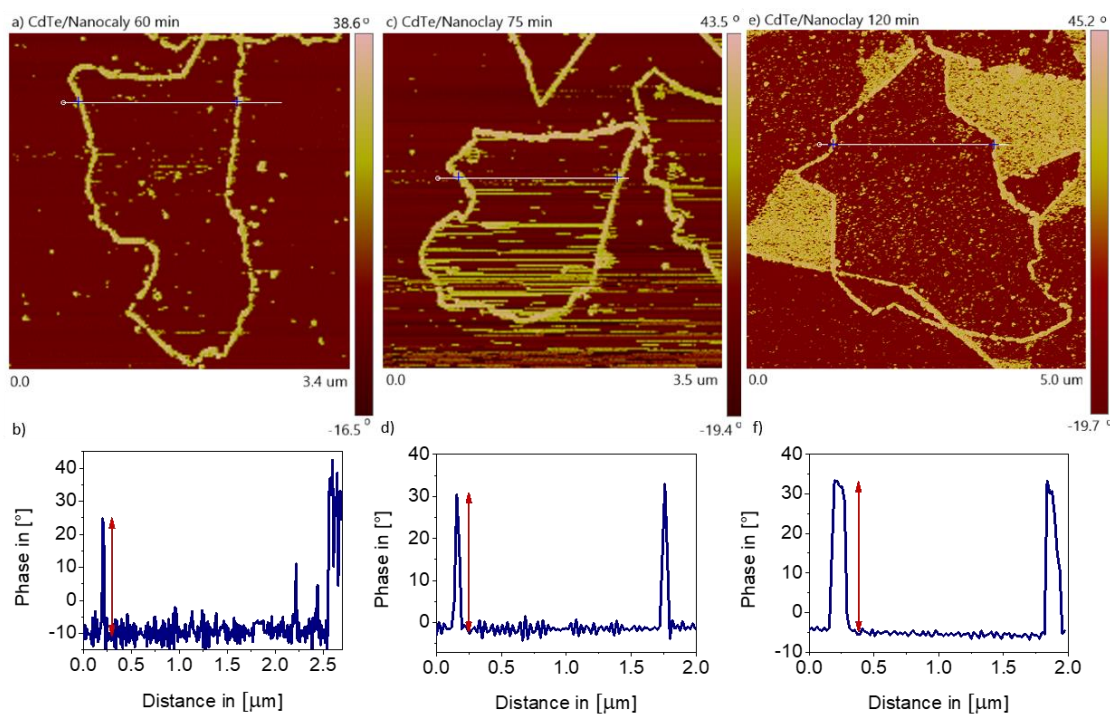


Figure 25: Phase AFM images (a) of nanocomposites QDN-60 and the corresponding cross section (b) after 60 min synthesis gave QD with 32.18° phase difference. After 75 min reaction time (QDN-75) the phase profile of 37.9° difference (c) and (d) show delaminated nanoclay composites a phase lag of 34.6° could be detected for QDN-120 after 120 min (e) and (f).

Figure 25 shows the corresponding cross-sectional profile of the phase images with the same selected line as for the topographical image. The phase difference in the chemical-dependent phase image is about 36° for moderate tapping. The cross-section profile matches the results of the corresponding valleys of the topographical image. It can be surely concluded, that the QD are arrayed along the nanoclay edges. The phase image differs strong from that of the topography and show artifacts around the nanoclay platelet (phase lag around 40°). The cantilever loses contact with the objects in tapping mode due to stacked nanoplatelets differing in height and depth. The tapping mode allows the detection of chemical-dependent phase data which informs one about the roughness of the composite material, but the information obtained depends strongly on the cantilever shape. The limited lateral resolution is caused by the finite tip-end radius which leads to enlarged objects. The accurate shape and size detection of nanocrystals with sizes around 2 nm to 6 nm is very difficult. It is also not possible to discern two neighboring nanocrystals. In our case, we used the vertical height data to get information from the nanocrystals on the solid substrate.

4.4.4 Transmission Electron Microscopy

AFM measurements and fluorescence microscopy are consistent and demonstrate selective QD growth along the edges. TEM offers an alternative method for detection of QD in the nm-region to verify the results from the previous methods and get detailed information about the QD arrangement. The particle size, morphology, size distribution and interparticle distance need to be explored.

TEM measurements are challenging for nanocrystals on macroscopic substrates, because the detection of nanomaterials becomes impossible when the inorganic support material is not transparent to the electron beam. The consequences are a low contrast and the distinction between substrate and quantum dots is not possible. The identification and size estimation of smaller CdTe quantum dots is quite demanding. We know from previous results that QD are arranged along clay edges, hence a detailed analysis is more promising.

For the TEM analysis a few droplets of the CdTe/nanoclay dispersion were deposited on carbon coated copper grids. After the solvent evaporation in air and at room temperature, the detection of nanocomposites only gave reliable results for aliquots taken after 75 min and 120 min reaction time (figure 26).

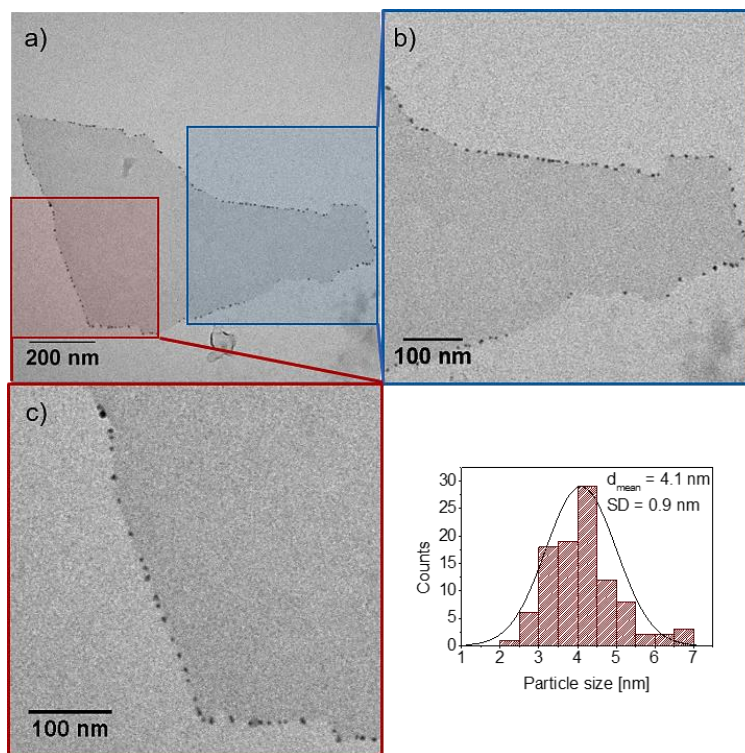


Figure 26: TEM images after the in-situ growth process (QDN-75: T=100 °C, 75 min) illustrate the size distribution of the well-separated nanocrystals as well as the nearly monodisperse morphology of the highly emissive CdTe quantum dots with an average size of 4.1 nm \pm 0.9 nm (1 wt% in water, (a) scale bar 200 nm (b) scale bar 100 nm (c) scale bar 100 nm).

The TEM images of sample QDN-75 reaction time lead to an organized attachment of QD. In contrast to AFM images, the QD appear well-separated. The colloid array consists of single nanocrystals along the nanoclay edges with interparticle spacings controlled by the inorganic support material and stabilizing ligands.^[2] On one site, the arrangement along the edges is closely packed but not completely saturated, since the preferred adsorption on active octahedral sites of the nanoclays prevents closer contact and leads to the absence of agglomeration of the products. On the other side, the bound QD are exposed to solutions of thiol-bearing stabilizing ligands which control the nanocrystal size due to limited monomer diffusion to the QD surface and electrostatic repulsion between particles.

The mean particle diameter of QDN-75 was calculated to be 4.1 nm and the standard deviation to 0.9 nm based on 100 particles ($N=100$). The relative standard deviation (RSD) is around 21.9 %. The values are significantly greater than the mean feature height measured with AFM indicating that the QD are not completely spherical.

TEM analysis of QDN-120 (figure 27) also gave more clarity about the synthesized nanocomposites, displaying arranged QD with mean particle diameters of 6.9 nm and a standard deviation of 1.5 nm ($N=100$, RSD=21.7 %). The size values are significantly greater than the mean feature height measured with AFM. The samples show an overall increase of the QD size for longer reaction times.

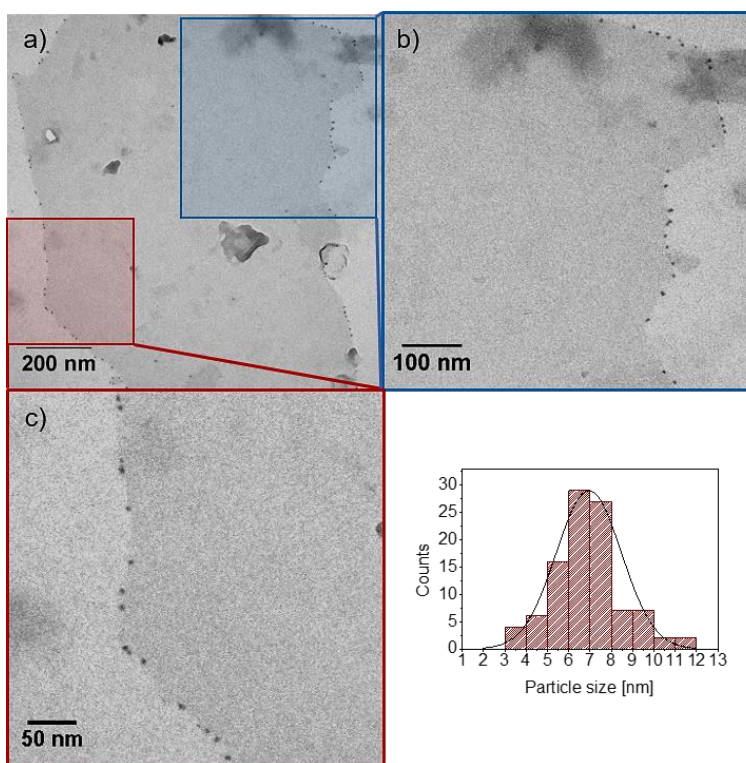


Figure 27: TEM images after the in-situ growth process (QDN-120: T=100 °C, 120 min) illustrate the size distribution of the well-separated nanocrystals as well as the nearly monodisperse morphology of the highly emissive CdTe quantum dots with an average size of $6.9 \text{ nm} \pm 1.5 \text{ nm}$ (1 wt% in water, (a) scale bar 200 nm (b) scale bar 100 nm (c) scale bar 50 nm).

The TEM characterization support the results obtained from AFM and fluorescence microscopy. TEM illustrates the good size distribution of the well-separated CdTe quantum dots, with uniform

morphology corresponding to the growth time. In contrast to the conventional synthesis, smaller CdTe quantum dots could be obtained with longer reaction times. The presence of the support material and a high ligand concentration makes monomer diffusion to the particle surface less easy. The stepwise synthesis, which starts with electrostatic adsorption of ions at defined positions at low ion concentration, and a certain pH value, on the substrate, leads to a controlled colloid deposition along the edges. This approach gives organized arrays and a lower coverage of well-spaced QD. Due to their defined attachment and accessibility, the optimal emissive potential can be achieved at low QD concentration. Towards further spectroscopic applications, the size-dependent properties of both materials can be exploited. The QD must be strongly bound because the samples are washed several times with water without dislodging them. This fact makes these materials attractive for further fabrication and processing. Table 7 highlights the characteristics of the nanoclay-based composites.

Table 7: Characteristics of CdTe quantum dots attached on nanoclay edges at different reaction times.

Sample	Reflux time [min]	Temperature [°C]	Abs. max [nm]	AFM height [nm]	TEM d_{mean} [nm]
QDN-05	5	100	433	-	-
QDN-30	30	100	512	-	-
QDN-60	60	100	594	2.0	-
QDN-75	75	100	654	2.9	4.1 ± 0.9
QDN-120	120	100	729	5.8	6.9 ± 1.5

There are some reports in the literature, which investigated the size-dependent optical properties of CdTe quantum dots.^{[52][53]} The studies demonstrated, that the extinction coefficient of nanocrystals at the first excitonic absorption peak correlates strongly with the size of the nanocrystals. The term of the empirical fitting function is provided below where D is the nanocrystal diameter in nm and λ the wavelength of the first excitonic absorption peak.

$$D = (9.8127 \cdot 10^{-7})\lambda^3 - (1.7147 \cdot 10^{-3})\lambda^2 + (1.0064)\lambda - (194.84) \quad (4.1)$$

In our case, the dilute solutions of QDN-75 and QDN-120 in water show absorbance edges around 654 nm and 729 nm due to the spatial confinement in three dimensions. Furthermore, their mean particle diameter (determined by TEM) was calculated to be around 4.1 nm and 6.9 nm.

A comparison of the data to equation 4.1 shows, that the obtained data are in close agreement with the corresponding quantum dots sizes determined by TEM. The quantum dot size of QDN-75 was calculated to be 4.4 nm and diameter of QDN-120 is around 7.7 nm. It clearly indicates that the band edge increases with size and the impact on the electronic structure through clay material or interparticle coupling between the nanocrystals can be neglected.

4.5 Conclusion

In this chapter the in-situ growth process of colloidal CdTe quantum dots onto hectorite nanoclays was examined. It was found that with this hot-injection approach, the formation of nanocrystals takes part preferentially on the edges of the exfoliated nanoclays and results in well-organized colloidal structures. Direct imaging of the nanoparticle arrays with Fluorescence Microscopy, Atomic Force Microscopy (AFM), and Transmission Electron Microscopy (TEM) enabled us to control the structural and optical features of the nanocomposite.

The special chemical structure of nanoclays and their responsiveness to environmental conditions are perfectly compatible with the reaction conditions of the CdTe quantum dots synthesis previously reported. The synthetic approach can be divided in two stages. The nucleation process which includes the adsorption of the precursor cations onto the matrix system, followed by the second step which describes the nanoparticle growth in the presence of stabilizing agents at higher pH values. Nearly monodisperse, well-separated and highly stable quantum dots can be synthesized while maintaining their unique properties. The influence of the reaction time results in tuning of the optical properties including emission ranging from the visible and to the near infrared region.

This versatile method could be suitable for other nanoparticles. Small, perfectly covered regions of quantum dots are synthesized under Schlenk conditions. The outstanding properties of quantum dots and nanoclays are combined by taking the advantage of low ion concentration and exploiting the maximum potential of optoelectronic nanocrystals. The selective attachment of the single CdTe/aluminosilicates layers opens the way for alignment of anisotropic nanocrystals (e.g. sensor functions). The high surface-area of nanoclays could make a positive contribution in view of catalytically active nanocomposites. The combination of more nanomaterials of different nature are interesting to build ternary systems. The specific adsorption of nanocrystals on inorganic support material, the ease of fabrication of the construct, as well as the resulting optical features, are showing a strong contribution to the research field of 'smart materials' which can be used to create a variety of optoelectronic devices.

Appendix 1

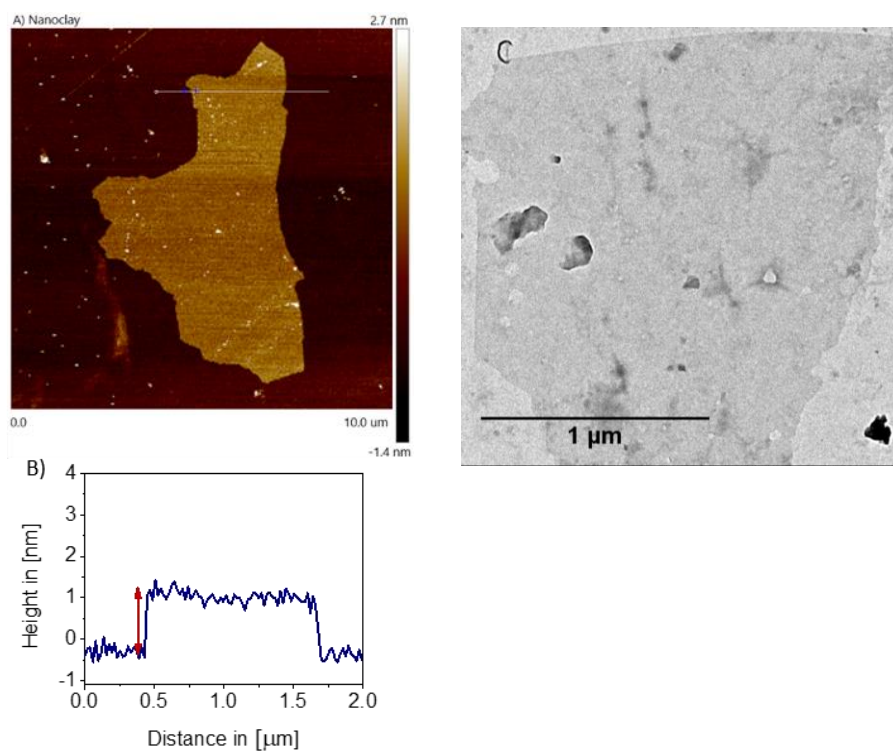


Figure S1: Additional data of AFM (left) and TEM (right) analysis of $[\text{Na}_{0.5}]^{\text{inter}} [\text{Mg}_{2.5}\text{Li}_{0.5}]^{\text{octr}} [\text{Si}_4]^{\text{tetr}} \text{O}_{10}\text{F}_2$ hectorite to prove the delamination into single lamellae with lateral dimensions reaching from 0.5 to 10 μm and the typical height of the lamellae is found to be around 1.2 nm.

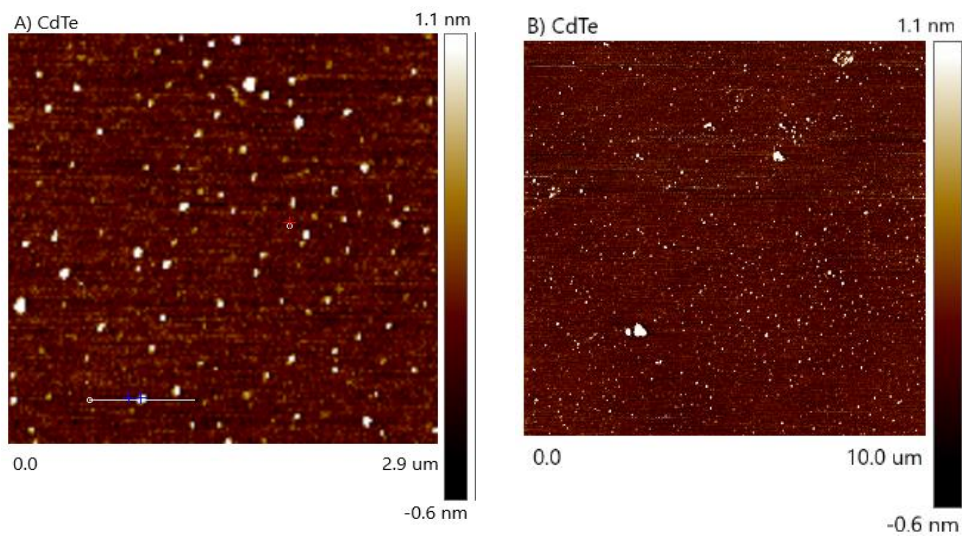


Figure S2: Additional data of AFM analysis of CdTe quantum dots synthesized via hot-injection method at 100 °C in aqueous medium.

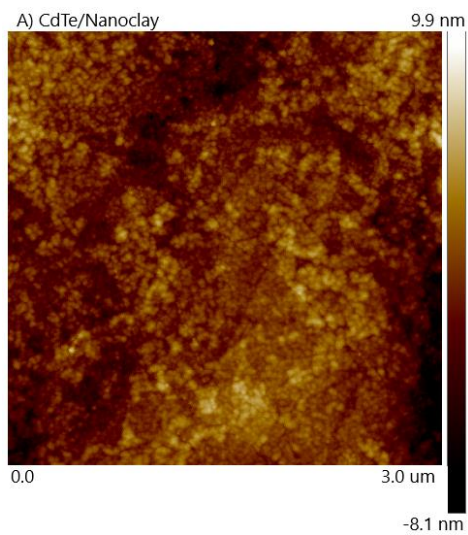


Figure S3: AFM image to study the surface modification of $[\text{Na}_{0.5}]^{\text{inter}} [\text{Mg}_{2.5}\text{Li}_{0.5}]^{\text{oct}} [\text{Si}_4]^{\text{tet}} \text{O}_{10}\text{F}_2$ nanoclays after the in-situ growth of CdTe nanocrystals. The 7-fold amount of cadmium precursor (resp. $\text{Na}_{0.5}$ -hectorite, 14.8 g $\text{Cd}^{2+}/100$ g clay and 35 g $\text{Cd}(\text{acetate}) \times 2\text{H}_2\text{O}/100$ g clay) results in fully covered nanoclay lamellae.

References

- [1] D. Varade, K. Haraguchi, 'Synthesis of Highly Active and Thermally Stable Nanostructured Pt / Clay Materials by Clay Mediated In Situ Reduction', *Langmuir*, vol. 26, no. 6, pp. 1977–1984, 2013.
- [2] I. W. Andrew N. Shipway Eugenio Katz, 'Nanoparticle Arrays on Surfaces for Electronic, Optical, and Sensor Applications', *ChemPhysChem*, vol. 1, no. 15, pp. 18–52, 2000.
- [3] R. Srinivasan, 'Advances in application of natural clay and its composites in removal of biological, organic, and inorganic contaminants from drinking water', *Advances in Materials Science and Engineering*, vol. 2011, pp. 1-17, 2011.
- [4] M. Ramiasa, K. Locock, C. Abrahamsson, and M. Nyden, 'Smart polymer-clay composite nanomaterials', *International Conference on Nanoscience and Nanotechnology* pp. 50–53, 2014.
- [5] M. Galimberti, Ed., *Rubber-Clay Nanocomposites*. Hoboken, NJ, USA: John Wiley & Sons, Inc., 2011.
- [6] K. C. Grabar *et al.*, 'Two-Dimensional Arrays of Colloidal Gold Particles: A Flexible Approach to Macroscopic Metal Surfaces', *Langmuir*, vol. 12, no. 10, pp. 2353–2361, 1996.
- [7] N. A. Kotov, I. Dekany, and J. H. Fendler, 'Layer-by-layer self-assembly of polyelectrolyte-semiconductor nanoparticle composite films', *Journal of physical chemistry*, vol. 99, no. 35, pp. 13065–13069, 1995.
- [8] G. Chumanov, K. Sokolov, B. W. Gregory, and T. M. Cotton, 'Colloidal metal films as a substrate for surface-enhanced spectroscopy', *Journal of physical chemistry*, vol. 99, no. 23, pp. 9466–9471, 1995.
- [9] N. Z. Rosly, S. A. A. Ahmad, J. Abdullah, and N. A. Yusof, 'Patterned array of poly(Ethylene glycol) silane monolayer for label-free detection of dengue', *Sensors (Switzerland)*, vol. 16, no. 9, pp. 1–11, 2016.
- [10] Q. Zhang, C. Xue, Y. Yuan, J. Lee, D. Sun, and J. Xiong, 'Fiber surface modification technology for Fiber-Optic localized surface plasmon resonance biosensors', *Sensors*, vol. 12, no. 3, pp. 2729–2741, 2012.
- [11] J. F. Lemineur and A. M. Ritcey, 'Controlled growth of gold nanoparticles preorganized in Langmuir-Blodgett monolayers', *Langmuir*, vol. 32, no. 46, pp. 12056–12066, 2016.
- [12] A. Doron, E. Katz, and I. Willner, 'Organization of Au Colloids as Monolayer Films onto ITO Glass Surfaces: Application of the Metal Colloid Films as Base Interfaces to Construct Redox-Active Monolayers', *Langmuir*, vol. 11, no. 4, pp. 1313–1317, 1995.

- [13] C. Song, Y. Wei, B. Da, H. Zhang, X. Cong, and B. Yang, 'In situ growth of monolayer porous gold nanoparticles film as high-performance SERS substrates', *Materials Research Express*, vol. 3, no. 7, pp. 1–9, 2016.
- [14] S.-K. Li, Y.-X. Yan, J.-L. Wang, and S.-H. Yu, 'Bio-inspired in situ growth of monolayer silver nanoparticles on graphene oxide paper as multifunctional substrate', *Nanoscale*, vol. 5, no. 24, p. 12616, 2013.
- [15] F. Gao *et al.*, 'CdTe-montmorillonite nanocomposites: Control synthesis, UV radiation-dependent photoluminescence, and enhanced latent fingerprint detection', *Journal of Physical Chemistry C*, vol. 115, no. 44, pp. 21574–21583, 2011.
- [16] G. Lagaly and S. Ziesmer, 'Colloid chemistry of clay minerals: The coagulation of montmorillonite dispersions', *Advances in Colloid and Interface Science*, vol. 100–102, no. SUPPL., pp. 105–128, 2003.
- [17] M. K. Uddin, 'A review on the adsorption of heavy metals by clay minerals, with special focus on the past decade', *Chemical Engineering Journal*, vol. 308, no. September, pp. 438–462, 2017.
- [18] D. A. Kunz, J. Schmid, P. Feicht, J. Erath, A. Fery, and J. Breu, 'Clay-based nanocomposite coating for flexible optoelectronics applying commercial polymers', *ACS Nano*, vol. 7, no. 5, pp. 4275–4280, 2013.
- [19] M. Jawaid, A. el K. Qaiss, and R. Bouhfid, Eds., *Nanoclay Reinforced Polymer Composites*. Singapore: Springer Singapore, 2016.
- [20] J. Zhu *et al.*, 'Novel intercalation mechanism of zwitterionic surfactant modified montmorillonites', *Applied Clay Science*, vol. 141, pp. 265–271, 2017.
- [21] R. Celis, M. Carmen Hermosín, and J. Cornejo, 'Heavy metal adsorption by functionalized clays', *Environmental Science and Technology*, vol. 34, no. 21, pp. 4593–4599, 2000.
- [22] M. L. Chan, K. T. Lau, T. T. Wong, M. P. Ho, and D. Hui, 'Mechanism of reinforcement in a nanoclay/polymer composite', *Composites Part B: Engineering*, vol. 42, no. 6, pp. 1708–1712, 2011.
- [23] P. C. LeBaron and T. J. Pinnavaia, 'Clay nanolayer reinforcement of a silicone elastomer', *Chemistry of Materials*, vol. 13, no. 10, pp. 3760–3765, 2001.
- [24] A. A. Adeyemo, I. O. Adeoye, and O. S. Bello, 'Adsorption of dyes using different types of clay: a review', *Applied Water Science*, vol. 7, no. 2, pp. 543–568, 2017.
- [25] M. Elmuntasir Ibrahim Ahmed, 'Selective Adsorption of Cadmium Species onto Organic Clay Using Experimental and Geochemical Speciation Modeling Data', *International Journal of Engineering and Technology*, vol. 8, no. 2, pp. 128–131, 2016.
-

- [26] M. Stöter *et al.*, ‘Nanoplatelets of sodium hectorite showing aspect ratios of $\approx 20\,000$ and superior purity’, *Langmuir*, vol. 29, no. 4, pp. 1280–1285, 2013.
- [27] P. T. Hang and G. W. Brindley, ‘Methylene blue absorption by clay minerals. Determination of surface areas and cation exchange capacities (clay-organic studies XVIII)’, *Clays and Clay Minerals*, vol. 18, no. 4, pp. 203–212, 1970.
- [28] S. Rosenfeldt *et al.*, ‘In-Depth Insights into the Key Steps of Delamination of Charged 2D Nanomaterials’, *Langmuir*, vol. 32, no. 41, pp. 10582–10588, 2016.
- [29] H. A. Patel, R. S. Somani, H. C. Bajaj, and R. V. Jasra, ‘Nanoclays for polymer nanocomposites, paints, inks, greases and cosmetics formulations, drug delivery vehicle and waste water treatment’, *Bulletin of Materials Science*, vol. 29, no. 2, pp. 133–145, 2006.
- [30] F. Bergaya, B. K. Theng, and G. Lagaly, *Handbook of Clay Science*. Elsevier Ltd, 2006.
- [31] E. M. Pecini and M. J. Avena, ‘Measuring the isoelectric point of the edges of clay mineral particles: The case of montmorillonite’, *Langmuir*, vol. 29, no. 48, pp. 14926–14934, 2013.
- [32] E. Paineau *et al.*, ‘Aqueous suspensions of natural swelling clay minerals. 1. structure and electrostatic interactions’, *Langmuir*, vol. 27, no. 9, pp. 5562–5573, 2011.
- [33] C. Zhang, X. Liu, X. Lu, M. He, E. Jan Meijer, and R. Wang, ‘Surface complexation of heavy metal cations on clay edges: insights from first principles molecular dynamics simulation of Ni(II)’, *Geochimica et Cosmochimica Acta*, vol. 203, pp. 54–68, 2017.
- [34] U. K. Saha, S. Taniguchi, and K. Sakurai, ‘Adsorption behavior of cadmium, zinc, and lead on hydroxyaluminum- and hydroxyaluminosilicate-montmorillonite complexes’, *Soil Science Society of America Journal*, vol. 65, no. 3, pp. 694–703, 2001.
- [35] I. Aziz, M. Sirajuddin, M. H. Khan, S. Nadeem, S. A. Tirmizi, and R. A. Khan, ‘Investigation of adsorption of lead(II) onto a montmorillonite clay modified by humic acid’, *Journal of the Chemical Society of Pakistan*, vol. 37, no. 5, 2015.
- [36] F. Ciesielczyk, P. Bartczak, and T. Jesionowski, ‘Removal of cadmium(II) and lead(II) ions from model aqueous solutions using sol–gel-derived inorganic oxide adsorbent’, *Adsorption*, vol. 22, no. 4–6, pp. 445–458, 2016.
- [37] S. Madala, S. K. Nadavala, S. Vudagandla, V. M. Boddu, and K. Abburi, ‘Equilibrium, kinetics and thermodynamics of Cadmium (II) biosorption on to composite chitosan biosorbent’, *Arabian Journal of Chemistry*, vol. 10, pp. S1883–S1893, 2017.
- [38] M. Boroumand Jazi, M. Arshadi, M. J. Amiri, and A. Gil, ‘Kinetic and thermodynamic investigations of Pb(II) and Cd(II) adsorption on nanoscale organo-functionalized SiO₂Al₂O₃’, *Journal of Colloid and Interface Science*, vol. 422, pp. 16–24, 2014.

- [39] A. Moghimi, 'Selective pre-concentration and solid phase extraction of mercury(II) from natural water by silica gel-loaded (E)-N-(1-thien-2'-ylethylidene)-1,2- phenylenediamine phase', *Chinese Journal of Chemistry*, vol. 25, no. 10, pp. 1536–1541, 2007.
- [40] C. H. Weng, Y. C. Sharma, and S. H. Chu, 'Adsorption of Cr(VI) from aqueous solutions by spent activated clay', *Journal of Hazardous Materials*, vol. 155, no. 1–2, pp. 65–75, 2008.
- [41] F. Ciesielczyk, P. Bartczak, and T. Jesionowski, 'Removal of nickel(II) and cadmium(II) ions from aqueous solutions using an oxide adsorbent of MgO·SiO₂ type', *Desalination and Water Treatment*, vol. 55, no. 5, pp. 1271–1284, 2015.
- [42] C. Zhang *et al.*, 'Cadmium(II) Complexes Adsorbed on Clay Edge Surfaces: Insight From First Principles Molecular Dynamics Simulation', *Clays and Clay Minerals*, vol. 64, no. 4, pp. 337–347, Aug. 2016.
- [43] H. Ohtaki and T. Radnai, 'Structure and Dynamics of Hydrated Ions', *Chemical Reviews*, vol. 93, no. 3, pp. 1157–1204, 1993.
- [44] L. Zou *et al.*, 'Ultrafast synthesis of highly luminescent green- to near infrared-emitting CdTe nanocrystals in aqueous phase', *Journal of Materials Chemistry*, vol. 18, p. 2807, 2008.
- [45] M. S. Carvalho, C. Mayrinck, E. Raphael, J. Bettini, J. L. Ferraria, and M. A. Schiavon, 'The role that electrolytes play in the synthesis of water-soluble cdte quantum dots prepared at ambient temperature', *Journal of the Brazilian Chemical Society*, vol. 28, no. 7, pp. 1167–1176, 2017.
- [46] S. Rosenfeldt, 'SAXS measurements on sodium hectorite', manuscript 2014.
- [47] J. P. Reganold and J. B. Harsh, 'Expressing cation exchange capacity in milliequivalents per 100 grams and in SI units', *Journal of Agronomic Education*, vol. 14, no. 2, pp. 84–90, 1985.
- [48] M. Gao *et al.*, 'Strongly Photoluminescent CdTe Nanocrystals by Proper Surface Modification', *The Journal of Physical Chemistry B*, vol. 102, no. 43, pp. 8360–8363, 1998.
- [49] C. D. Shackelford and D. E. Daniel, 'Diffusion in Saturated Soil. I: Background', *Journal of Geotechnical Engineering*, vol. 117, no. 3, pp. 467–484, 1991.
- [50] P. Leclère, R. Lazzaroni, J. L. Brédas, J. M. Yu, P. Dubois, and R. Jérôme, 'Microdomain Morphology Analysis of Block Copolymers by Atomic Force Microscopy with Phase Detection Imaging', *Langmuir*, vol. 12, no. 18, pp. 4317–4320, 1996.
- [51] M. Stark, C. Möller, D. J. Müller, and R. Guckenberger, 'From images to interactions: High-resolution phase imaging in tapping-mode atomic force microscopy', *Biophysical Journal*, vol. 80, no. 6, pp. 3009–3018, 2001.
- [52] W. W. Yu, L. Qu, W. Guo, and X. Peng, 'Experimental determination of the extinction coefficient of CdTe, CdSe, and CdS nanocrystals', *Chemistry of Materials*, vol. 15, no. 14, pp.

2854–2860, 2003.

[53] J. Jasieniak, L. Smith, J. Van Embden, P. Mulvaney, and M. Califano, ‘Re-examination of the size-dependent absorption properties of CdSe quantum dots’, *Journal of Physical Chemistry C*, vol. 113, no. 45, pp. 19468–19474, 2009.

Chapter 5

Study of Nucleation and Growth Kinetics of Perovskite Nanocrystals with In-situ UV-Vis/Scattering Experiments

5.1 Introduction and Motivation

In the last years the field of optoelectronic materials has paid much attention to the properties of semiconducting perovskite materials, with many promising results and applications resulting.^{[1][2][3][4][5]} Galian and Perez-Prieto^{[6][7]} reported in 2014 the colloidal synthesis of metal halide perovskite nanocrystals $\text{CH}_3\text{NH}_3\text{PbBr}_3$ with organic ammonium ligands to stabilize the perovskite crystallites. According to this synthetic procedure, perovskite self-assembly is initiated by anti-solvents which induce the precipitation of the nanocrystals. Several nucleation crystals are formed due to supersaturation of the system which lead to further crystal growth. For the soft-template method according Zhu et al.^[8], specific precursor ratios as well as the solvent/anti-solvent ratio play the critical role in the formation of perovskite nanocrystals. The change in composition and reaction conditions results in various morphologies (i.e. spherical dots, nanocubes, nanoplatelets). Numerous research groups modified this ligand-assisted precipitation technique by varying the temperature, halide or solvent composition. These studies have given a better insight into the formation process and allowed better control over this material.^{[6][7][9][10][11]} Bandgap tunability due to varying material composition allows in-situ detection with optical methods and the subsequent fabrication of colorful solar cells.^{[12][13][14][15]} The dimensionality may also tune the electronic and optical properties which can be attributed to the quantum confinement effect.^{[16][17][18][19][20]}

The perovskite synthesis is a rapid process with immediate precipitation of semiconducting nanocrystals.^{[7][10][21]} Due to the low formation energy and fast crystallization rate it is hard to monitor the formation process. The aim of this chapter is to investigate the structural development of organohalide lead perovskites $\text{CH}_3\text{NH}_3\text{PbBr}_3$ with the main focus being to adapt this room temperature synthesis to a microfluidic chip and a capillary interdiffusion system for in-situ studies and to underpin these results with those of electron microscopy.

Microfluidic technologies have the ability to access the kinetics of reactions in continuous-flow conditions. Obtaining quantitative information about the reaction and developing of diverse nanocrystal morphologies are both possible in this way.^{[21][22][23]} The laminar flow and the chip

channel geometry permit controlled mixing conditions with microfluidic devices. The entire chip is optically transparent and planar so that emissive properties can be observed easily via confocal microscopy.^[24]

Compared to fast mixing in the microfluidic chip, the slow capillary interdiffusion experiment^[24] results in a controlled perovskite formation. The combination of real-time spectroscopic and scattering experiments allows better insight into the structural evolution. The formation of ultrathin crystalline MAPbBr₃ platelets, and their transformation into monocrystalline platelets and 3D stacked superstructures are investigated.^{[7][8][18][25]} To our knowledge, both setups have not been combined to study the in-situ nucleation and growth processes of organohalide lead perovskites CH₃NH₃PbBr₃ via soft-template methods. The growth mechanism of perovskites is elucidated by combining the experimental results with the principles of nucleation and growth models.

5.2 Structural Evolution of Perovskite Nanocrystals

5.2.1 AMX₃ Organohalide Lead Perovskites

The general chemical formula of pure perovskite AMX₃ structures correspond to an ideal cubic-symmetry.^{[7][26]} The symbols A and M represent the position of the cations and X the anion. These AMX₃ perovskite structures account for a large number of well characterized species,^[26] which can be divided into the alkali-halide and halide perovskites (Figure 28).

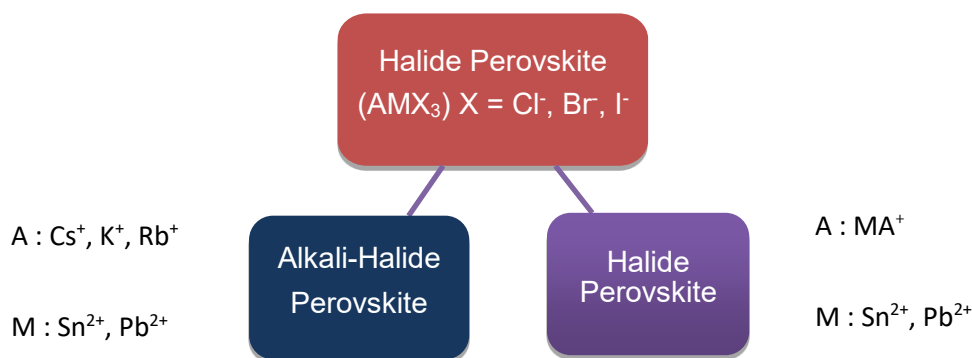


Figure 28: Classification of AMX₃-type perovskites into the alkali-halide perovskites and halide perovskites with monovalent (A), divalent (M) cations and a monovalent halide anion (X).

As it relates to this work, the organohalide category is described in greater detail. The organohalide perovskites consist of monovalent A^I -($CH_3NH_3^+$) and divalent M^{II} -cations (Pb^{2+}), as well as the bromide halide anion ($X=Br^-$). The Pb^{2+} -cation is ideally surrounded by an octahedron of the anions ($PbBr_6$) and the organic compound methylammonium (MA^+ , $CH_3NH_3^+$) is twelve-fold coordinated by the bromide anions ($CH_3NH_3Br_{12}$ -cubooctahedra) (Figure 29). A reduced coordination number or substitutions of cations results in distortion of the ideal cubic-like crystal lattice (expressed by the tolerance factor $t = 1$; R_A, R_M, R_X : ionic radii of A, M and X). This affects the electronic, magnetic and dielectric properties of perovskites.^{[27][28][29]} A controlled combination of all three ionic components allows band gap tuning over almost the entire visible spectrum (direct energy gaps 1.4 eV–2.2 eV).^{[12][26]}

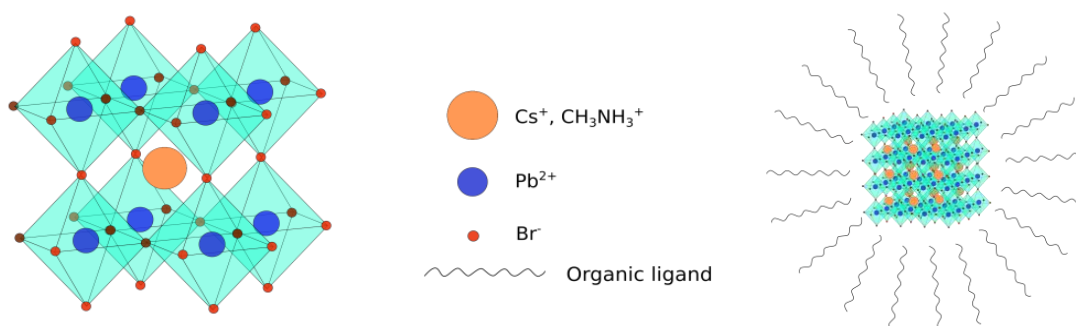


Figure 29: Schematic illustration of a cubic halide perovskites $CH_3NH_3PbBr_3$ unit cell (left) and perovskite nanocube surrounded by organic stabilizing ligands (right).

The high absorption coefficient, a high yield of free electrons and holes and a long lifetime/diffusion length of charge carrier due to the absence of recombination are some of the requirements to reach high performance levels in optoelectronic devices.^{[29][30][31]} Monocrystalline $MAPbBr_3$ perovskite platelets have a reduced dimensionality in one dimension (thickness, quantum confined) resulting in useful spectral features.^[32] The higher lateral dimension enables guiding of electromagnetic waves within the material with reduced non-radiative decay. According to the well-established template-based method^{[8][18][25]} of Schmidt et al.^[7] colloidal nanoplatelets could be synthesized in the presence of long aliphatic ligands and fully characterized by optical and electron microscopy methods. The presence of octylammonium bromide keeps the quantum platelet thin by allowing further attachment of unit cells only on the (001)-facet. The increase in length occurs on the higher energy (011)- and (022)-planes of the crystal.^[25] The long chain aliphatic amines also

act as surface-passivating ligands.^{[33][34][35]} Therefore, non-radiative recombination on crystal defects and quenching on grain boundaries can be reduced and the emissive properties improved. A few publications investigate the formation of two-dimensional nanocrystals via an oriented-attachment growth process. Weller et al.^[36] reported also the fusion of PbS nanocrystals into nanoplatelets driven by dense packing of organic ligands between the nanocrystals. Hu et al.^[37] reported that oxide perovskite nanoplatelets were composed of nanowires. Sardar and co-workers^[25] assumed a solvent-induced self-assembly process of CH₃NH₃PbBr₃ quantum platelets. We decided to investigate and to exploit this hypothesis, follow the nanocrystal structural evolution by qualitative in-situ and ex-situ techniques.

5.2.2 Kinetic Studies of Nanoparticle Formation with Microfluidic Systems

The introduction of microfluidic systems has allowed the downscaling of conventional flask-based systems. Conventional laboratory-based characterization methods need to be adapted to a new class of devices. We have used microfluidic channels in the past for chemical transport and nanoparticle formation.^{[21][22][23][38]} Micrometer-scaled chips allow the integration of data analysis^{[39][40]} for in-situ detection of experimental conditions. The employ of high-precision syringe pumps for liquid transport^{[24][40]} through the channels. Detection techniques include Confocal Laser Scanning Microscopy (CLSM). Therefore, the microfluidic approach is suitable for monitoring the rapid reaction kinetics of nanoparticle formation and allows a precise study of nucleation and growth of crystals within the chip. The microfluidic channel length can be correlated with the reaction time which provide access to very short reaction times. The diffusion controlled process can also be followed over long time scales by performing measurements at different regions along the channel. Evaluating the emission characteristic along the microfluidic device give a better insight in the nucleation and growth process.

The structural evolution from perovskite nanocrystals is a very fast diffusion-controlled reaction occurring on time scales of a few milliseconds for large scale syntheses at room temperature. In a second approach, a capillary interdiffusion setup is used to slow down the reaction and to detect the formation process in a glass capillary (analysis cell). Compared to microfluidic dimensions, similar volumes were used for the vertically mounted capillary. The capillary interdiffusion perovskite formation is followed by UV-Vis measurements and X-ray scattering experiments with very high sensitivity. To adapt and monitor the synthesis, the perovskite formation should be

sufficiently slowly which can be realized using a buffer layer that slows diffusion. The structural evolution of the reactant interdiffusion within the microfluidic chip, and the slow capillary interdiffusion in the capillary, provide detailed insight into kinetic pathways and intermediate states of the perovskite formation.

5.3 Experimental Section

Perovskite Sample Preparation

The precursor octylammonium bromide and methylammonium were synthesized according to literature reports with slight modifications and stored in a vacuum oven until use.^[41]

For the $\text{CH}_3\text{NH}_3\text{PbBr}_3$ perovskite synthesis, four different ratios of PbBr_2 :methylammonium bromide (MAmBr):octylammonium bromide (OAmBr) were tested with a fixed solvent/anti-solvent ratio DMF:Toluene of 1:5 at room temperature (Chapter 3, Table 2) in a conventional large synthesis. The precursor salts were mixed in DMF and slowly injected into the anti-solvent toluene. The reaction mixture was cooled and centrifuged. The redispersed sample was then used for further analysis.

The ligand-assisted synthesis^[8] was optimized for our needs to adapt the recipe to the microfluidic channel and capillary interdiffusion model. For optimal experimental conditions the molar ratio of PbBr_2 :OAmBr:MAmBr 0.10:0.16:0.24 was held constant and the precursors were dissolved in Toluene/DMF 1:1. Additionally, a solvent mixture of Toluene/DMF 2:1 was prepared for the microfluidic experiment. The capillary interdiffusion experiment works with an additional buffer layer of 1:1 DMF/Toluene. The relevant details will be reported in each subchapter.

5.4 Results and Discussion

5.4.1 Perovskite Large Scale Synthesis

Research has shown that the variation of composition $\text{PbBr}_2:\text{MAmBr}:\text{OAmBr}$ and reaction conditions (injection speed, temperature and growth time) results in various morphologies, predominantly influenced and controlled by long alkyl-chain cations.^{[8][9][10][11][18]} The ligand-assisted synthesis^[8] was modified to a suitable recipe wherein the perovskite formation could be detected in an adequate time window. The perovskite crystal formation as well as the buildup of ligand-stabilized surfaces/facets can be demonstrated.

The synthesis of $\text{CH}_3\text{NH}_3\text{PbBr}_3$ perovskites was carried out with a fixed solvent/anti-solvent ratio of DMF 1:5 Toluene at room temperature. The precursors were dissolved in DMF and the slowly injected into toluene. Systematical tests by adjusting the molar ratio between PbBr_2 , MAmBr and OAmBr to 0.1:0.1:0.3 (P03), 0.1:0.3:0.1 (P02) and 0.3:0.1:0.1 (P01) give an overview of the perovskite formation. Instantaneous precipitation and a color change to yellow/orange was observed. The synthesis shows a gradual aggregation of the product arising from larger aggregates which precipitate out from the toluene solution. The dispersion was placed on carbon-coated copper grids. After solvent evaporation in air, the detection of products at advanced growth stages was observed. The sample P03 is shown in figure 30.

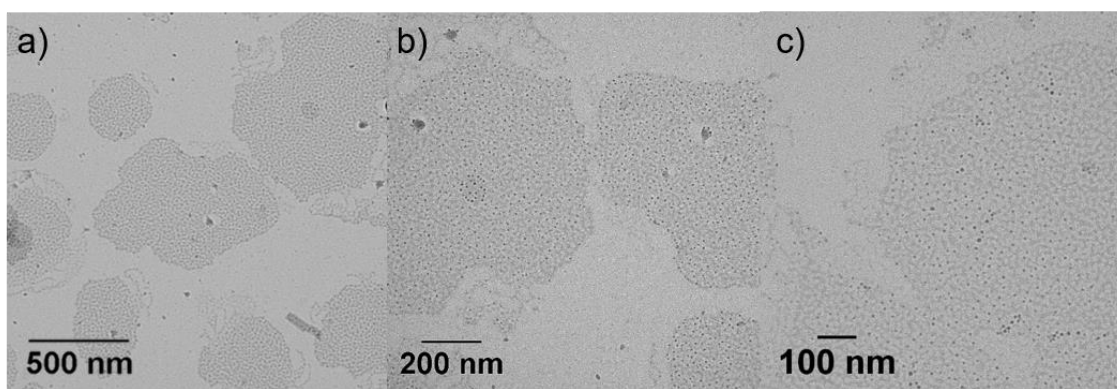


Figure 30: TEM images ((a)–(c)) show the formation of nanocrystal islands prepared with ratio $\text{PbBr}_2:\text{OAmBr}:\text{MAmBr}$ 0.1:0.3:0.1 (P03) in toluene ($5.3 \text{ nm} \pm 1.0 \text{ nm}$ in diameter).

We obtained islands of well-separated spherical nanospheres with 3-fold excess of OAmBr. The nanocrystals show a size distribution of $5.3 \text{ nm} \pm 1.0 \text{ nm}$ surrounded by weak contrasted regions due to organic ligands. Two-dimensional organometallic halide perovskite nanoplatelets could be obtained by TEM analyses of MAmBr rich samples (P02). The produced platelets present, showed a mixture of small- and large-sized particles with varying thickness (figure 31). Smaller spots decorate the nanoplatelets. These results coincide with that one reported by Zhu et al.^[8]

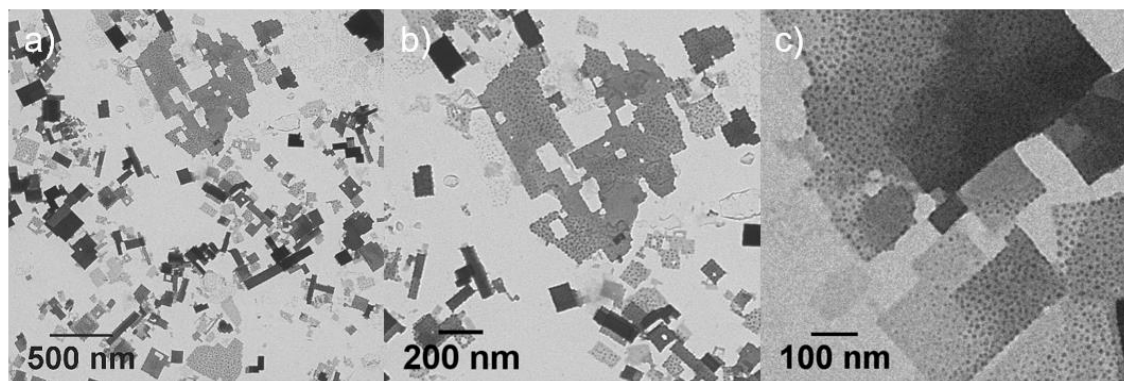


Figure 31: TEM images ((a)–(c)) show the formation of ultra-thin nanoplatelets of various size prepared with ratio $\text{PbBr}_2:\text{OAmBr}:\text{MAmBr}$ 0.1:0.1:0.3 (P02) in toluene.

An increase in the lead bromide content leads (P01) to three-dimensional nanocube formation. The ligands cannot effectively restrain the growth process in three dimensions but OAmBr is still able to coordinate at the surface of the perovskite crystals and contain smaller nanocrystals (figure 32).

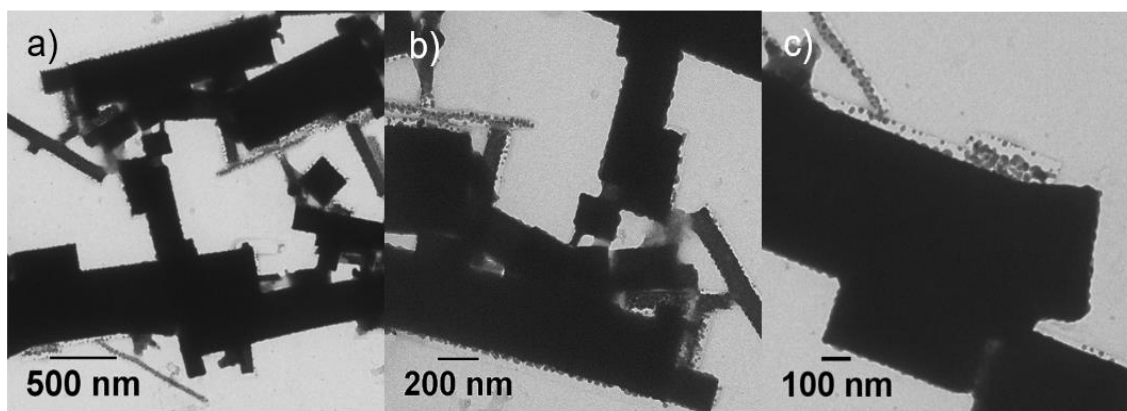


Figure 32: TEM images ((a)–(c)) show the formation of three-dimensional nanocubes prepared with ratio $\text{PbBr}_2:\text{OAmBr}:\text{MAmBr}$ 0.3:0.1:0.1 (P01) in toluene.

It is clear that the ratio $\text{PbBr}_2:\text{OAmBr}:\text{MAMBr}$ influences the perovskite morphology and its associated structural development. The extreme ratios depicted above, are similar to the results reported elsewhere. The ligand ratio plays an important role in promoting the growth process and determining the final structure and optical properties. For a more detailed understanding of the shape-controlled synthesis, anisotropic nanocrystals were synthesized. Their structure-property relationship was studied directly after the preparation and one day after. The perovskites were synthesized with a fixed sample composition of $\text{PbBr}_2:\text{OAmBr}:\text{MAMBr}$ 0.1:0.16:0.24 (P04) allowing their ex-situ optical detection and their morphology in the earlier growth stages and after 24 h (figure 33).

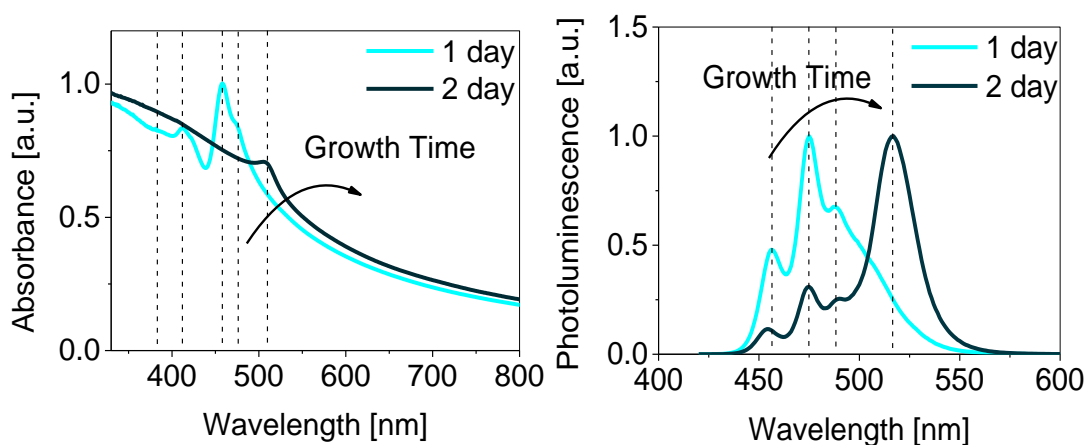


Figure 33: UV-Vis (left) and photoluminescence spectra (right) of $\text{CH}_3\text{NH}_3\text{PbBr}_3$ perovskites with ratio $\text{PbBr}_2:\text{OAmBr}:\text{MAMBr}$ 0.1:0.16:0.24 (P04) in toluene ($\lambda_{\text{exc}}=350$ nm) over 2 days.

Absorbance signals could be detected at 385 nm, 411 nm, 455 nm and 473 nm immediately after the injection (figure 33, left). After 24 h, the signals are slightly red-shifted towards 505 nm. Structures of lower dimensionality are mainly responsible for the broad absorbance in the lower wavelength region. The long scattering tail at higher wavelength indicates the presence of larger structures (e.g. superstructures). These observations are in agreement with the literature^{[8][25][42]} where the blue-shift of smaller-dimension nanocrystals is explained by the quantum confinement effect in nanometer dimensions. The presence of 0-dimensional spherical nanocrystals of $4.6 \text{ nm} \pm 1.7 \text{ nm}$ is depicted in figure 34.

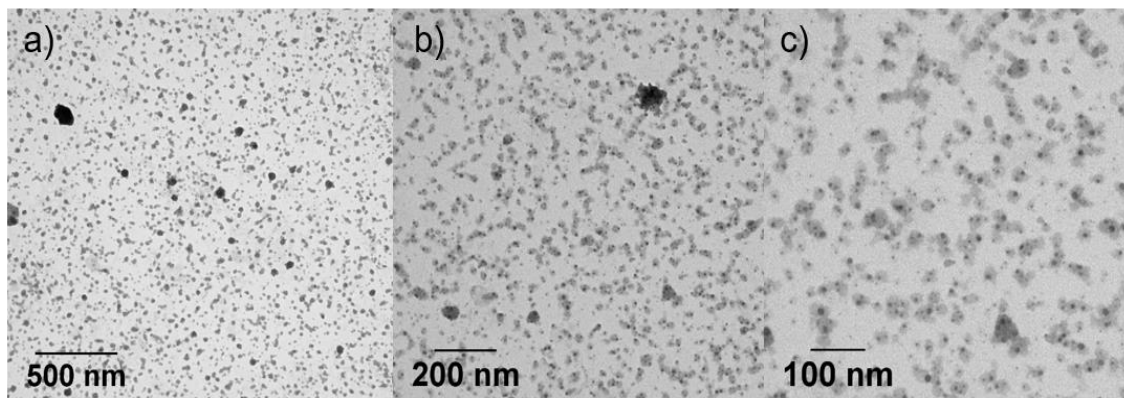


Figure 34: TEM images during the formation of smaller nanocrystals ((a)–(c)) in the early growth stages ($4.6 \text{ nm} \pm 1.7 \text{ nm}$ in diameter) prepared with the ratio $\text{PbBr}_2\text{:OAmBr:MAMBr}$ 0.1:0.16:0.24 (P04) in toluene.

The perovskite formation at room temperature leads in the early growth stages to the instantaneous formation of small particles (colloidal solutions of 3–5 nm nanocrystals) and can be visualized by TEM. The nanocrystals are embedded in an amorphous material.^{[6][42]} In contrast to MAMBr, the OAmBr ligands are not able to be incorporated into the perovskite crystals because of their long hydrocarbon tail. With further reaction time, the formation of nanosheets with varying lengths and widths of 100–600 nm (figure 35 (a–c)) could be visualized via TEM.

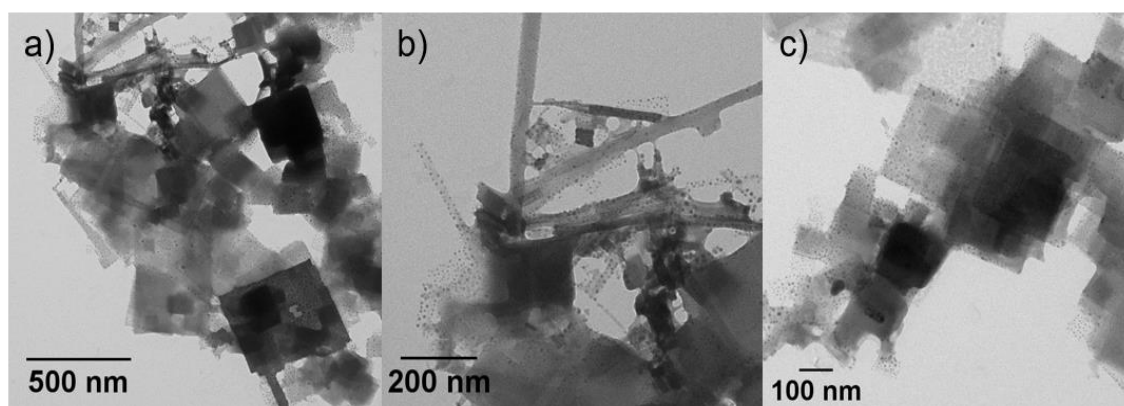


Figure 35: TEM images during the formation of nanocrystals and nanosheets, and smaller nanocrystals prepared with the ratio $\text{PbBr}_2\text{:OAmBr:MAMBr}$ 0.1:0.16:0.24 (P04) in toluene after one day.

Due to the low contrast in TEM imaging compared to the nanocrystals, the sheets are estimated to be much thinner. On the carbon layer the pseudorectangular-shaped quantum platelets are separated by an OAmBr ligand layer. This confirms that the long hydrocarbon chain of amine ligands is on the flat (001) plane of the cubic $\text{CH}_3\text{NH}_3\text{PbBr}_3$.^[25] At longer reaction times the formation of perovskites with a higher dimension framework are stabilized by a ligand-layer. The corresponding photoluminescence spectra (figure 33, right) of the perovskites show the beginnings of the perovskite formation with multiplex emission at 456 nm, 475 nm, 488 nm and 518 nm ($\lambda_{\text{exc}} = 350$ nm). The large blue shift is indicative for the quantum confinement effect of the unpurified sample consisting of various nanostructures.^[19] The emission wavelength maximum after one day shifted towards 518 nm with the corresponding peak position in the absorption spectrum at 505 nm (Stokes shift = 13 nm). The symmetrical band edge emission at 518 nm has a full width at half-maximum (FWHM) of 24.3 nm. The small Stokes shift of perovskites originates from the direct band gap recombination.^[33]

The absorption spectra, the PL peaks, and the corresponding TEM images all suggest, that perovskite growth starts with the formation of subunits in form of spherical nanocrystals. The effect of aging time leads to the formation of higher dimensional structures.^[42] While this large scale approach allows ex-situ characterization, the structural development will be addressed in more detail later on with in-situ experiments.

5.4.2 Ex-situ Electron Microscopy

To explore the size and morphology at different growth stages, ex-situ imaging methods like Scanning and Transmission Electron Microscopies (SEM and TEM) were used. For this investigation the perovskite was prepared according to the large scale synthesis mentioned above. The ratios of PbBr_2 :OAmBr:MAmBr 0.1:0.16:0.24 (P04) and 0.1:0.1:0.3 (P01) were chosen. The corresponding product phase identification only gave reliable results for advanced growth stages.

Transmission Electron Microscopy-Selected Area Electron Diffraction (TEM-SAED)

As a result of the preliminary large scale synthesis, three different growth stages were characterized with the TEM-SAED method. The electron beam interacts with the crystalline perovskite specimen

and morphology-dependent reflections and diffraction of the electrons are used for phase identification. The diffraction pattern particularly provides information about the structural development.

As aforementioned TEM images of spheroidal nanocrystals with a rectangular background were detected in the earlier growth stages (P04). They show diffraction patterns consisting of rings with discrete spots. The scattering patterns support the presence of multiple crystals. After comparison with standardized crystallographic diffraction patterns^[43] scattering on the formed lattice planes can be reliably attributed to randomly distributed nanocrystals of lead Pb^0 (face-centered cubic lattice, fcc, $\text{Fm}\bar{3}\text{m}$) with sizes between 2 nm to 12 nm. Manna et al.^[44] described the reduction of Pb^{2+} to Pb^0 atoms of inorganic CsPbBr_3 perovskites under electron beam exposure. The degradation under high energy electron beam (80 keV/200 keV) through excessively long observation was studied. The mechanism cannot be fully elucidated but the process can be described as follows: Directly after the electron beam exposure we can identify low-contrast nanoplatelets decorated by darker spots. A further irradiation of the anisotropic structures leads to a rearrangement of the rectangular sheets into more spherical particles with higher contrast. The degradation first occurred on the edges and rapidly propagated inwards caused by the decomposition of the organic material. In contrast to this investigation, Udayabhaskararao et al.^[42] suggested that Pb^0 nanocrystals are the base for seed-mediated nucleation with subsequent oriented attachment for CsPbBr_3 perovskites.

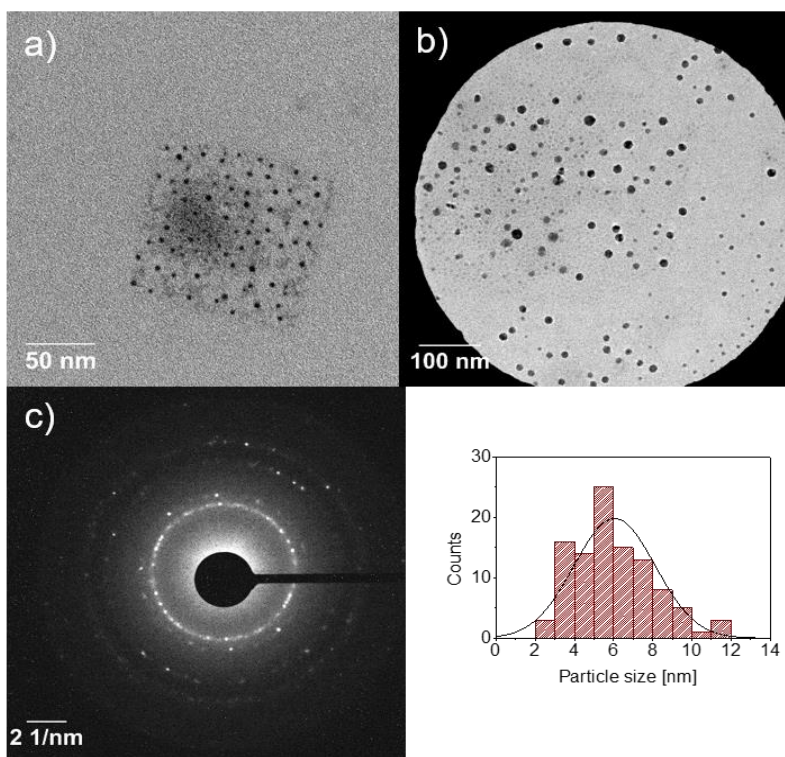


Figure 36: TEM results of perovskite nanocrystals: a) TEM image of the formation of nanocrystals and nanosheets (scale bar: 50 nm), b) selected area for the diffraction pattern (scale bar: 100 nm), d) SAED pattern (scale bar: 2 1/nm) of the marked area in (b) and the size distribution of the Pb⁰ seeds (6.1 ± 2.1 nm in diameter).

The determination of the real crystal structure is possible but the origin of these nanocrystals is still unclear. Nanocrystals with high surface-to-volume ratio (ultra-thin nanoplatelets) are prone to decompose whereas bulkier nanocrystals (at later growth stages) are more robust against the electron beam. The TEM images in figure 36 also depicted that nanoseeds are bound to the perovskite lattice.

Table 8: Summary of experimental and standard diffraction patterns of lead nanocrystals.

Bragg reflections	Ref. ^a		Exp.		rel. Intensity [norm.]
	2 θ [°]	d-spacing [Å]	2 θ [°] ^b	d-spacing [Å]	
111	31.2867	2.8574	31.7	2.818	100
200	36.2828	2.4746	36.6	2.450	52.87
220	52.2506	1.7498	53.3	1.718	24.47
311	62.1757	1.4922	62.8	1.478	19.87
222	65.2722	1.4287			
400	77.0311	1.2373			

^a JCPDS: 65-2873^[43]

^b d-spacing calculated according Bragg equation^[45]

Interesting observations were made during the TEM measurements of single perovskite layers at later growth stages of P04 (figure 37). They show higher contrast compared to the previous samples and only a percentage of thinner nanoplatelets show quasi-spherical nanocrystals.

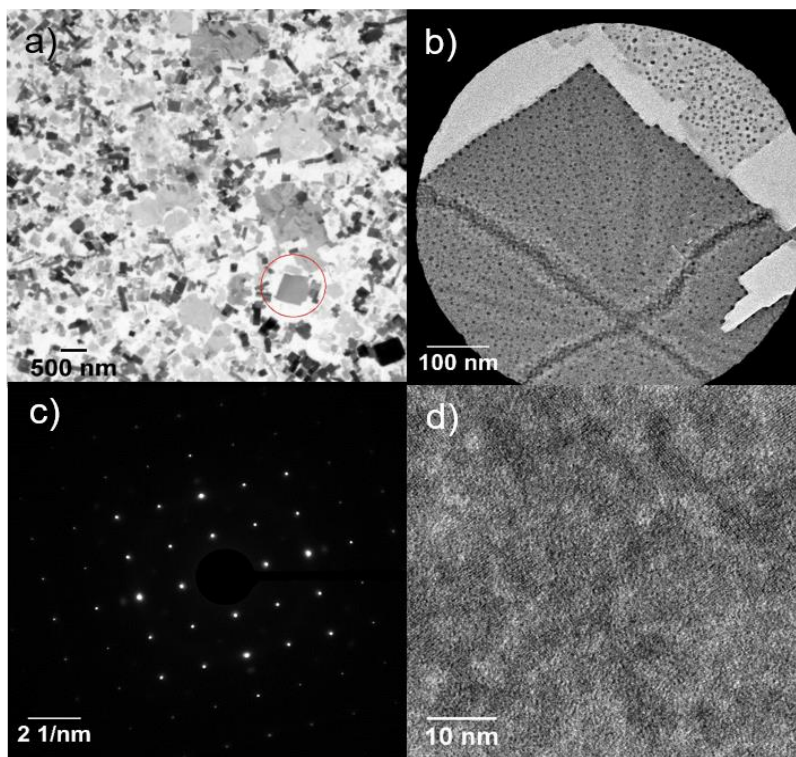


Figure 37: TEM results of perovskite nanoplatelets: (a), (b) TEM image of the selected area for the diffraction pattern (scale bar: 500 nm and 100 nm), (c) SAED pattern (scale bar: 2 1/nm) of the marked area in (a) and (b), (d) the magnified image shows the crystal lattice of the perovskite grains (scale bar: 10 nm).

The nanoplatelets show diffraction patterns consisting of discrete spots. The periodic arrangement of atoms leads to scattering of the X-rays in one specific direction with high intensity and small width of single spots after radial averaging (figure 37, d). The SAED pattern for nanoplatelets is consistent with a lattice spacing of 5.9 Å which conforms to the value for the bulk material.^[12] The spherical nanocrystals are still visible but become less pronounced, possibly due to diffusion and rearrangement steps within the perovskite lattice (figure 37, b). Only a small amount of side products could be detected.

Table 9: Data of experimental and standard diffraction pattern of perovskite nanoplatelets.

Bragg reflections	Ref. ^a		Exp.		
	2 θ [°]	d-spacing [Å]	2 θ [°] ^b	d-spacing [Å]	rel. Intensity [norm.]
001	14.9	1.684	14.9	1.6776	100
011	21.6	2.434	21.1	2.3747	33
002	30.2	3.380	29.9	3.3514	80.5
021	33.8	3.775	33.6	3.7503	28.4
211	37.0	4.120	35.8	3.9851	6.6
022	43.1	4.770	42.8	4.7382	12.1
003	45.6	5.033	45.5	5.0327	8.3
			48.2	5.3011	4.9
			55.4	6.0392	3.7

^a XRD pattern for CH₃NH₃PbBr₃ perovskite nanoplatelets according Sardar et al.^[25]

^b d-spacing calculated according Bragg equation^[45]

From the TEM measurement in diffraction mode, diffraction peaks (2 θ) at 14.9°, 21.1°, 29.9°, 33.6°, 35.8°, 42.8° and 45.5° correspond to (001), (011), (002), (021), (211), (022) and (003) planes identifying the cubic CH₃NH₃PbBr₃ perovskite.^[25] The relative intensity of the (001), (011), (002), (021) and (022) planes are very high in comparison to the rest of the standard pattern. This observation strongly suggests that the platelet growth occurs through continuous attachment of monomers predominantly along these planes and the intense (001) diffraction peak reflects a high degree of crystallinity which indicates an expanded monocrystalline surface (figure 37, d) covered with the layer of amine ligands. The growth process along the (011)- and (022)-planes is inhibited through chemisorbed ligands which keeps the platelets thin.^{[8][18][46]} Due to the anisotropic nanocrystal growth, the expanded crystallinity, and the presence of nanocrystal seeds before the extensive irradiation under TEM, we suggest that the 2D self-organization occurs by oriented attachment as the growth mechanism.^{[25][36]}

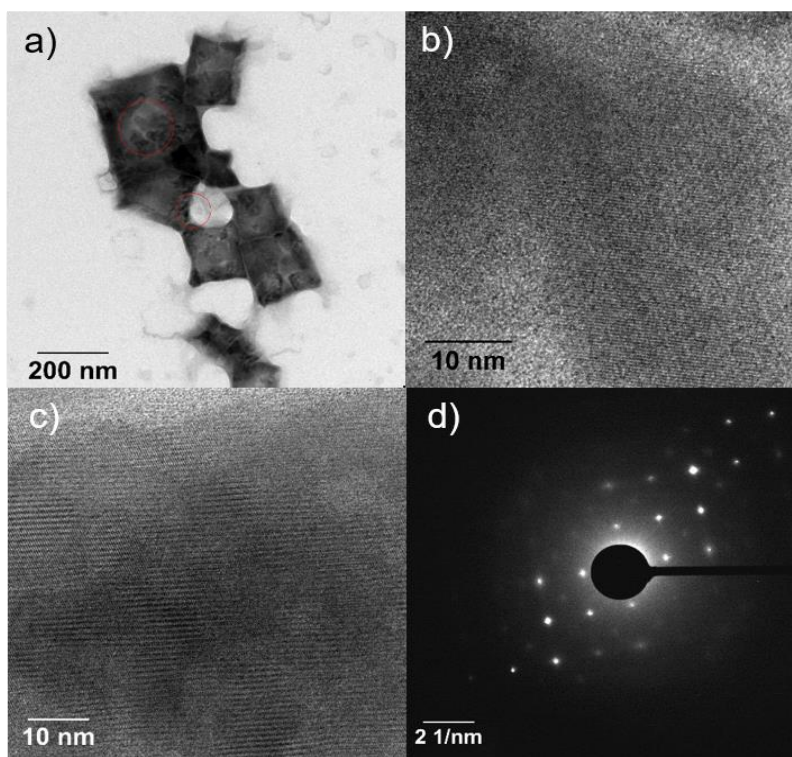


Figure 38: TEM results of perovskite nanocubes: (a), (b) TEM image of the selected area for the diffraction pattern (scale bar: 200 nm and 10 nm), (c) the magnified image shows the expansion of the monocrystalline surface (scale bar: 10 nm), d) SAED pattern of the marked area (scale bar: 2 1/nm) in (a)(c).

The nanocubes (figure 38, P01) show intense peaks at the (011) planes which match the cubic crystal structure of bulk perovskites. They show a continuous crystalline character (figure 38, b & c). The absence of further peaks makes it more difficult to explain details about the growth mechanism. The preferred growth directions along specific crystal planes are evidenced by one pronounced diffraction peak in the (011) direction and similar intensities for (002), (021) and (022) facets. The TEM picture (figure 38) shows higher stability under the electron beam and the enormous expansion of the monocrystalline perovskite crystals. The surface atoms are systematically aligned and satisfy the Bragg conditions.

Table 10: Data of experimental and standard diffraction patterns of perovskite cubic bulk-like nanocrystals.

Bragg reflections	Ref. ^a		Exp.		
	2 θ [°]	d-spacing [Å]	2 θ [°]	d-spacing [Å]	Rel. Intensity [norm.]
001	14.48	1.684			
011	20.72	2.434	20.9	2.3598	100
002	29.68	3.380	29.6	3.3141	55.72
021	33.31	3.775	33.6	3.7503	56.66
211	36.66	4.120			
022	42.65	4.770	42.5	4.7046	40.29
003	45.40	5.033			
			55.5	6.0504	18.22

^a XRD pattern for CH₃NH₃PbBr₃ perovskite nanocubes according Zhang et al.^[47]

^b d-spacing calculated according Bragg equation^[45]

Morphological Properties via Scanning Electron Microscopy (SEM)

The study of the 3D structure of CH₃NH₃PbBr₃ perovskites under the Scanning Electron Microscope (SEM) in combination with Cathodoluminescence (CL) detection is helpful to investigate the structural evolution and morphology. CL is the emission of light due to the stimulation of material by an electron beam. SEM-CL images were taken of perovskite material emission under high-energy electron microscopy. The images show a high spatial resolution in the nanometer regime and the optoelectrical properties correlate with the perovskite morphology and composition. Perovskites of different composition were investigated using various detectors, included Inlens, SE (Secondary Electron) and CL detectors.

The sample preparation involved drop-casting of freshly prepared perovskite samples on pre-cleaned silicon wafers. The nanocrystals were examined by SEM and we found perovskite samples of different morphology depending on their composition. Two representatives are depicted, showing interesting features coming from the different ligand to lead precursor ratio.

The first extreme composition had an excess of lead source PbBr_2 (P01: PbBr_2 :OAmBr:MAMBr 0.3:0.1:0.1). The produced perovskites presented a mixture of large-sized cubic crystals (figure 39, (a)-(f)) with lateral dimensions reaching from the nanometer to the micrometer scale.

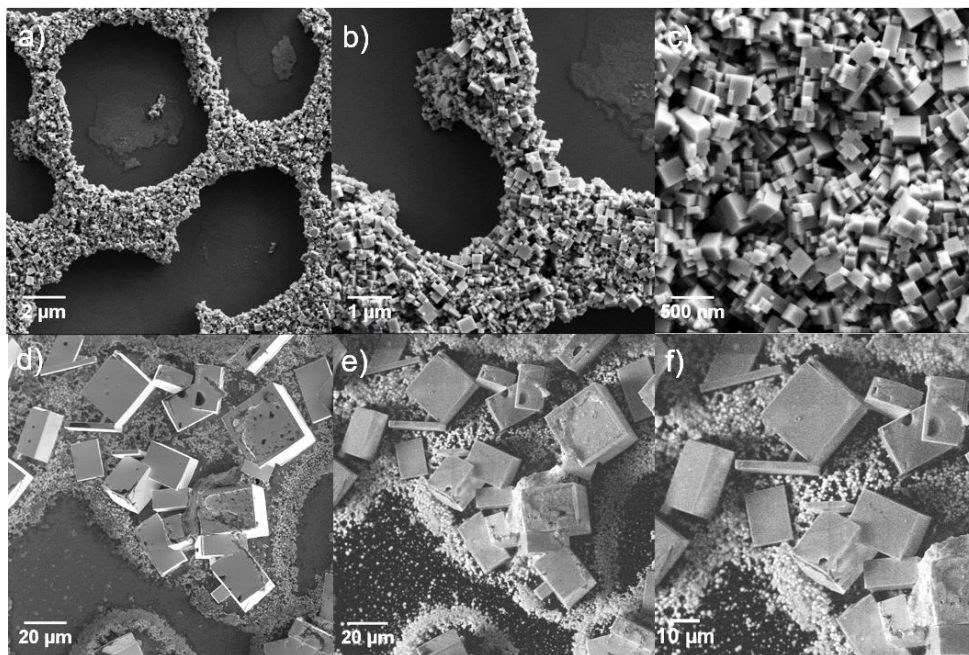


Figure 39: SEM surface images of $\text{CH}_3\text{NH}_3\text{PbBr}_3$ nanocrystals synthesized via large scale synthesis result in cube-like morphologies of various sizes in the nm to μm region (P01: PbBr_2 :OAmBr:MAMBr 0.3:0.1:0.1). The images were taken with different detector combinations ((a-d) SE2 detector and (e, f) CL together with Inlens detector).

The combination of SE detectors (figure 39, d) shows clearly the nearly defectless and smooth surface facets of the bulkier perovskite crystals. With the assistance of organic ligands, the shape of $\text{CH}_3\text{NH}_3\text{PbBr}_3$ could be evolved to sharp-edged cubes due to the $\text{Pm}\bar{3}\text{m}$ space group symmetry.^[12] Smaller spherical nanocrystals are present which show a high stability concerning the electron beam. The SEM image taken using the Inlens detector together with the CL detector (figure 39, e & f) combines the detection of photons and the high resolution of the electron microscopy and show an increased resolution.

A higher ligand concentration (P04: PbBr_2 :OAmBr:MAMBr 0.10:0.16:0.24) is responsible for a controlled anisotropic growth along the (001)-facet and consequently sheet-like structures^[25] could be detected (figure 40, (a)-(f)). The images of nanosheets and superstructures were generated by

the SE2 detector in combination with the Inlens detector. Besides the confined platelet structures in one direction, stacked assemblies of $\text{CH}_3\text{NH}_3\text{PbBr}_3$ nanocrystals also formed. The nanosheets show a tendency to form 2D sheets of square/rectangular shapes with lateral dimensions of a few nm to μm . The higher ratio of long surface-passivating amines OAmBr are responsible for the stacking of the sheets and therefore for tailoring the nanocrystal structure. The platelets show a highly flat and smooth surface which is a requirement for the exactly oriented stacked sheets. Sichert and co-workers^[18] found different results with sheet dimensions of a few nanometers.

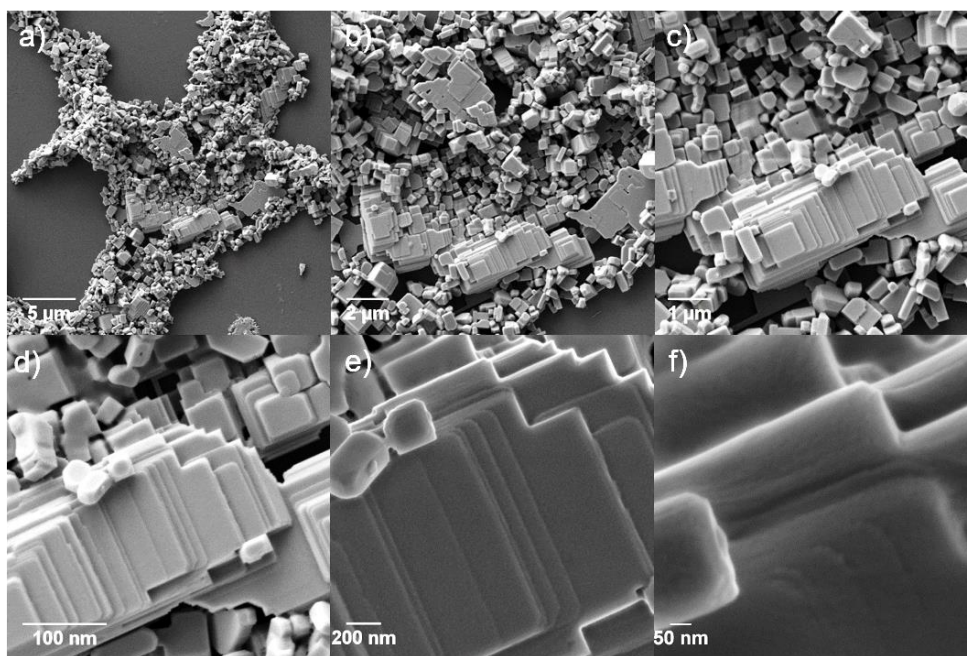


Figure 40: SEM images of $\text{CH}_3\text{NH}_3\text{PbBr}_3$ nanocrystals synthesized at room temperature according to the large scale synthesis (P04: PbBr_2 :OAmBr:MAmBr 0.10:0.16:0.24). Ultrathin nanoplatelets stacked together to form superstructures were detected with ((a-d) SE2 detectors, (e, f) Inlens detectors).

Besides the topographical evidence of nanoplatelets aligned perpendicular to the substrate and stacked on top of each other, the presence of ultra-small spherical nanocrystals with a narrow size distribution of $6.5 \text{ nm} \pm 1.0 \text{ nm}$ was also observed (figure 41, (e) & (f)). Ultrathin 2-dimensional nanomaterials are attracting increasing attention due to their outstanding and extraordinary electronic, optical and mechanical properties.^[32]

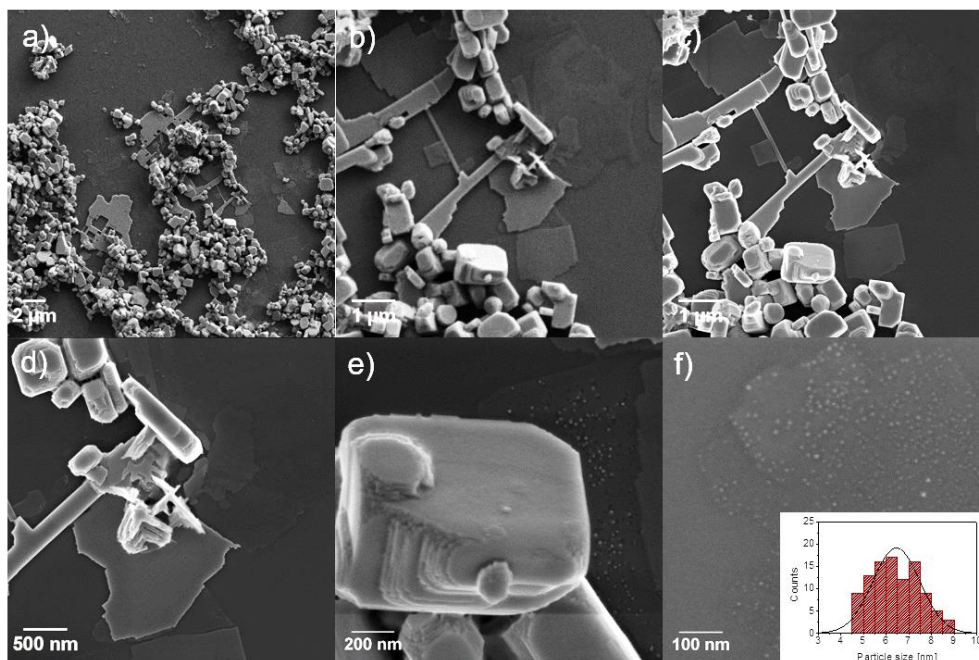


Figure 41: SEM images of colloidal $\text{CH}_3\text{NH}_3\text{PbBr}_3$ nanocrystals synthesized via large scale synthesis to adapt the reaction conditions on the capillary diffusion approach. The images ((a), (b), (e) SE2 detector and (c), (d), (f) Inlens detector) show ultrathin plate-like nanosheets and narrow distributed spherical nanocrystals ($6.5 \text{ nm} \pm 1.0 \text{ nm}$ in diameter).

Based on these observations, with increasing the long-chain amine ligand concentration, small spherical nanocrystals with sizes around $6.5 \text{ nm} \pm 1.0 \text{ nm}$ and ultrathin nanosheets could be detected by slow addition into the anti-solvent toluene.

With ex-situ experiments like TEM and SEM the different morphologies could be visualized. Both compositions employed the presence of smaller nanospheres which strengthen our hypothesis that perovskites are build up by spherical subunits. In-situ experiments should provide more results regarding the crystal growth mechanism and the structural evolution.

5.4.3 Microfluidic Experiments

A sequence of preparation steps was required to realise our microfluidic strategy. These include manufacturing the microfluidic chip, choosing a suitable channel design, and predicting the microfluidic flow by computational fluid dynamics simulation.^[48] These steps were followed by the introduction of our large lab-scale synthesis into the analytical device with consideration of compatibility between reaction components and chip material as well as the effects of down-scaling.

Experimental Setup for Microfluidic Systems

Confocal Laser Scanning Microscopy (CLSM) took place in combination with the microfluidic setup for flow-control and in-situ photoluminescence detection (PL). The growth process with one specific precursor ratio P04 was accessible. The setup was based on a special microfluidic chip design which was developed in-house.^[49] The EH09 chip in figure 42 combines multiple functional elements for soft-template perovskite formation in continuous flow. The chip material consists of poly(dimethylsiloxane) and the inner chip was coated with poly(p-xylylene) (PPXn) to guarantee a better solvent resistance. The microchannel was designed with five inlets, a 3D flow focussing channel, two mixing crosses and is connected to a high precision syringe pump to guarantee a parallel flow of the reactants. For the extension of the main channel a glass capillary is inserted, which leads to a hybrid chip (Outlet).

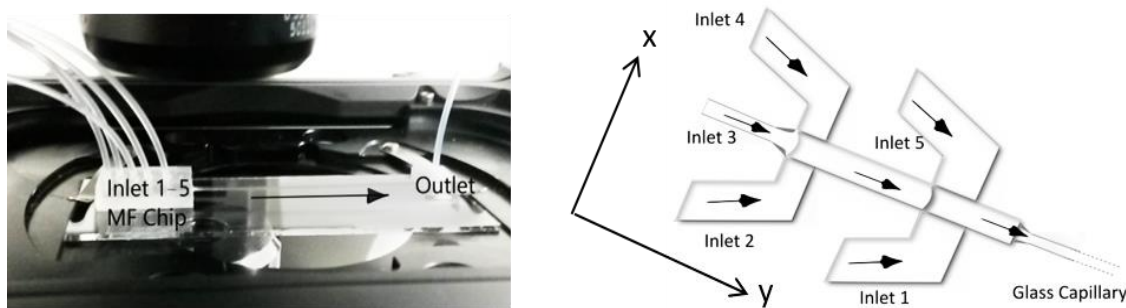


Figure 42: Photograph of the microfluidic chip mounted on the translational stage of the CLSM (right). Schematic PDMS-PPXn-based 3D double focusing hybrid chip connected to a 2-mm quartz capillary for photoluminescence detection during nanocrystal formation. Inlet 3 acts as the main channel and the inlets 1, 2, 4, 5 as side channels for buffer and precursor solutions (left).

Through diffusion controlled mixing, the anti-solvent/solvent mix exceeds the critical solvent ratio along microfluidic channel. The flow as well as the temporal evolution was proven with CLSM. Next, microfluidic chip was placed on the translational stage of the microscope (figure 42, left) and the highly-concentrated precursor solution and solvent mixtures (Chapter 3, table 2) were filled in five separate syringes. A precision syringe pump delivered the solution into five inlets of the microfluidic channel. The adjustment of the relative flow rates of precursor solutions and solvent mixtures allows the control of the stoichiometry of the solvent composition along the microfluidic channel and the solvent-induced precipitation of perovskite nanocrystals.

Size-related optical properties give information about the dimensionality of the nanocrystals.^{[18][50][51]} A schematic overview is given in figure 43 for the perovskite formation in a microfluidic channel.

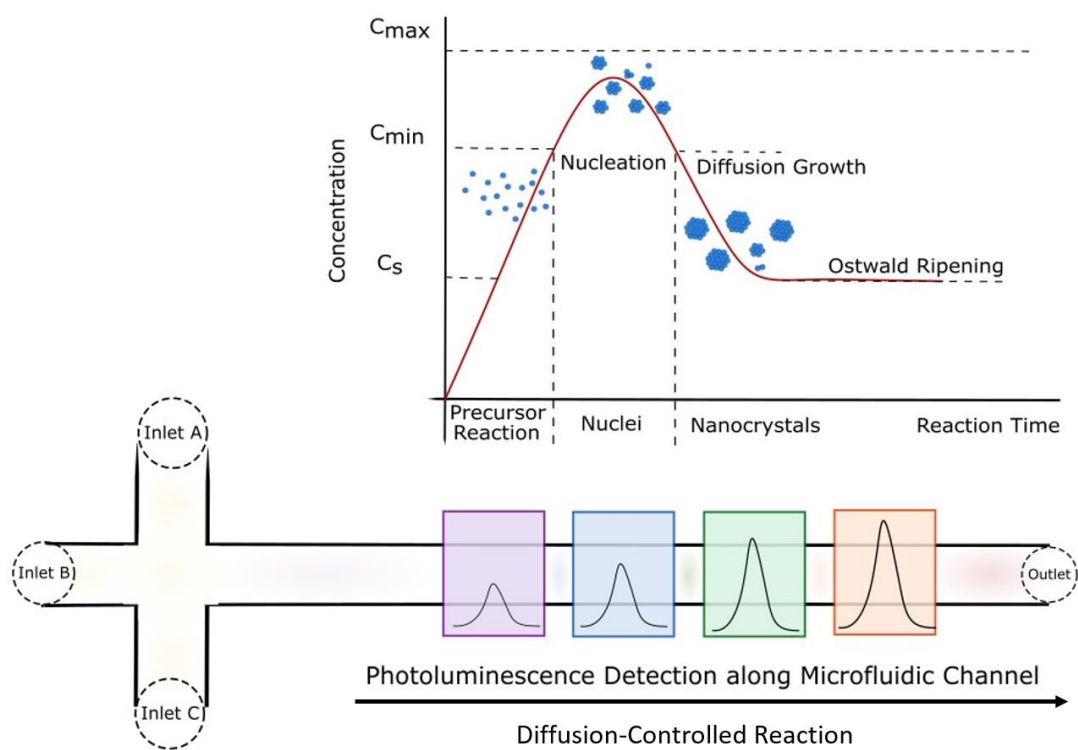


Figure 43: Simplified overview of the microfluidic device after the second mixing cross. Fluorescence detection with Confocal Laser Scanning Microscopy (CLSM) along the channel gives information about the solvent-induced precipitation of perovskites.

Observing Perovskite Formation via the Confocal Microscopy Technique

The syringes were filled according table 2 in Chapter 3 and connected to the inlets of the microfluidic device (figure 44). The middle stream (A, Inlet 3) consists of the precursor salts dissolved in a solvent mixture of Toluene:DMF 1:1 and the velocity was adjusted to 125 $\mu\text{L/h}$. Two solvent streams (B, Inlet 2 and 4) with an increased toluene ratio 2:1 and flow rates of 250 $\mu\text{L/h}$ surround the middle stream after the first mixing cross x1. The solvent stream acts as buffer layer and reduces the solubility due to increased anti-solvent content (~ 1.6 fold excess).

After the second mixing cross x2, two sheathing streams C with toluene (flow rates 3000 $\mu\text{L/h}$, Inlet 1 and 5) were introduced to induce the perovskite formation along the channel.

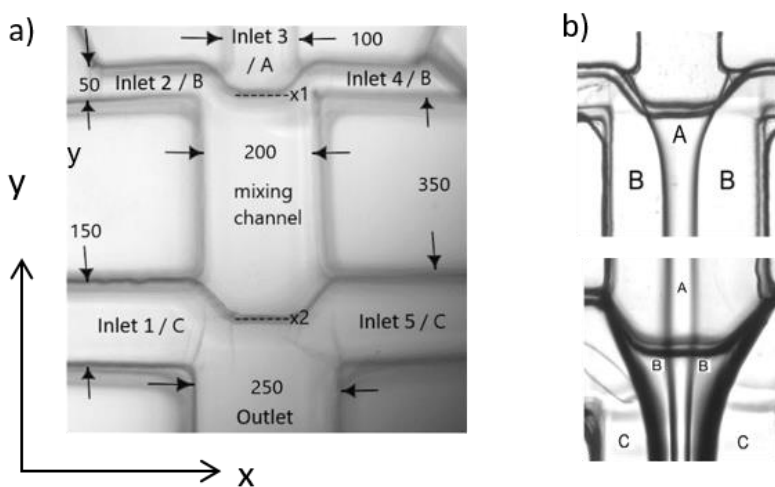


Figure 44: Brightfield images of the microfluidic channel. Image (a) was taken without solutions showing the first x1 and second channel cross x2 and the dimensions in μm . Image (b) shows the zoom-in of x1 and x2 with 3D focused streams A and B and the sheathing stream C.

Figure 44 (b) shows the three dimensional focussed stream in the downstream region. The middle flow A is constrained to a small region after the 3D focusing with B and C to avoid wall contact with the reagents. The diffusion-controlled mixing depends on the flow velocity of stream A and C as well as the middle protective layer B. The concentric sheathing flow should lead to the precipitation of perovskite with the addition of the toluene stream C. The flow simulation for similar previous designs was investigated by numerical calculations^{[52][53]} and experimental images. They show clearly the parallel flow of the reactants A and B to guarantee flow stability and a

suitable mixing time. The dimensions of inlet 3 are 100 μm in diameter and become wider along the y-direction (230 μm and 250 μm in height and width). The side channels have dimensions of 50 μm and 150 μm . The distance between the channel crosses x1 and x2 is 350 μm .

Upon reaching equilibrium, the translating specimen stage position of the microscope was changed to allow for scanning along the channel to the region of interest (figure 45). The collimated laser beam ($\lambda_{\text{exc}}=405\text{ nm}$) was focused into the microfluidic channel and the emission originating from the perovskites was collected. The investigation of the particle structural evolution is possible from the resulting scanned images.

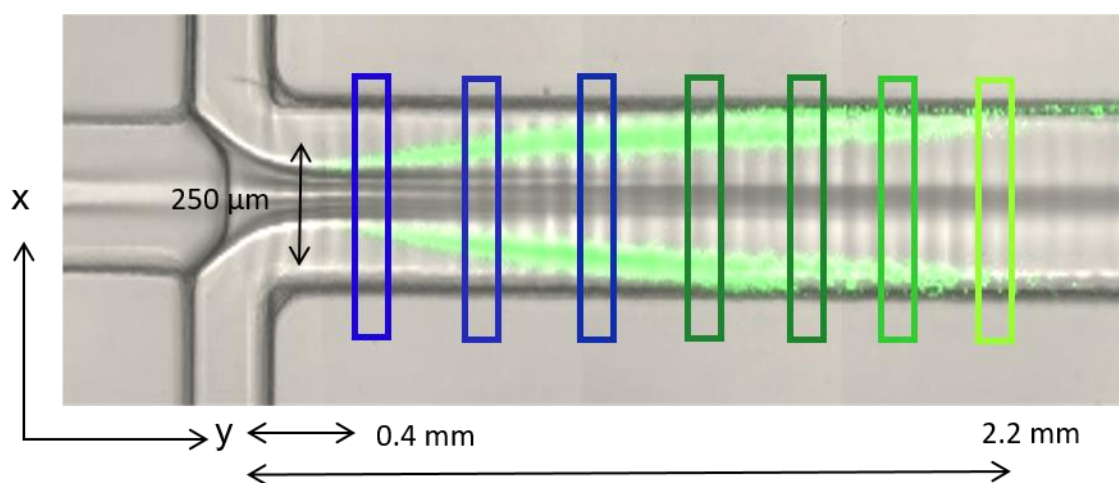


Figure 45: CLSM image of the EH09 chip during the perovskite formation along the microfluidic channel. Emission scans ($\lambda_{\text{exc}}=405\text{ nm}$) were taken along the channel ($\Delta d_{x2}=0.4\text{--}2.2\text{ mm}$).

From the emission scans along the channel the different growth stages of the perovskite nanocrystals were detected (indicated by the coloured boxes in figure 45). The channel distances (table 12) from the second mixing cross x2 and the corresponding confocal images clearly demonstrate the ongoing diffusion process within the channel length (y-direction) in toluene rich regions. The perovskite emission from the CLSM detection is highlighted in figure 45. The in-line emission spectra were measured with a distance of $\Delta d_{x2}=0.4\text{--}2.2\text{ mm}$ between them starting from the beginning of the channel cross (figure 46). The channel distance from the mixing cross is proportional to the reaction time and therefore the reaction in microfluidic channel is related in time and space. After the first contact of excess toluene and the precursor, each channel position in y-direction and the corresponding diffusion time can be calculated.

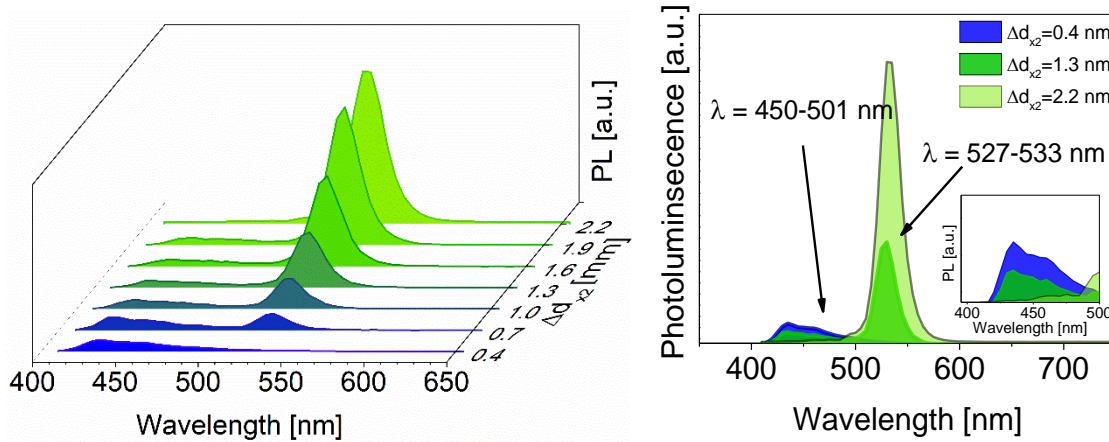


Figure 46: Multiplex emission spectra along the microfluidic channel ($\lambda_{\text{exc}}=405$ nm). A series of PL peaks could be detected which implies various numbers of corner-sharing PbBr_6 octahedra (attached unit cells) between 450 nm and 501 nm. The dominant emission peak shows a red-shift from 527 nm to 533 nm.

For the approximation, the x-position at the beginning of the channel cross is the starting point of mixing between the precursor in DMF and the excess of toluene.^[24] The time after mixing Δt can be calculated from the channel position x , the channel width w and height h and the average volumetric flow rate \bar{Q} according to equation 5.1.

$$\Delta t = \frac{w \cdot h \cdot x}{\bar{Q}} \quad (5.1)$$

With distances larger than the channel geometry (w, h), we assume that the parabolic flow profile has already developed at position x . Therefore, we can take the average velocity \bar{Q} downstream of the 3D focusing channel^[52]

$$\bar{Q} = \frac{Q_1 + Q_2 + Q_3 + Q_4 + Q_5}{(h \cdot w)} \quad (5.2)$$

including all flow streams $Q_1 - Q_5$ (resp. Inlet 1-5) of the microfluidic system to calculate the time after mixing Δt . The interdiffusion time t_D across the central stream can be estimated according to equation 5.3 and 5.4 and gives us more information about the mixing point in our microfluidic setup.^[24]

$$w_f = \frac{Q_3}{Q_1 + Q_2 + Q_3 + Q_4 + Q_5} \cdot w_c \quad (5.3)$$

$$t_D = \frac{w_f^2}{8D} \quad (5.4)$$

The width of the focused central stream w_f , the channel width w_c , and the volumetric flow rate of all flow streams needs to be taken into account. The calculated time t_D for a solvent to diffuse from both sides into the central stream includes a typical solvent diffusion coefficient of $D=10^{-9} \frac{m^2}{s}$ and could be calculated to be 2.8 ms. This is in good agreement with our first calculated values of $\Delta d_{x2}=0.4$ mm and $\Delta t=2.3$ ms. It clearly shows that the diffusion controlled mixing of toluene and the precursor occurred directly after the mixing cross. The calculated values are summarized in table 12.

At early reaction times ($\Delta d_{x2}=0.4$ mm, $\Delta t=2.3$ ms), the absence of a dominant perovskite peak around ~ 525 nm is conspicuously absent.^[7] Instead, a broad signal between $\lambda=450$ nm and 501 nm could be detected which is attributed to the PDMS absorbance signal.^[54] The observation of a sharp emission peak at $\lambda=527$ nm later ($\Delta d_{x2}=0.7$ mm, $\Delta t=4.2$ ms) shows the beginning of the bulk-like perovskite formation and this signal becomes more dominant when scanning further along the channel in y-direction (figure 46, left). Interestingly, the intensity of the emission peak series at lower wavelength regions $\lambda=450$ nm to 501 nm, decreases continuously (figure 46, inset right). This observation is indicative of the presence a multiplex emission series which originates from confined perovskite nanocrystals in lower concentrations. Our large-scale approach and the literature^{[16][17][18][51]} confirm our hypothesis that quantized emission peaks of unpurified samples can be attributed to nanoplatelets of different thicknesses. The layered structures are ligand-separated unit cells n ($n=1-n=\infty$, table 10). Similar observations were made for $CH_3NH_3PbBr_3$ and $CsPbBr_3$ nanocrystals by identifying photoluminescence signals.

The emission peaks red-shift over the reaction time and along the channel and the peak series in the higher energy region grows in intensity due to the larger nanostructures. Within the real-time emission scan ($\Delta d_{x2}=0.7$ mm, $\Delta t=4.2$ ms), the dominant bulk peak in the PL spectrum shows a red-shift from 527 nm to 533 nm and an increase in intensity. The corresponding FWHM of the 533 nm emission peak was determined to be 24.4 nm after $\Delta d_{x2}=2.2$ mm, $\Delta t=13.2$ ms.

Inspection of figure 45 reveals clearly stronger perovskite signals with ongoing reaction time and this could also be monitored by emission detection (figure 46). The evolution of the emission spectra is more complicated due to overlapping of the emission arising from the population of ultra-small perovskite nanocrystals and the chip material. However, the rapid evolution of the bulk

emission peak can be explained through the rapid consumption of smaller nanocrystals. A strong correlation between perovskite emission and nanocrystal dimensionality is evident. In conclusion, the synthetic route was successfully adapted to a microfluidic channel to detect a series of emission peak from 450 to 501 nm which can be identified and attributed to 2D nanoplatelets (table 11).

Table 11: Comparison of the PL peaks during the formation process of large-scale synthesis and reported PL signals.

n ^a	PL (Exp1) ^b [nm]	PL (Ref1) ^[17] [nm]	PL (Ref2) ^[47] [nm]
1	-	405	403
2	-	442	435
3	456	456	-
4	475	482	474
5	488	492	489
∞	518	534	508

^a n=numbers of layers of nanoplatelets (attached unit cells)

^b Large Scale Approach

According to Sichert et al.^[18] the band-gap size relationship of the semiconducting perovskite nanostructures cannot be calculated by the effective mass approximation. However, the spectrum can still be correlated to the particle size based on the TEM images. In the thesis, we used the correlation from literature^{[17][19][47]} and found a good agreement with previously reported photoluminescence signals. The emission features can be assigned to nanoplatelets with different unit cell layers.

The perovskite formation is very fast and diffusion-limited. On time scales of a few milliseconds we can observe the structural evolution (table 11) by detecting the emission peak series and characteristic perovskite signal around ~527 nm.

Table 12: Calculated parameters for the emission detection after the time Δt with respect to the channel position Δd_{x2} and the beginning of the interdiffusion process.

Channel Position	Δd_{x2} [μm]	Δt [ms]
1	0.4	2.3
2	0.7	4.2
3	1.0	6.0
4	1.3	7.8
5	1.6	9.6
6	1.8	10.8
7	2.2	13.2

5.4.4 Capillary Interdiffusion Experiment

A similar principle was used in a vertical capillary approach where a density gradient enables the interdiffusion of perovskite precursor into the anti-solvent toluene. The capillary interdiffusion experiment includes in-situ UV-Vis and Small-Angle X-ray Scattering (SAXS) detection. UV-Vis is helpful to investigate the strongly quantum-confined exciton peak and the scattering method SAXS experiments are very useful to follow the formation of colloidal nanomaterials. In-situ monitoring of the crystal formation provides information on the nanometer scale. SAXS experiments give better insight into the superatomic scale and the subsequent self-organization into larger colloidal structures.

With this approach, convective motion can be excluded and the diffusion controlled process can be followed over longer time scales. A capillary interdiffusion setup is used to slow down the reaction and to detect the formation process in a glass capillary which acts as an analysis cell.

To adapt and monitor the synthesis, the perovskite diffusion should be sufficiently slow, which can be realized with a buffer layer. After a certain time Δt the total ion concentration (perovskite precursor) in the anti-solvent is high enough and the perovskite formation will be induced. The ratio of $\text{PbBr}_2:\text{OAmBr}:\text{MAmBr}$ for this adaption is 0.10:0.16:0.24 (P04).

In a typical experiment, the different reaction components were filled in a vertically positioned quartz capillary ($\varnothing = 1$ mm) with the help of a syringe pump to guarantee separated layers (figure 47). The two precursors lead(II)bromide and MAmBr, together with OAmBr as stabilizing agent, were dissolved in N,N-dimethylformamide (DMF) and placed at the top. The bottom layer consists of the anti-solvent toluene which induces the precipitation of the perovskites. The buffer layer (middle layer) consists of a DMF:Toluene solvent mixture in 1:1 ratio. The solvent mixture leads to reduced interfacial tension between the bottom and top layer which is exhibited by the curvature of the meniscus. Furthermore, the extended diffusion pathway through the buffer layer leads to a slower diffusion limited reaction of perovskites and the density gradient of the organic solvents enables an entropically driven process (DMF $\rho_{298.15\text{ K}}=0.9445\text{ g/cm}^3$, DMF : Toluene (1:1) $\rho_{298.15\text{ K}}=0.9063\text{ g/cm}^3$, Toluene $\rho_{298.15\text{ K}}=0.8622\text{ g/cm}^3$).^[55] The addition of the precursor salts effects the density by increasing the density of the solvent DMF.^[56] After the precursor injection the perovskite formation could be monitored with scattering and spectroscopic methods.

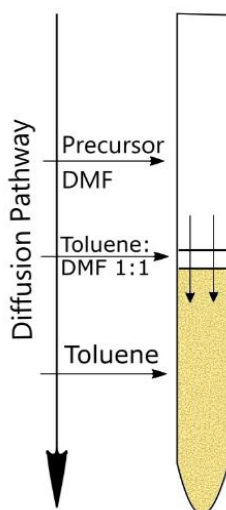


Figure 47: Schematic representation of the diffusion process in a quartz capillary. The reaction components consist of the precursor salt (PbBr_2 , MAmBr) and the organic ligand (OAmBr) dissolved in DMF, buffer layer (DMF: Toluene 1:1), toluene.

In-situ UV-Vis-Monitoring of $\text{CH}_3\text{NH}_3\text{PbBr}_3$ Growth Process

The quantum size effect and the size-dependent properties of perovskite nanocrystals are well-known.^[19] The structural evolution during slow interdiffusion in the capillary however can provide more insight into different possible kinetic pathways and intermediate states of perovskite formation. The in-situ growth experiment is evidenced by monitoring excitonic absorbance peaks and their red-shift as a consequence of their dimensionality. The ionic nature of the reaction shows a fast nucleation and growth within a reaction time of 16 min at room temperature.

A precision syringe pump delivers the bottom layer, 83.5 μL toluene, in a quartz capillary followed by 10 μL buffer layer (DMF/Toluene 1:1). The existing double layer was coated with 16.5 μL precursor solution. Directly after the injection of the perovskite precursor the formation of semiconducting nanocrystals is evidenced by a color change from colorless to green/yellow (figure 48).

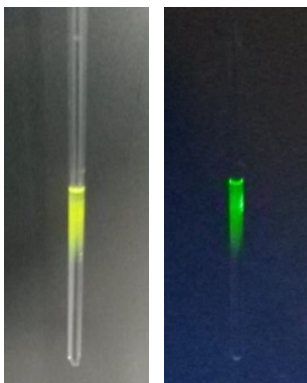


Figure 48: The perovskite nucleation and growth visualized by the instantaneous color change which can be monitored with in-situ UV-vis experiments (left: under normal light, right: under the UV-lamp $\lambda=365$ nm).

The detection of the perovskite growth starts with the injection of the precursor solution. The first significant absorption peak arises at 437 nm corresponding to bilayer $\text{CH}_3\text{NH}_3\text{PbBr}_3$ after $t=7$ sec (figure 49, (a)). Two additional broad signals 315 nm and around 389 nm occur which indicate a lower fraction of $0\text{D}^{[16]}$ and monolayer nanoplatelets.^{[17][47]} The intensity of the signal increases in direct proportion to the number of nanocrystals. The absorbance features at 389 nm and 437 nm confirm the confinement in one dimension compared to the bulk absorbance edge of 525 nm.^{[17][47]}

The red-shift of a single excitonic absorbance feature at 437 nm towards 451 nm (figure 49, (b)) within the next $t=19$ seconds implies nanocrystal growth and these peaks are assigned to the thickness of 2 and 3 perovskite unit cells n ($n=2$ layer to $n=3$ layer).^[17] Less pronounced shoulders around ~ 473 nm, 488 nm and 501 nm demonstrate the presence of thin sheets ($n=4$, $n=5$ layer) and the beginning of the transformation to 3D nanocrystals. With proceeding reaction time, the intensity of the 451 nm peak decreases due to formation of larger products of higher dimensionality and sedimentation of the large bulk-like particles (figure 50, (c) & (d)). The transition of 0D-nanocrystals into nanosheets where only the absorption edge can be observed 501 nm ($n=\infty$) is around $t=60$ sec. Within 16 min the edge shifts from 501 nm to 522 nm originating from bulk-like structures.

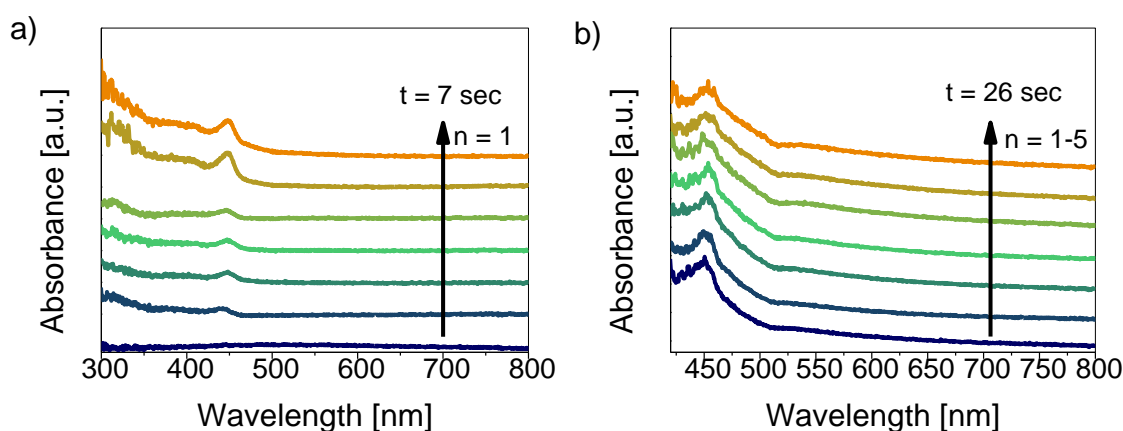


Figure 49: UV-vis spectra: nucleation and growth of spheroidal $\text{CH}_3\text{NH}_3\text{PbBr}_3$ nanocrystals through interdiffusion in the capillary process. Increase of the intensity (a) and a red-shift from 437 nm to 451 nm (b) within $t = 26$ sec implies the attachment of unit cells.

This temporal evolution describes the complete transition from 0D-nanocrystals, likely thin 1D-nanoplatelets, into 3D-bulk material within 16 min. The absorbance signals of all these fractions can be assigned to different numbers of attached perovskite unit cells.^{[17][47]} Our product consists of colloidal perovskites nanoplatelets with prominent excitonic absorbance peaks at 315 nm, 389 nm, 437 nm, 451 nm, 473 nm, 488 nm, 501 nm to 525 nm relating to 0D nanocrystals and 2D nanoplatelets of $n = 1 \rightarrow 2 \rightarrow 3 \rightarrow 4 \rightarrow 5$ and ∞ layers of nanoplatelets.

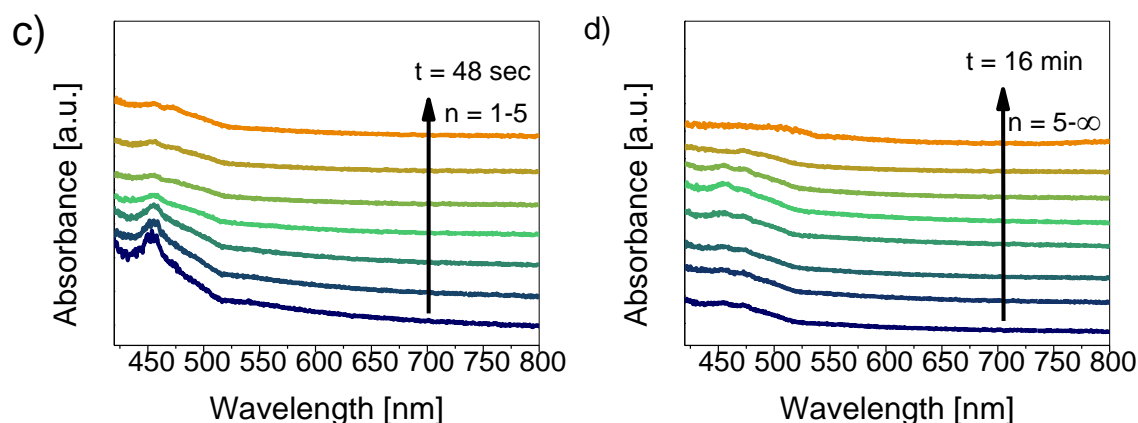


Figure 50: UV-vis spectra: transformation of spheroidal $\text{CH}_3\text{NH}_3\text{PbBr}_3$ nanocrystals into nanosheets occurs with arising of the absorbance edge around 501 nm (c) due to attachment of corner-sharing PbBr_6 octahedra after 60 sec and the absorbance edge at 522 nm (d) after 16 min.

Kinetic studies of the absorption intensity of the unpurified product are illustrated in figure 51. The strong nanocrystal growth at the beginning ($t=0$ and 22 sec, Stage I) decreases at the expense of larger lattice extension (Stage II). Both stages are not clearly separated, but this study is proof-of-concept that the presence of alkyl ammonium chains restricts the formation of bulk-like materials directly after the interdiffusion process and has significant impact on the nanocrystal shape during the growth process.

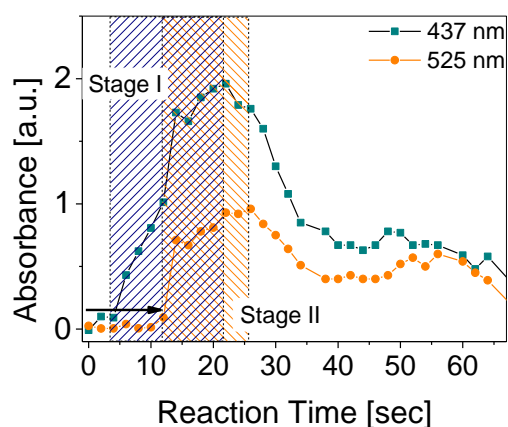


Figure 51: Kinetic studies of the perovskite nucleation and growth monitored with in-situ UV-vis experiments.

The formation of the spheroidal nanocrystals and their self-assembly into ultrathin sheets and superstructures (figure 52) was investigated. The process is driven by the minimization of high energy surfaces.^[36] Highly reactive facets on that cubic subunits merge into flat sheets. This indicates that the perovskite formation in the sample P04, as well as the solvent/non-solvent ratio of (DMF:Toluene 1:5), is very robust towards the adapt the preparation with various methods.

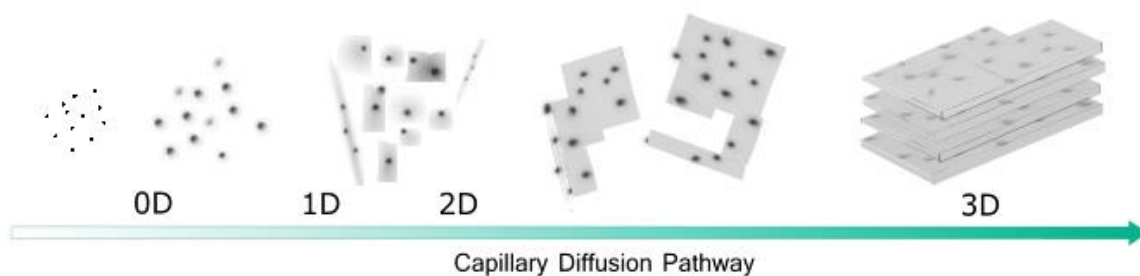


Figure 52: The time evolution of the ligand-assisted synthesis over the entire growth period. The stacks are formed from the 0-dimensional spheroidal nanocrystals via self-assembly processes over 2-dimensional precursor nanosheets into highly ordered stacks.

Table 13: Comparison of the absorption peaks during the formation process in capillary, large-scale synthesis and reported absorption signals.

n^a	Abs (Exp1) ^b [nm]	Abs (Exp) ^c [nm]	Abs (Ref1) ^[16] [nm]	Abs (Ref2) ^[47] [nm]
1	385	389	396	395
2	411	437	434	431
3	455	451	450	448
4	473	473	472	470
5	-	488	490	485
∞	505	533	532	-

^a n =numbers of layers of nanoplatelets (attached unit cells)

^b Large Scale Approach

^c Capillary Interdiffusion Experiment

CH₃NH₃PbBr₃ Nanocrystal Growth Followed by In-situ SAXS Experiments

This is the first example of using in-situ Small-Angle X-ray Scattering (SAXS) experiments to follow the growth of nanocrystals and their transition to anisotropic colloidal nanostructures in real time at room temperature. It provides valuable insights into the ligand-assisted nucleation, growth, and subsequent self-assembly into 2-dimensional nanosheets which possess extraordinary properties. In-situ UV-Vis results successfully described the gradual red-shift of the excitonic peak, therefore the same experimental conditions were used for in-situ SAXS detection.

Perovskite formation in the capillary interdiffusion experiment was monitored over 20 min. In a typical SAXS experiment, the quartz capillary was placed in the sample holder and toluene and the buffer layer were loaded into the analysis cell. The detector was placed below the buffer layer and scanning started with the addition of the precursor/DMF solution (figure 53). The measurements were taken in 0.5 sec intervals. The sample-to-detector distances were chosen to be 1.66 m and 2.54 m to detect the expected scattering vector range from $0.1 \text{ nm}^{-1} \leq q \leq 3.5 \text{ nm}^{-1}$ for the nanoparticle formation, the stacking behavior and the lateral dimensions of nanosheets.

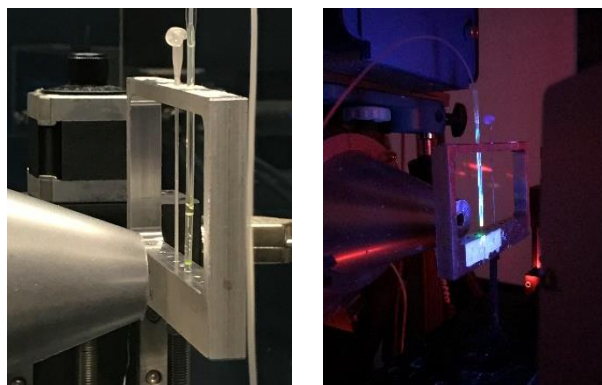


Figure 53: Photograph of the setup used to monitor the perovskite nucleation and growth process with in-situ SAXS experiments (left: under normal light, right: under the UV-lamp $\lambda=365 \text{ nm}$).

The precursor diffusion into the ‘poor’-solvent phase leads to the formation of spherical nanocrystals directly after the nucleation around $t=9 \text{ sec}$. For further analysis, the background of pure toluene was subtracted and the scattering pattern was radially averaged. Figure 54 displays the sequence of 1D scattering curves measured over the q range from $0.1 \text{ nm}^{-1} \leq q \leq 1.8 \text{ nm}^{-1}$ at one fixed position over the 20 min that the structural development becomes more apparent.

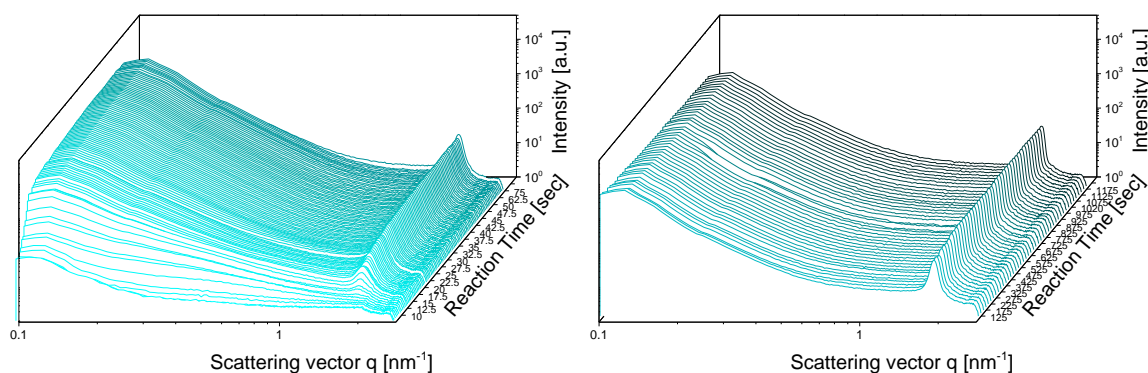


Figure 54: SAXS measurement with 2.54 m sample-to-detector distance for sample P04. The scattering profile (left) shows the development of the structured peak at higher q-values within 100 sec and (right) the temporal structural evolution for the following minutes.

The scattering curves (figure 54, left) show that directly after injection $t=9$ sec a flat scattering signal is observed which shows in the first $\Delta t=20$ sec a drastic increase in intensity at lower q-values ($0.12 \text{ nm}^{-1}-1 \text{ nm}^{-1}$), reaching a maximum at 0.12 nm^{-1} after 50 sec. The drop in the intensity between $0.1 \text{ nm}^{-1} \leq q \leq 0.12 \text{ nm}^{-1}$ is ascribed to interactions between the spherical nanocrystals. The intensity increases in the first 50 sec due to a high concentration of perovskite nanocrystals. The interaction of the particles leads to aggregation and the intensity at 0.12 nm^{-1} decreases again (figure 55).

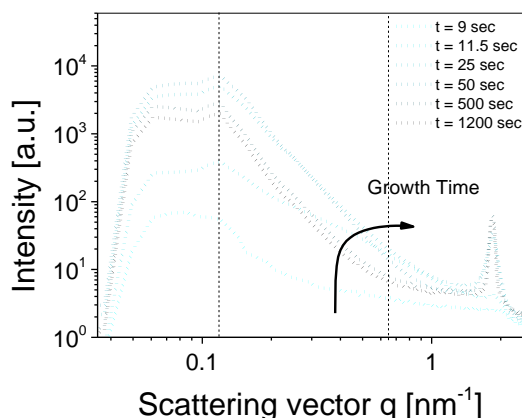


Figure 55: Six representative SAXS patterns showing significant features for understanding the structural evolution after 9 sec, 11.5 sec, 25 sec, 50 sec, 500 sec and 1200 sec.

For a more detailed analysis, scattering patterns at six different times, $t=9, 11.5, 25, 50, 500$ and 1200 sec, were selected which show significant features in their scattering pattern (figure 56). The patterns can be fitted to simple models and show a close agreement between the experimental SAXS data (data points) and the corresponding fits (solid lines).

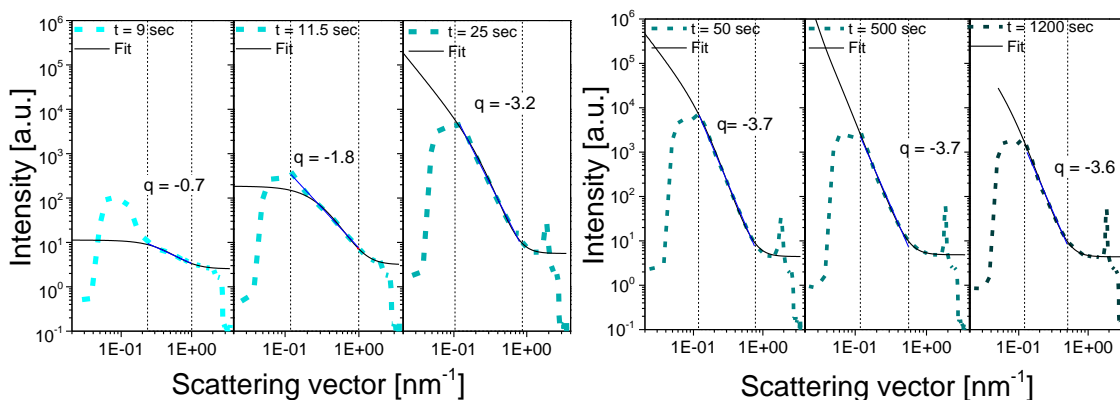


Figure 56: Six representative SAXS patterns showing close agreement between experimental SAXS data (data points) and the corresponding fits (solid lines) for (left) $t=9$ sec, 11.5 sec, 25 sec and (right) $t=50$ sec, 500 sec and 1200 sec.

By fitting lines to the natural log of the intensity, the slope of the scattering changes with ongoing reaction time could be extracted (figure 56). The transition from $q^{-0.7}$ ($0.2-1 \text{ nm}^{-1}$, 9 sec), $q^{-1.8}$ ($0.1-1.0 \text{ nm}^{-1}$, 11.5 sec), $q^{-3.2}$ ($0.1-1.0 \text{ nm}^{-1}$, 25 sec), $q^{-3.7}$ ($0.1-0.8 \text{ nm}^{-1}$, 50 sec), $q^{-3.7}$ ($0.1-0.6 \text{ nm}^{-1}$, 500 sec) to $q^{-3.6}$ ($0.1-0.5 \text{ nm}^{-1}$, 1200 sec) is observed and can be directly related to the shape of the objects.

Simple modelling of the q -region shows the change of the exponents of the slopes from the value 0 for spheres to -2 for thin nanosheets and $-3/4$. A slope steeper than $-3/4$ demonstrates that the particles have become too big to be redissolved. The first scattering curve after $t=9$ sec could be fitted to the form factor of polydisperse spheres with a mean radius R of 4.2 nm . In the next $t=3$ sec the transition from spheres towards ultra-thin nanosheets could be detected. The thickness $d=3.04 \text{ nm}$ and the lateral dimensions of 18.9 nm could be fitted at $t=25$ sec. By modelling the q -dependency, the onset of the slope shifts from 1 nm^{-1} towards lower q -values. At $t=11.5$ sec the minima are around 1.61 nm^{-1} (3.90 nm) and move toward smaller q -values 1.37 (4.58 nm) for

$t=25$ sec. It becomes broader over the next $\Delta t=20$ min, indicating the growth of the nanoplatelets ($t=1200$ sec with 0.86 nm^{-1} , 7.31 nm).

The most prominent feature in these scattering patterns is the development of the peak around 1.89 nm^{-1} after $t=11.5$ sec (figure 56). This peak can be described as a structure factor peak of an ordered superstructure caused by self-assembly of plate-like nanocrystals.^[57] The peak can be assigned to stacks of nanoplatelets which shows a good coincidence with the SEM images (e.g. figure 41). The well-ordered superstructure caused by the ligand separated platelets self-organizing into nanosheets.

The structure peak arising from stacking of nanosheets at 1.89 nm^{-1} is followed by intensity increases over the next 20 min after the nucleation. Zoom of the structure factor peak associated with stacks of nanosheets, and a shift of the peak maximum from 1.89 nm^{-1} to 1.83 nm^{-1} , could be detected. A small shift to smaller q -values ($d = \frac{2\pi}{q}$) means a shift from 3.39 nm to 3.42 nm in real space which can be explained by a larger inter-nanosheet separation after the early stages of sheet stacking. This is in good coincidence with ex-situ SAXS measurement in the literature.^[25] The structure peak becomes more pronounced when the particle positions become increasingly ordered.

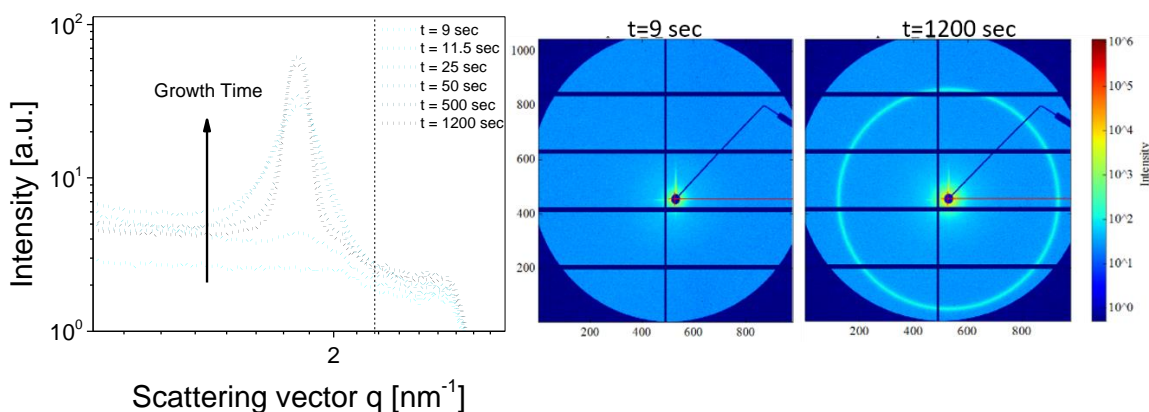


Figure 57: SAXS patterns showing the development of the structure factor peak around 1.89 nm^{-1} after $t=11.5$ sec (left). The structural evolution of the structure factor peak can be detected after 1200 sec in the 2D scattering pattern (right).

The intensity of the structure factor peak increases rapidly over the whole reaction due to stacking nanosheets and the particle intensity decreases ($0.1 \text{ nm}^{-1} \leq q \leq 0.12 \text{ nm}^{-1}$). This means that the spherical nanocrystals eventually convert to flat perovskite sheets. The change of the q dependency is associated with the lateral growth and the conversion into highly ordered stacks (figure 58, left).

The kinetic process can be followed over time scales from seconds to minutes. The intensity of the structure peak factor remains constant from $t=400 \text{ sec}$ to $t=20 \text{ min}$ and becomes narrower according the FWHM (0.17 nm^{-1} to 0.09 nm^{-1}) (figure 58, right).

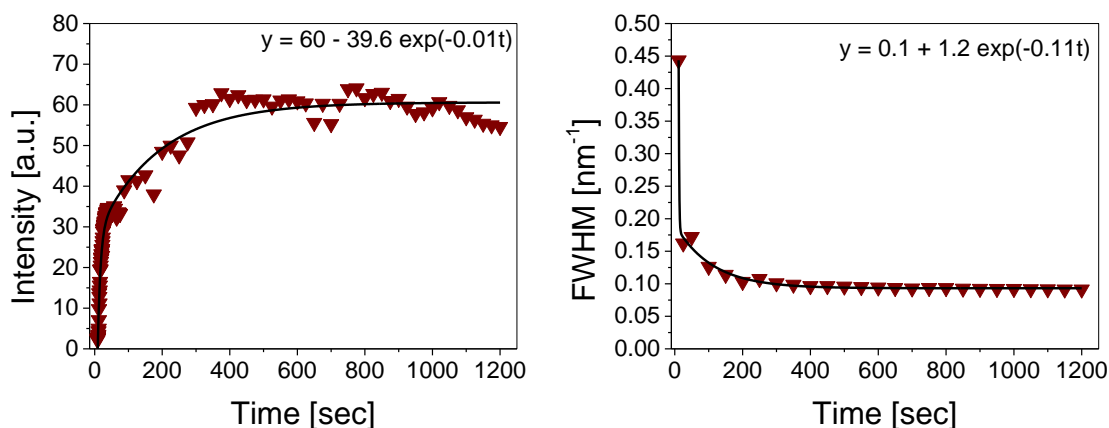


Figure 58: Intensity (left) of the structure factor peak and FWHM (right) versus reaction time. The intensity remains constant and the FWHM becomes narrower from $t=400 \text{ sec}$ to $t=20 \text{ min}$.

This indicates that the preferred number of the stacks remains nearly constant over the time period of this experiment. The domain size of the ordered particles increases and describes the long-range order in one direction. This describes also the strong anisotropic growth (figure 58, left). A further decay of the scattering intensity can be explained by the sedimentation of the perovskite nanocrystals.

The variation of the sample-to-detector distance to 1.66 m allows the detection of larger q -values up to $q \leq 1.8 \text{ nm}^{-1}$ (figure 59).

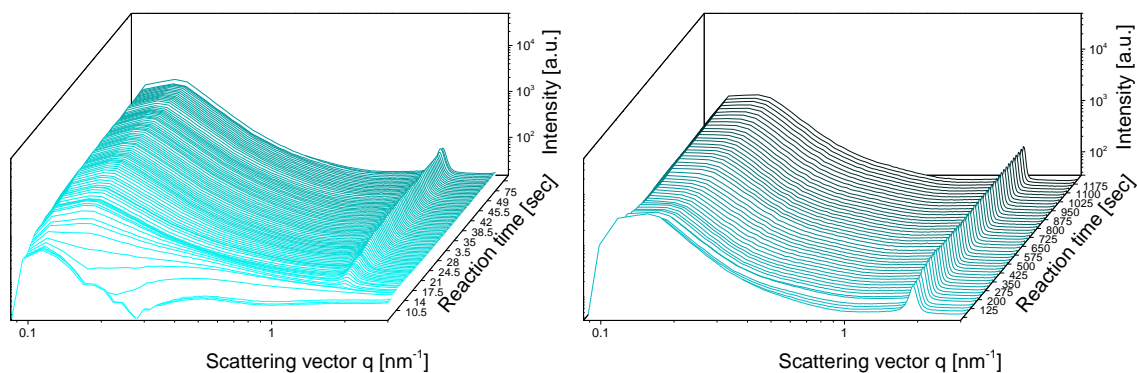


Figure 59: SAXS measurement with 1.66 m sample-to-detector distance of sample P04. Scattering profile (left) shows the development of the structure peak at higher q -values within 100 sec and (right) the temporal structure evolution for the following minutes.

The scattering profiles shows the formation of perovskite and stacking of sheets in the same time window. Scattering results in the higher q -region can be excluded. The structure peak intensity increases over the 20 min and shows a similar peak at 1.82 nm^{-1} (3.45 nm).

In-situ SAXS studies clearly reveal details of the stacked perovskite nanosheet formation mechanism. The complex formation includes at the beginning the formation of polydisperse spherical nanocrystals resulting later in flat sheets. The soft-template method is highly reproducible and the attachment of smaller nanocrystals onto highly ordered lamellar stacks has been observed.

5.5 Conclusion

In this work we have investigated the formation of the perovskites $\text{CH}_3\text{NH}_3\text{PbBr}_3$ via soft-template method at room temperature. The development of the perovskites in a dual solvent system was studied with ex-situ electron microscopic methods. The preparation of anisotropically shaped nanosheets and the subsequent ordered superstructures resulting from a specific precursor composition were elucidated. The solvent induced self-assembly process can be clearly described by SEM-CL and TEM-SAED techniques where the organic ligands stabilize specific facets to maintain the quantum confined structure of the highly crystalline perovskites.

We established a more accurate representation of the selected perovskite nanocrystal growth with optical in-situ techniques. The conventional perovskite synthesis was adapted onto an automated microfluidic device including confocal laser scanning microscopy (CLSM) analysis. The rapid reaction kinetics for nanoparticle formation within a PDMS chip allows one to collect and evaluate the emission in early growth stages. The spectral monitoring of the diffusion controlled process evidenced the formation of larger nanocrystals and their emissive properties.

Furthermore, we demonstrated the first time a capillary interdiffusion approach for perovskites nanocrystal synthesis in combination with UV-Vis and small angle X-ray scattering techniques. We used this setup to slow down the fast kinetics of the reaction. The temporal evolution from spherical perovskite nanocrystals, to nanosheets, to highly-ordered stacked layers shows the influence of the long-tail hydrocarbon stabilizing ligand octylammonium bromide.

The methodologies developed above can be directly applied to the study of nanoparticle formation. The data collection of in-situ UV-Vis and emission spectroscopy, as well as SAXS and ex-situ analysis describe the growth of spherical seed nanocrystals through oriented attachment onto selective crystal facets. The highly crystalline order of quantum platelets resulting from well-controlled and reproducible synthesis provides more insight into the optoelectronic properties of the materials and has great potential for future studies.

References

- [1] N. G. Park, 'Organometal perovskite light absorbers toward a 20% efficiency low-cost solid-state mesoscopic solar cell', *Journal of Physical Chemistry Letters*, vol. 4, no. 15, pp. 2423–2429, 2013.
- [2] C.-C. Chueh, C.-Z. Li, and A. K.-Y. Jen, 'Recent progress and perspective in solution-processed Interfacial materials for efficient and stable polymer and organometal perovskite solar cells', *Energy Environ. Sci.*, vol. 8, no. 4, pp. 1160–1189, 2015.
- [3] H. Tan *et al.*, 'Efficient and stable solution processed planar perovskite solar cell via contact passivation', *Science*, vol. 355, no. 6326, pp. 722–726, 2017.
- [4] S. Yang, W. Fu, Z. Zhang, H. Chen, and C.-Z. Li, 'Recent advances in perovskite solar cells: efficiency, stability and lead-free perovskite', *J. Mater. Chem. A*, vol. 5, no. 23, pp. 11462–11482, 2017.
- [5] J.-P. Correa-Baena *et al.*, 'The rapid evolution of highly efficient perovskite solar cells', *Energy Environ. Sci.*, vol. 10, no. 3, pp. 710–727, 2017.
- [6] S. Gonzalez-Carrero, R. E. Galian, and J. Pérez-Prieto, 'Maximizing the emissive properties of CH₃NH₃PbBr₃ perovskite nanoparticles', *J. Mater. Chem. A*, vol. 3, no. 17, pp. 9187–9193, 2015.
- [7] L. C. Schmidt *et al.*, 'Nontemplate synthesis of CH₃NH₃PbBr₃ perovskite nanoparticles', *Journal of the American Chemical Society*, vol. 136, no. 3, pp. 850–853, 2014.
- [8] F. Zhu *et al.*, 'Shape evolution and single particle luminescence of organometal halide perovskite nanocrystals', *ACS Nano*, vol. 9, no. 3, pp. 2948–2959, 2015.
- [9] Y. Chen, M. He, J. Peng, Y. Sun, and Z. Liang, 'Structure and growth control of organic–inorganic halide perovskites for optoelectronics: From polycrystalline films to single crystals', *Advanced Science*, vol. 3, no. 4, 2015.
- [10] B. A. Rosales, M. P. Hanrahan, B. W. Boote, A. J. Rossini, E. A. Smith, and J. Vela, 'Lead Halide Perovskites: Challenges and Opportunities in Advanced Synthesis and Spectroscopy', *ACS Energy Letters*, vol. 2, no. 4, pp. 906–914, 2017.
- [11] J. Chen *et al.*, 'The Role of Synthesis Parameters on Crystallization and Grain Size in Hybrid Halide Perovskite Solar Cells', *Journal of Physical Chemistry C*, vol. 121, no. 32, pp. 17053–17061, 2017.
- [12] J. H. Noh, S. H. Im, J. H. Heo, T. N. Mandal, and S. Il Seok, 'Chemical management for colorful, efficient, and stable inorganic-organic hybrid nanostructured solar cells', *Nano Letters*, vol. 13, no. 4, pp. 1764–1769, 2013.

- [13] H. Huang *et al.*, ‘Growth mechanism of strongly emitting CH₃NH₃PbBr₃perovskite nanocrystals with a tunable bandgap’, *Nature Communications*, vol. 8, no. 1, pp. 1–7, 2017.
- [14] S. Meloni, G. Palermo, N. Ashari-Astani, M. Grätzel, and U. Rothlisberger, ‘Valence and conduction band tuning in halide perovskites for solar cell applications’, *J. Mater. Chem. A*, vol. 4, no. 41, pp. 15997–16002, 2016.
- [15] C. M. Sutter-Fella *et al.*, ‘High Photoluminescence Quantum Yield in Band Gap Tunable Bromide Containing Mixed Halide Perovskites’, *Nano Letters*, vol. 16, no. 1, pp. 800–806, 2016.
- [16] G. C. Papavassiliou and I. B. Koutselas, ‘Structural, optical and related properties of some natural three-and lower-dimensional semiconductor systems’, *Synthetic Metals*, vol. 71, no. 1, pp. 1713–1714, 1995.
- [17] G. C. Papavassiliou, ‘Three- and low-dimensional inorganic semiconductors’, *Progress in Solid State Chemistry*, vol. 25, no. 3–4, pp. 125–270, 1997.
- [18] J. A. Sichert *et al.*, ‘Quantum Size Effect in Organometal Halide Perovskite Nanoplatelets’, *Nano Letters*, vol. 15, no. 10, pp. 6521–6527, 2015.
- [19] P. Tyagi, S. M. Arveson, and W. A. Tisdale, ‘Colloidal Organohalide Perovskite Nanoplatelets Exhibiting Quantum Confinement’, *Journal of Physical Chemistry Letters*, vol. 6, no. 10, pp. 1911–1916, 2015.
- [20] L. Polavarapu, B. Nickel, J. Feldmann, and A. S. Urban, ‘Advances in Quantum-Confined Perovskite Nanocrystals for Optoelectronics’, *Advanced Energy Materials*, no. April, 2017.
- [21] R. W. Epps, K. C. Felton, C. W. Coley, and M. Abolhasani, ‘Automated Microfluidic Platform for Systematic Studies of Colloidal Perovskite Nanocrystals: Towards Continuous Nano-Manufacturing’, *Lab Chip*, vol. 17, pp. 4040–4047, 2017.
- [22] T. L. Sounart *et al.*, ‘Spatially-resolved analysis of nanoparticle nucleation and growth in a microfluidic reactor’, *Lab on a Chip*, vol. 7, no. 7, p. 908, 2007.
- [23] I. Lignos, R. Maceiczky, and A. J. DeMello, ‘Microfluidic Technology: Uncovering the Mechanisms of Nanocrystal Nucleation and Growth’, *Accounts of Chemical Research*, vol. 50, no. 5, pp. 1248–1257, 2017.
- [24] C. Fürst, P. Zhang, S. V. Roth, M. Drechsler, and S. Förster, ‘Self-assembly of block copolymers via micellar intermediate states into vesicles on time scales from milliseconds to days’, *Polymer (United Kingdom)*, vol. 107, pp. 434–444, 2016.
- [25] M. B. Teunis, M. A. Johnson, B. B. Muhoberac, S. Seifert, and R. Sardar, ‘Programmable Colloidal Approach to Hierarchical Structures of Methylammonium Lead Bromide Perovskite Nanocrystals with Bright Photoluminescent Properties’, *Chemistry of Materials*, vol. 29, no. 8, pp. 3526–3537, 2017.

- [26] A. R. B. M. Yusoff and M. K. Nazeeruddin, 'Organohalide Lead Perovskites for Photovoltaic Applications', *Journal of Physical Chemistry Letters*, vol. 7, no. 5, pp. 851–866, 2016.
- [27] G. Kieslich, S. Sun, and A. K. Cheetham, 'An extended Tolerance Factor approach for organic–inorganic perovskites', *Chem. Sci.*, vol. 6, no. 6, pp. 3430–3433, 2015.
- [28] Z. Li, M. Yang, J. S. Park, S. H. Wei, J. J. Berry, and K. Zhu, 'Stabilizing Perovskite Structures by Tuning Tolerance Factor: Formation of Formamidinium and Cesium Lead Iodide Solid-State Alloys', *Chemistry of Materials*, vol. 28, no. 1, pp. 284–292, 2016.
- [29] C. C. Stoumpos, C. D. Malliakas, and M. G. Kanatzidis, 'Semiconducting tin and lead iodide perovskites with organic cations: Phase transitions, high mobilities, and near-infrared photoluminescent properties', *Inorganic Chemistry*, vol. 52, no. 15, pp. 9019–9038, 2013.
- [30] Y. Li *et al.*, 'Direct Observation of Long Electron-Hole Diffusion Distance in CH₃NH₃PbI₃ Perovskite Thin Film', *Scientific Reports*, vol. 5, no. April, pp. 1–8, 2015.
- [31] S. D. Stranks *et al.*, 'Electron-Hole Diffusion Lengths Exceeding', *Science (New York, N.Y.)*, vol. 342, no. 2013, pp. 341–344, 2014.
- [32] W. Mao *et al.*, 'Controlled Growth of Monocrystalline Organo-Lead Halide Perovskite and Its Application in Photonic Devices', *Angewandte Chemie - International Edition*, vol. 56, no. 41, pp. 12486–12491, 2017.
- [33] Z. Y. Zhang *et al.*, 'The role of trap-assisted recombination in luminescent properties of organometal halide CH₃NH₃PbBr₃ perovskite films and quantum dots', *Scientific Reports*, vol. 6, no. June, pp. 1–7, 2016.
- [34] S. Lee *et al.*, 'Amine-Based Passivating Materials for Enhanced Optical Properties and Performance of Organic-Inorganic Perovskites in Light-Emitting Diodes', *Journal of Physical Chemistry Letters*, vol. 8, no. 8, pp. 1784–1792, 2017.
- [35] B. Luo, S. B. Naghadeh, A. Allen, X. Li, and J. Z. Zhang, 'Peptide-Passivated Lead Halide Perovskite Nanocrystals Based on Synergistic Effect between Amino and Carboxylic Functional Groups', *Advanced Functional Materials*, vol. 27, no. 6, 2017.
- [36] C. Schliehe *et al.*, 'Ultrathin PbS sheets by two-dimensional oriented attachment.', *Science (New York, N.Y.)*, vol. 329, pp. 550–553, 2010.
- [37] Y. Hu, H. Gu, and Z. Wang, 'The Anisotropic Growth of Perovskite Oxide Nanowires', *Nanowires - Fundamental Research*, pp. 141–160, 2011.
- [38] R. M. MacEiczyk, K. Dübgen, I. Lignos, L. Protesescu, M. V. Kovalenko, and A. J. Demello, 'Microfluidic reactors provide preparative and mechanistic insights into the synthesis of formamidinium lead halide perovskite nanocrystals', *Chemistry of Materials*, vol. 29, no. 19, pp. 8433–8439, 2017.

- [39] J. Polte *et al.*, ‘Nucleation and Growth of Gold’, *ACS Nano*, vol. 4, no. 2, pp. 1076–1082, 2010.
- [40] X. Chen, J. Schröder, S. Hauschild, S. Rosenfeldt, M. Dulle, and S. Förster, ‘Simultaneous SAXS/WAXS/UV-Vis Study of the Nucleation and Growth of Nanoparticles: A Test of Classical Nucleation Theory’, *Langmuir*, vol. 31, no. 42, pp. 11678–11691, 2015.
- [41] S. Zhuo, J. Zhang, Y. Shi, Y. Huang, and B. Zhang, ‘Self-Template-Directed Synthesis of Porous Perovskite Nanowires at Room Temperature for High-Performance Visible-Light Photodetectors’, *Angewandte Chemie International Edition*, vol. 54, no. 19, pp. 5693–5696.
- [42] T. Udayabhaskararao, M. Kazes, L. Houben, H. Lin, and D. Oron, ‘Nucleation, Growth, and Structural Transformations of Perovskite Nanocrystals’, *Chemistry of Materials*, vol. 29, no. 3, pp. 1302–1308, 2017.
- [43] T. Theivasanthi and M. Alagar, ‘Konjac Biomolecules Assisted–Rod/Spherical Shaped Lead Nano Powder Synthesized by Electrolytic Process and Its Characterization Studies’, *Nano Biomedicine and Engineering*, vol. 5, no. 1, 2013.
- [44] Z. Dang *et al.*, ‘In Situ Transmission Electron Microscopy Study of Electron Beam-Induced Transformations in Colloidal Cesium Lead Halide Perovskite Nanocrystals’, *ACS Nano*, vol. 11, no. 2, pp. 2124–2132, 2017.
- [45] C. G. Pope, ‘X-ray Diffraction and the Bragg Equation’, *Journal of Chemical Education*, vol. 74, no. 1, p. 129, 1997.
- [46] A. Ghezelbash and B. A. Korgel, ‘Nickel sulfide and copper sulfide nanocrystal synthesis and polymorphism’, *Langmuir*, vol. 21, no. 21, pp. 9451–9456, 2005.
- [47] X. Fu *et al.*, ‘Controlled synthesis of brightly fluorescent $\text{CH}_3\text{NH}_3\text{PbBr}_3$ perovskite nanocrystals employing $\text{Pb}(\text{C}_{17}\text{H}_{33}\text{COO})_2$ as the sole lead source’, *RSC Advances*, vol. 8, no. 2, pp. 1132–1139, 2018.
- [48] J. Zhang *et al.*, ‘Fundamentals and applications of inertial microfluidics: a review’, *Lab Chip*, vol. 16, no. 1, pp. 10–34, 2016.
- [49] E. Hofmann, ‘PDMS PPXn EH09 Microfluidic Chip’, unpublished manuscript 2017.
- [50] Q. A. Akkerman *et al.*, ‘Solution Synthesis Approach to Colloidal Cesium Lead Halide Perovskite Nanoplatelets with Monolayer-Level Thickness Control’, *Journal of the American Chemical Society*, vol. 138, no. 3, pp. 1010–1016, 2016.
- [51] Y. Bekenstein, B. A. Koscher, S. W. Eaton, P. Yang, and A. P. Alivisatos, ‘Highly Luminescent Colloidal Nanoplates of Perovskite Cesium Lead Halide and Their Oriented Assemblies’, *Journal of the American Chemical Society*, vol. 137, no. 51, pp. 16008–16011, 2015.

- [52] N. Sundararajan, M. S. Pio, L. P. Lee, and A. A. Berlin, 'Three-dimensional hydrodynamic focusing in polydimethylsiloxane (PDMS) microchannels', *Journal of Microelectromechanical Systems*, vol. 13, no. 4, pp. 559–567, 2004.
- [53] Y. Gambin, C. Simonnet, V. VanDelinder, A. Deniz, and A. Groisman, 'Ultrafast microfluidic mixer with three-dimensional flow focusing for studies of biochemical kinetics', *Lab Chip*, vol. 10, no. 5, pp. 598–609, 2010.
- [54] M. J. González-Vázquez and M. Hautefeuille, 'Controlled solvent-free formation of embedded PDMS-derived carbon nanodomains with tunable fluorescence using selective laser ablation with a low-power CD laser', *Micromachines*, vol. 8, no. 10, 2017.
- [55] P. S. Nikam, S. J. Kharat, P. Chemistry, M. S. G. College, and M. Camp-, 'Density and Viscosity Studies of Binary Mixtures of N , N -Dimethylformamide with Toluene and Methyl Benzoate at (298 . 15 , 303 . 15 , 308 . 15 , and 313 . 15) K', pp. 455–459, 2005.
- [56] B. Hemalatha, P. Vasantharani, N. Senthilkumar, A. Nagar, and T. Nadu, 'Solute-solvent and Solute-Solute Interactions of Tetrabutylammonium bromide in DMF-Water Systems at Different Temperatures', *International Journal of Advances in Engineering & Technology*, vol. 6, no. 2, pp. 795–803, 2013.
- [57] Wim H. de Jeu, *Basic X-ray Scattering for Soft Matter*, Oxford UK, Oxford University Press, 2016.

Chapter 6

Novel Scalable Synthesis of Semiconducting Magic-sized Clusters and Nanocrystals

6.1 Introduction and Motivation

Synthetic Intermediates: Semiconducting Clusters

Colloidal semiconductor quantum dots have received considerable attention due to their size-related absorption properties and their technological potential.^{[1][2][3]} One current topic concerns their structural evolution, because significant interest has arisen in molecule-like clusters, which are intermediate products or byproducts in the regular quantum dot synthesis. So-called magic-size clusters (MSC) were encountered at the early stages of quite a few syntheses of II-VI and IV-VI semiconductor materials.^{[4][5][6][7][8]}

In contrast to bulk materials, the lowest-energy absorption peaks of nanoclusters show a strong blue-shift with decreasing nanocluster size.^[9] In-situ UV-Vis investigations demonstrate their growth process.^{[7][10][11]} Magic-sized clusters are mostly transiently observed during syntheses and therefore are relatively unexplored.

Henglein et al. described the formation of small colorless CdS particles synthesized at -78 °C.^[12] He postulated that the combination of organic solvent, lower temperature and strong CdS stabilizer is responsible for the fluorescent colloidal products. In general, the nanocluster formation starts with the decomposition of monomeric precursors which in a subsequent step act as nuclei for the synthesis of nanocrystals.^{[13][14]}

AgI quantized clusters could be successfully stabilized with amine-bearing water-soluble polymers.^[15] Their kinetics and the light-sensitivity of quantitatively-reacted silver and iodide ions were investigated. Calzaferri and Leiggener^[16] showed that zeolite cavities can act as host material for the synthesis of size-restricted Ag₂S and PbS clusters.

Cluster intermediates have special geometries and show elevated thermodynamic stability. Marynick and co-workers published computational results of low-energy geometric structures and UV-Vis absorbance spectra of (AgBr)₁₋₉ clusters.^[17] Furthermore, they highlighted the density functional theory (DFT) study of (PbS)₁₋₉ and (CdS)₁₋₆ clusters which significantly contribute to the fundamental understanding of the optical properties and structural stability.^{[18][19]}

Zope et al. summarized the study of ZnS clusters by describing the structural and electronic properties of confined structures.^[20] All research groups highlighted that the cluster properties should vary as a function of the cluster size in the extreme quantum confinement regime.

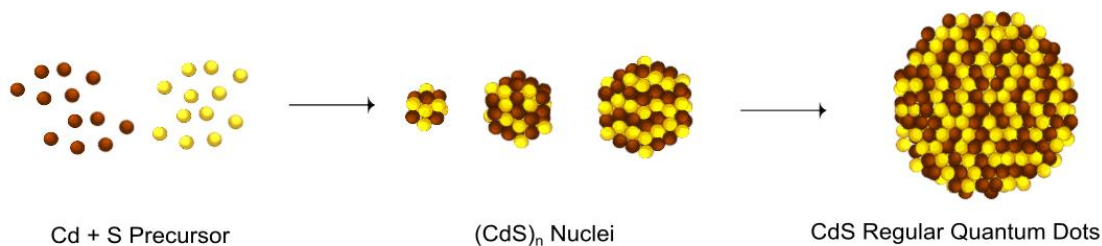


Figure 60: Semiconducting material CdS, resulting in regular quantum dots. Ligand-stabilized Cd and sulfur precursors act as source materials in an organic solvent and the heterogeneous formation includes the nucleation and growth periods.

These systems represent new types of materials which lie in the region of molecule-like structures (very small clusters) and size-limited solids (large clusters). In 1994 Vossmeier et al.^[21] synthesized CdS nanoclusters with diameters ranging from 0.5 nm to 2 nm and showing well-structured UV-Vis spectra with bands below 476 nm. Similar studies with CdSe, including TEM analysis^{[22][23]} and AFM height studies, indicated the cluster sizes were smaller than 2 nm.^[24] Mass spectroscopy analyses underline the magic-size characteristic with the detection of a discrete number of atoms within cluster intermediates.^{[25][26][27][28]} ESI-MS and also MALDI-TOF are applicable to the analysis of cluster materials but there is still an uncertainty whether the masses obtained are from the original clusters or fragmented products.

6.2 Semiconducting Clusters and Quantum Dots

6.2.1 Living-Metal Polymer Concept

The high and increasing demand for semiconductor quantum dots requires the detailed understanding of magic-sized clusters (MSC). Their relevance and their mechanistic role in the quantum dot growth process are the major factors of attraction for numerous research groups.^{[21][27][29][30]} The MSC and QD formation process and the proposed size evolution mechanism requires detailed structural analyses which are based mainly on optical measurements.

The growth process of semiconducting clusters resulting in quantum dots involves a multi-step nucleation process. The evolution is characterized by distinct stages of intermediates with extraordinary thermodynamic stability. Ultraviolet and visible spectroscopic techniques enable researcher to observe isosbestic points during the growth process which can be clearly assigned to intermediates. The discrete red-shift of excitonic peaks in absorbance spectra is consequence of the heterogeneous cluster growth.^[7]

According to the results of optical investigations, the cluster formation is comparable with the 'living polymer concept'.^[23] This is a plausible and simplified model to describe the structural development shown in figure 61. After mixing the precursor components, the cluster growth proceeds through overcoming energy barriers and the formation of small clusters. The MSC represent minima in the potential energy landscape because of their increased thermodynamic stability over other cluster species. In the presence of unreacted precursor, a given cluster can evolve into larger MSCs through a series of jumps over the potential energy barriers, resulting in subsequent cluster families with outstanding stability. In view of the absorption spectra, the degradation of peaks and the creation of new absorbance peaks at higher wavelength can be monitored.^{[30][31]} The depletion of cluster peaks and simultaneous accumulation of other cluster species with different stoichiometries are obtained. This could be observed at higher temperatures and ongoing monomer consumption, revealing the heterogeneous cluster growth from MSC to a variety of nanostructures.

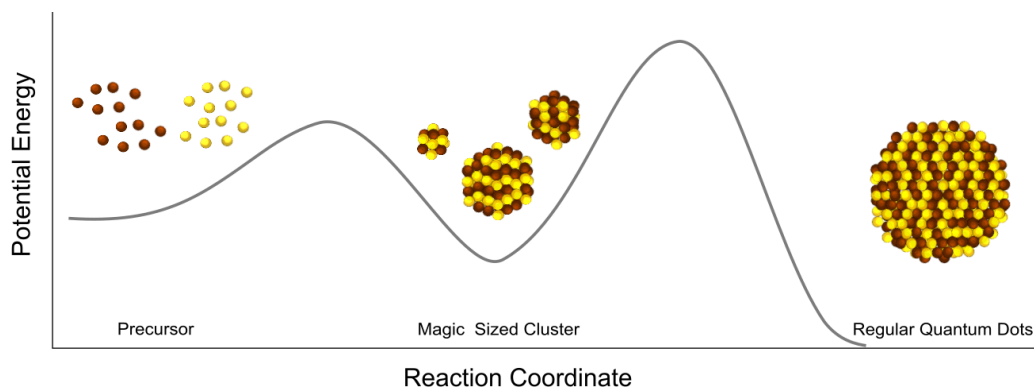


Figure 61: Illustration of the two-step nucleation mechanism for the quantum dot growth starting with molecular precursor and magic-sized clusters as key intermediates.

6.2.2 Surfactant-Controlled Synthesis of Semiconductor MSC and QD

Synthesis of small uniform colloidal particles proceeds best from wet-chemical synthesis.^{[30][32][33]} The literature suggests special steps need to be taken to fabricate such semiconducting nanoclusters. Mello Donega^[34] provide a good overview where a few of important synthetic factors have been investigated. These include that the growth temperature has a substantial impact on the MSC growth kinetic and stability. Typically, overcoming the activation barriers allows the observation of MSC families and they are mostly observed below the usual synthetic temperature of QDs.^{[25][35]} Mostafavi^[36] used a radiolytic technique to demonstrate that final particle size of the cluster is influenced by the dose rate. This is comparable with the precursor consumption at progressively longer reaction times and it is used for an efficient route to tune the cluster size towards higher wavelength.^{[7][27][37]}

Xie et al. examined cluster formation experimentally and theoretically and especially the effect of supersaturation in the synthesis of InP nanoclusters and nanocrystals.^[38] According to their results, the extremely high degree of supersaturation drives the formation of magic-sized cluster and influences the nucleation and growth of colloidal particles.^[39] The proposed model for the formation of thermodynamically stable nuclei underline these results, the higher the supersaturation, the smaller the critical nucleus could be. The higher the temperature and the monomer solubility (resulting from monomer-ligand complexes), the smaller the supersaturation

and the MSC yield. Higher reaction temperatures promote a rapid growth of relatively large colloidal particles.

The observation of MSC families can be promoted by the precursor reactivity and by so-called template synthesis. The latter can be realized by using porous materials and interstitial spaces.^{[16][40]} Confined spaces can also be achieved through ligand-stabilized approaches to limit the cluster size during the growth process.^{[41][42][43]} Rosenthal and co-workers^[31] have given an overview of the nature of stabilizing surfactants for CdSe with different binding affinity and binding strength. Commonly used ligands, such as amines, phosphinic acids, and oleic acids favor the formation of magic-sized clusters due to their capability of forming coordination bonds with metal atoms at the nanocluster or nanocrystal surfaces.^{[2][34][44][45][46]} They are essential to control the shape and size, but the full mechanism is not clearly understood. Owen and co-worker suggested that ligands may be able to reduce the activation barrier for cluster growth.^[43] Similar results were obtained for ZnTe clusters, where ligands are able to modify the free energies of the NC surface resulting in the stabilization or destabilization of specific nanocrystal facets, thus influencing the formation kinetics of colloidal nanomaterials.^[34] Landes et al.^[47] highlighted that the addition of amines leads to destabilization of nanocrystals and the formation of thermodynamically stable structures. The role of amines in the synthesis of cluster and quantum dots ranges from ligands to bases but a detailed understanding is still limited. However, the presence of ligands is crucial for the MSC synthesis and modulates the growth process. Various research groups^{[27][30][48]} showed that the growth of clusters proceeds through a series of jumps over energy barriers as mentioned in chapter 6.2.1. Weiss and co-workers described the conversion of MSC to QD as a competing step-growth and living chain-growth mechanism in the presence of stabilizing agents.^[49] An excess of surfactants favours a fast growth of clusters resulting in smaller final QD sizes. The mechanism is termed a living chain-growth mechanism due to the consecutive monomer addition, whereas a stoichiometric amount of ligands controls the rapid consumption of monomeric precursors (step-growth mechanism). In situ scattering methods can monitor the evolution of primary precursors into crystalline ordered structures.^[50] Inspired by a large body of work on the synthesis and handling of semiconducting nanoclusters and particles, this chapter demonstrates a novel preparation method of ligand stabilized clusters. The synthetic approach is applicable to a range of semiconductor systems consisting of metal sulfide and metal halides in organic solvents. The unique and element-specific properties originating from their size and shapes are systematically studied by monitoring the absorption and emission spectra. Ex-situ characterization methods such TEM and X-ray diffraction techniques support the results.

6.3 Experimental Section

6.3.1 Novel Scalable Synthesis

Herein we present a chemical synthesis to prepare stable MSC at room temperature. For the multicomponent synthesis, ionic reaction components were introduced into organic solvents together with stabilizing ligands (organic precursor). For the batch synthesis, the organic precursors were synthesized and the solvent system optimized. The synthesis of metal chalcogenide semiconductor clusters based on Lewis acid-base reactions between metal oleate and sulfur-stabilized precursor at room temperature which can be applied to metal halide systems. Figure 62 shows a schematic illustration of the synthesis of metal chalcogenide and metal halide cluster.

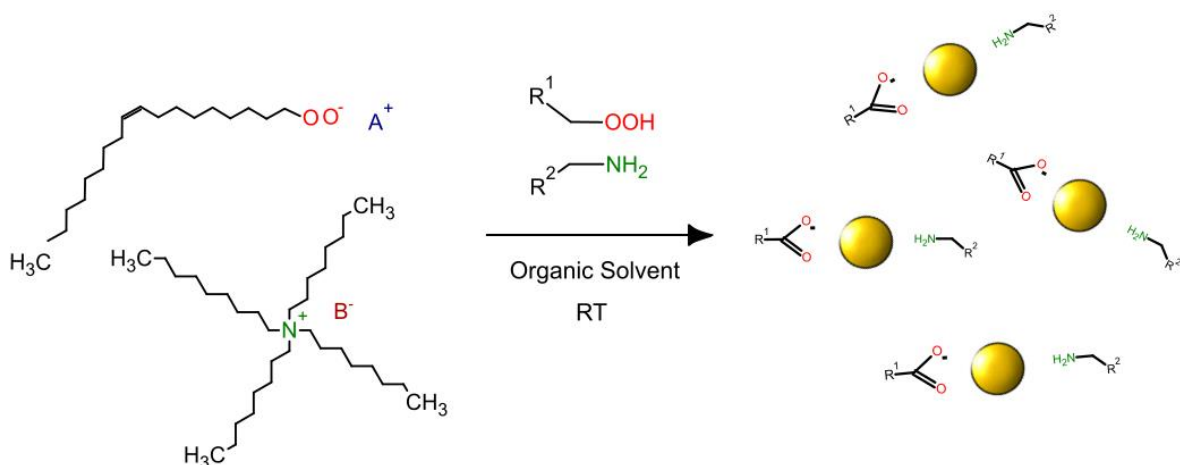


Figure 62: General approach for the synthesis of metal halide and metal chalcogenide magic-sized clusters at room temperature (RT) in organic solvents. A^+ represents the metal ion, B^- the halide or sulfur ion. Organic ligands act as stabilizing agents during the synthesis.

6.3.2 Metal Precursor

A large body of work has been carried out on the development and handling of metal-based nanoclusters and nanocrystals. Cadmium oleate, tin oleate, silver oleate and lead oleate were chosen as metal precursors. In general, metal oleates show poor solubility in organic solvents. To overcome this problem and guarantee the complete solubility of these metal oleates, either the temperature can be increased or a minimum amount of amines can be added to form complexes with the metal and increase the solubility (figure 63).^{[44][51]}

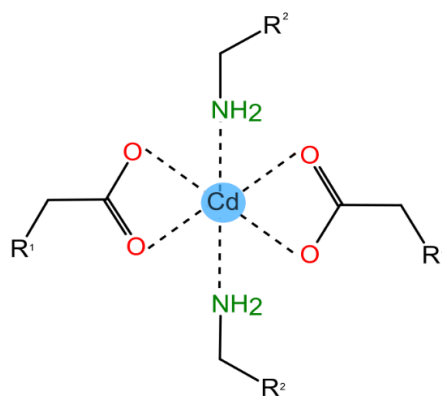


Figure 63: Metal oleate reacts with primary amines to form metal oleate-amine complexes to achieve complete solubility of the metal precursor.

The ionic precursor is responsible for the generation of metals ions which are stabilized by conventional ligands. From literature, oleic acid and different amines have been used in the synthesis of metal chalcogenide clusters.^{[31][43][52][53]} The ligands show a high binding affinity towards metal ions and slow the reaction kinetics. To allow UV-Vis monitoring of the metal chalcogenide and metal halide cluster formation, cyclohexane was used as the organic solvent because of its low cut-off wavelength.^[54] This allows the detection of the precursor degradation as well as the early growth stage of the semiconductor material. Moreover, the required supersaturation (poor solubility of the ligand-metal complex) could be achieved using cyclohexene.

6.3.3 Anionic Precursor

Halide Precursor

The iodide precursor was synthesized via the exchange of halogen atoms according the Finkelstein reaction.^[55] It is an equilibrium reaction and driven by the different solubility of halide salts where bromide is replaced by iodide. The reaction was expanded to our system where sodium iodide was dissolved in water and the precursor tetraoctylammonium bromide was dissolved in toluene. The reaction is driven by the conversion to tetraoctylammonium bromide in the organic phase. The

toluene phase shows a yellow colour after the successful replacement of bromide and the conversion efficiency/purity was determined by the melting point of the salt.

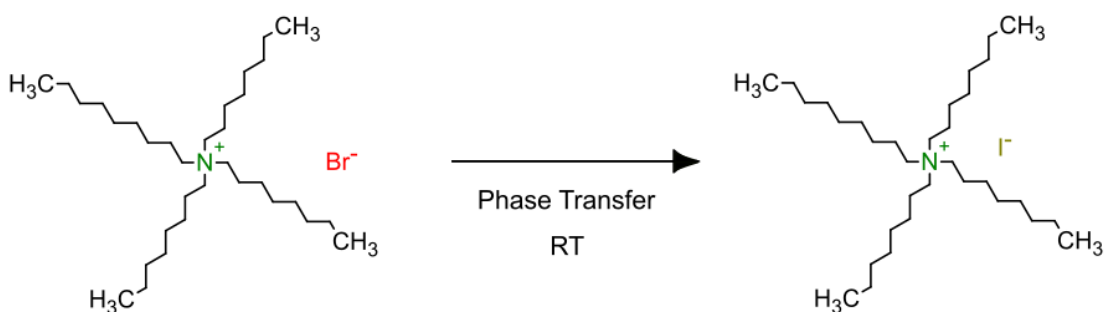


Figure 64: General approach for the Finkelstein reaction for the conversion of tetraoctylammonium bromide to tetraoctylammonium iodide in presence of sodium iodide.

Sulfur Precursor

The sulfur precursor, tetraoctylammonium sulfide was prepared via liquid-liquid phase transfer according the literature Li et al.^[56] In the first step, optimal conditions like the S:Na₂S ratio and the operating temperature and time were chosen to prepare an aqueous sodium disulfide solution (Step I, stock solution). For the reaction, sulfur and sodium sulfide were mixed under vigorous stirring in water at 50 °C. The size of the polysulfide anion in water (S^{2-x}, x=2, 3, 4, 5) can be influenced by controlling the sulfide/sodium sulfide ratio which was set to be S:Na₂S 0.6, but an equilibrium between all synthesized polysulfide anion still exists after the conversion.

In the subsequent step, tetraoctylammonium bromide TOABr was dissolved in chloroform under Schlenk conditions (absorption below 250 nm). The sulfide anions tend to go into the organic phase (Step II, figure 65) with the help of the phase transfer agent. Therefore, the subsequent reaction between polysulfide anions and the phase transfers agent TOABr leads to the replacement of bromide. The conversion can be clearly indicated by a color change of the chloroform phase from colorless into dark yellow/green.

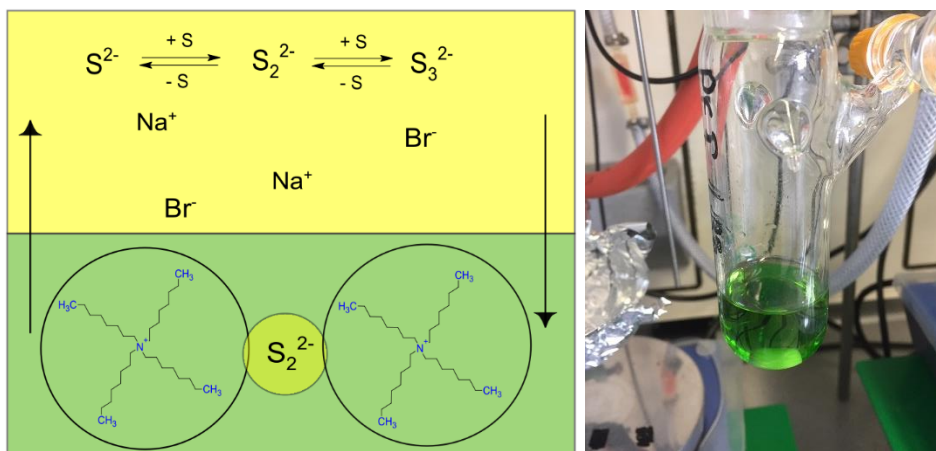


Figure 65: Illustration of the liquid-liquid phase transfer of polysulfide anions into the organic phase with the help of the phase transfer agent tetraoctylammonium bromide (left). The photograph was taken directly after starting the phase transfer reaction (right).

Pure Na_2S shows an absorbance signal between 220 nm and 230 nm in water, whereas polysulfide anions show strong absorbance in the higher wavelength region with peak maxima around 298 nm and 369 nm (figure 66, left). The peak positions depend on the S/ Na_2S ratio and the individual polysulfide which shows a linear intensity increase with increasing concentration.^[57] The transfer efficiency can be monitored by UV-vis-spectroscopy (figure 66, right). Due to the phase transfer, the peak intensity at $\lambda=339$ nm increases within 24 h and reaches equilibrium. This represents the higher binding affinity of the ammonium ions towards the sulfide anions.^{[58][59][60]} The absence of the 618 nm peak in the final product is evidence of the absence of 'dissolved' sulfur.^[61] The conversion can be detected with a control experiment detecting the remaining sulfur in the water phase.

Both the binding capability and the concentration of these sulfur anions determine which anion will be phase-transferred and generate the corresponding products in the phase-transfer reaction. The steric hindrance of the large quaternary ammonium cation influences the binding capability. It favors the binding of bigger disulfide anion with two TOA^+ cations, whereas binding of smaller monosulfide anions is relatively difficult.

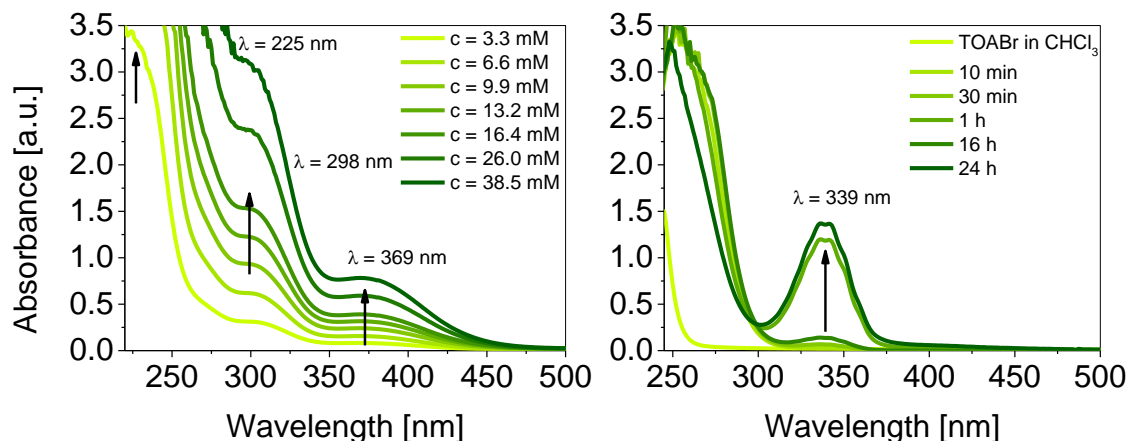


Figure 66: Absorbance spectra directly after the conversion of S/Na₂S in water. The main peaks are around 225 nm, 298 nm, 369 nm representing the coexistence of polyanions (left). After the phase transfer (S:TOABr 1:1) into the chloroform phase, the absorbance signal around 339 nm increases within 24 h. The phase transfer agent TOABr shows absorbance $\lambda < 250$ nm.

Taking into account the UV-Vis spectra, we assume that higher polysulfides are synthesized but it is not possible to distinguish between the individual polysulfides in this reaction.^[62] For simplicity, all co-existing forms will be referred to as 'sulfide'. To avoid numerous side reactions, the sulfide precursor was stored under inert gas atmosphere in the dark. The high reactivity of the sulfur precursor in the presence of amines was studied (Appendix).^[60] The degradation of the sulfur-bearing precursor is ascribed as the reaction with amines forming alkylammonium polysulfide and acting in subsequent steps as sulfur precursor. Furthermore, the relative amount of the sulfur species depends on temperature, pH, ionic strength, amount of H₂S gas leaving the solution, and diverse side reactions (including sulfide oxidation). These products are hard to characterize. According to former studies, it is known that under basic conditions the sulfide ion S²⁻ is predominant whereas under acidic conditions hydrogen sulfide gas H₂S will be released.^[63]

For the synthesis, the surfactant-controlled nanocluster growth of metal halides and metal chalcogenide is monitored at low temperatures in a supersaturated system with in-situ optical measurements and ex-situ TEM. This method effectively provides information about the development and regulation of MSCs. Further studies were performed to suppress the evolution of regular quantum dots. Alkylammonium stabilized anions as well as the Lewis bases and fatty acids bind strongly to the precursor to minimize the formation of larger nanocrystals. Additionally, the

amine ligand is able to passivate the nanocrystal by acting as an electron-donating ligand. Synthesis in an organic system is important to later use MSC as seeds for high temperature studies and in view of various microfluidic applications^{[50][64]}. The growth process could be applied to a wide range of binary semiconductor MSCs and QD. Beside the material dependency, the intermediates sizes depend on the synthetic parameters. In the following chapter, we adapt our CdS model system to ZnS, PbS, Ag₂S and the halide systems AgI and AgBr. The development of ideal conditions for stepwise growth in various semiconductor MSC materials is developed, excluding pathways of continuous growth, and to guarantee the formation of stable MSC. From here, a new regime can be entered where well-defined nanocrystals form MSCs to act as seed nuclei and reservoirs.

6.4 Results and Discussion

6.4.1 Metal Chalcogenide

CdS Cluster Growth

Now we report our novel approach for preparing stable CdS magic-sized clusters at room temperature. The challenges are the regulation of the cluster development and suppression of the evolution of regular quantum dots. The MSC are synthesized in organic solvent and show element-specific absorbance peaks. For the synthesis, the ligand terminated cation complex Cd(oleate)₂ was mixed with the sulfur-bearing ammonium precursor TOA₂S₂ and the electronic structure was monitored by optical spectroscopy (figure 67).

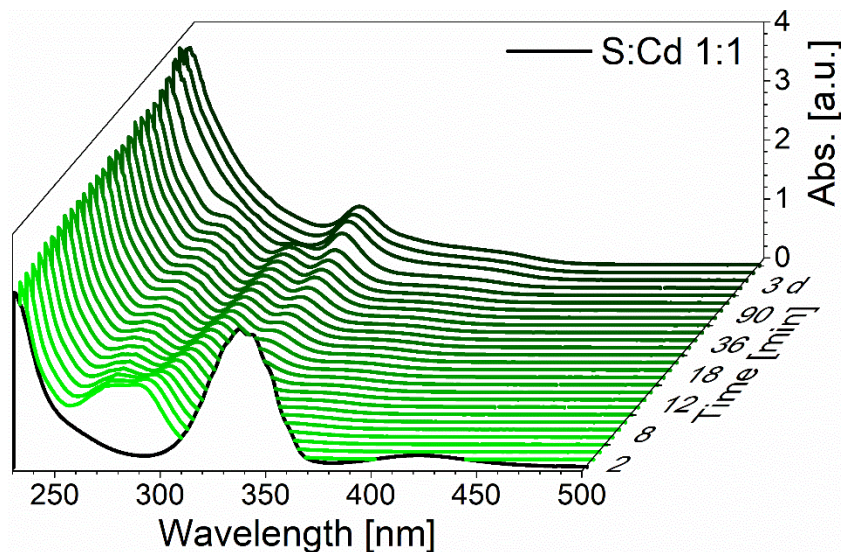


Figure 67: In-situ UV-Vis detection showing the temporal evolution of CdS clusters with stoichiometric ratio of S:Cd 1:1 in cyclohexane at room temperature. The sulfur precursor (black curve) decomposes directly after injecting amine and cadmium oleate and induces the CdS cluster growth (green curves).

The cuvette, containing sulfur pre-mixed with amine in cyclohexane (figure 67, black curve), was placed in the spectrometer and Cd(oleate)₂ was quickly injected. The addition of Cd²⁺ (figure 67, green curves) leads instantaneously to nucleation and the development of small clusters (S:Cd 1:1). The absorbance intensity immediately started increasing at shorter wavelengths ($\lambda < 300$ nm) suggesting the onset of the formation of Cd-S bonds. Starting with excess of sulfur, the

consumption of $\text{Cd}(\text{oleate})_2$ allows the observation of isosbestic points during the slow growth process. The peak around $\lambda=279$ nm evolves into absorbance peaks around 259 nm, 285 nm, 311 nm, 348 nm and 380 nm (figure 68, left). The sulfur ion shows a characteristic absorbance signal at around 246 nm^[65] and smaller molecular species absorbing around 259 nm.^[36] The absorption peak at 311 nm is claimed to be a magic-size cluster and this is the major component in our systems. Absorption features at longer wavelength, at around ~ 350 nm, are assigned to the peaks of larger CdS.^[66]

The high reactivity of the sulfur precursor in presence of amines allows the detection of an induction period prior to the nucleation and growth of CdS cluster families, showing high stability under ambient conditions. Instead of overcoming strong C-S binding energy at higher temperatures^[67], the preparation of sulfur precursor in proper organic solvents is directly used to study the in-situ CdS cluster growth with sub-nanometer radii at room temperature. The coexistence of small clusters (285 nm), and their transformation^{[36][53]} into larger CdS magic-sized clusters with absorption peaks at around 311 nm, are evidenced by the temporal evolution starting with monomeric species and the subsequent formation of CdS clusters.

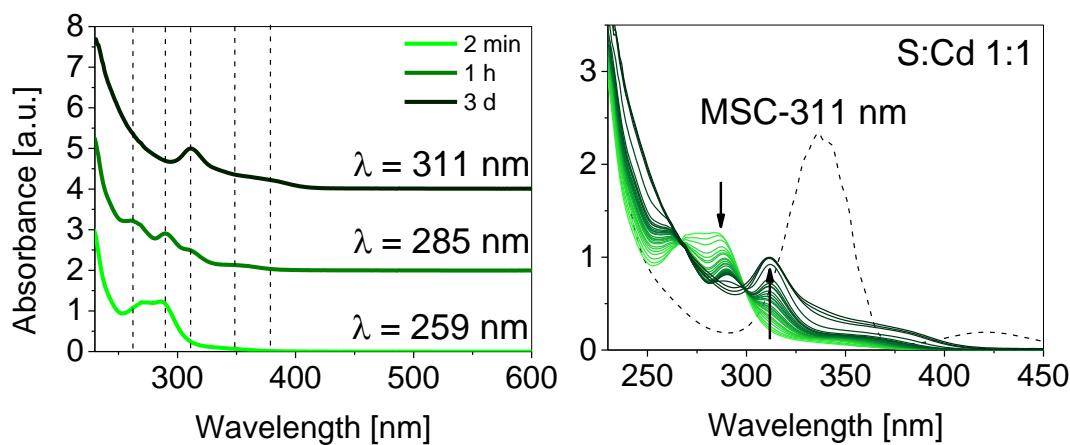


Figure 68: Absorption spectra of CdS nanoclusters demonstrating heterogeneous growth with discrete steps at 259 nm, 285 nm, 311 nm, 348 nm and 380 nm (left). The sulfur precursor (dashed line) decomposes after the injection of amine and cadmium oleate and induces the CdS cluster growth (right).

Typical characteristics of magic-sized nanoclusters include the heterogeneous growth mechanism, and the discrete red-shift of clusters towards the thermodynamically stable 311 nm-species accompanied by a simultaneous decrease of the peak around 285 nm (figure 68, right). The intensity

of MSC absorption shows a strong increase over time and the narrow Gaussian curve shows a FWHM of 17 nm after 3 days. The colloidal solutions remain clear and colorless after subsequent coalescence into larger clusters and show little change according to the absorbance spectra after one month in the reaction mixture due to the slow growth rate in the system (quasi-stationary situation).

The formation of QD requires strong complexers like amines (R-NH_2)^[43] or carboxylic end-groups^[67] to prevent the evolution of the CdS bulk material with a direct band gap of ~ 2.42 eV and exciton Bohr radius of ~ 3 nm.^[68] The addition of R-NH_2 leads to the decomposition of the sulfur precursor TOA_2S_2 and triggers the nucleation and cluster growth. The absence of strongly complexing amines leads to rising absorption bands around 380 nm and scattering in the low energy region of the absorbance spectra. Metal fatty acids and ammonium compounds are necessary to solubilize the Cd^{2+} and S^{2-} ions. Moreover, the additional ligands favor cluster formation and the long-term stability of smaller CdS clusters.

In the subsequent chapter, synthetic parameters were systematically studied to investigate their role during the quantum dot synthesis. General trends during the synthesis of clusters with local thermodynamic minima were monitored via UV-Vis spectroscopy, highlighting the impact of precursor ratio, injection order, nature of surfactants, growth temperature, solvent properties and reaction concentration.

Effect of Cd:S Ratio

Characteristic absorbance features were detected during the heterogeneous cluster evolution by varying the stoichiometric ratio of Cd and S. The variation of precursor should give a better insight, showing different sets of magic-sized clusters formed by fatty acid and amine ligands. Various amounts of metal oleate, reaching from S:Cd 1:0.5 to 1:2, were quickly injected into sulfide-rich organic solvents at room temperature. The energetically favored clusters are seen in figure. 69. The labels on the graphs refer to the initial ratio and the growth periods.

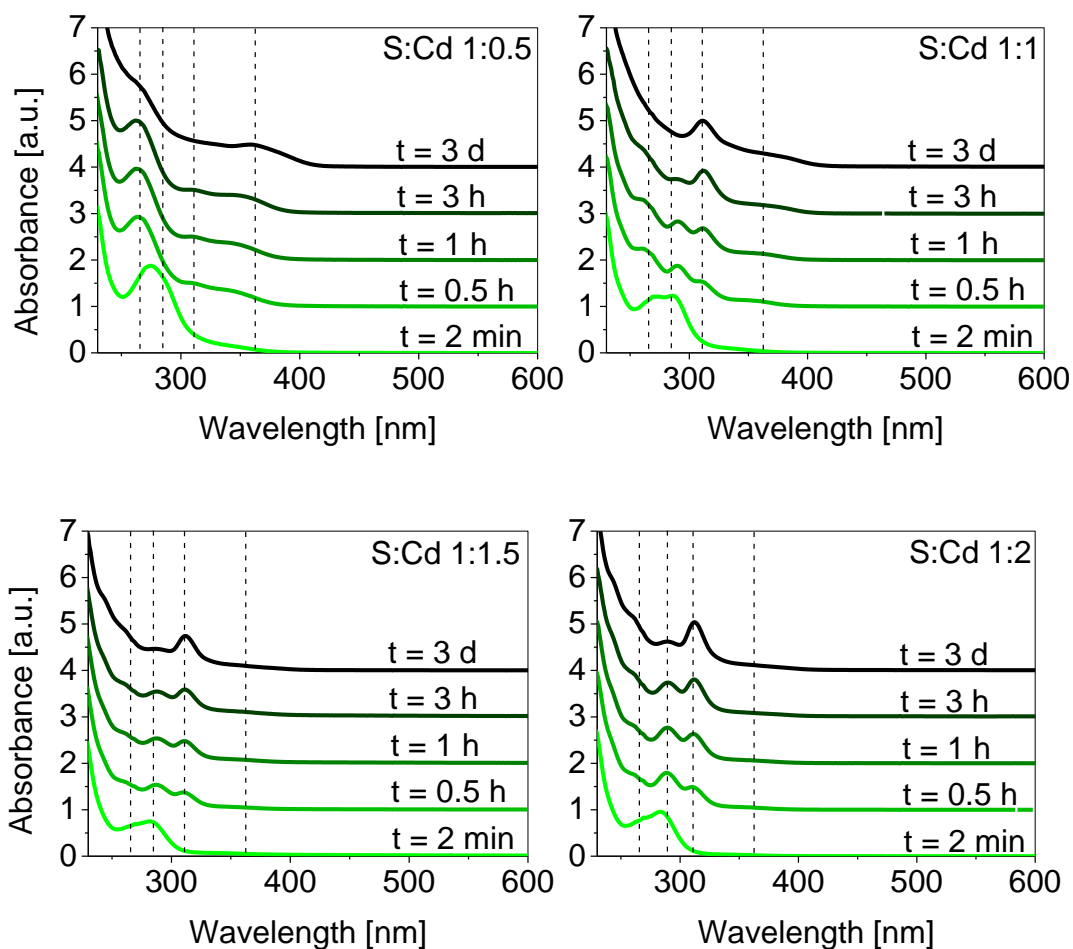


Figure 69: Synthesis of CdS clusters differing in their amounts of Cd(oleate)₂. The metal oleate was quickly injected into the sulfide-rich organic solvent at room temperature. Cd(oleate)₂ increases the yield of the 285 nm- and 311 nm-species, whereas a higher sulfur content favours larger CdS clusters.

During the growth process, cadmium oleate acts as a modulator of the cluster size.^{[36][37]} Starting with the ratio of S:Cd 1:2 leads to the absence of large 360 nm-absorbing clusters in a metal-rich environment. In the early growth stages, up to 1 h, the peak at 285 nm dominates the spectrum and decreases at the expense of the 311 nm-absorbing species within 3 days. Lowering the stoichiometric ratio of cadmium oleate triggers the formation of larger clusters around 360 nm. In general, after the injection of Cd(oleate)₂, the total number of ions remains unchanged, but the average number of clusters increases over time (3 d). The nanoclusters at 311 nm seem to be especially stable and show an extraordinary life-span.

There are three possibilities that could cause these distinct sets of magic-sized clusters. The exact number of Cd and S ions, which form energetically favored clusters sizes.^[36] Another possibility is that the energy of the band gap is dependent on the ligand system.^{[31][69]} For our designed synthetic approach, cadmium and sulfur ions are coupled with stabilizing agents and we cannot clearly distinguish what causes these distinct sets of magic-sized clusters. Both fatty acids and amines bind strongly to the metal ions and their influence was further investigated by using additional amine and carboxylic ligands.

Transmission Electron Microscopy

For large nanoparticle sizes, Transmission Electron Microscopy (TEM) provides accurate information about the morphology and size. However, for smaller particles the limited resolution and the poor electron scattering contrast makes the determination more difficult. The CdS MSC are quite stable, as confirmed by monitoring the UV-Vis spectra. The TEM samples were prepared under ambient conditions via drop-casting of the CdS dispersion. CdS nanoclusters with the corresponding ratio of S: Cd 1:2 show the strong pronounced absorption peak around 311 nm. The corresponding TEM images show clearly that spherical particles are formed which are uniform in size 1.6 ± 0.3 nm.

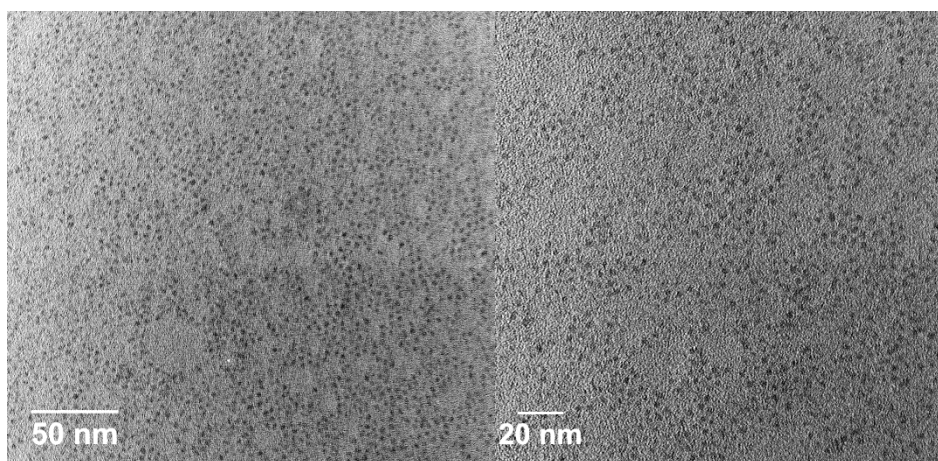


Figure 70: TEM images of 1.6 nm CdS nanoclusters synthesized in cyclohexane (ratio S: Cd 1:2). The standard deviation could be calculated to 0.3 nm.

The synthetic method thus allows one to obtain very small sized CdS clusters with a high monodispersity (figure 70). We found that the cluster size in the TEM images correlated very well with that reported in the literature^{[21][22][36][66][70]} and additionally confirms that the absorbance peaks $\lambda \leq 320$ nm arise from cluster radii smaller than 1 nm.

To verify the size of small CdS nanoclusters, the following equation is used which shows size-dependency of the optical absorption coefficient.^[22]

$$D = (-6.6521 \cdot 10^{-8})\lambda^3 + (1.9557 \cdot 10^{-4})\lambda^2 - (9.2352 \cdot 10^{-2})\lambda + (13.29) \quad (6.1)$$

The size calculation in the quantum confinement size regime is independent of the capping ligands, the temperature and the refractive index of the solvent and match the results of the TEM measurements very well.

Table 14: Structural information for CdS clusters including the calculated diameter D of the given nanocrystal sample with respect to the wavelength λ of the first excitonic absorption peak in the UV-Vis spectrum.

λ [nm]	D ^a [nm]	D ^b [nm]	D ^c [nm]
285	1.3		
311	1.5	1.6 ± 0.3	
325	1.6		1.7 ± 0.4
360	2.3		4.0 ± 0.7

^a Diameter D determined according the empirical fitting functions from Peng et al.^[22]

^b Sizes determined from TEM images of sample S: Cd 1:2

^c Sizes determined from TEM images of sample Cd: S 1:0.5

The experimental determination of the extinction coefficient of the first excitonic absorption peak λ of CdS semiconductor nanocrystals leads to diameter D which shows a good agreement with our TEM results (table 14).

The CdS nanoclusters with ratio Cd:S 1:0.5 show, in contrast to a strong and dominating 311 nm-absorbing species, broad absorbance signals around 325 nm and 360 nm. According to the TEM measurements, these absorptions correspond to two detectable cluster size fractions with diameters of 1.7 ± 0.4 nm and 4.2 ± 0.7 nm respectively.

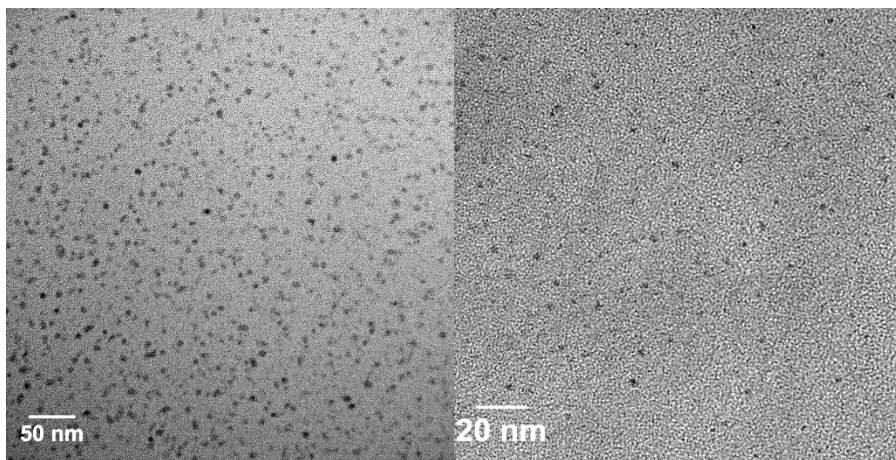


Figure 71: TEM image of CdS clusters synthesized with ratio Cd:S 1:0.5 in cyclohexane. The corresponding diameter of 4.0 ± 0.7 nm and 1.7 ± 0.4 nm could be detected.

By applying the empirical formula above, the absolute value for a given sized CdS cluster excitonic absorption peak at 325 nm and 360 nm were found to be 1.6 nm and 2.3 nm. In general, the optical absorption shows strong blue-shifts from the onset, indicating the strong quantum confinement effects. The observed nanostructures were slightly larger than the proposed cluster model according Peng.^[22] The experimental errors of the measurement should mainly come from the determination by TEM. Direct imaging of colloidal CdS clusters in this size region are close to the TEM detection limit, hence errors are included. Additionally, the experimental spectra are a sum of various crystallite sizes^[9], therefore a broadened absorption edge complicates the comparison with the empirical models.

Effect of Injection Order

The variation of precursor ratio and the injection order could give better insight into the CdS cluster formation. Various amounts of sulfur precursor, ratios from Cd:S 1:0.5 to 1:2, were quickly injected

into the metal-rich organic solvent at room temperature in the presence of amines. The structural evolution of energetically favored clusters is illustrated in selected absorption spectra (figure 72). The labels on the graphs refer to the initial ratio and the growth periods.

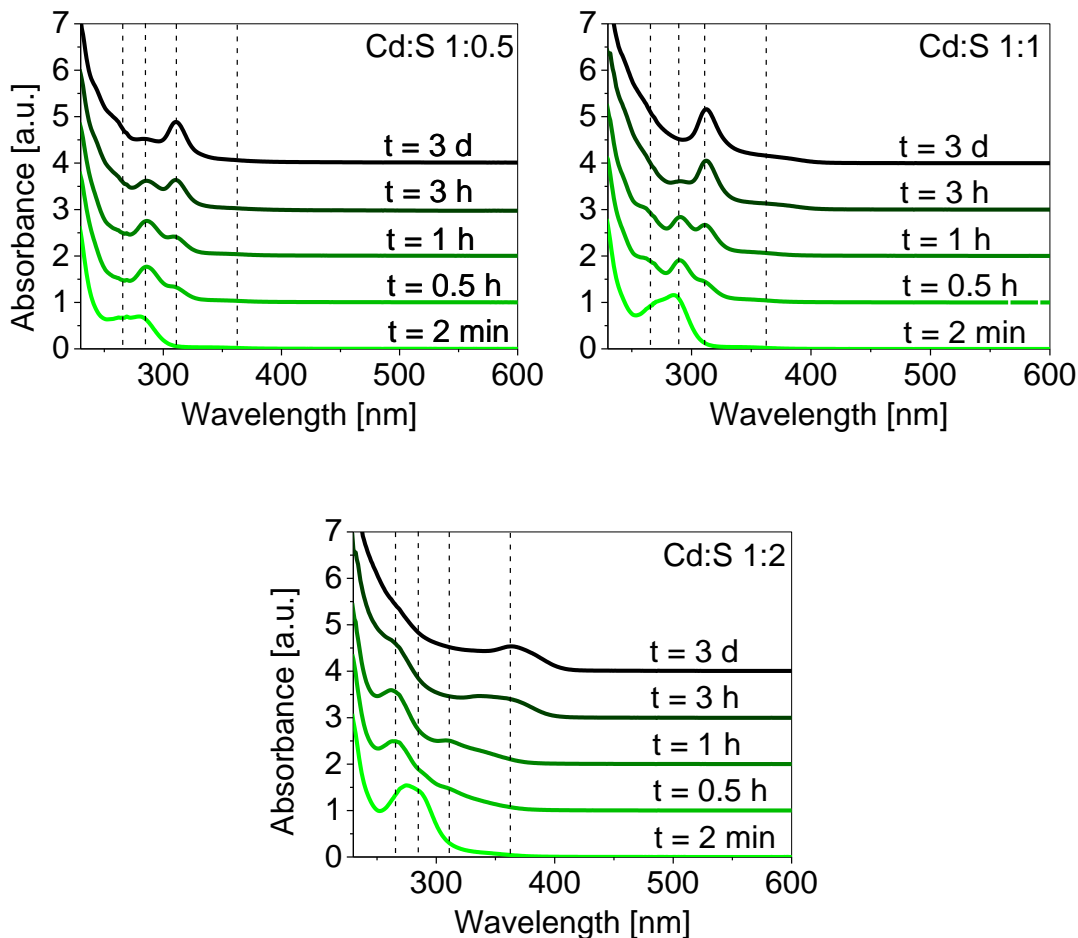


Figure 72: Synthesis of CdS clusters differing in the initial ratio of sulfide precursor. The sulfur precursor was quickly injected into the metal-rich organic solvent at room temperature. Cd(oleate)₂ increases the yield of the 285 nm- and 311 nm-species, whereas a higher sulfur content favours larger CdS clusters.

The concentration of the metal complexes, consisting of amine and oleic acid, was held constant. The results clearly demonstrate that the injection order has no influence on the magic-sized clusters. The set of magic-sized cluster reaches its equilibrium after 3 d and show quasi-stationary absorbance features. The excess of Cd(oleate)₂ favors 285 nm and 311 nm clusters. After exceeding the stoichiometric ratio of 1:1, a higher sulfur content favors selectively higher cluster species. Both

the chemical bond between S^{2-} and ammonium ions, as well as the amine-metal bonding is strong. The incorporation of foreign atoms into each system influences the evolution of the cluster growth and the cluster size can be adjusted by the relative concentration of the precursor.

Effect of Amine

Amines and oleic acid are well-known as coordinating agents for nanocrystal systems. In a first approach, the necessity and influence of *n*-octylamine $R-NH_2$ was studied by varying their concentration. The reaction was monitored by UV-Vis spectroscopy. The absence of *n*-octylamine leads to a slow conversion of the sulfur precursor and an uncontrolled formation of large nanostructures absorbing around 370 nm after 3 days (figure 73). The significant cluster peaks at 285 nm and 311 nm could not be detected.

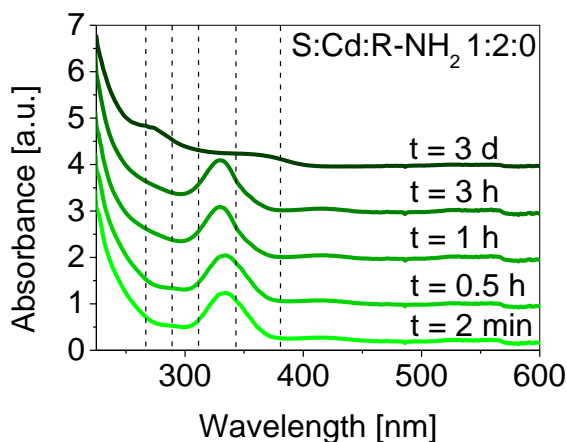


Figure 73: Synthesis of CdS nanostructures with the initial ratio of S:Cd:R-NH₂ 1:2:0. The metal oleate was quickly injected into the sulfur-rich organic solvent at room temperature. The 285 nm- and 311 nm-MSCs were not formed without the coordinating agents R-NH₂.

Similar results were obtained for the CdS synthesis as the amine concentration slightly increases. From the spectra in figure 74, the presence of amines lead to the fast decomposition of the sulfur precursor ($\lambda=279$ nm) and weak signals around 285 nm and 311 nm can be detected during the slow CdS formation. The absorbance maximum shifts with the ratios S:Cd:R-NH₂ 1:2:14 and 1:2:28 towards higher wavelength, with dominant peaks around 330 nm and 360 nm after 3 days. We

suggest that the influence of the concentration of amine on CdS nanostructures is dramatic and the MSCs clusters cannot be formed in absence of strong coordinating agents.

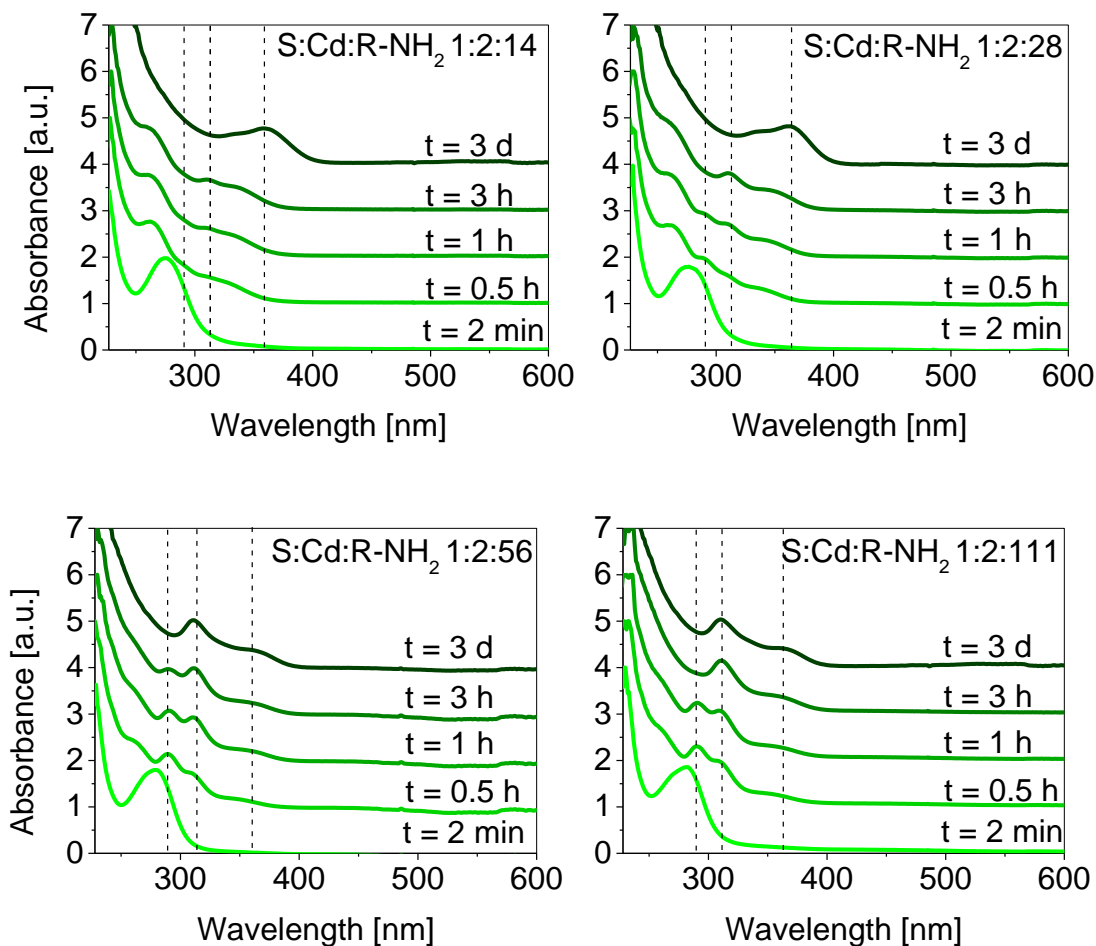


Figure 74: Synthesis of CdS nanostructures with the initial ratio of sulfide and Cd(oleate)₂ precursor of 1:2. The metal oleate was quickly injected into the sulfur-rich organic solvent at room temperature. Various amine amounts demonstrate the necessity of the coordinating agent R-NH₂.

After further increase of the amine concentration R-NH₂ it is safe to conclude that the resulting nanoclusters around 285 nm and 311 nm were formed with an excess of amines. In contrast to S:Cd:R-NH₂ 1:2:14 and 1:2:28, sharp peaks at 285 nm and 311 nm become dominant during the formation process (S:Cd:R-NH₂ 1:2:56 and 1:2:111) and are stable up to a few months in the dark.

Amines are activating agents, leading to the decomposition of the sulfur precursor, and play a second role as strong coordinating ligands for metals. Initially, tiny molecular clusters are formed and grow into stable clusters which are trapped thermodynamically. Due to the reduction of the activation barrier^[43], the CdS cluster undergoes a step-wise growth and the final spectrum is dominated by the 311 nm-species after 3 days. Magic-sized clusters cannot be formed in the pure reaction mixture, consisting of sulfur precursor and cadmium oleate. Both 'ionic monomers' are not able to stabilize the clusters sufficiently. Apparently, the formation of MSC needs an appropriate amount of amines to promote the synthesis and to stabilize the cluster sizes. The strong metal-amine complex prevents further growth into regular quantum dots.

Effect of Oleic Acid

In this study, we investigated the presence of further additives such as oleic acid. The structure of MSC was found to be dependent on the choice of ligand and high-quality carboxylate-capped nanostructures, as reported in the literature.^{[44][53][71]} The reaction in the absence of amines but in the presence of pure oleic acid results in an uncontrolled growth of larger nanostructures. Therefore, a minimum amount of *n*-octylamine was necessary to stabilize the desired cluster sizes. By operating at room temperature, identical reaction conditions were chosen and the concentration of oleic acid R-COOH was varied. The cluster formation in cyclohexane is depicted in the following UV-Vis spectra (figure 75).

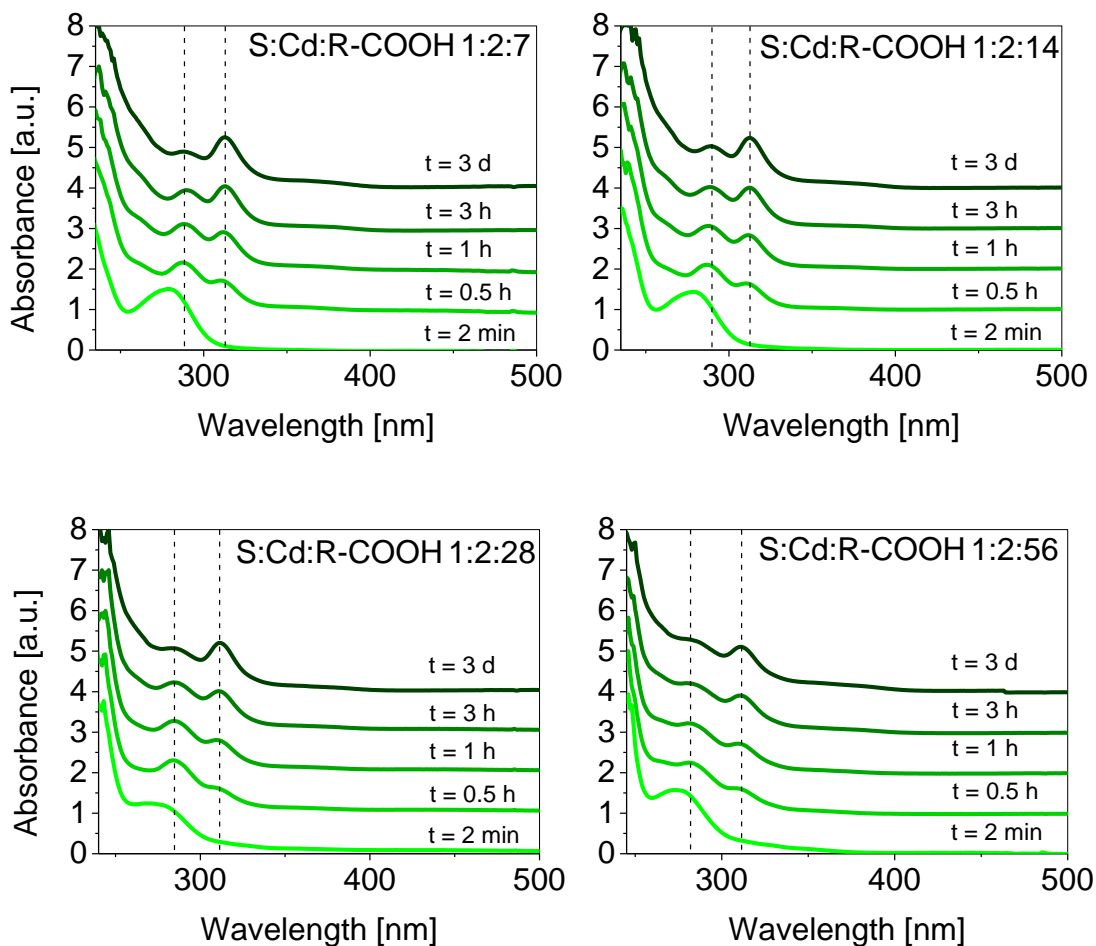


Figure 75: Synthesis of CdS nanostructures with the initial ratio of sulfide and Cd(oleate)₂ precursor of 1:2. The metal oleate was quickly injected into the sulfur-rich organic solvent at room temperature. Various amounts of oleic acid demonstrate the influence of the coordinating agent R-COOH.

In comparison to the effect of *n*-octylamine, the influence of oleic acid is not as obvious. Therefore, an overview of the various oleic acid ratios after 3 days is given in figure 76. With a low oleic acid amount (S:Cd:R-COOH 1:2:7), the 311 nm-absorbing species dominates the spectrum after 3 days. Similar results were obtained for S:Cd:R-COOH 1:2:14 and 1:2:28 ratios. As the concentration of oleic acid in cyclohexane increases (from S:Cd:R-COOH 1:2:14, to 1:2:28 to 1:2:56), the formation of smaller nanoclusters at 285 nm is more favored. The ratio S:Cd:R-COOH 1:2:56 differs from the other results, because the relative absorption intensity of the excitonic peak (285 nm to 311 nm) has changed. The dynamic equilibrium favors the 285 nm-peak absorbance signal. Additionally,

the formation of larger clusters is suppressed, which is also attributed to the large excess of fatty acids.

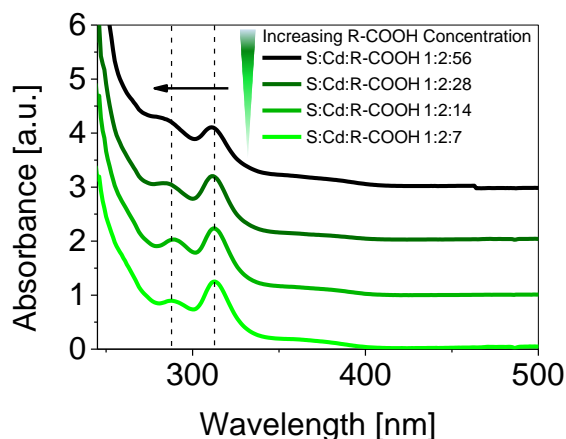


Figure 76: Synthesis of CdS nanostructures with the initial ratio of sulfide and Cd(oleate)₂ precursor of 1:2. The metal oleate was quickly injected into the sulfur-rich organic solvent at room temperature. In presence of oleic acid the equilibrium between 285 nm and 311 nm MSCs could be influenced towards the formation of the smaller species.

Oleic acid together with amines lead to the protonation of *n*-octylamine and acid-base complexes (C₁₇H₃₃COO⁻:C₈H₁₇NH₃⁺).^[71] The deprotonation of oleic acid leads to an enhanced electron-donating ability and guarantees a preferential binding with cadmium ions and the generated alkylammonium ion stabilizes the sulfur ions.^[60] The result of the study shows that the additional stabilizing agents are in competition with the CdS cluster formation and smaller clusters around 285 nm are thermodynamically favored.

The control over cluster peak position and thermodynamically favoured cluster size arises from amines. The surface chemistry plays a critical role in the stability of MSCs. Amines^[43] and carboxylic acids are strongly coordinating capping agents and stabilize cadmium effectively. Steric and electronic effects are the explanation. Amines are electron rich and polarizable complementing the soft Lewis acidic cadmium ions. The long hydrocarbon tail provides steric repulsion and maintains the solubility in organic solvents.

Effect of Temperature

The temperature dependence of CdS nanocluster formation was studied under a variety of conditions. Optical spectra were taken of a series of CdS magic-sized clusters synthesized with ratio S: Cd 1:2 and in the temperature ranges from $T=10\text{ }^{\circ}\text{C}$ to $40\text{ }^{\circ}\text{C}$. The range is restricted because of the solvent properties (boiling point) and the solubility of the precursor. Metal oleate and the sulfur precursor were dissolved in cyclohexane in the presence of *n*-octylamine and set to the desired temperature. The structural evolution was detected and selected absorption features are shown after $t=30\text{ min}$, 3 h , 24 h , and 72 h .

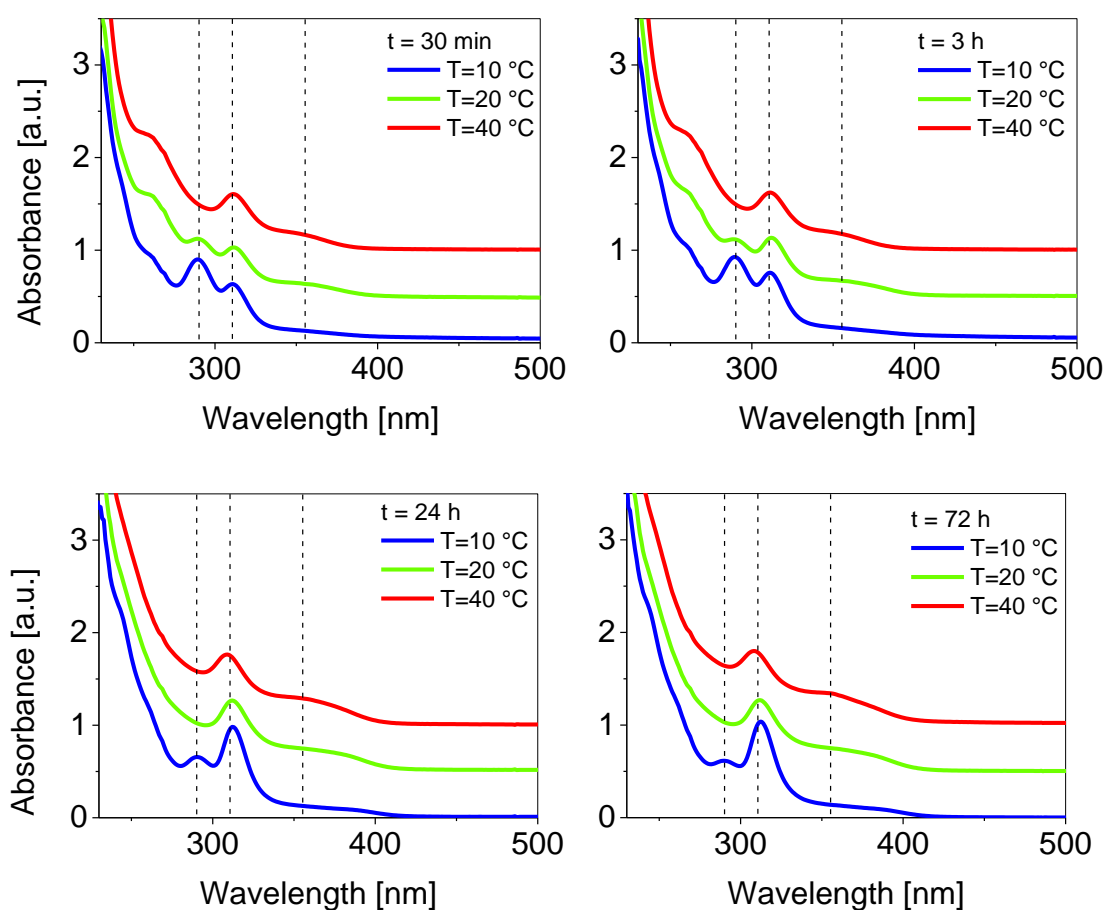


Figure 77: Synthesis of CdS clusters with fix initial ratio of sulfide precursor and $\text{Cd}(\text{oleate})_2$ of 1:2 at three different temperatures ($T=10\text{ }^{\circ}\text{C}$, $20\text{ }^{\circ}\text{C}$ and $40\text{ }^{\circ}\text{C}$). The metal oleate was quickly injected into the sulfide-rich organic solvent. Lower temperatures favour the yield of the 285 nm- and 311 nm-species, whereas a higher temperatures favour the growth of regular CdS QD $\geq 350\text{ nm}$.

The structural evolution differs for all three temperatures. At lower temperature $T=10\text{ }^{\circ}\text{C}$, the 285 nm peak dominates over all the other peaks after 30 min. With proceeding reaction time, a red-shift occurs due to the ongoing monomer conversion and the system shows stable 311 nm-cluster peaks after 3 days. The formation of regular quantum dots was largely suppressed.

With increasing temperature, the 311 nm-clusters are more favored. At a temperature of $T=40\text{ }^{\circ}\text{C}$, the 285 nm was not detectable during the CdS formation, but an increasing signal around 350 nm was monitored. The exceedingly fast conversion generates larger CdS clusters. With proceeding reaction time, the relative intensity of the fraction increases due to the ongoing monomer conversion. The higher the temperature, the more pronounced are the cluster peaks and absorption signals at higher wavelength. The temperature affects the set of magic-sized clusters. The temperature has an influence on the solubility of the precursor, the monomer diffusion towards the CdS particle surface, as well as the surface reaction and the intramolecular rearrangement of the system.^[41] We suggest a two-step nucleation process with 285 nm and 311 nm species where the heterogeneous growth process with discrete absorbance peaks is more pronounced at lower temperatures. It is well-known that classical nucleation cannot account for the formation process which occurs via stable nanoclusters with distinct structures and at high supersaturation.^{[38][72]} The conversion to larger detectable clusters occurs on time-scales which are practicable for further kinetic analysis. The temperature- and time-dependent change of the absorption peak 285 nm and 311 nm provides more information about the cluster development (figure 78).

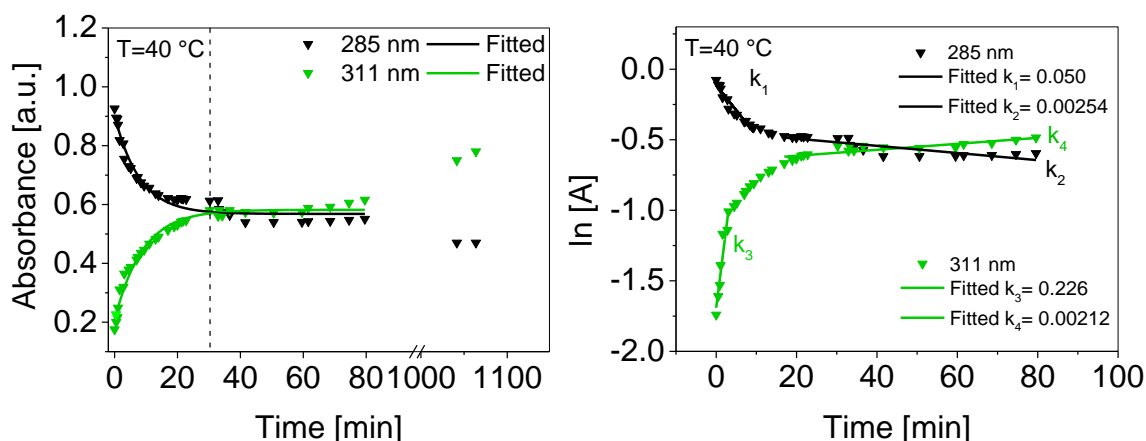


Figure 78: Kinetic data demonstrate the absorbance at 311 nm and 285 nm as a function of time during the CdS clusters synthesis with sulfide precursor and $\text{Cd}(\text{oleate})_2$ ratio of 1:2 at $T=40\text{ }^{\circ}\text{C}$ (left). Semi-logarithmic plots were used for the calculation of the rate constants $k_1=0.050\text{ min}^{-1}$, $k_2=0.00254\text{ min}^{-1}$, $k_3=0.226\text{ min}^{-1}$ and $k_4=0.00212\text{ min}^{-1}$ (right).

We can distinguish between two regions. The first region shows the noticeable increase of the 311 nm-species and the absorbance at 285 nm decreasing in the same time window. The 285 nm clusters act in such conditions as nuclei for the larger magic-sized clusters (heterogeneous growth). The second region is characterized by a slower increase in the absorbance of the 311 nm signal at the expense of the 285 nm-species.

It should be pointed out, that each kinetic curve of the corresponding reaction contains two exponential components in a semi-logarithmic coordinate system which supports our assumption of a more complex reaction (figure 78, right). The two regions can be approximated by straight lines with slopes of $k_1=0.050 \text{ min}^{-1}$, $k_2=0.00254 \text{ min}^{-1}$, $k_3=0.226 \text{ min}^{-1}$ and $k_4=0.00212 \text{ min}^{-1}$. It is a difficult task to ascertain the mechanism of the reaction that proceeds (etc. two parallel reactions, sequential reactions, competitive reactions or a two-component heterogeneous model).^[73]

For the 285 nm-species, the asymptotes of these curves show that $k_1 \gg k_2$ with proceeding reaction time ($t \gg 0$). Therefore, the second exponential term $\exp(-k_2t)$ becomes negligible in comparison to $\exp(-k_1t)$ ($t \geq 0$). For simplification and to display and compare the reaction rate, the development of the 285 nm peak is exponential fitted by the pseudo-first order reaction equation 6.2. The solid lines in figure 78 are fitted to

$$[A]_t = A_1 \exp(-k_1 t) \quad (6.2)$$

where $[A]_t$ is the absorbance detected at time t , k_1 is the first order rate constant and t the reaction time. Taking the logarithm leads to

$$\ln[A]_t = \ln[A]_1 - k_1 t \quad (6.3)$$

where the concentration of the 285 nm-species at time 0, described by the ordinate axis intercept $\ln[A]_1$ with corresponding rate constant k_1 .

The 311 nm-absorbing species follows the same behaviour with $k_3 \gg k_4$. This fact is very important and indicates the transformation of the 285 nm cluster into highly stable MSC intermediates at $t \geq 0$. It allows the assertion of a heterogeneous cluster growth mechanism for the reaction which includes a multi-step nucleation process for semiconductor CdS clusters. The fitted curves describe the main development of the cluster peaks at 285 nm obeying a first order kinetic model with rate constant k of 0.127 min^{-1} and the 311 nm rate constant k of 0.113 min^{-1} . The fitted curves for all temperatures according to equation 6.2 are shown in figure 79 and describe model curves for the

cluster transformation. The temperature-dependent cluster growth, with the colours corresponding to those of the experimental data, show times up to only 150 min.

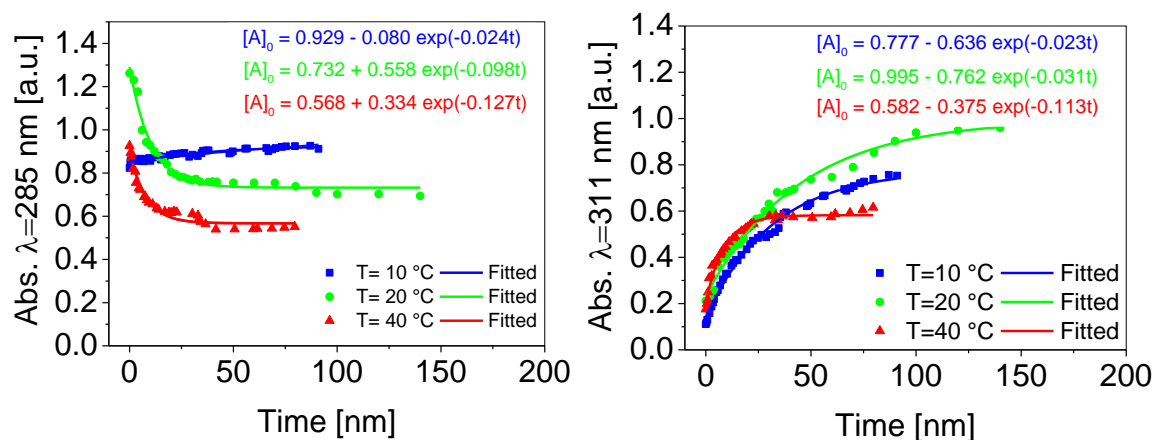


Figure 79: Kinetic plots demonstrate the absorbance at 311 nm and 285 nm as a function of time during the CdS cluster synthesis at three different temperatures ($T=10$ °C, 20 °C and 40 °C).

The main development of the cluster peaks at 285 nm shows an increase in the rate constant k from 0.024 min^{-1} , to 0.098 min^{-1} and to 0.127 min^{-1} with temperature. Similar results were obtained for the magic-size cluster peak at 311 nm. The rate constant k increases from 0.023 min^{-1} , to 0.031 min^{-1} and to 0.113 min^{-1} with increasing temperature. At three different temperatures, the 311 nm-species grows at the expense of the 285 nm-species and the reaction is accelerated at higher temperatures and obeys Arrhenius kinetics.^[38] However, the formation and the reaction rate of larger clusters is not considered. The crossing points of the 285 nm and the 311 nm fitted lines are observed at times longer than 33 min for $T=40$ °C, 47 min for $T=20$ °C, and > 28 h for $T=10$ °C.

Effect of Precursor Concentration

The special stability of the MSCs can be studied by changing the concentration of the CdS reaction mixture. Yu et al.^[39] has predicted that the degree of supersaturation can influence the formation and the final size of the metal-based clusters. To confirm this assumption, we investigated the growth kinetics of CdS MSCs at four different precursor concentrations (0.18 mM, 0.25 mM,

0.35 mM and 0.75 mM). The absorption spectra were monitored and selected absorption features are shown after $t=30$ min, 1 h, 3 h, and 3 d (figure 80).

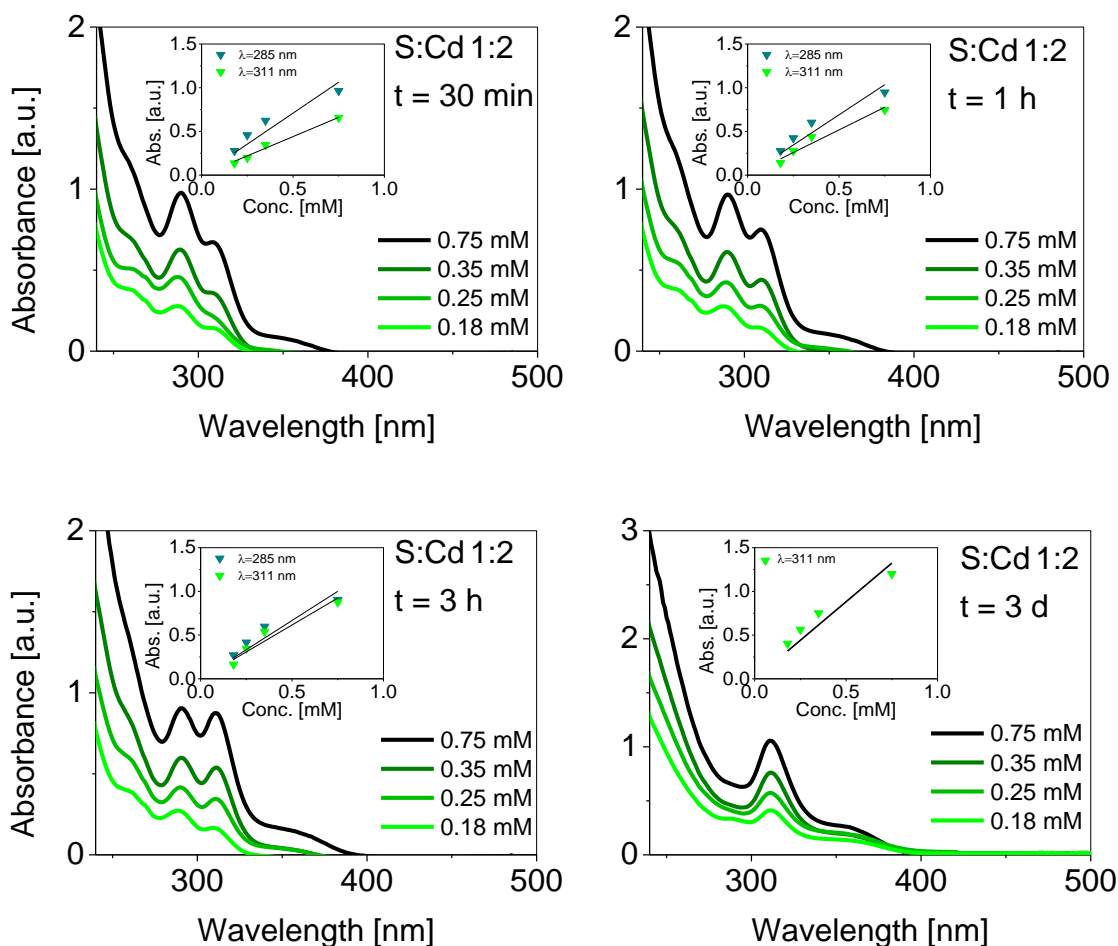


Figure 80: Synthesis of CdS clusters with fixed initial ratio of sulfide precursor and $\text{Cd}(\text{oleate})_2$ 1:2 and four different precursor concentrations at room temperature. The metal oleate was quickly injected into the sulfide-rich organic solvent and the absorbance values are proportional to the precursor concentration during the synthesis (Inset).

Spectroscopic monitoring suggest that the final MSC size does not correlate with the absolute monomer concentration. The variation of precursor concentration under such identical reaction conditions shows similar growth behavior and the peak positions remain constant while the intensity increases. The 285 nm-species dominates the synthesis within the first hour of cluster growth and shows a red-shift in the following hours, resulting in stable CdS MSC samples. The

absolute increase of the cluster population is proportional to the precursor concentration and shows a strong linear correlation. The relative concentration of MSC family's increases as the precursor concentration is raised from 0.18 mM to 0.25 mM to 0.35 mM and to 0.75 mM.

The concentration effect in the system was found to be negligible and the cluster size is sufficiently stabilized by the present ligands. In order to understand the formation of CdS, the time-dependent absorbance at 285 nm and 311 nm was studied (figure 81).

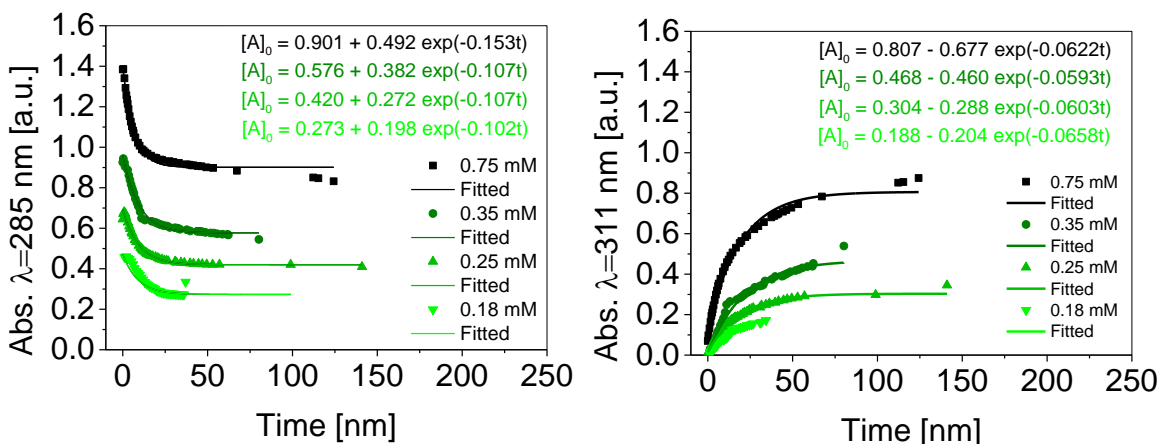


Figure 81: Kinetic data from the growth of 285 nm and 311 nm CdS cluster of different concentrations. The time-dependent absorbance was detected at four different concentrations of 0.18 mM, 0.25 mM, 0.35 mM and 0.75 mM.

The experimental results could be well fitted with the chemical kinetic equation 6.2. Rate constants can be obtained by assuming pseudo-first order reaction conditions and the reproducible studies represent similar values for the 285 nm-species reaching from 0.102 min^{-1} to 0.153 min^{-1} . The fitted lines for the absorption peak at 311 nm show rate constants k from 0.0593 min^{-1} to 0.0658 min^{-1} . Deviations can be explained due to the pseudo-first order approximation. Furthermore, the formation of higher CdS nanostructures could not be completely suppressed and has not been taken into account for the study. The kinetic analysis show that the rate constants are only affected by the temperature and not by the concentration.

Effect of Solvent Polarity

With increasing solvent polarity, from octadecene (ODE), cyclohexane (CH), chloroform (CHCl_3) to ethanol (EtOH), the absorption features show a red-shift of the band-edge absorption of stabilized CdS nanoclusters towards higher wavelength.^{[11][66]} The growth kinetics were investigated systematically and show the generation, life-span and consumption of MSCs. Figure 82 shows the temporal evolution of UV-Vis absorption spectra for the synthesis in different solvents.

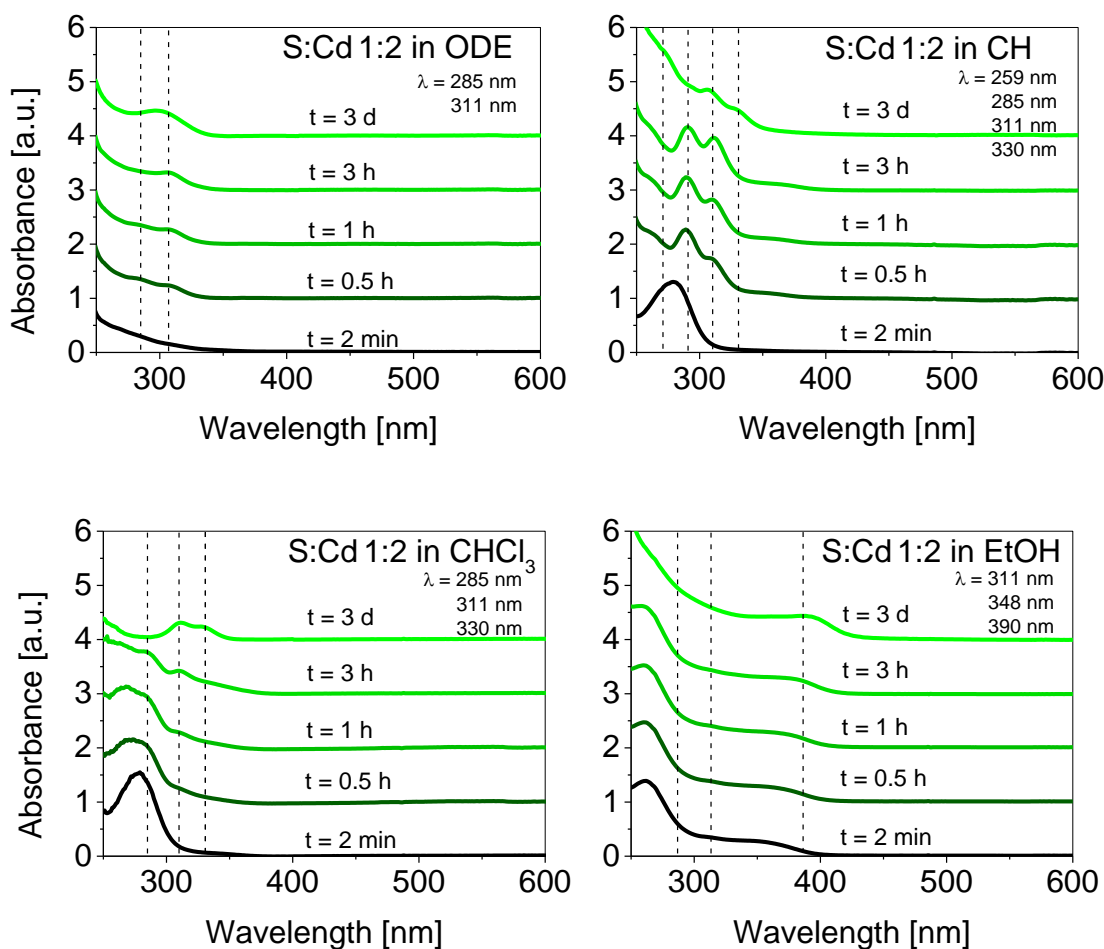


Figure 82: Synthesis of CdS clusters with fixed initial ratio of sulfide precursor and $\text{Cd}(\text{oleate})_2$ of 1:2 in solvents of different polarity. The metal oleate was quickly injected into the sulfide-rich organic solvent and the temporal evolution monitored by UV-Vis spectra.

The cluster development as function of the reaction time indicates that the solvent polarity and viscosity affects the set of CdS clusters. The high viscosity of the non-polar solvent ODE prevents the growth of larger CdS clusters and regular QD.^[11] We can observe the transformation of the 285 nm- and 311 nm-absorbing species into a single broad absorbance peak with maximum at 298 nm (figure 83). The CdS clusters were formed in a quite broad temperature range up to $T=200\text{ }^{\circ}\text{C}$ in this specific reaction system. The excess of ligands helped to maintain colloidal stability of nanoclusters due to the strong stabilization in ODE during heating. We carried out some measurements and found that they show the identical peak position but the precursor conversion increases at higher temperature.

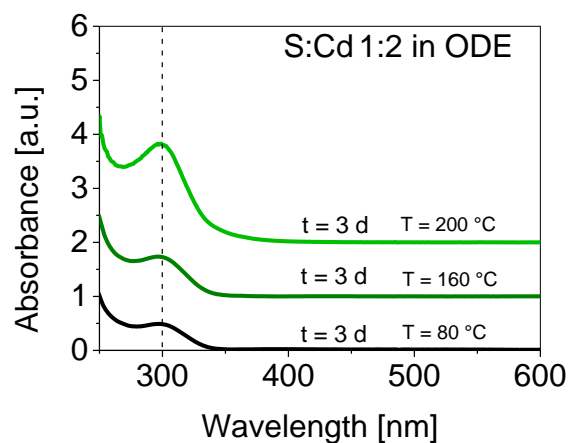


Figure 83: Absorbance spectra of CdS nanoclusters formed in octadecene ODE. A considerable amount of stabilizing ligands helped to maintain the colloid stability of clusters at higher temperatures.

As aforementioned, the maximum concentration of the 311 nm-species was found in the low polarity solvent CH (polarity index, PI: 0.2, 0.001 Pa·s).^[74] From the absorbance spectra shown in figure 82, an aging time of 3 days results in the absence of the 285 nm-species and yielded a small fraction of 330 nm clusters. The life-span of the MSCs is longer than a few months indicating a slow growth process (quasi-stationary).

As the polarity increases, the life-span of 311 nm MSC in the reaction solution is shortened, for instance in chloroform (PI: 4.1, 0.00057 Pa·s)^[74]. The higher polarity solvent favours two cluster sizes with isosbestic points at around 311 nm and 330 nm. The relative intensity of the 330 nm nanoclusters formed in CHCl_3 was found to be higher than those generated in cyclohexane.

Ethanol (PI: 5.2, 0.0012 Pa·s)^[74] with highest solvent polarity in this experiment favours the formation of larger clusters at around 348 nm and 390 nm. The life-span of the 311 nm species is drastically shortened with increasing solvent polarity. The magic-sized clusters exist in EtOH over 30 min, but the 285 nm-species could not be detected.

The series of UV-Vis data shows that the peak at 311 nm occurs in all solvents, however the life-span drastically decreases in high polarity solvents to yield larger particles. The results could be tentatively explained by the fact that the ligand solubility shows a strong dependency on the polarity of the solvent. The reactivity of the monomeric precursor is faster in highly polar solvents due to the increased ligand solubility in the system. It is also reasonable to assume that structural rearrangement results in the formation of larger clusters. The temporal evolution of the UV-vis measurements and the interpretation above verified these assumptions.

Purification and Stability of MSC

The nanoclusters were purified with an extraction method, based on the fact that the solubilities of the unreacted cadmium and sulfur precursor used in the synthesis and the resulting magic-sized clusters were significantly different in a two-phase system of methanol and cyclohexane. It was critical to remove any unreacted precursor in the CdS samples because we demonstrated above, that chemical treatments affect the CdS nanocluster system.

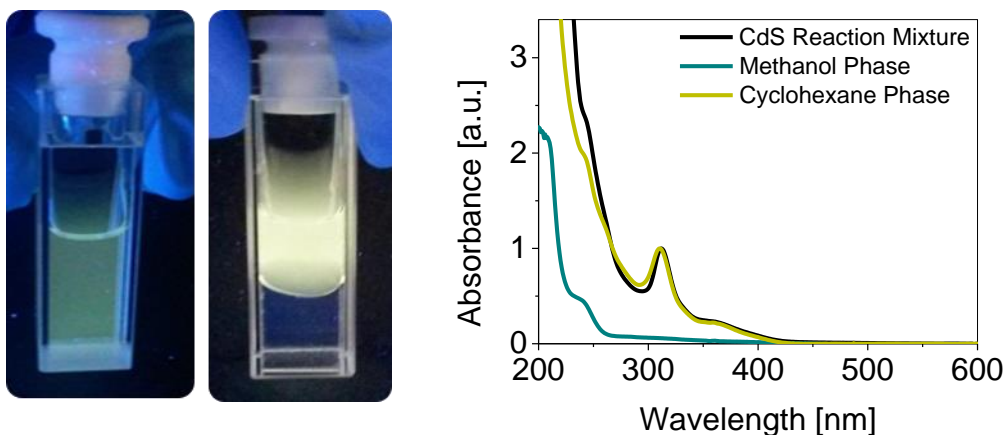


Figure 84: CdS MSCs in cyclohexane show the characteristic yellow fluorescence under the UV lamp ($\lambda=365$ nm) (left) before and after the extraction with methanol in a two-phase system.

In a typical purification step, a solution of CdS magic-sized clusters was gently covered with methanol. Evidently in the photograph above, the two-phase system allows the phase-transfer of the cadmium and sulfur precursor. Both precursors are very soluble in the methanol phase and barely soluble in cyclohexane at room temperature, therefore they tend to go into the methanol phase. The MSC were insoluble in methanol and stayed in the cyclohexane phase. The efficiency and completion of the separation was monitored by UV-vis absorption (figure 84).

Emission of CdS Nanoclusters

The UV-Vis signals of CdS clusters can be detected in the size-quantization regime as illustrated and discussed above. The distinguishable absorption peaks at 285 nm and 311 nm were repeatedly observed in the organic reaction medium (figure 85). During the course of studies, the corresponding emission spectra of the room-temperature synthesized CdS nanoclusters and the yellow fluorescence under the UV lamp ($\lambda_{\text{exc}}=365$ nm) were obtained.

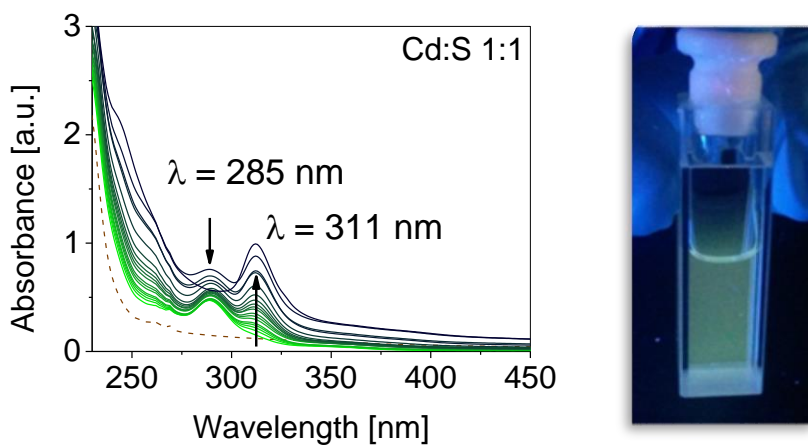


Figure 85: Time evolution of the absorbance spectra of CdS clusters for the sample containing the ratio Cd:S of 1:1 at T=20 °C. The sulfur precursor was quickly injected into the metal-rich organic solvent at room temperature. The yellow fluorescence is clearly visible under the UV lamp ($\lambda=365$ nm) after 1 day (right).

Observations relating size effects on the fluorescence efficiency are detected depicted below.

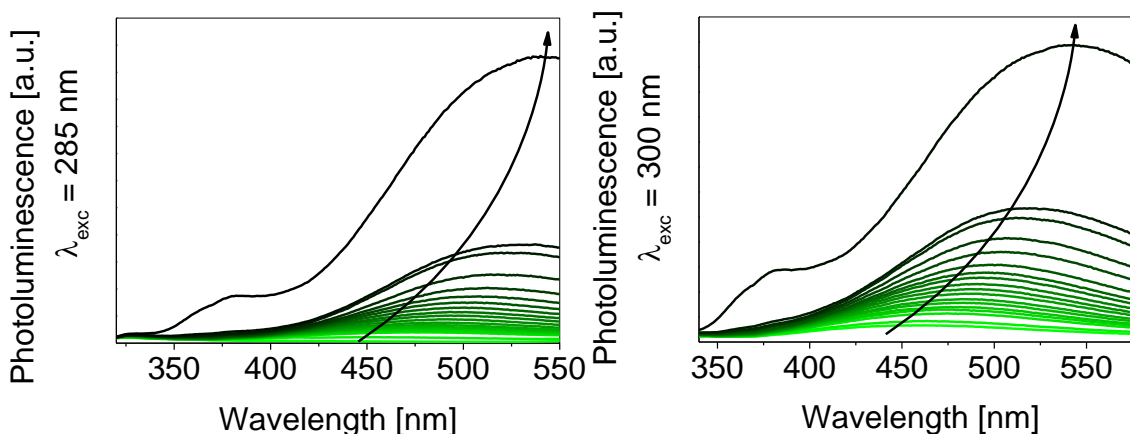


Figure 86: Time evolution of the corresponding fluorescence spectra of CdS clusters ($\lambda_{\text{exc}}=285$ nm and 300 nm) for the sample containing the ratio of Cd:S 1:1 at T=20 °C.

The evolution of absorption and fluorescence spectra as a function of the reaction time (3 d) shows that the concentration of the 285 nm CdS clusters decreases as the 311 nm-species increases. Two emission bands can be detected, a strongly red-shifting emission with maximum from 453 nm to 542 nm, and a side peak at 383 nm. Fluorescence emission and excitation spectra of the corresponding samples were taken after 3 days (figure 87). The excitation spectrum shows which wavelengths absorb to give rise to emission and the corresponding emission spectrum shows the photoluminescence arising from the sample. The fluorescence excitation spectrum shows weak but pronounced signals around 285 nm and 311 nm and strong signals arising from a CdS species at 417 nm. The CdS clusters whose absorption band lies in the higher energetic region do not fluoresce efficiently in contrast to the clusters within the lower energy range. Therefore, we assume that the weak absorbance at wavelength 360 nm and higher are responsible for the strong emission signal centered around 541 nm.

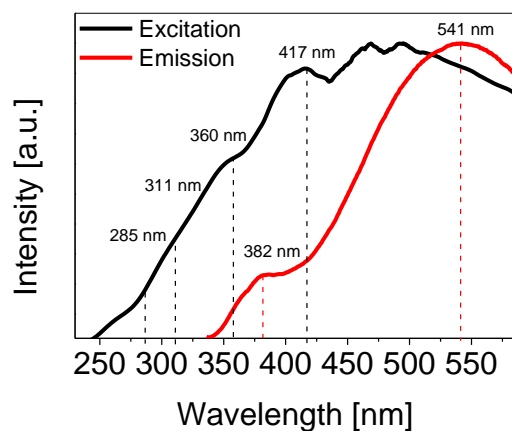


Figure 87: Emission and excitation spectra of CdS clusters at room temperature. The excitation was performed at 285 nm for the sample containing the ratio Cd:S of 1:1. The sulfur precursor was quickly injected into the metal-rich organic solvent at room temperature.

Concomitantly, the continuously red-shifting absorption and emission could be observed after increasing the sulfide content resulting in the size increase of CdS clusters (figure 88).

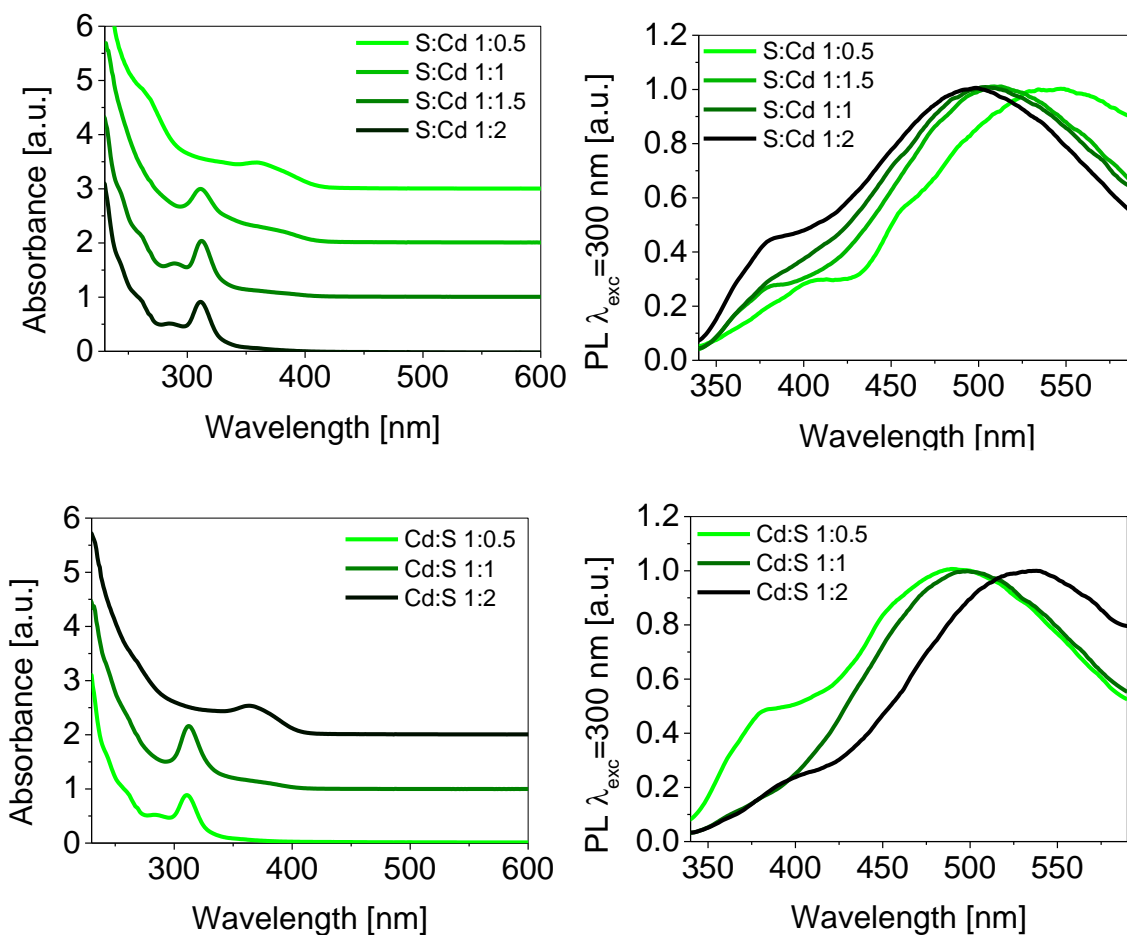


Figure 88: Absorption (left) and emission spectra (right) of CdS nanoclusters shows a strong dependency on the initial ratios of Cd(oleate)₂ and the sulfur precursor. The heterogeneous growth shows a set of magic-sized clusters at 259 nm, 285 nm, 311 nm, 348 nm and 380 nm.

The CdS clusters whose absorption band lies around $\lambda=311$ nm do not fluoresce efficiently in contrast to the clusters within the lower energy range. The results can be explained by the cluster size effect and the confined carriers which affects the energetic level of the electron. The high surface-to-volume ratio also lowers the quantum yield due to non-radiative recombination. The ligand coverage is very sensitive to the photoluminescence quantum yield. Using a high concentration of amines ligand gives an increased quantum yield which is supported by numerous

publications.^[43] When increasing the aging time, the fluorescence intensity increases and the fluorescence maximum is shifted slightly to longer wavelength, arising from the confining potential caused by the surface coverage of amine ligands.

Adaption to Microfluidic Systems

The mechanism of particle nucleation and growth within the nanometer volumes is of great interest. Microfluidic setups are powerful tools for the fast and automated mixing of reaction fluids to investigate the temporal evolution in view of X-ray experiments (SAXS). Therefore, a 10-fold concentrated CdS reaction system, including stabilizing ligands and co-solvent, was adapted on a facile Teflon based y-mixture stopped-flow device. The microfluidic setup is shown in figure 89.

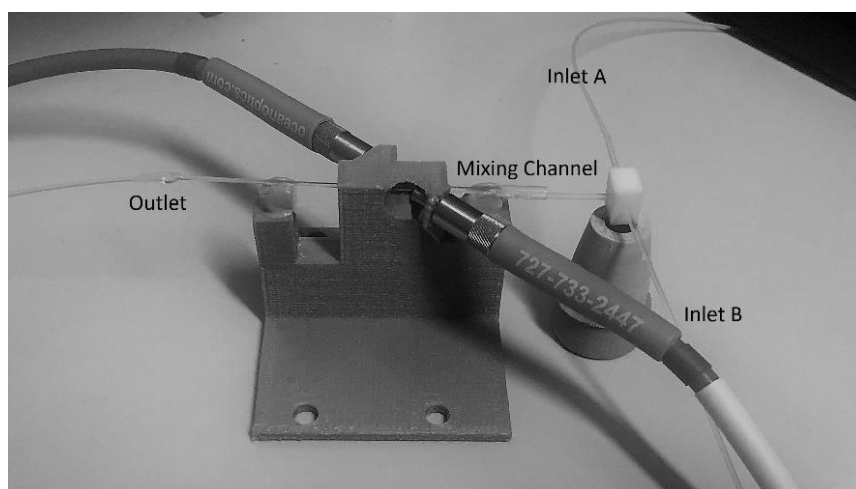


Figure 89: Photograph of Teflon-based y-mixer connected to a 1-mm quartz capillary for spectroscopic detection during nanocluster synthesis. The precursor solutions are pumped through the Inlet A and Inlet B to the inlet junction. The structural evolution was monitored via an Ocean Optics spectrometer.

This approach enables one to follow the temporal evolution of CdS nanoclusters by detecting their optical properties.^[64] The precursor solutions were pumped with a high precision syringe pump through the Inlets (Inlet A and B) and the y-mixer into quartz capillary. The geometry of each inlet and the pressure for each sub-stream at the inlet junction is equal. For fast mixing, they were pumped with high flow rates (5 mL/h) into the quartz capillary and after reaching stationary flow

conditions, the pumps were stopped. With the y-mixer, we achieve rapid mixing of the laminar flow streams by maximizing the diffusion interface. The mixer provides very small diffusion distances and thus the diffusion time is really fast and could be achieved after the mixing cross where both flow streams join (interdiffusion zone).^{[75][76]} The capillary acts as an analysis cell and we performed the study on CdS nanocluster formation with in-situ time-resolved UV-Vis spectroscopy (figure 90) The 311 nm CdS nanoclusters were formed within 3 h (figure 90, inset). We obtained very good agreement with previous optical and kinetic studies for the structural evolution at room temperature.

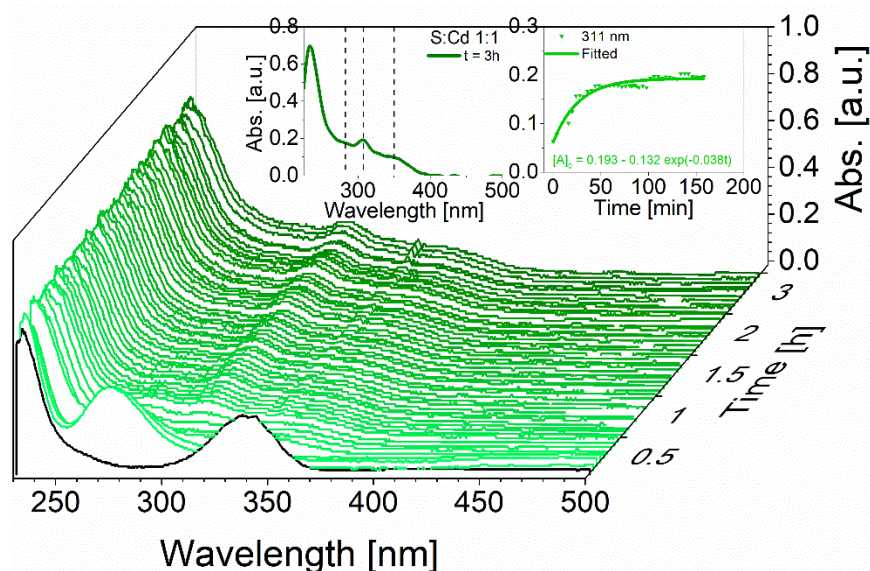


Figure 90: In-situ UV-Vis detection within a microfluidic setup to investigate the temporal evolution of CdS clusters with stoichiometric ratio S:Cd of 1:2 in cyclohexane. The sulfur precursor (black curve) decomposes directly after injecting amine and cadmium oleate and induces the CdS cluster growth (green curves).

A potential pathway to follow the nanocluster formation are in-situ techniques. Using spectroscopic methods, the optical peak positions and intensities change, implying nanocluster and regular QD growth. The CdS system under specified reaction conditions was studied systematically to examine the experimental behavior of all reaction parameters in detail. The main reaction system used in this work was initiated by mixing of Cd(oleate)₂ and the pre-synthesized sulfur precursor. The ligand solubility shows a strong dependency on the temperature and polarity of the solvent. A high supersaturation could be achieved by using cyclohexane together with the co-solvent CHCl₃. The distinct set of highly stable clusters find its origin in the interplay of the exact number of Cd and S

ions as well as the presence of amine and oleic acid ligands. The monomer-driven growth leads to the formation of energetically favored clusters through templating with organic ligands. The colloidal CdS MSC can be well-regulated due to strong coordinating functional groups to prevent further growth to regular quantum dots. The system is unaffected by the monomer concentration and the injection order. Therefore, it can be easily adapted to microfluidic-based setups for further studies.

Adaption of the Chalcogenide Systems

In addition to the CdS nanostructures, the synthesis and characterization of a variety of nano-sized metal chalcogenides was studied due to the fact that their properties are remarkably different from their bulk materials.

ZnS

Zinc sulfide is an important type of II-VI group semiconductor and the bulk material shows a band gap energy of 3.67 eV at room temperature.^[77] The reproducible approach based on the conversion of Zn(oleate)₂ and the ammonium-stabilized sulfur precursor in cyclohexane. In this method, *n*-octylamine R-NH₂ was used as an activating agent and to control size of the nanocluster. The necessity and influence of *n*-octylamine was investigated in the previous studies of CdS clusters. The temporal evolution after the injection of zinc oleate to the sulfur precursor (S:Zn 1:0.5, 1:1, 1:1.5 and 1:2) was monitored by UV-Vis spectroscopy (figure 91). The following chapter provides a summary of ZnS nanoclusters and their size-dependent optical properties taken during their synthesis at room temperature.

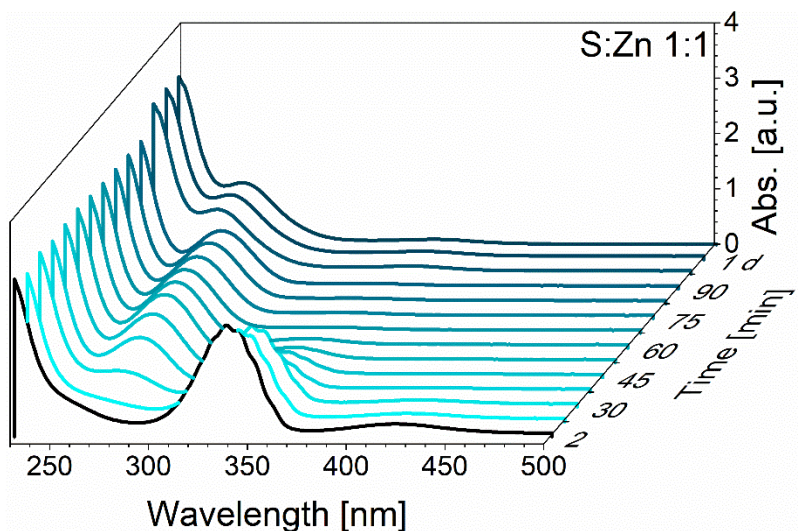


Figure 91: In-situ UV-Vis detection showing the temporal evolution of ZnS clusters with stoichiometric ratio S:Zn of 1:1 in cyclohexane at room temperature. The sulfur precursor (black curve) decomposes directly after injecting amine and zinc oleate and induces the ZnS cluster growth (blue curves).

The sulfur precursor was dissolved in cyclohexane (figure 91, black curve) and Zn(oleate)_2 was quickly injected. The addition of Zn^{2+} (figure 91, blue curves) leads instantaneously to nucleation and development of small ZnS clusters (S:Zn 1:1) at wavelength $\lambda < 300$ nm. Starting with excess of sulfur, the conversion of Zn(oleate)_2 allows the observation of isosbestic points during the slow growth process. The peak around $\lambda=279$ nm evolves into absorbance peaks at $\lambda=230$ nm, 264 nm and 282 nm (figure 91). Similar to the formation of CdS clusters, the precursor ratio of S:Zn plays a critical role. ZnS clusters prepared with an excess of sulfur favor small cluster sizes (S:Zn 1:0.5 and 1:1) ≤ 264 nm. The absorption shoulder is red-shifted with increasing zinc content, indicating the growth of larger ZnS clusters (S:Zn 1:1.5 and 1:2) ≥ 282 nm (figure 92).

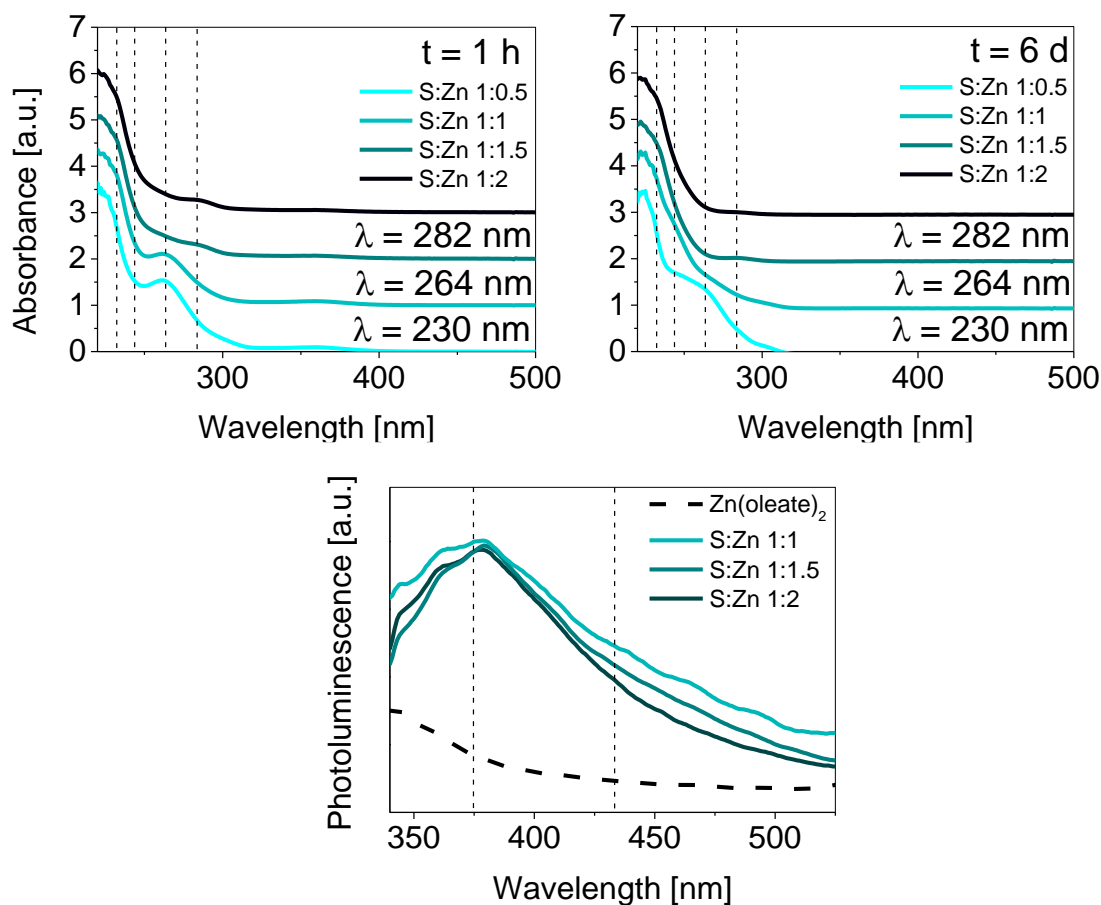


Figure 92: Absorption spectra of ZnS nanoclusters with discrete absorbance signals at 230 nm, 264 nm and 282 nm (left). The synthesis of ZnS clusters with different ratios of sulfide precursor and Zn(oleate)_2 reaching from 1:0.5 to 1:2. The metastable ZnS products shown after one week (right) and the corresponding luminescence spectra with the emission maximum at $\lambda_{\text{max}}=380$ nm (bottom).

Instead of the characteristic sulfur signal^[65], small ZnS intermediates show optical features similar to numerous research groups.^{[4][78][79][80][81]} The metastable products convert within one week into smaller clusters (figure 92, right). This type of behavior may be attributed to changes in shape and size. In literature reports, the cluster growth in the molecular size regime shows oscillating red- and blue-shifts of the absorption bands.^[82] Due to the quantum confinement effect, the prepared nanoclusters show one weak emission at $\lambda_{\text{max}}=380$ nm ($\lambda_{\text{exc}}=300$ nm) which is assigned to defect-related emission.^{[83][84]}

By changing the injection order, sulfur was quickly injected into the organic reaction mixture containing Zn(oleate)_2 and *n*-octylamine (Zn:S 1:0.5 and 1:1). The UV-vis spectra of the reacting solution (stabilized Zn^{2+} and S^{2-} ions) shows characteristic absorption shoulders around $\lambda=230$ nm,

264 nm, 282 nm and 325 nm, which are fairly blue-shifted from the bulk absorption edge of 345 nm (figure 93).

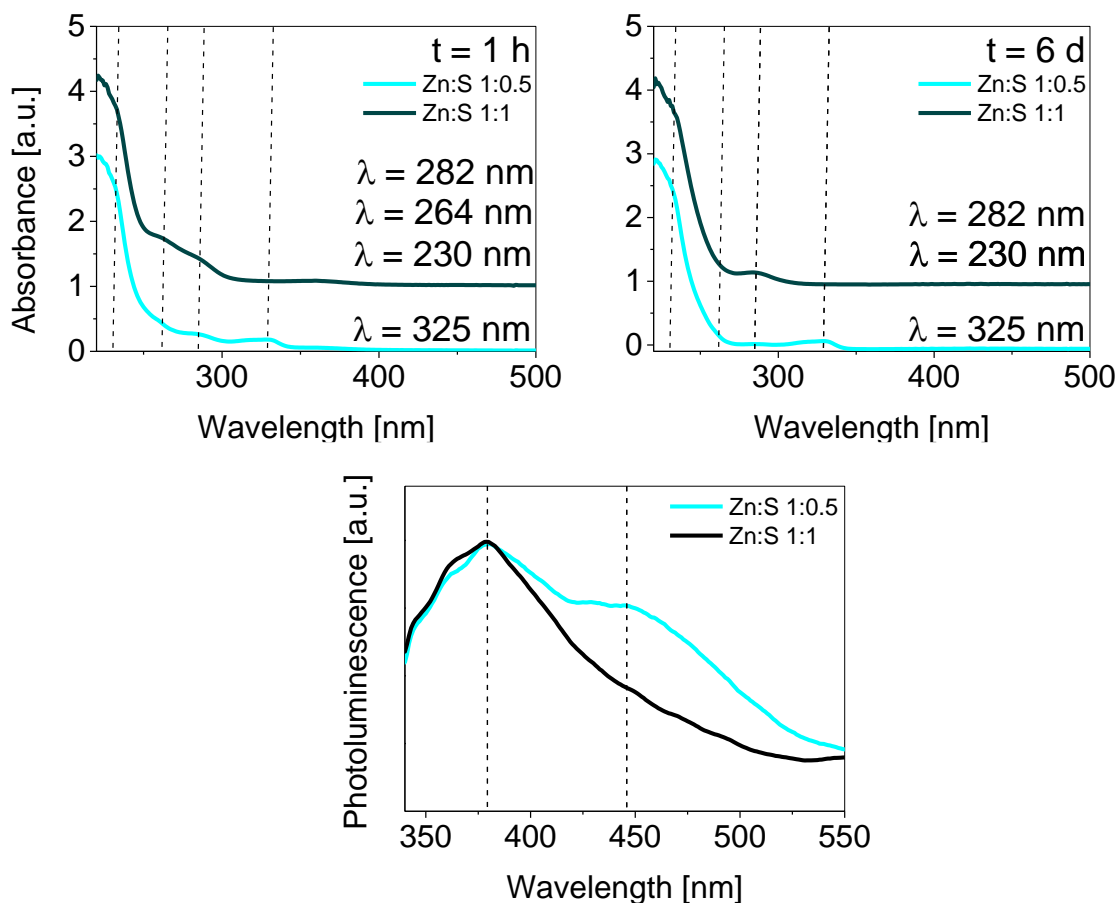


Figure 93: Absorption spectra of ZnS nanoclusters with discrete absorbance signals at 230 nm, 264 nm, 282 nm and 325 nm (left). The synthesis of ZnS clusters with the Zn(oleate)₂ and sulfide precursor ratio of 1:0.5 and 1:1 show metastable ZnS products which convert to smaller cluster species after one week (right). The corresponding luminescence spectra shows emission maxima at $\lambda_{\text{max}}=380$ nm and 450 nm (bottom).

The absorption signals show an inverse trend, where excess metal favors larger ZnS clusters. The corresponding emission spectra show two emission signals at $\lambda_{\text{max}}=380$ nm and $\lambda_{\text{max}}=450$ nm (for Zn:S 1:0.5, $\lambda_{\text{exc}}=300$ nm) which match literature reports very well.^{[79][85][86][87]} The presence of multiple emission peaks is assigned to defects in the ZnS lattice (Schottky or Frenkel point defects).

The size of the ultra-small clusters can be observed in TEM photographs. TEM samples were prepared via drop-casting for the sample S:Zn 1:0.5 with the characteristic absorbance signal at 230 nm, and for Zn:S 1:0.5 with signals at 230 nm and 325 nm (figure 94).

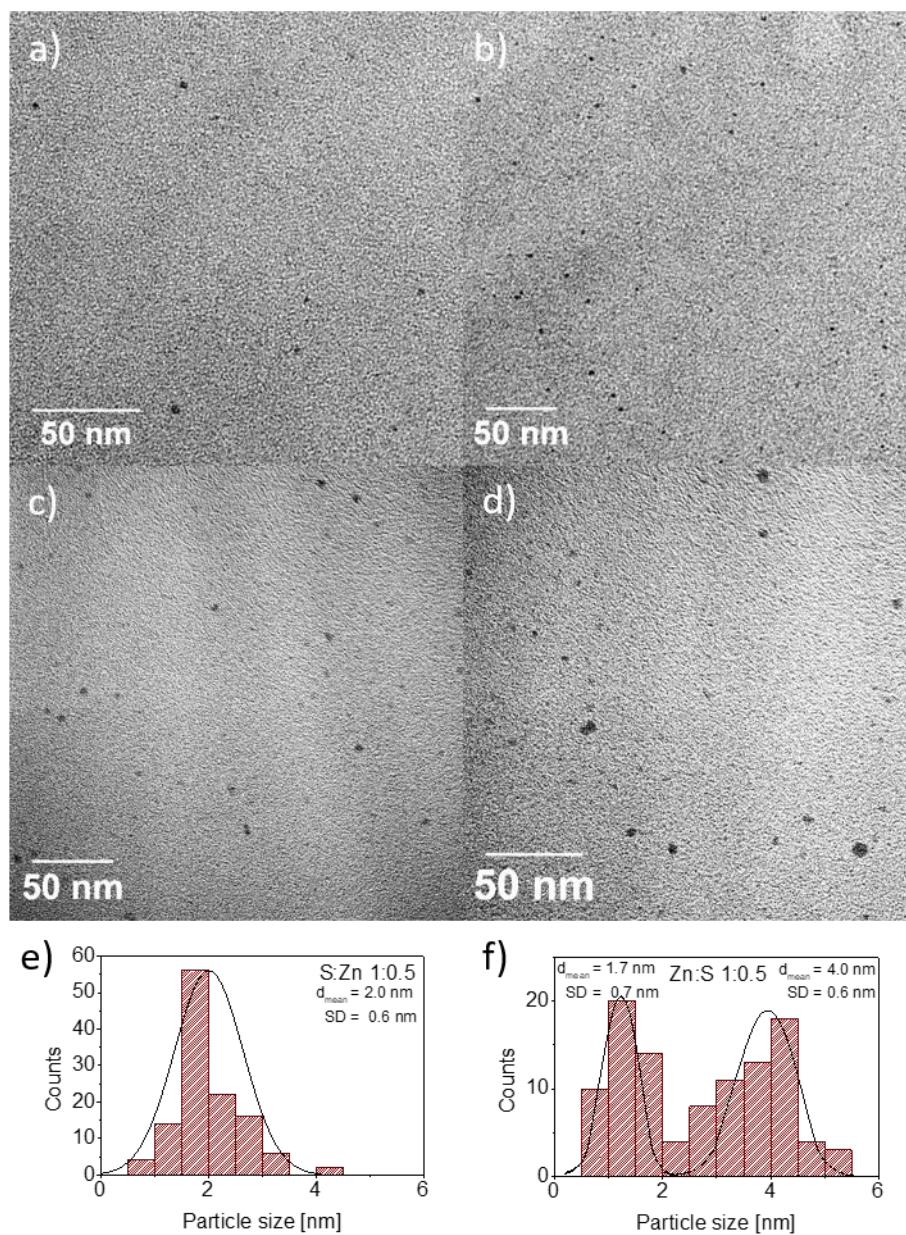


Figure 94: TEM images of ZnS nanoclusters synthesized in cyclohexane S:Zn 1:0.5 (a, b, e) and Zn:S 1:0.5 (c, d, f). The well-separated nanoclusters show average sizes of 2.0 nm \pm 0.6 nm for S:Zn 1:0.5 and two fractions with 1.7 nm \pm 0.7 nm and 4.0 nm \pm 0.6 nm for Zn:S 1:0.5.

The size for S:Zn 1:0.5 is in the range of $2.0 \text{ nm} \pm 0.6 \text{ nm}$, based on analysis of 100 particles. The inverse injection order (Zn:S 1:0.5) allows the synthesis of ZnS nanoclusters which includes two different cluster fractions. The mean diameters of the fractions were determined to be 1.7 nm and 4.0 nm. The deviation from the average particle sizes is around 0.7 nm and 0.6 nm respectively. The limited resolution makes the determination more difficult.

The spectroscopic data are consistent with the quantum confinement effect^[79] and the maximum diameter of the clusters can be calculated using the Brus equation^[9]

$$\Delta E = \frac{\pi \hbar^2}{2r^2} \left[\frac{1}{m_e^*} - \frac{1}{m_h^*} \right] - \frac{1.8 e^2}{\epsilon r} \quad (6.4)$$

where ΔE is the blue-shift of the band gap of the cluster material compared to the bulk material, m_e^* is the effective mass of the electron $0.34 m_e$ and m_h^* the effective mass of the hole $0.23 m_e$ with the free electron mass m_e . The dielectric constant ϵ is $8.3^{[88]}$ and the diameter $D=2r$ calculated from the average radius r .

Table 15: The structural information regarding ZnS clusters, including the calculated diameter D of the given nanocrystal sample with respect to the band gap of the cluster material.

λ [nm]	D^a [nm]	D^b [nm]	D^c [nm]
230	1.9	2.0 ± 0.6	1.7 ± 0.7
264	2.4		
282	2.8		
325	4.25		4.0 ± 0.6

^a Diameter D determined according the Brus equation^{[9][87]}

^b Sizes determined from TEM images of sample S:Zn 1:0.5

^c Sizes determined from TEM images of sample Zn:S 1:0.5

The values of the average diameter obtained from Brus equation^[9] are listed in table 15 and compared with the average sizes observed from TEM. The calculated mean cluster diameter matches very well with the electron microscopy results.

The facile synthesis developed for CdS nanoclusters could be adapted to the ZnS system. The semiconducting clusters were obtained from the reaction of Zn(oleate)₂ and the ammonium-stabilized sulfur precursor in cyclohexane. The cluster size was controlled by the ratio of Zn²⁺ and S²⁻ ions in presence of *n*-octylamine. The band gap values were calculated from optical measurements to determine the diameter of the ZnS clusters using the effective mass approximation given by the Brus equation.^[9] The results are in good agreement with the TEM images.

PbS

Lead sulfide PbS crystals were also synthesized and studied optically in colloidal solutions. Bulk PbS has a metallic appearance and suspensions are blackish colored. The cubic rock salt structure of lead sulfide has a bulk band gap at 0.41 eV (3020 nm).^[89] Developing a PbS cluster synthesis with narrow size distribution is one of the key objectives in this chapter. The quantum-sized materials were synthesized via the reaction of Pb(oleate)₂ and the ammonium-stabilized sulfur precursor in cyclohexane at room temperature. The absorption edge exhibits a large blue shift ($\lambda=200$ nm to 350 nm) when the crystallite size shrinks to the nanometer regime. This can be explained by density functional theory (DFT) calculations.^[18] The injection order of both precursors was varied in the presence of *n*-octylamine R-NH₂. Presented in figure 95, the temporal evolution was monitored after the injection of lead oleate to the sulfur precursor (S:Pb 1:0.5, 1:1, 1:1.5 and 1:2). An overview of PbS nanoclusters and their size-dependent optical properties after their synthesis is provided.

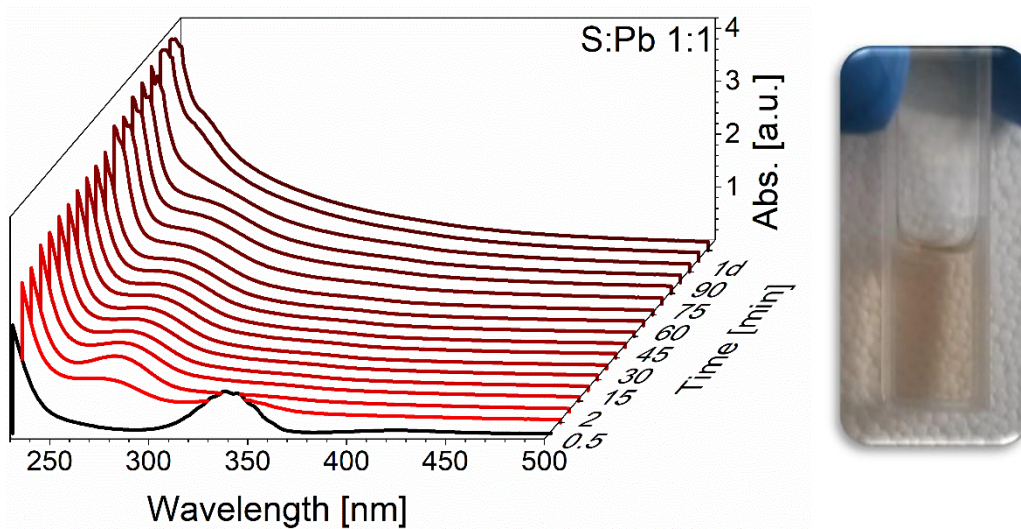


Figure 95: In-situ UV-Vis detection showing the temporal evolution of PbS clusters with stoichiometric ratio S:Pb of 1:1 in cyclohexane at room temperature. The sulfur precursor (black curve) decomposes directly after injecting amine and lead oleate and induces the PbS cluster growth (red curves).

Pb(oleate)₂ was quickly injected into the sulfur precursor in cyclohexane (figure 95, black curve) and the resulting UV-Vis spectra show absorbance signals < 500 nm (red curves) for S:Pb1:1. For the prepared PbS products with ratios of S:Pb 1:0.5, 1:1, 1:1.5 and 1:2, weak pronounced absorbance signals are found at 253 nm, 293 nm and 336 nm (figure 96, left) demonstrating the quantum confinement effect.^{[90][91]} The absorption spectra show the monomolecular absorption peak around ~260 nm.^[90] Changing the injection order lead to a long absorbance tail (< 560 nm or 2.2 eV) and quite clearly defined absorption edges at 266 nm, 310 nm, 360 nm and 450 nm (figure 96, right). The samples show long-term stability and absorbance features above 600 nm are not observed. In contrast to CdS and ZnS, lead sulfide spectra show the development of a characteristic long tail^{[16][78]} which explains the color of the stable orange-brown dispersion (figure 95, right).

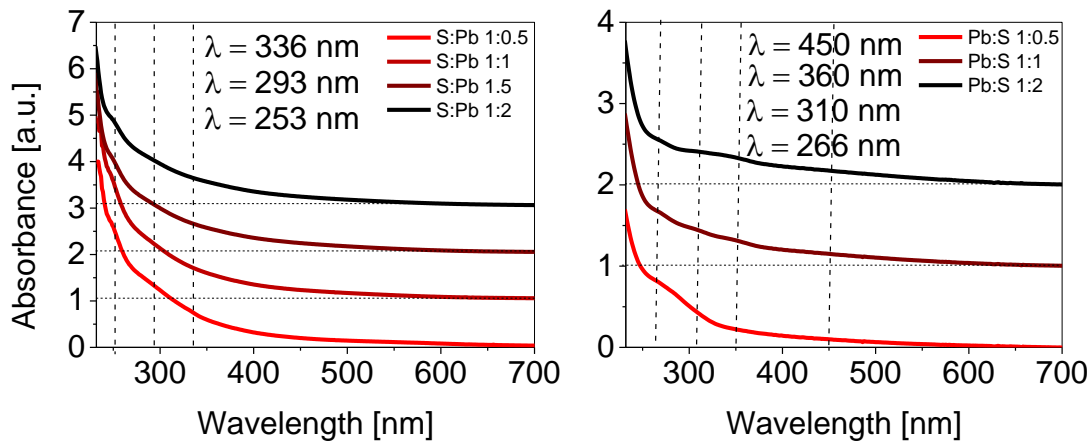


Figure 96: Absorption spectra of PbS nanoclusters showing weak but pronounced absorbance signals at 253 nm, 293 nm and 336 nm (left) according to their synthesis with different ratios of sulfide precursor and Pb(oleate)₂ (S:Pb1:0.5 to 1:2). Changing the injection order lead to pronounced absorbance signals at 266 nm, 310 nm, 360 nm and 450 nm (right) after one day.

Directly after mixing of the precursor strong absorbance signals were observed which clearly show the formation of small clusters. The slow growth process takes six hours to complete. The study of Marynick et al.^[18] shows the same trend of lead sulfide clusters slowly growing into PbS nanostructures. Even very small clusters begin to exhibit the characteristics of bulk crystals with the dominant absorbance tail. The absorbance spectra show that a higher sulfur content results in the formation of larger clusters and the initially clear, colorless sample changes to orange. From the spectroscopic data, the long tail makes precise determination of the band gap difficult. The weak but pronounced size-dependent exciton peaks at the absorption threshold might reflect inhomogeneous broadening due to the size distribution. Lattice defects and a small fraction of larger particles are the reason for the absorption at higher wavelength.

The absorption data were fitted according the Tauc function (equation 6.5) to analyze the optical band gap E_g of semiconductors.^[89]

$$[\hbar\omega\sigma(\omega)]^{\frac{1}{n}} = A_n(\hbar\omega - E_g) \quad (6.5)$$

Where ω is the frequency with $2\pi/\lambda$ and $\hbar\omega$ the photon energy, $\sigma(\omega)$ is the absorbance coefficient, and A_n a frequency independent constant. Extrapolating the linear parts of $[\hbar\omega\sigma(\omega)]^2$ against $\hbar\omega$ gives E_g from the intersection with the $\hbar\omega$ -axis (figure 97). The weak absorption tail is ignored in

the data analysis and the band gap value of the first allowed excited state (> 2 eV) is attributed to cluster sizes of around 2-3 nm.^{[92][93]}

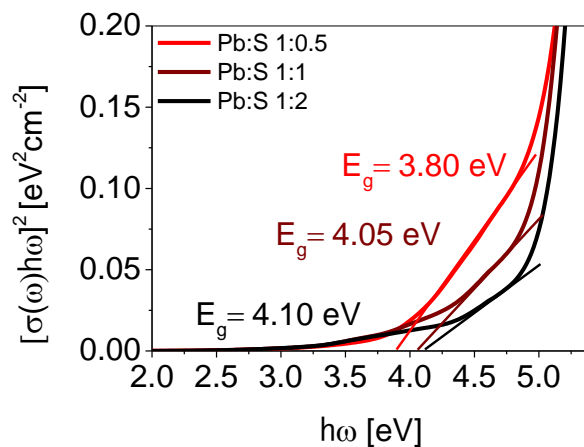


Figure 97: The observable band gaps determined by the experimental data. Extrapolating the linear parts of $[\hbar\omega\sigma(\omega)]^2$ against the energy axis $\hbar\omega$ gives $E_g=3.80$ eV, 4.05 eV and 4.10 eV for Pb:S 1:0.5, 1:1 and 1:2.

The optical observations are in qualitative agreement with the TEM measurements (figure 98). The TEM images of the as-prepared PbS products show a diameter of $2.5 \text{ nm} \pm 0.9 \text{ nm}$ for S:Pb 1:0.5 and $2.4 \text{ nm} \pm 0.7 \text{ nm}$ for Pb:S 1:2. The size distributions are determined by statistical analysis of 100 particles.

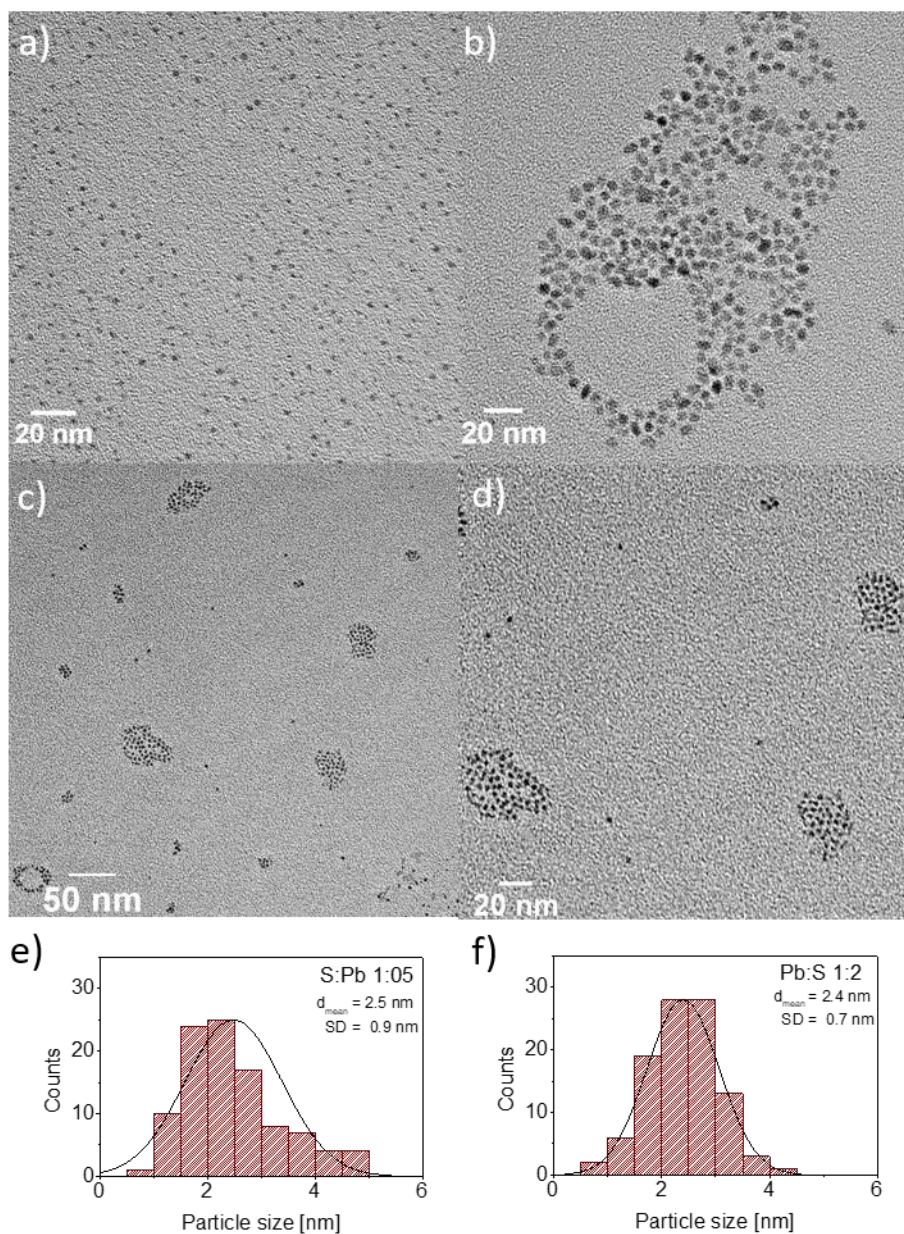


Figure 98: TEM images of PbS nanostructures synthesized in cyclohexane S:Pb 1:0.5 (a, b, e) and Pb:S 2:1 (c, d, f). The well-separated nanoclusters show average sizes of $2.5 \text{ nm} \pm 0.9 \text{ nm}$ for S:Pb 1:0.5 and $2.4 \text{ nm} \pm 0.7 \text{ nm}$ for Pb:S 1:2.

A unique property associated with PbS semiconductor colloids is their luminescence characteristics (figure 99). The emission peak of $\text{Pb}(\text{oleate})_2$ has a maximum at 409 nm and the cluster growth leads to strong detectable emissions around 568 nm ($\lambda_{\text{exc}}=310 \text{ nm}$). The various ratios of S:Pb 1:1.5

to 1:2 and Pb:S 1:0.5 to 1:2 show similar emission features. A higher sulfur content favors the conversion of Pb(oleate)_2 resulting in smaller clusters and the injection of the sulfur precursor to Pb(oleate)_2 leads to the complete conversion of oleate.

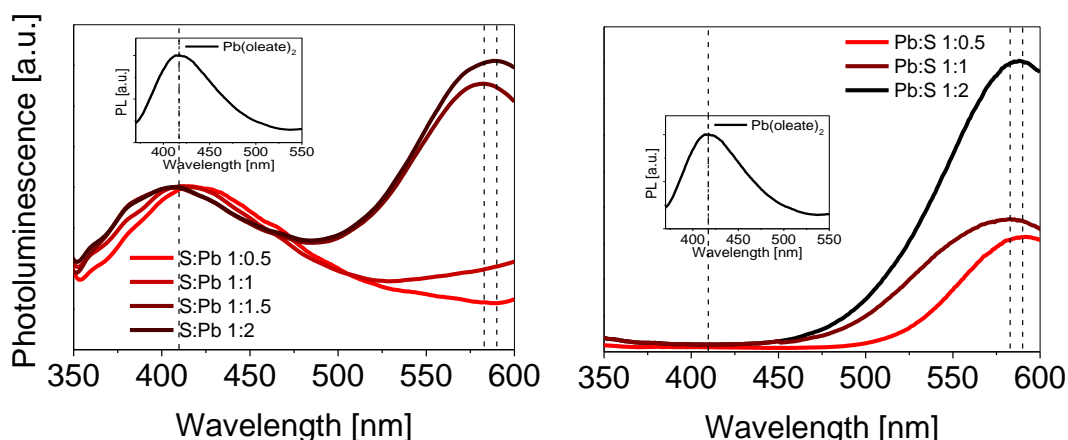


Figure 99: The corresponding luminescence spectra show emission maxima around $\lambda_{\text{max}}=409$ nm and 568 nm.

The luminescence maximum is consistent with observations for PbS in solid zeolite matrices.^{[16][94]} Leiggener and Czaferis' samples show similar UV-Vis spectra but their samples also show a color change to yellow after exposure to H_2S gas. The emission signal can be explained by the energy of the HOMO-LUMO transition of the calculated and experimental results for PbS monomers^[95]. After rehydration the color becomes stronger and more orange^[16] but there are probably some larger nanoclusters present.

The synthesis approach using oleate-based and ammonium-stabilized precursors could be used for the formation of 2 to 3 nm sized colloidal PbS particles. The semiconducting clusters in cyclohexane are controlled by the organic ligand *n*-octylamine, and the total amount of Pb^{2+} and S^{2-} ions. Methanol/Cyclohexane extraction was used as the purification step. The band gap values from optical measurements^[89] were determined from Tauc-plots and support the TEM results of the PbS clusters.

Ag₂S

Nanocrystalline silver chalcogenides show unique optical properties and are low-toxicity quantum dots which are of great interest. Ag₂S has three polymorphic modifications, the low-temperature monoclinic α -Ag₂S (acanthite), as well as the high-temperature body-centered cubic (bcc) β -Ag₂S (argentite) and face-centered cubic (fcc) γ -Ag₂S phase.^[96] The bulk band gap of silver sulfide is around ~ 1.1 eV and the Bohr radius around 2.2 nm.^[97]

Nano-sized Ag₂S particles have been formed by the conversion of Ag(oleate) and the sulfur precursor described above. The room temperature synthesis in cyclohexane gives well-dispersed nanocrystals. The optically clear solution permits monitoring of the colloid formation by spectroscopic methods which should give a better insight (figure 100).

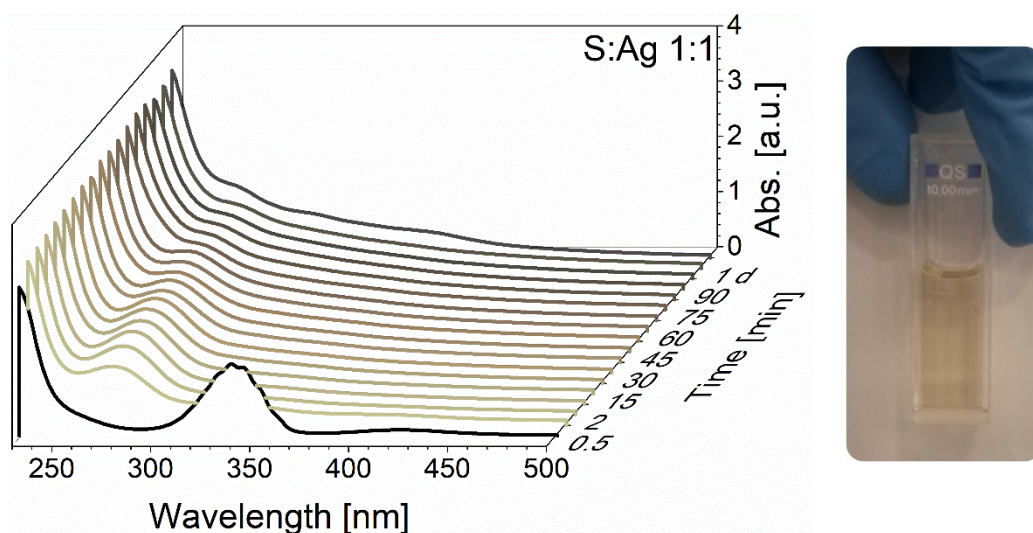


Figure 100: In-situ UV-Vis detection showing the temporal evolution of Ag₂S clusters with stoichiometric ratio S:Ag of 1:1 in cyclohexane at room temperature. The sulfur precursor (black curve) decomposes directly after injecting amine and silver oleate and induces the Ag₂S cluster growth (grey curves).

The first samples were prepared with high sulfur content and the fast injection of Ag⁺ ions to form silver oleate. The monitored absorbance features differ from the precursor signals which explains the interaction and complex formation of sulfide and the silver ions. Silver sulfide is formed immediately and all dispersions show a clear solution with colors ranging from colorless to yellow/brown (figure 100). We conclude that the color change is caused by the presence of

quantum-sized silver sulfide. The colloidal dispersions are stable for at least two months in the dark. Various initial ratios of sulfide and silver are investigated ranging from S:Ag 1:0.25 to 1:2. The second approach includes the addition of the sulfide precursor to the stabilized silver solution in presence of *n*-octylamine (Ag:S 1:0.5 and 1:1).

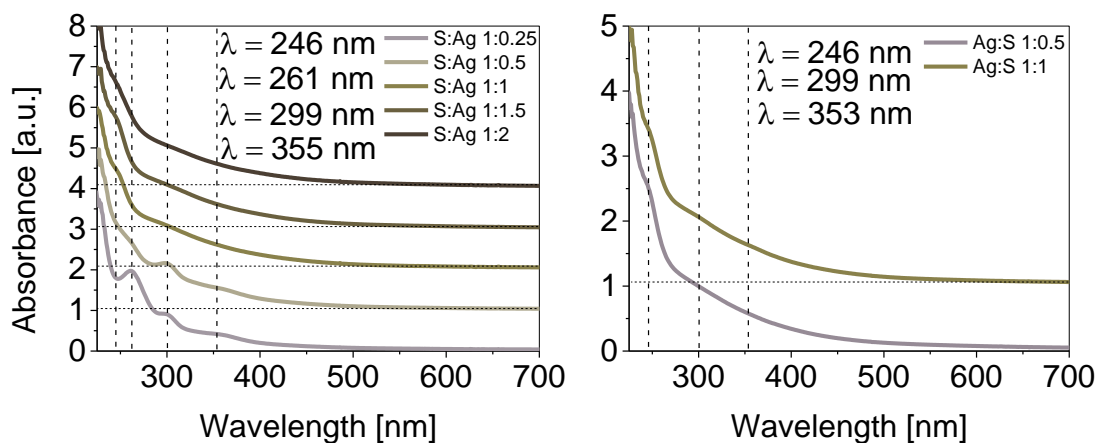


Figure 101: Absorption spectra of Ag₂S nanocluster samples showing weak but pronounced absorbance signals at 246 nm, 261 nm, 299 nm and 355 nm (left) depending on their synthesis with different ratios of sulfide precursor and Ag(oleate) (S:Ag 1:0.25 to 1:2). Changing the injection order leads to pronounced absorbance signals at 246 nm, 299 nm, and 353 nm (right) after one day.

Ag₂S nanostructures show the same behaviour as the slowly growing PbS nanostructures. A broad absorbance tail with onset at 500 nm and defined absorption edges at 246 nm, 261 nm, 299 nm and 355 nm (figure 101, left) appears at low silver concentrations S:Ag 1:0.25 to 1:0.5. The absorbance spectra with the inverse injection order show the direct conversion of the sulfur precursor and absorbance signals at 246 nm, 299 nm and 353 nm (figure 101, right). Besides the signal at 246 nm^[65], the monitored absorbance features differ from the precursor signals which explains the interaction and complex formation of sulfide and the silver ions. The absorption threshold might reflect inhomogeneous broadening due to the size distribution. Furthermore, no absorption band in the 380 nm to 430 nm region due to the development of pure colloidal silver can be observed. However, the measurements have shown that increasing the silver content leads the development of the characteristic long pronounced absorption tail.

The TEM grids of the products were prepared without further purification. The detected nanostructures show uniform and well-separated particles with spherical morphology. The average sizes were determined to be $5.8 \text{ nm} \pm 0.8 \text{ nm}$ for S:Ag 1:0.5 (figure 102, a, b, e) and $3.0 \text{ nm} \pm 0.7 \text{ nm}$ for S:Ag 1:2 (figure 102, c, d, f).

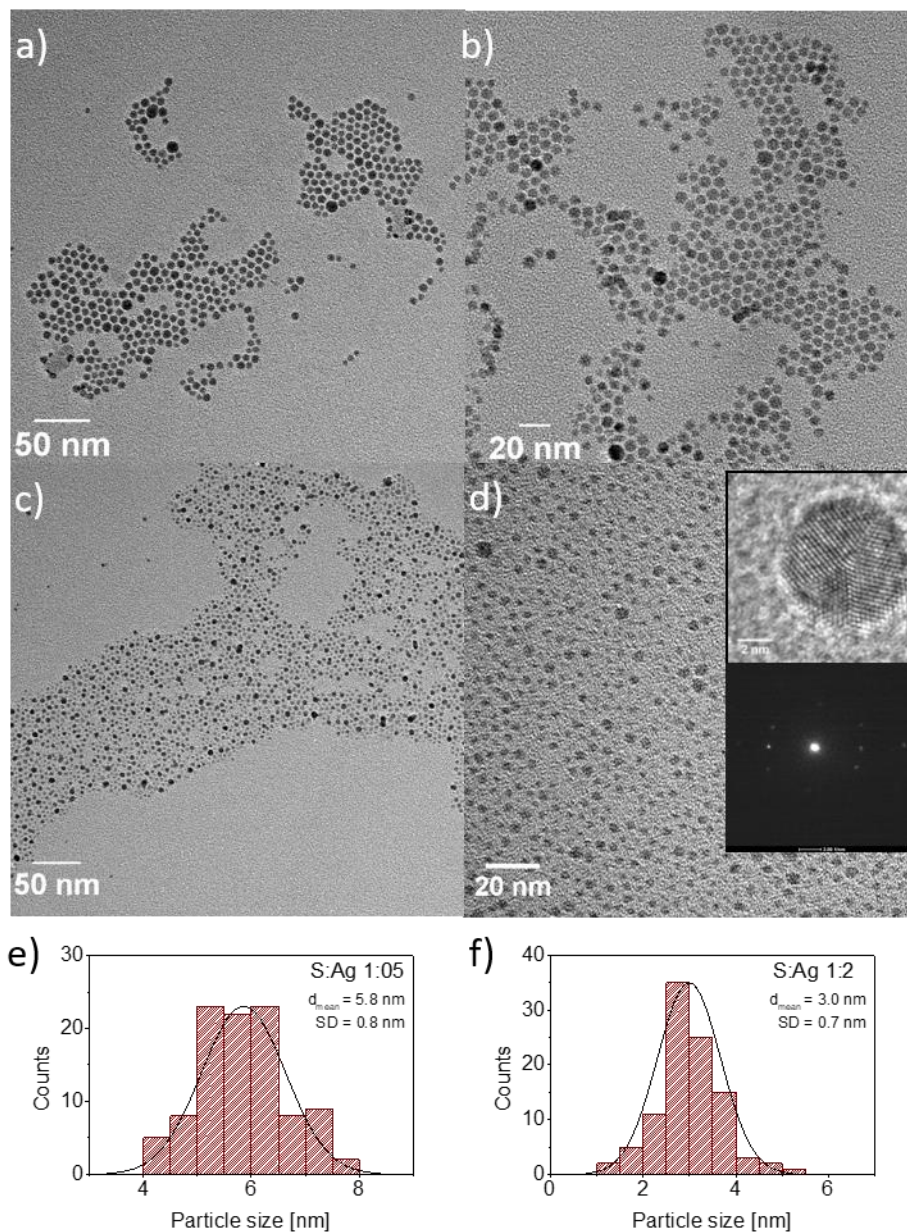


Figure 102: TEM images of Ag_2S nanostructure synthesized in cyclohexane with S:Ag 1:0.5 (a, b, e) and S:Ag 1:2 (c, d, f). The well-separated nanoclusters show average sizes of $5.8 \text{ nm} \pm 0.8 \text{ nm}$ for S:Ag 1:0.5 and $3.0 \text{ nm} \pm 0.7 \text{ nm}$ for S:Ag 1:2.

Moreover, the images show a 2D hexagonal structure of the nano-sized particles with interparticle distance of ca. 2.5 nm. The highly crystalline internal structure (figure 102, insets) confirm the interplanar spacing of 0.255 nm which is in good correspondence with the $(\bar{1}21)$ plane of the monoclinic Ag_2S .^{[98][99]}

The material silver sulfide shows composition- and size-dependent luminescence properties. A low silver sulfide content is characterized by a blue-green emission (distinct absorbance signals), while samples with higher silver sulfide content show orange-colored emission corresponding to the continuous absorption tail.^[100] The photoluminescence spectra of our Ag_2S colloidal solutions show the characteristic signals of remaining silver oleate at $\lambda_{\text{max}}=380$ nm in all samples (figure 103).

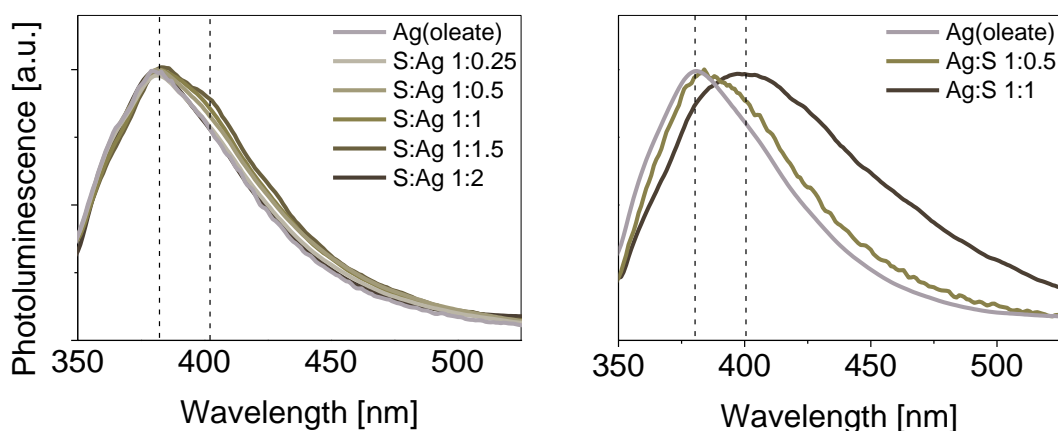


Figure 103: The corresponding photoluminescence spectra show emission maxima around $\lambda_{\text{max}}=380$ nm and 401 nm.

The absence of emission signals at 490 nm and 610 nm^[16] suggests that metastable monomeric Ag_2S and Ag_4S_2 species are not present. However, the red-shift of sample suggests Ag:S 1:0.5 explains that higher stoichiometries of silver sulfide are obtained. Gusev and co-worker elucidated size-dependent Ag_2S emission spectra^[101] which clearly demonstrate that nanocrystals with sizes larger than ~ 2.3 nm in diameter show emission maxima at around 1000 nm. The luminescence in our samples could not be detected due instrumental limitations. Furthermore, silver rich clusters can be excluded due to the missing characteristic cluster features in UV-Vis and emission spectra.^{[29][102]}

For more phase and structural information, XRD patterns were recorded to characterize CdS, ZnS, PbS and Ag₂S products. All samples exhibit broad Bragg peaks (2θ : 25-30° and 40-55°), indicating the presence of small nanocrystals. The results are not indicative of an ordered crystalline solid and allow only a vague suggestion of the final composition. Therefore, the XRD characterization was not followed with deeper investigation.

Our aim was to develop a cluster synthesis that is applicable to various semiconductor systems. The Ag₂S synthesis was effective and controllable and nano-sized particles could be successfully synthesized in cyclohexane. The formation of semiconducting colloidal Ag₂S particles with sizes around 3 to 6 nm could be obtained with metal oleate and ammonium stabilized sulfur precursor by the reaction of Ag⁺ and S²⁻ ions. Ideal conditions need to be fixed for ZnS, PbS and Ag₂S to optimize the size-controlled synthesis of nanocluster and nanocrystals with a single approach.

6.4.2 Silver Halides

Studies of the formation of silver halides have been undertaken under various synthetic conditions. To access quantized growth, we prepared the silver precursor Ag(oleate) and used tetraoctylammonium bromide and tetraoctylammonium iodide as halide precursor in organic solvents. Compared to the previous metal chalcogenide MSC, the silver precursor bears one oleate and the halide precursor bears only one ammonium ligand. We used a similar synthetic approach to the synthesis of clusters at room temperature. The titration of monomer and the gradual red-shift of the products were studied by optical measurements.

Silver Bromide

When solutions of bromide and Ag ions in the stoichiometric ratio 1:1 are rapidly mixed, pale yellow dispersions of AgBr nanocrystals are formed which show distinct ripening processes over several hours followed by sedimentation of the particles. The characteristic optical band edge arises at 304 nm and shows a strong size- and shape-dependence on the nanocrystals. Chen et al.^[103] was able to synthesize 30–100 Å sized AgBr clusters using a reverse micelle approach. They found that the energy gap increases by decreasing cluster size which is typical in the quantum confinement

regime. Shelly and co-workers^[104] described the AgBr cluster signal at around 274 nm, the existence of which is underpinned by theoretical calculations by Marynick et al.^[17]

With the results for the metal chalcogenide systems in mind, our aim was to use similar synthetic conditions to access quantized growth for the halides. We synthesized the silver precursor Ag(oleate) and used the phases transfer agent tetraoctylammonium bromide. Briefly, the standard method includes complete dissolution of the bromide precursor in cyclohexane and in the presence of the co-solvent CHCl₃. This is followed by the injection of *n*-octylamine and different volumes of silver(oleate) in cyclohexane (figure 104, Br:Ag 1:0 to 1:0.55).

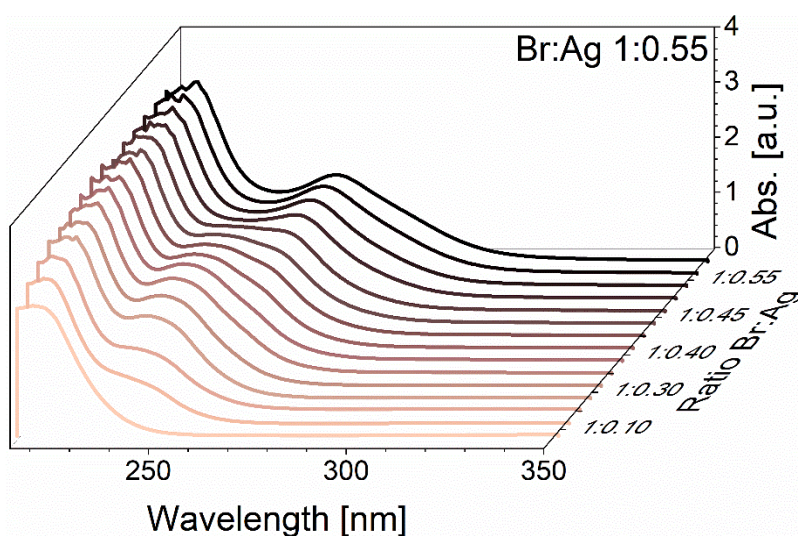


Figure 104: The UV-vis spectra of energetically favored AgBr clusters show their absorbance peaks around 240 nm, 255 nm, 273 nm in cyclohexane and CHCl₃ as co-solvent.

Due to the high affinity of both ions, the controlled cluster formation occurs instantaneously after the injection. The rapid addition of Ag⁺ ions to an excess of stabilized bromide ions results in a colorless dispersion with signal at 240 nm, 255 nm and 273 nm. TOABr as precursor shows absorbance up to 235 nm. The sequential silver addition affects a gradual red-shift of the absorbance signal. Each peak position corresponds to a AgBr cluster size and we suggest that their cluster stability is given by the strong amine-silver complexation.

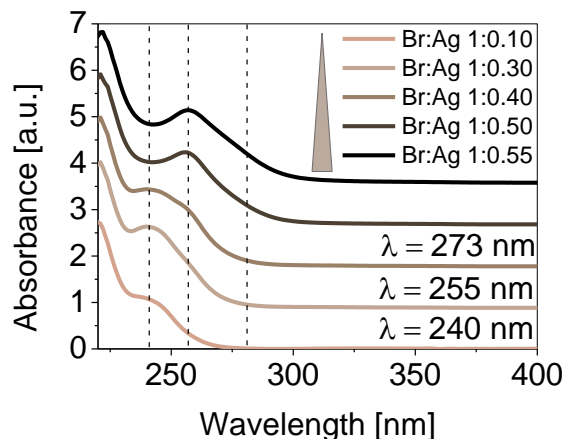


Figure 105: Absorption spectra of AgBr nanoclusters with absorbance signals at 240 nm, 255 nm, 273 nm. Nanoclusters were prepared with different ratios of bromide precursor and Ag(oleate) (Br:Ag 1:0.10 to 1:55).

The Ag^+ ions originally surrounded by strong coordinating ligands and Br^- ions are in the bulk medium. The reaction occurs directly after the injection of Ag(oleate) into the bulk medium. Furthermore, the solvent system shows a poor solubility for the precursor which favors the cluster formation. The overview in figure 105 shows the dominance of two cluster peaks at 240 nm and 273 nm which are stable for one month in the dark.

The reduction of Ag^+ to Ag can be excluded by the absence of absorbance signals in the 400 nm region. When exceeding the Br:Ag ratio of 1:0.6, an uncontrolled formation of nanocrystals is unavoidable. The growth of regular AgBr nanocrystals becomes dominant due to consumption of small cluster particles.

In contrast to the metal chalcogenide systems, the injection order has a strong influence on the colloid synthesis. The injection of *n*-octylamine and different volumes of bromide precursor to silver rich reaction mixture in cyclohexane results in the formation of regular AgBr nanocrystals. Figure 106 show the pronounced AgBr absorbance signals at 273 nm and 304 nm with the ratios Ag:Br 1:0.6 to 1:1.0. The intensity of the characteristic peaks increases by the sequential bromide addition. We suggest that the clusters contain excess silver ions and the particle growth occurs by the reaction with bromide ions. Ag^+ ions in excess can adsorb at the surface of the AgBr clusters and the injected Br^- is able to react with the positively charged clusters. The size of the cluster depends clearly on the concentration of Br^- ions which were injected.

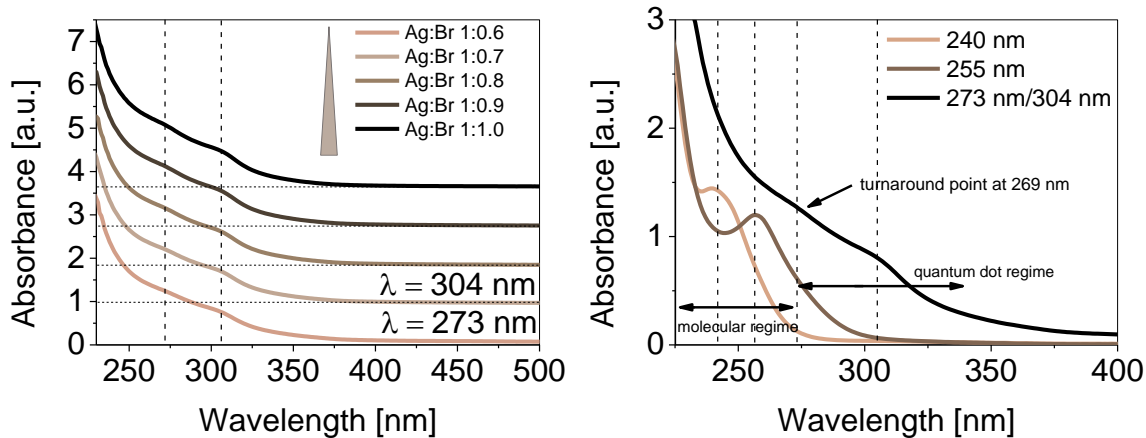


Figure 106: Absorbance spectra of AgBr clusters and regular quantum dots with ratios Ag:Br 1:6 to 1:1.0. Pronounced absorbance signals could be detected at 273 nm and 304 nm (left). The absorbance spectra (right) gives an overview of stable AgBr clusters synthesized by the two approaches.

Considerable work has been done on silver bromide systems. According to computational studies, the bond length of the AgBr monomer is 2.39 Å and the neutral (AgBr)_n clusters n=1-9 show a HOMO-LUMO band gap between 219 nm and 292 nm.^[17] This matches very well our investigations with absorbance peaks detected from 240 nm to 304 nm (figure 106).^{[104][105][106]}

TEM images show particles with uniform sizes and a spherical morphology (figure 107). They correspond to the cluster peaks at 240 nm and 255 nm.

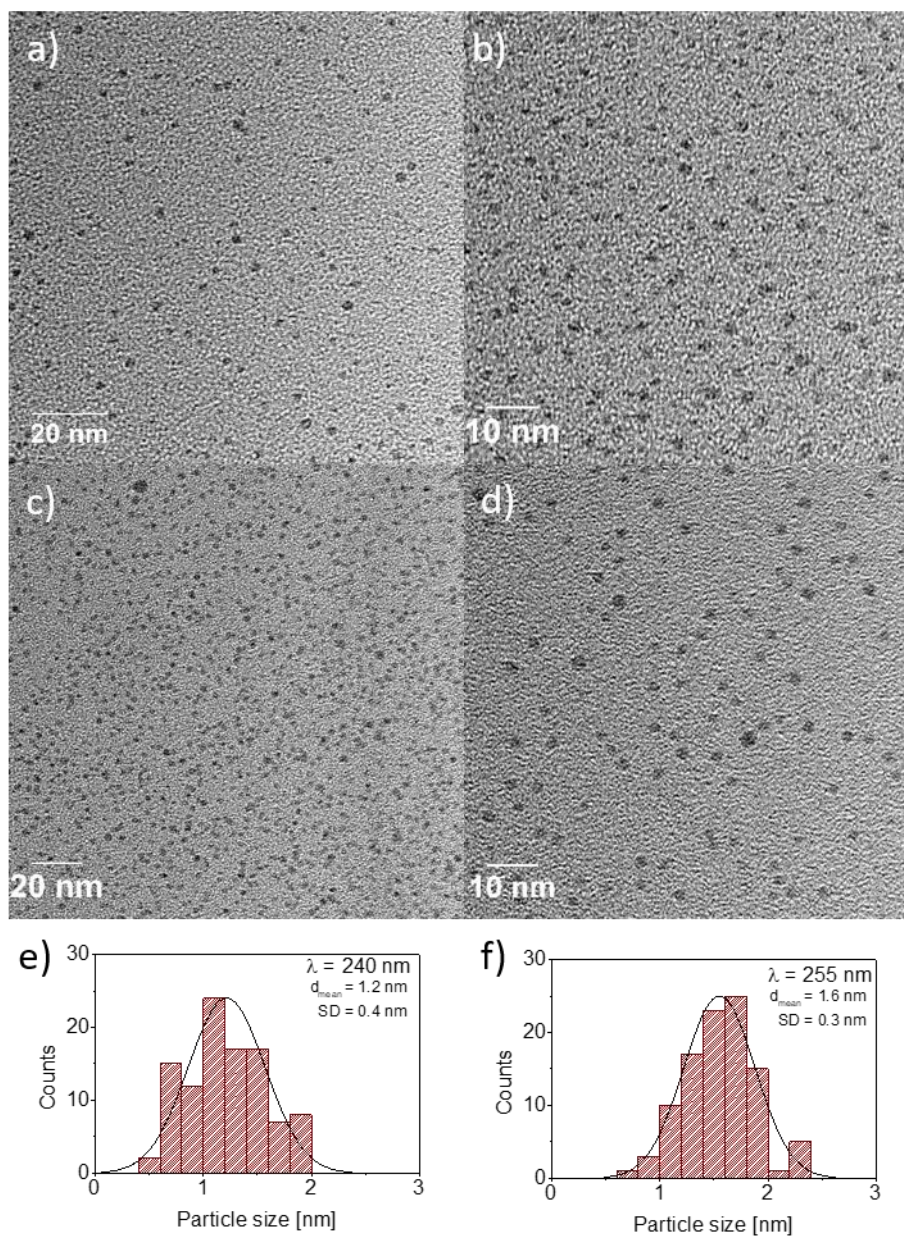


Figure 107: TEM images of AgBr nanostructures synthesized in cyclohexane Br:Ag 1:0.30 (a, b, e) and Br:Ag 1:0.55 (c, d, f). The well-separated nanoclusters show average sizes of $1.2 \text{ nm} \pm 0.4 \text{ nm}$ for Br:Ag 1:0.30 and $1.6 \text{ nm} \pm 0.3 \text{ nm}$ for Br:Ag 1:0.55.

Measuring the cluster samples reveals that their average diameter is around $1.2 \text{ nm} \pm 0.4 \text{ nm}$ and $1.6 \text{ nm} \pm 0.3 \text{ nm}$. While the smaller cluster particles are stable, a significant portion of the regular quantum dots undergo morphological changes under electron beam exposure and produce silver

atoms (figure 108). The TEM images show AgBr quantum dots with an average diameter of $21.0 \text{ nm} \pm 3.0 \text{ nm}$.

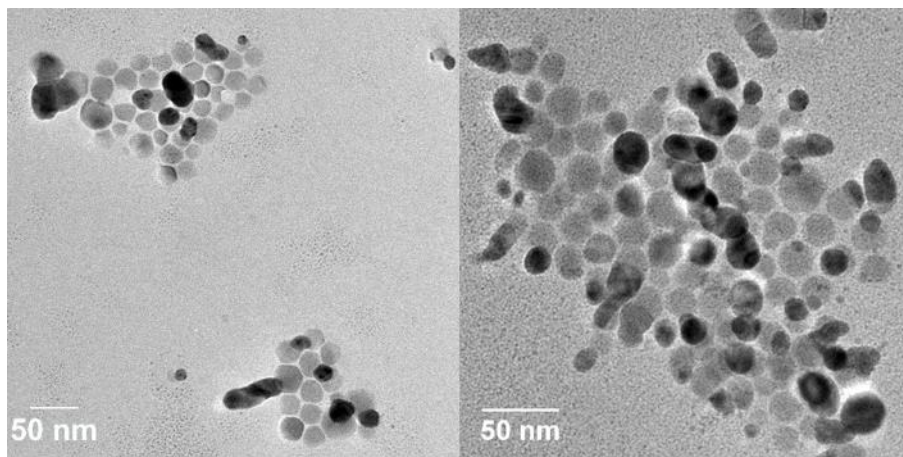


Figure 108: TEM images of AgBr nanocrystals synthesized in cyclohexane Ag:Br 1:1.0 show average sizes of $21.0 \text{ nm} \pm 3.0 \text{ nm}$.

The stepwise growth of larger products can be attributed to presence of more monomers, with their consumption resulting in the formation of larger clusters.

Previous studies have shown that AgBr and AgI synthesized according to our novel synthetic route behave in the same way. In a subsequent step, systematic studies on silver halides are performed and the results summarized in a subsequent chapter.

The temperature dependence of the cluster-growth process was investigated next. Ag(oleate) was injected into bromide solutions at three different temperatures ($T=10 \text{ }^\circ\text{C}$, $T=20 \text{ }^\circ\text{C}$ and $T=40 \text{ }^\circ\text{C}$) with four different ratios Br:Ag 1:20 to 1:0.55 (figure 109). The temperature range is limited by the boiling point of the solvents and the precursor solubility. UV-Vis spectra were taken during the reactions at all temperatures.

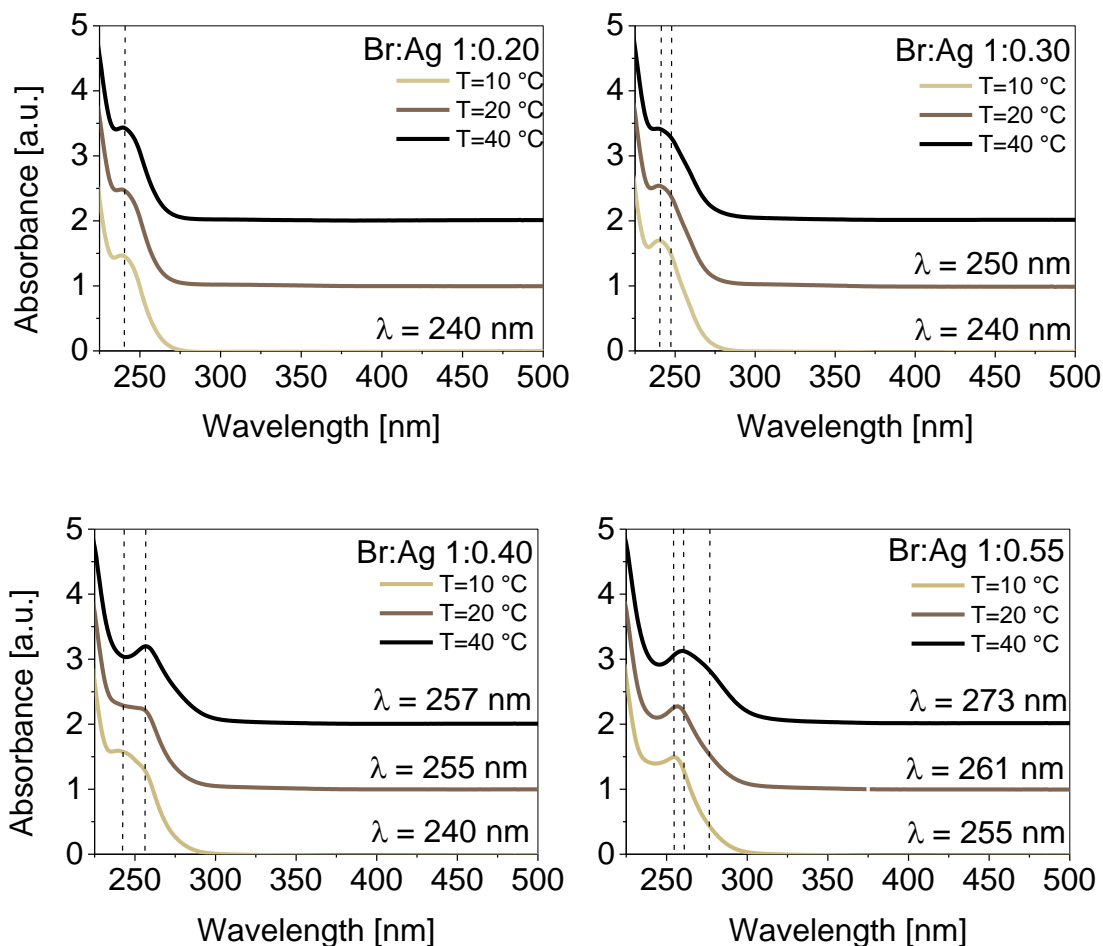


Figure 109: UV-vis spectra showing the cluster formation at three different temperatures ($T=10\text{ }^{\circ}\text{C}$, $T=20\text{ }^{\circ}\text{C}$ and $T=40\text{ }^{\circ}\text{C}$) and four different ratios Br:Ag 1:20 to 1:0.55. At higher temperature, the absorption decreases due to peak broadening (FWHM at ratio Br:Ag 1:0.55: $T=10\text{ }^{\circ}\text{C}$: 14 nm, $T=20\text{ }^{\circ}\text{C}$: 15 nm, $T=40\text{ }^{\circ}\text{C}$: 25 nm).

According to our expectations, smaller clusters are favored at lower temperature. The characteristic absorbance signals shift towards higher energies at lower temperature and the absorbance bands become sharper and show an increase in intensity. At ratio Br:Ag 1:0.55, the absorbance peak was studied at $\sim 255\text{ nm}$ by determining the FWHM. The comparison shows a broadening of the absorbance signals with the corresponding FWHM of $T=10\text{ }^{\circ}\text{C}$: 14 nm, $T=20\text{ }^{\circ}\text{C}$: 15 nm, $T=40\text{ }^{\circ}\text{C}$: 25 nm. Whereas at $T=10\text{ }^{\circ}\text{C}$ the AgBr cluster species shows a sharp absorbance signal, at $T=40\text{ }^{\circ}\text{C}$, the peak shows the beginning of the 273 nm species. The temperature during the reaction plays an important role.

The effect of amines on the AgBr cluster suggests that the surface chemistry plays a critical role. We synthesized AgBr clusters with a minimum amount of amines according the conventional recipe with Br:Ag:R-NH₂ 1:0.55:25 and the UV-Vis signal instantaneously arises at 255 nm (figure 110). Further samples were prepared with increasing amine content, reaching from Br:Ag:R-NH₂ 1:0.55:40 to 1:0.55:80. Comparing the UV-Vis absorption spectra from the samples show that strongly coordinating capping ligands clearly influence the stability of the clusters. Due to the high binding strength of amines towards the silver ions, the signals from the UV-Vis spectra become broader and less defined. The final spectra Br:Ag:R-NH₂ 1:0.55:80 are indicative of the presence of more cluster species at around 255 nm and 312 nm. We observed cluster growth in all three samples growing in the time period of one hour after reaching their equilibrium (figure 110).

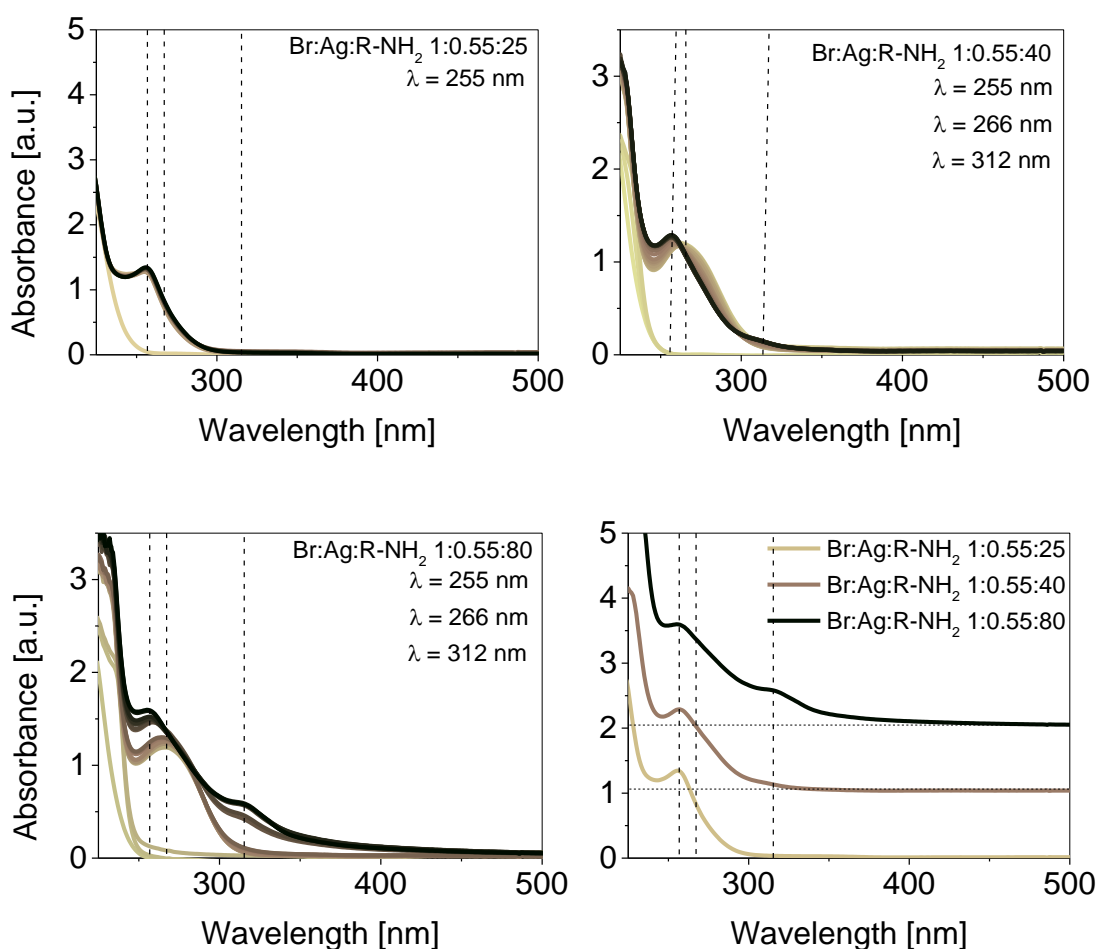


Figure 110: UV-vis spectra showing the cluster formation at three amine ratios Br:Ag:R-NH₂ 1:0.55:25 to 1:0.55:80. A higher amine content leads to the formation of red-shifted and broadened AgBr cluster species.

The addition of a minimum amount of amine lead to the dissolution of the precursor and the stabilization of AgBr clusters at 255 nm. With an excess of amine, we hypothesize, that the direct interaction of amines with unstable clusters lead to their dissolution and provide a molecular feedstock for the formation of larger cluster where the UV-Vis signals are broadened and red-shifted.^{[30][49]}

Silver Iodide

AgI has attracted much attention because of the possibilities for applications in solid electrolytes and future nano-devices. Depending on the atmospheric pressure^[107] and the temperature, silver iodide has been reported to be trimorphic.^[108] Below the temperature of 147 °C, two phases coexist, the cubic-sphalerite type (γ -AgI) and the hexagonal wurtzite-type, designated as β -AgI. After the phase transition, the α -AgI phase occurs with the very high ionic conductivity.^[109] Research groups have found that the electric conductivity of AgI nanocrystals increases with decreasing nanoparticle size^[110] and the phase-transition temperature can be tuned by the nanoparticle size.^[111] In light of this assumption, many synthetic routes have been developed to prepare stable nanocrystals and to synthesize particles with several or several tens of nanometres. Henglein et al.^[112] were able to stabilize the AgI nanocrystals with polymers such as PVA, PEG and poly(N-vinyl)pyrrolidone. During the first stages of the particle growth they were able to monitor size quantization effects with optical methods. Chen and co-workers^[40] prepared AgI clusters in zeolites. The observation indicated that silver and silver halide clusters were present with a uniform size from 1.0 nm to 2.0 nm. We synthesized the silver iodide according to our standard procedure by mixing Ag(oleate) and the halide precursor (figure 112, I:Ag 1:0 to 1:0.55). The iodide precursor was prepared via phase-transfer of tetraoctylammonium bromide in toluene and sodium iodide in water. The clear identification of the organic compound was possible by melting point determination. The standard method for the metal halide synthesis includes complete dissolution of the iodide precursor in cyclohexane in the presence of the co-solvent CHCl_3 . This is followed by the injection of *n*-octylamine and different volumes of silver(oleate) in cyclohexane.

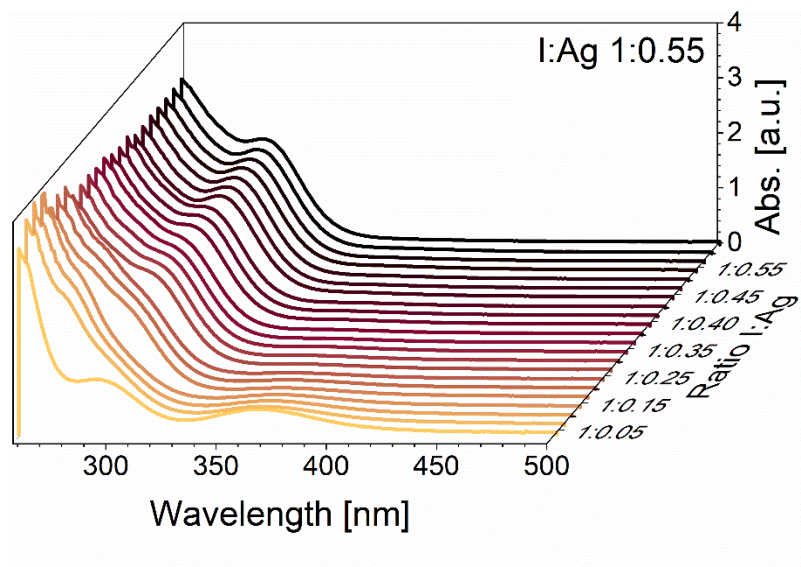


Figure 111: The UV-vis spectra of energetically favored AgI clusters show their decomposition of the iodide precursor (265 nm and 293 nm) and absorbance peaks around 274 nm, 295 nm in cyclohexane and CHCl_3 as co-solvent.

The formation of silver iodide clusters follows a similar behavior to the silver bromide case. Due to the high affinity of both ions, the cluster formation occurs instantaneously after the injection. The rapid addition of Ag^+ ions to an excess of stabilized iodide ions results in a colorless dispersion with absorption bands at 274 nm and 295 nm. The iodide precursor TOAI shows two absorbance peaks at 265 nm and 293 nm (figure 111 and 112).

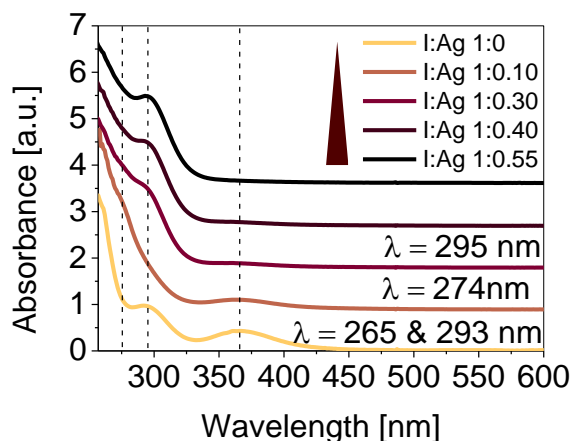


Figure 112: The UV-vis spectra of energetically favored AgI clusters shows the decomposition of the iodide precursor (265 nm and 293 nm) and absorbance peaks around 274 nm, 295 nm in cyclohexane and CHCl_3 as co-solvent. Nanoclusters were prepared with different ratios of iodide precursor and Ag(oleate) (I:Ag 1:0 to 1:55).

The growth of the ionic, sparingly soluble salts is believed to start with the degradation of the precursors and the formation of molecules and minor complexes. The sequential silver addition lead to a gradual red-shift of the absorbance signals. The dominant cluster peaks are stable for month in the dark. Each peak position is attributed to a AgI cluster size and we suggest that the cluster stability is due to the strong amine-silver complexation. There were no absorbance signals in the 400 nm region initially, however after exceeding the critical ratio I:Ag ratio of 1:0.6 the uncontrolled growth of regular AgI nanocrystals around 422 nm becomes dominant.

To understand the formation mechanism, the injection order of this synthetic approach was varied. The injection of *n*-octylamine and different volumes of iodide precursor to the silver-rich reaction mixture results in the formation of regular AgI nanocrystals. Figure 113 shows the pronounced AgI absorbance signals at 274 nm, 300 nm, 325 nm and 422 nm with the ratios Ag:I 1:0.10 to 1:0.50. The intensity of the characteristic peaks increases with sequential iodide addition. Similar to AgBr, we suggest that Ag^+ ions in excess can adsorb at the surface of the AgI clusters and the injection of I results in the formation of larger particles. The size of the cluster clearly depends on the concentration of I ions.

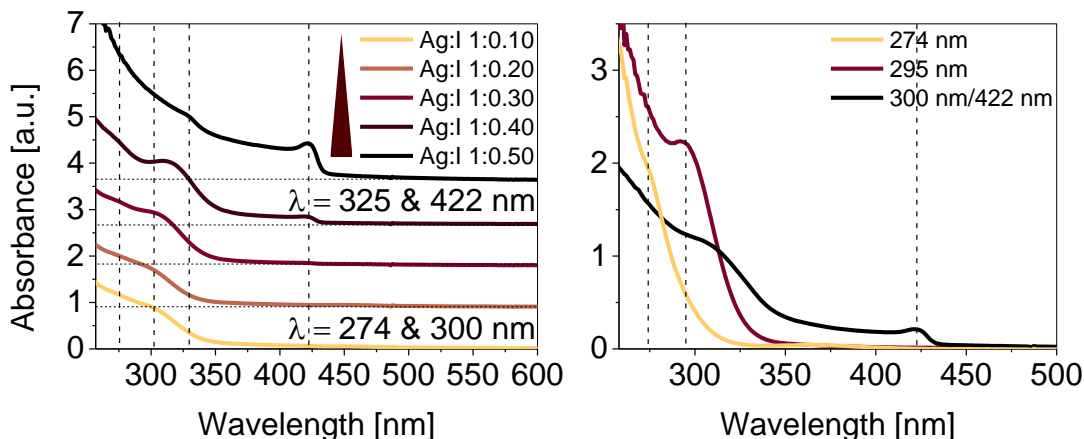


Figure 113: Absorbance spectra of AgI clusters and regular quantum dots with ratios Ag:I 1:10 to 1:0.50. Pronounced absorbance signals could be detected at 274 nm, 300 nm, 325 nm and 422 nm (left). The absorbance spectra (right) gives an overview of stable AgI clusters synthesis by the two approaches.

Figure 113 (right) confirms that the peak position for bulk AgI is around 422 nm^{[78][112]} The excitonic peak around 326 nm was also monitored by Validžić et al.^[113] who explained the blue-shift from the bulk value to 326 nm as a consequence of the size quantization effect. The signals at around 4.2 eV (295 nm) and 4.6 eV (269 nm) correspond to small clusters which were synthesized in zeolite cages^[114] and similar absorption features could be observed during the formation process of AgI prepared in aqueous solutions.^[110]

The formation of silver sulfide nanoclusters was confirmed by TEM results. In figure 114, the uniform and monodisperse spots represent the synthesized nanoclusters with strongly pronounced signals at 274 nm and 295 nm.

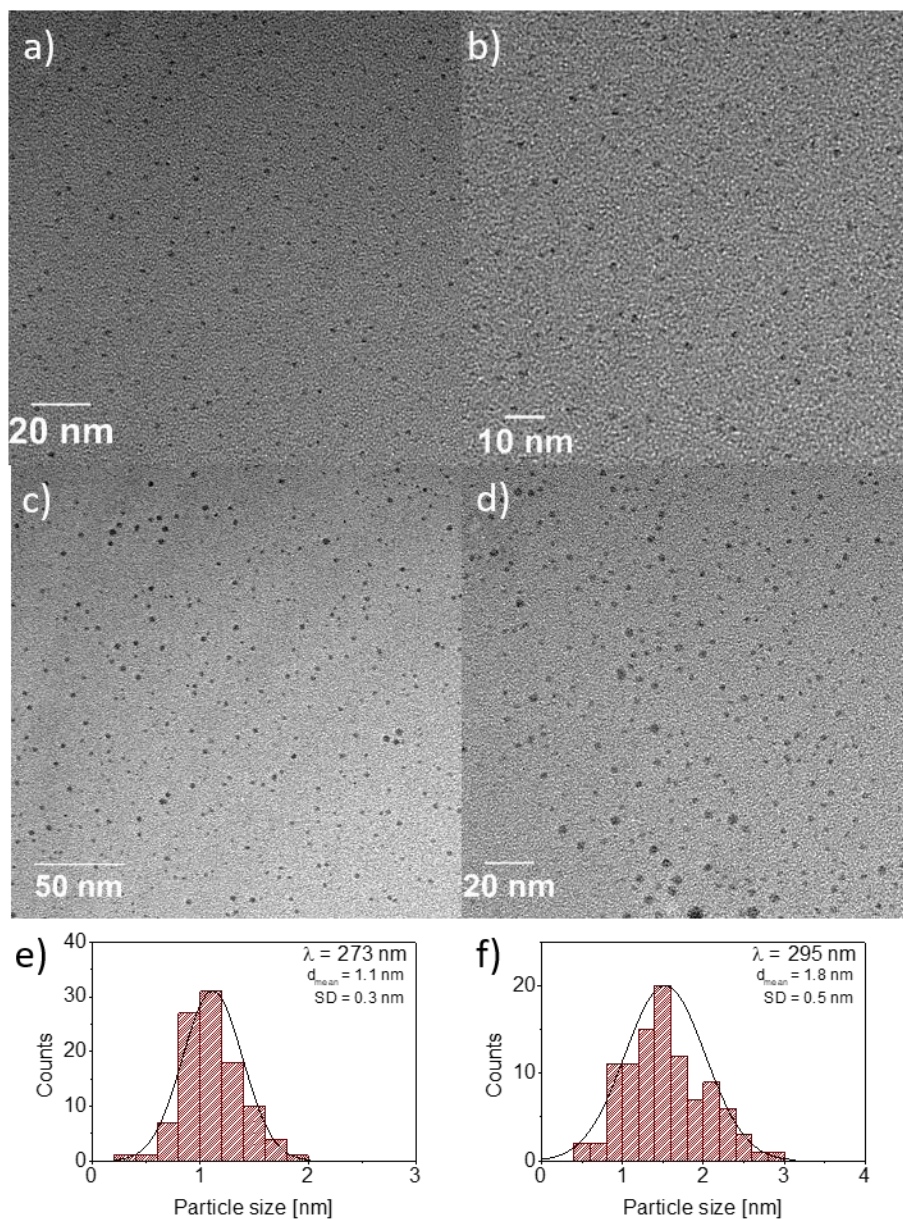


Figure 114: TEM images of AgI nanostructures synthesized in cyclohexane I:Ag 1:0.10 (a, b, e) and I:Ag 1:0.55 (c, d, f). The well-separated nanoclusters show average sizes of $1.1 \text{ nm} \pm 0.3 \text{ nm}$ for I:Ag 1:0.10 and $1.8 \text{ nm} \pm 0.5 \text{ nm}$ for I:Ag 1:0.55.

After statistical analysis of 100 particles, it was found that the mean diameter of the nanoclusters was $1.1 \text{ nm} \pm 0.3 \text{ nm}$ for I:Ag 1:0.10 and $1.8 \text{ nm} \pm 0.5 \text{ nm}$ for I:Ag 1:0.55. The characteristic 422 nm bulk material peak was attributed to AgI particles with mean size of 38.0 nm and standard

deviation of 8.6 nm due to subsequent ripening processes (figure 115). The quantum confinement effect is not apparent for those particles sizes.^[110]

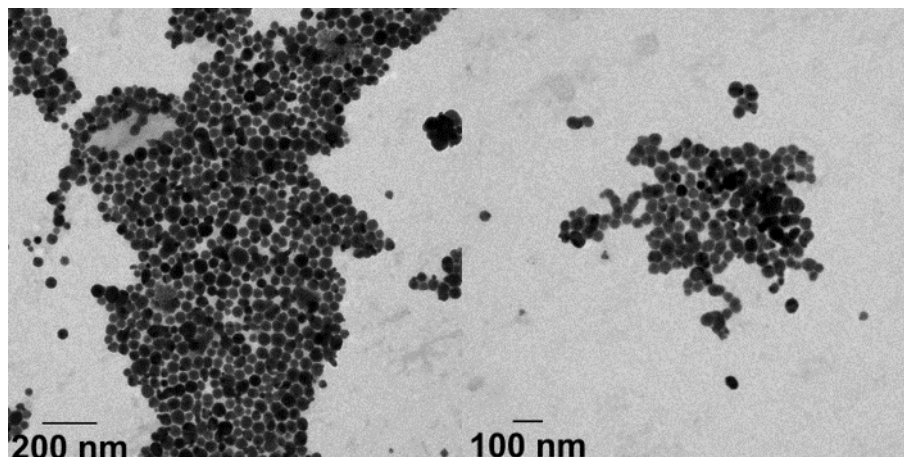


Figure 115: TEM images of AgBr nanocrystals synthesized in cyclohexane Ag:I 1:0.50 showing average sizes of $38.0 \text{ nm} \pm 8.6 \text{ nm}$.

As aforementioned, previous studies have shown that AgBr and AgI behave in the same way depending on our novel synthetic route. Moreover, changing parameters such as the addition of amines and temperature show similar results. Moreover, our systems show that the polarity of the solvent can strongly influence the particle size. For that reasons we used the AgI nanocluster and n nanocrystals in combination with different solvents. The solvents CHCl_3 and EtOH were quickly injected into the silver iodide dispersion and the results were detected by UV-Vis spectroscopy (figure 116). Whereas the addition of various volumes of cyclohexane results only in diluting, the increase of the polarity through CHCl_3 and EtOH can influence the solubility of the precursor in the system.

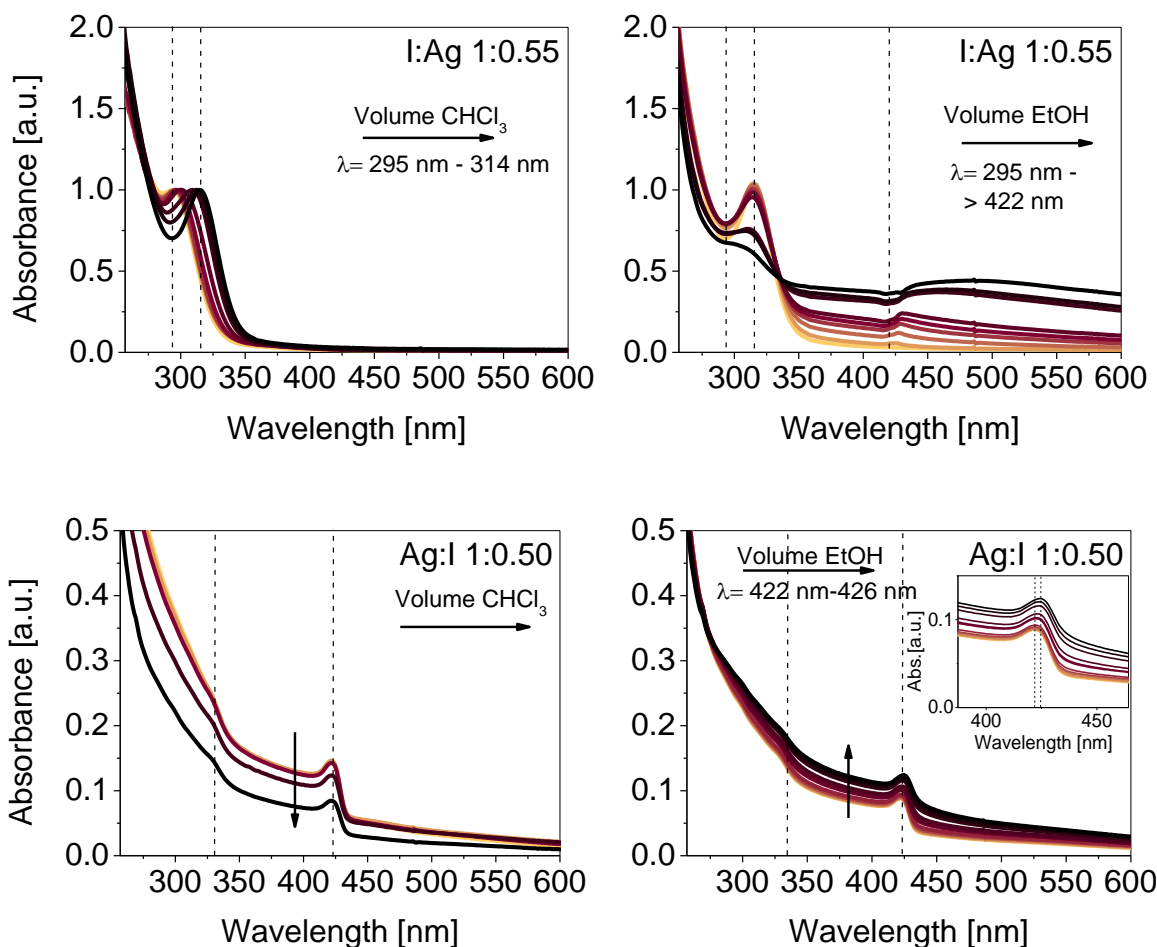


Figure 116: Absorbance spectra of AgI clusters and regular quantum dots with ratios of I:Ag 1:0.55 and Ag:I 1:0.50. The AgI dispersion can be influenced by the addition of solvents CHCl_3 and EtOH with higher polarity resulting in red-shifts of the absorption signals.

The increase of solvent polarity increases the availability of silver and halide ions and causes red-shifts of absorption features arising from AgI nanoclusters and nanocrystals. The red-shifts are correlated with the particle size in the system. Whereas the addition of the same volume of CHCl_3 (resp. CH) typically shows a slight red-shift from 295 nm to 314 nm in the cluster systems, the addition of EtOH leads to an alcohol-mediated growth process.

The AgI nanocrystals with the signal at 422 nm shows a higher stability concerning the injection of chloroform and ethanol. The peak position did not change with the addition of CHCl_3 . However, EtOH increases the availability of free ions in the reaction medium and lead to an enhanced

desorption of stabilizing ligands from the particle surface. This favours the particle growth and destabilizes the clusters. The strength of the solvent polarity and the supersaturation of the system play an important role in the growth process.

The fluorescence properties of silver bromide and silver iodide are presented in normalized spectra (figure 117). Both systems show similar behaviour with weak emission signals around 360 nm and 370 nm for the ratio halide to silver 1:0.55. The emission signals show slight shifts attributed to the influence of pure silver oleate as precursor. The emission spectra in figure 117 show, that the content and influence of the corresponding halide may be lower than that of silver.

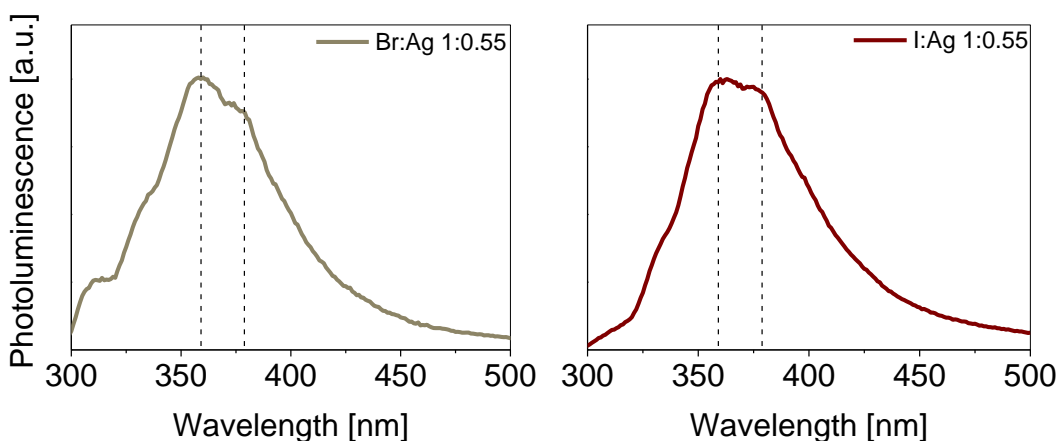


Figure 117: Emission spectra of AgI clusters and regular quantum dots with ratios of Br:Ag 1:0.55 and I:Ag 1:0.55. Silver rich clusters for AgI and AgBr at 360 and 370 are formed along with pure silver rich clusters.

A closer look at the absorption spectra of AgBr and AgI shows that the cluster peaks arise at different positions in the spectra. AgBr shows nanoclusters around 240 nm, 255 nm, 273 nm and 304 nm and AgI at 274 nm, 300 nm, 325 nm and 422 nm. Due to the deviation among both samples, and due to the weak effect monitored with fluorescence spectroscopy, we assume that silver-rich clusters of AgI and AgBr may be formed and we assume also that pure silver complexes are present. After fluorescence and TEM measurements, the silver halide dispersion got darker, further confirming the disappearance of silver halides and the enlargement of silver Ag⁰ domains.^[40]

Using the inverse synthetic approach allows the formation of AgI and AgBr nanocrystals. For further structural analysis concerning the presence of silver and bromide, larger particles were used for STEM-EDS (Scanning Transmission Electron Microscopy Energy-Dispersive X-ray

Spectroscopy) and XRD (X-ray Powder Diffraction) measurements. In addition to the size and structure analysis of AgI nanocrystals, XRD clearly identified the structural composition (figure 118).

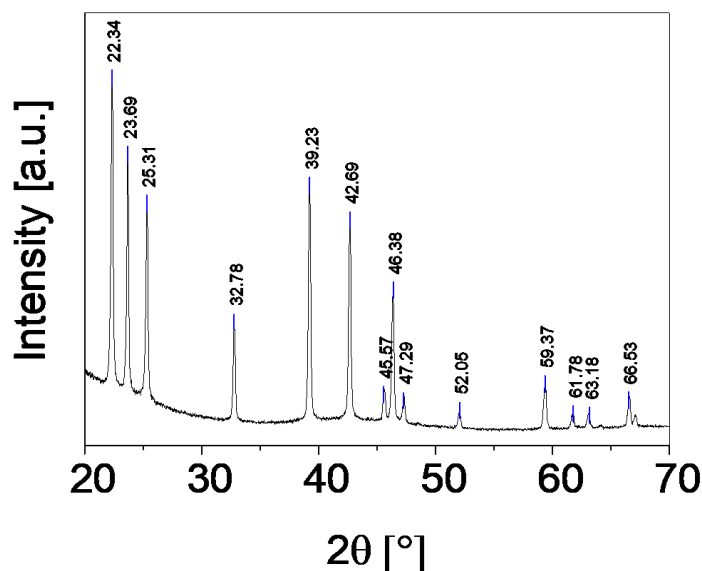


Figure 118: XRD spectrum of β - and γ -AgI nanocrystals at room temperature synthesized via our novel approach in organic solvent at room temperature.

The freeze-dried silver iodide samples can be clearly ascribed as a mix of β - and γ -phases. The observed diffraction patterns (Appendix, table S1) are characteristic for the room-temperature AgI phases.^{[110][115]} The relative composition of β - and γ -phases can be studied by comparing the relative intensities of the three peaks at $2\theta=22.3^\circ$, 23.7° and 25.3° . The intensity of the centre line is weaker for the pure wurtzite structure γ -AgI than the two outside lines of the sample. Therefore, the relative percentage of γ -AgI can be calculated to be 49 % in the prepared powder sample.^[110] Importantly, we found that the prepared sample undergoes at higher temperatures a phase transition into the α -AgI phase (Appendix, figure S1 and table S1).^[116] The gradual transformation to α -AgI starts at 145°C and is complete at 155°C (figure 119). During the phase transition, the nanocrystals were not sufficient stabilized, therefore a bulk-like end-product was obtained.

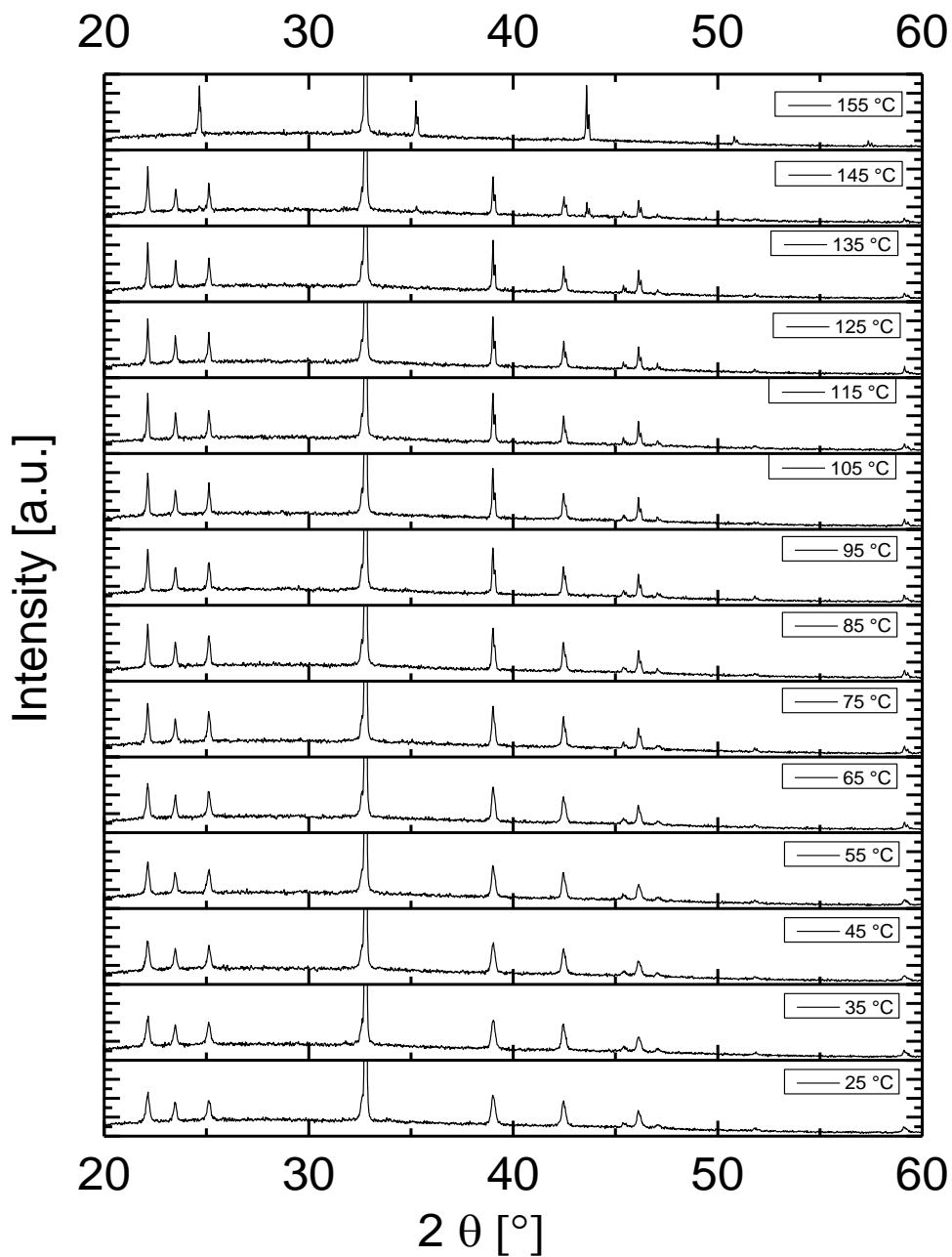


Figure 119: XRD spectrum of AgI nanocrystals synthesized via our novel approach in organic solvent at room temperature. The β - and γ -phases are stable at room temperature and undergo phase transition to the α -AgI phase at higher temperatures.

STEM-EDS measurements were used for studying the composition of AgBr nanocrystals with a mean diameter around 10 nm (figure 120, (a)) The TEM grids were prepared via drop-casting in the dark and directly analysed. Line profiling and element mapping of the dispersion shows clearly the presence of both elements silver and bromide. Element mapping of the region of interest (figure 120, a & b) reveals a Ag:Br ratio of 27 % Ag (red) & 73 % Br (blue) which matches the calculated composition of a Ag:Br 34.4 % to 65.6 % very well. According to the images, the bromide is incorporated in the AgBr nanocrystals.

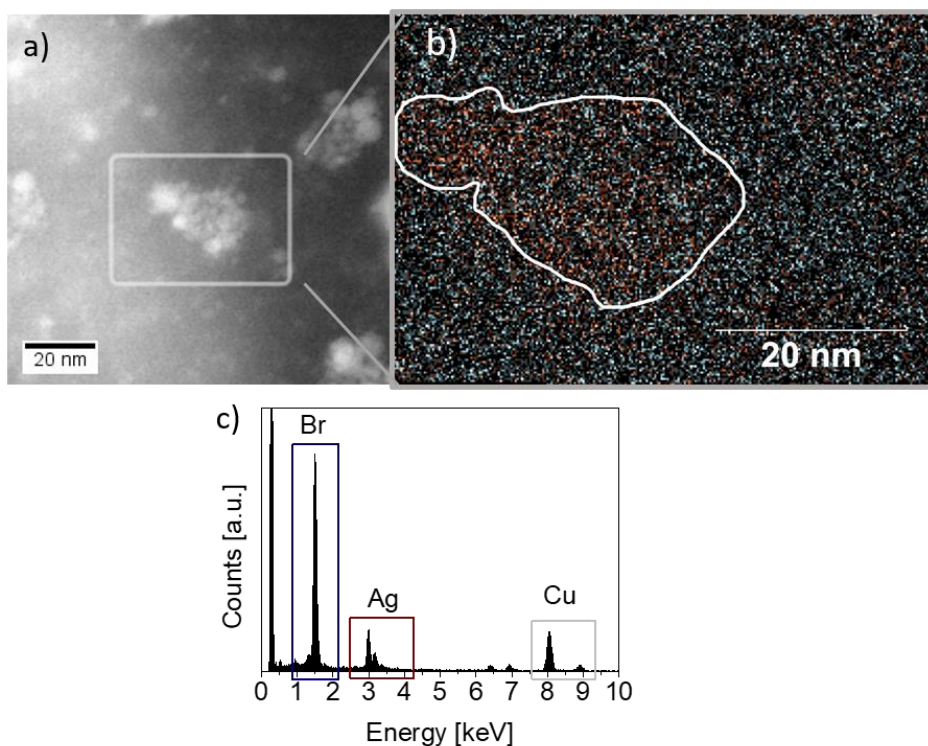


Figure 120: STEM-EDS analysis for studying the composition of AgBr nanocrystals (10 nm, STEM (a)). Elemental mapping (b) and line profiling (c) evidence the presence of bromide (blue) in AgBr nanocrystals.

This clear indication was given by line profiling from the same region, giving signals at 1.5 keV and 3.0-3.5 keV which originates from 24.2 % silver and 75.8 % bromide composition. The signal around 8.0 keV and 8.9 keV arises from the copper grid.

6.5 Conclusion

In this chapter, we reported the development of novel synthesis of nano-sized semiconductor particles. We provided insight into the surfactant-controlled nanocluster growth of metal halides and a wide range of metal chalcogenides in organic solvents. All fabrications were based on the same structure of the precursor and using metal oleates and tetraoctylammonium stabilized counter ions. The alkylammonium stabilized anions, the Lewis bases *n*-octylamine, and fatty acids, bind strongly to the particle surface to minimize the formation of larger nanocrystals. The development of ideal conditions for stepwise growth in various semiconductor cluster materials was achieved by balancing all synthetic parameters. The cluster formation was monitored in a supersaturated system with in-situ UV-Vis and fluorescence measurements as well as ex-situ TEM, STEM-EDS and XRD.

Beside the material dependency, the intermediates show size-dependent properties, from the CdS model system to ZnS, PbS, Ag₂S and the halide systems AgI and AgBr. The effective and adaptable synthesis provides information about the development and regulation of clusters and nanocrystals. The optical results clearly demonstrate quantum confinement behaviour, particularly by examining the spectral range into the ultraviolet. Especially for our model system, the heterogeneous growth process over two thermodynamically favored cluster sizes can be elucidated by kinetic investigations. Oleic acid and amines guarantees a preferential binding to the metal ions and are the key factors for the generation of thermodynamically favored cluster sizes. The surface chemistry and chemical-treatments play a critical role in the stability of clusters by influencing the stabilization of small clusters and the monomer consumption at the particle surface.

A new regime can now be entered by developing well-defined nanocrystals from clusters at room temperature. Our findings expand the fundamental understanding of diluted semiconductors of an extremely small-size regime. The properties of the intermediates are of fundamental interest for future application. To gain better understanding, the high stability, the slow cluster growth, the ease of synthesis of various clusters and adaption to microfluidic devices in combination with time-dependent scattering analysis (SAXS/WAXS) should be conducted in the future, allowing the precise identification of stoichiometry, geometry and electronic structure.

Appendix 2

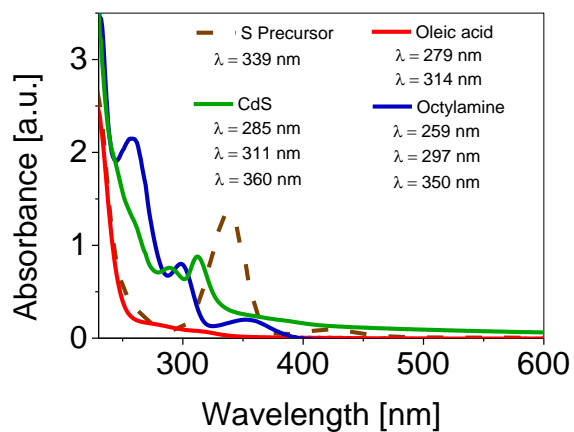


Figure S1: Absorbance spectra showing the characteristic signals of the sulfur precursor after the reaction with oleic acid and amine as well as the CdS cluster.

Table S1: 2θ values of the phases are stable at room temperature RT and after the phase transition into the α -AgI phase which are in good coincidence with the literature.

2θ [°] of β - / γ -AgI RT	2θ [°] of α -AgI
22.3	24.7
23.7	32.8
25.3	35.3
32.8	43.7
39.2	50.8
42.7	57.4
45.6	
46.4	
47.3	
52.0	
59.4	
61.8	

References

- [1] J. Park, J. Joo, G. K. Soon, Y. Jang, and T. Hyeon, 'Synthesis of monodisperse spherical nanocrystals', *Angewandte Chemie - International Edition*, vol. 46, no. 25, pp. 4630–4660, 2007.
- [2] C. de M. Donegá, 'Synthesis and properties of colloidal heteronanocrystals', *Chem. Soc. Rev.*, vol. 40, no. 3, pp. 1512–1546, 2011.
- [3] H. Gordillo, I. Suarez, R. Abargues, P. Rodriguez-Canto, and J. P. Martinez-Pastor, 'Color Tuning and White Light by Dispersing CdSe, CdTe, and CdS in PMMA Nanocomposite Waveguides', *IEEE Photonics Journal*, vol. 5, no. 2, pp. 2201412–2201412, 2013.
- [4] Y. Wang, Y. Zhou, Y. Zhang, and W. E. Buhro, 'Magic-size II-vi nanoclusters as synthons for flat colloidal nanocrystals', *Inorganic Chemistry*, vol. 54, no. 3, pp. 1165–1177, 2015.
- [5] N. Herron, Y. Wang, and H. Eckert, 'Synthesis and characterization of surface-capped, size-quantized cadmium sulfide clusters. Chemical control of cluster size', *Journal of the American Chemical Society*, vol. 112, no. 4, pp. 1322–1326, 1990.
- [6] J. Ouyang *et al.*, 'Multiple families of magic-sized CdSe nanocrystals with strong bandgap photoluminescence via noninjection one-pot syntheses', *Journal of Physical Chemistry C*, vol. 112, no. 36, pp. 13805–13811, 2008.
- [7] S. Kudera *et al.*, 'Sequential growth of magic-size CdSe nanocrystals', *Advanced Materials*, vol. 19, no. 4, pp. 548–552, 2007.
- [8] C. M. Evans, L. Guo, J. J. Peterson, S. Maccagnano, and T. D. Krauss, 'Ultra-bright PbSe magic-sized clusters', pp. 2–5, 2008.
- [9] L. Brus, 'Electronic wave functions in semiconductor clusters: Experiment and theory', *Journal of Physical Chemistry*, vol. 90, no. 12, pp. 2555–2560, 1986.
- [10] X. Peng, J. Wickham, and A. P. Alivisatos, 'Kinetics of II-VI and III-V colloidal semiconductor nanocrystal growth: "Focusing" of size distributions [15]', *Journal of the American Chemical Society*, vol. 120, no. 21, pp. 5343–5344, 1998.
- [11] D. Pan, X. Ji, L. An, and Y. Lu, 'Observation of nucleation and growth of CdS nanocrystals in a two-phase system', *Chemistry of Materials*, vol. 20, no. 11, pp. 3560–3566, 2008.
- [12] a Fojtik, H. Weller, U. Koch, and a. Henglein, 'Photo-Chemistry of Colloidal Metal Sulfides 8. Photo-Physics of Extremely Small CdS Particles: Q-State CdS and Magic Agglomeration Numbers', *Berichte der Bunsengesellschaft fur physikalische Chemie*, vol. 88, no. 10, pp. 969–977, 1984.

- [13] Y. Wang *et al.*, 'The magic-size nanocluster (CdSe)₃₄ as a low-temperature nucleant for cadmium selenide nanocrystals; Room-temperature growth of crystalline quantum platelets', *Chemistry of Materials*, vol. 26, no. 7, pp. 2233–2243, 2014.
- [14] D. Pan, S. Jiang, L. An, and B. Jiang, 'Controllable synthesis of highly luminescent and monodisperse CdS nanocrystals by a two-phase approach under mild conditions', *Advanced Materials*, vol. 16, no. 12, pp. 982–985, 2004.
- [15] P. Mulvaney, 'Nucleation and stabilization of quantized AgI clusters in aqueous solution', *Colloids and Surfaces A: Physicochemical and Engineering Aspects*, vol. 81, pp. 231–238, 1993.
- [16] C. Leiggener and G. Calzaferri, 'Synthesis and luminescence properties of Ag₂S and PbS clusters in zeolite A', *Chemistry - A European Journal*, vol. 11, no. 24, pp. 7191–7198, 2005.
- [17] H. Zhang, Z. A. Schelly, and D. S. Marynick, 'Theoretical Study of the Molecular and Electronic Structures of Neutral Silver Bromide Clusters (AgBr)_n, n=1-9', *Journal of Physical Chemistry A*, vol. 104, pp. 6287–6294, 2000.
- [18] H. Zeng, Z. a Schelly, K. Ueno-Noto, and D. S. Marynick, 'Density Functional Study of the Structures of Lead Sulfide Clusters (PbS)_n (n = 1–9)', *The Journal of Physical Chemistry A*, vol. 109, no. 8, pp. 1616–1620, 2005.
- [19] H. Zeng, R. R. Vanga, D. S. Marynick, and Z. A. Schelly, 'Cluster precursors of uncapped CdS quantum dots via electroporation of synthetic liposomes. experiments and theory', *Journal of Physical Chemistry B*, vol. 112, no. 46, pp. 14422–14426, 2008.
- [20] S. Bhusal, J. A. R. Lopez, J. U. Reveles, T. Baruah, and R. R. Zope, 'Electronic and Structural Study of Zn_xS_x [x = 12, 16, 24, 28, 36, 48, 96, and 108] Cage Structures', *Journal of Physical Chemistry A*, vol. 121, no. 18, pp. 3486–3493, 2017.
- [21] T. Vossmeier *et al.*, 'CdS nanoclusters: Synthesis, characterization, size dependent oscillator strength, temperature shift of the excitonic transition energy, and reversible absorbance shift', *Journal of Physical Chemistry*, vol. 98, no. 31, pp. 7665–7673, 1994.
- [22] W. W. Yu, L. Qu, W. Guo, and X. Peng, 'Experimental determination of the extinction coefficient of CdTe, CdSe, and CdS nanocrystals', *Chemistry of Materials*, vol. 15, no. 14, pp. 2854–2860, 2003.
- [23] M. A. Watzky and R. G. Finke, 'Nanocluster Size-Control and "Magic Number" Investigations. Experimental Tests of the "Living-Metal Polymer" Concept and of Mechanism-Based Size-Control Predictions Leading to the Syntheses of Iridium(0) Nanoclusters Centering about Four Sequential Magic ', *Chemistry of Materials*, vol. 9, no.
-

- 12, pp. 3083–3095, 1997.
- [24] Y. Park *et al.*, ‘Aqueous Phase Synthesized CdSe Nanoparticles with Well-Defined Numbers of Constituent Atoms’, *J. Phys. Chem. C*, vol. 114, no. 44, pp. 18834–18840, 2010.
- [25] J. Yang *et al.*, ‘Chemical Synthesis, Doping, and Transformation of Magic-Sized Semiconductor Alloy Nanoclusters’, *Journal of the American Chemical Society*, vol. 139, no. 19, pp. 6761–6770, 2017.
- [26] J. J. Gaumet, G. A. Khitrov, and G. F. Strouse, ‘Mass Spectrometry Analysis of the 1.5 nm Sphalerite–CdS Core of $[\text{Cd}_{32}\text{S}_{14}(\text{SC}_6\text{H}_5)_{36}\cdot\text{DMF}_4]$ ’, *Nano Letters*, vol. 2, no. 4, pp. 375–379, 2002.
- [27] T. Zhu *et al.*, ‘Two-Step Nucleation of CdS Magic-Size Nanocluster MSC-311’, *Chemistry of Materials*, vol. 29, no. 13, pp. 5727–5735, 2017.
- [28] G. A. Khitrov and G. F. Strouse, ‘ZnS nanomaterial characterization by MALDI-TOF mass spectrometry’, *Journal of the American Chemical Society*, vol. 125, no. 34, pp. 10465–10469, 2003.
- [29] A. Henglein, ‘Small-Particle Research: Physicochemical Properties of Extremely Small Colloidal Metal and Semiconductor Particles’, *Chemical Reviews*, vol. 89, no. 8, pp. 1861–1873, 1989.
- [30] D. C. Gary, M. W. Terban, S. J. L. Billinge, and B. M. Cossairt, ‘Two-step nucleation and growth of InP quantum dots via magic-sized cluster intermediates’, *Chemistry of Materials*, vol. 27, no. 4, pp. 1432–1441, 2015.
- [31] S. M. Harrell, J. R. McBride, and S. J. Rosenthal, ‘Synthesis of ultrasmall and magic-sized CdSe nanocrystals’, *Chemistry of Materials*, vol. 25, no. 8, pp. 1199–1210, 2013.
- [32] J. van Embden, A. S. R. Chesman, and J. J. Jasieniak, ‘The Heat-Up Synthesis of Colloidal Nanocrystals’, *Chemistry of Materials*, vol. 27, no. 7, pp. 2246–2285, 2015.
- [33] C. B. Murray, D. J. Norris, and M. G. Bawendi, ‘Synthesis and Characterization of Nearly Monodisperse CdE (E = S, Se, Te) Semiconductor Nanocrystallites’, *Journal of the American Chemical Society*, vol. 115, no. 19, pp. 8706–8715, 1993.
- [34] E. Groeneveld, S. Van Berkum, A. Meijerink, and C. De Mello Donegá, ‘Growth and stability of ZnTe magic-size nanocrystals’, *Small*, vol. 7, no. 9, pp. 1247–1256, 2011.
- [35] A. Kasuya *et al.*, ‘Ultra-stable nanoparticles of CdSe revealed from mass spectrometry’, *Nature Materials*, vol. 3, no. 2, pp. 99–102, 2004.
- [36] M. Mostafavi, Y. P. Liu, P. Pernot, and J. Belloni, ‘Dose rate effect on size of CdS clusters induced by irradiation’, *Radiation Physics and Chemistry*, vol. 59, no. 1, pp. 49–59, 2000.

- [37] T. Huber and E. Freisinger, 'Sulfide ions as modulators of metal–thiolate cluster size in a plant metallothionein', *Dalton Transactions*, vol. 42, no. 24, p. 8878, 2013.
- [38] Z. L. Renguo Xie and Xiaogang Peng, R. Xie, Z. Li, and X. Peng, 'Nucleation Kinetics vs Chemical Kinetics in the Initial Formation of Semiconductor Nanocrystals', *Journal of the American Chemical Society*, vol. 131, no. 42, pp. 15457–15466, 2009.
- [39] K. Yu, 'CdSe magic-sized nuclei, magic-sized nanoclusters and regular nanocrystals: Monomer effects on nucleation and growth', *Advanced Materials*, vol. 24, no. 8, pp. 1123–1132, 2012.
- [40] W. Chen, Z. Wang, L. Lin, J. Lin, and M. Su, 'Photostimulated luminescence of silver clusters in zeolite-Y', *Physics Letters, Section A: General, Atomic and Solid State Physics*, vol. 232, no. 5, pp. 391–394, 1997.
- [41] M. R. Friedfeld, J. L. Stein, and B. M. Cossairt, 'Main-Group-Semiconductor Cluster Molecules as Synthetic Intermediates to Nanostructures', *Inorganic Chemistry*, vol. 56, no. 15, pp. 8689–8697, 2017.
- [42] R. Celis, M. Carmen Hermosín, and J. Cornejo, 'Heavy metal adsorption by functionalized clays', *Environmental Science and Technology*, vol. 34, no. 21, pp. 4593–4599, 2000.
- [43] N. C. Anderson, M. P. Hendricks, J. J. Choi, and J. S. Owen, 'Ligand exchange and the stoichiometry of metal chalcogenide nanocrystals: Spectroscopic observation of facile metal-carboxylate displacement and binding', *Journal of the American Chemical Society*, vol. 135, no. 49, pp. 18536–18548, 2013.
- [44] X. Huang, V. K. Parashar, and M. A. M. Gijs, 'Synergistic effect of carboxylic and amine ligands on the synthesis of CdSe nanocrystals', *RSC Advances*, vol. 6, no. 91, pp. 88911–88915, 2016.
- [45] C. De Mello Donegá, *Nanoparticles: Workhorses of nanoscience*, vol. 9783662448. 2014.
- [46] R. A. Sperling and W. J. Parak, 'Surface modification, functionalization and bioconjugation of colloidal inorganic nanoparticles', *Philosophical Transactions of the Royal Society A: Mathematical, Physical and Engineering Sciences*, vol. 368, no. 1915, pp. 1333–1383, 2010.
- [47] C. Landes, M. Braun, C. Burda, and M. A. El-Sayed, 'Observation of Large Changes in the Band Gap Absorption Energy of Small CdSe Nanoparticles Induced by the Adsorption of a Strong Hole Acceptor', *Nano Letters*, vol. 1, no. 11, pp. 667–670, 2001.
- [48] S. Kudera, 'Formation of Colloidal Semiconductor Nanocrystals', 2007.
- [49] C. M. Evans, A. M. Love, and E. A. Weiss, 'Surfactant-controlled polymerization of semiconductor clusters to quantum dots through competing step-growth and living chain-
-

- growth mechanisms', *Journal of the American Chemical Society*, vol. 134, no. 41, pp. 17298–17305, 2012.
- [50] M. Zobel *et al.*, 'The evolution of crystalline ordering for ligand-ornamented zinc oxide nanoparticles', *CrystEngComm*, vol. 18, no. 12, pp. 2163–2172, 2016.
- [51] B. M. Cossairt and J. S. Owen, 'CdSe clusters: At the interface of small molecules and quantum dots', *Chemistry of Materials*, vol. 23, no. 12, pp. 3114–3119, 2011.
- [52] L. Qu, Z. A. Peng, and X. Peng, 'Alternative Routes toward High Quality CdSe Nanocrystals', *Nano Letters*, vol. 1, no. 6, pp. 333–337, 2001.
- [53] W. W. Yu and X. Peng, 'Formation of high-quality CdS and other II-VI semiconductor nanocrystals in noncoordinating solvents: Tunable reactivity of monomers', *Angewandte Chemie - International Edition*, vol. 41, no. 13, pp. 2368–2371, 2002.
- [54] 'NPL National Physical Laboratory, Tables of Physical and Chemical Constants'. [Online]. Available: http://www.kayelaby.npl.co.uk/chemistry/3_8/3_8_7.html.
- [55] H. Finkelstein, 'Preparation of Organic Iodides from the Corresponding Bromides and Chlorides.', *Berichte der Deutschen Chemischen Gesellschaft*, vol. 43, no. 2, pp. 1528–1532, 1910.
- [56] D. Li *et al.*, 'Efficient synthesis of functional long-chain alkyl disulfides under liquid-liquid phase-transfer catalysis: The analysis of chemical equilibrium and phase-transfer mechanism', *Catalysis Communications*, vol. 89, pp. 9–13, 2017.
- [57] D. L. Pringle, 'The nature of the polysulfide anion', 1967.
- [58] X. Liu and J. K. Thomas, 'Formation and Photophysical Properties of CdS in Zeolites with Cages and Channels', *Langmuir*, vol. 5, no. 1, pp. 58–66, 1989.
- [59] L. B. McCusker and K. Seff, 'Crystal structures of hydrated and partially dehydrated fully cadmium(II)-exchanged zeolite A', *Journal of Physical Chemistry*, vol. 85, no. 2, pp. 166–174, 1981.
- [60] J. W. Thomson, K. Nagashima, P. M. MacDonald, and G. A. Ozin, 'From sulfur-amine solutions to metal sulfide nanocrystals: Peering into the oleylamine-sulfur black box', *Journal of the American Chemical Society*, vol. 133, no. 13, pp. 5036–5041, 2011.
- [61] D. Inman and D. G. Lovering, Eds., *Ionic Liquids*. Boston, MA: Springer US, 1981.
- [62] M. M. Cortese-Krott *et al.*, 'Nitrosopersulfide (SSNO-) accounts for sustained NO bioactivity of S-nitrosothiols following reaction with sulfide', *Redox Biology*, vol. 2, no. 1, pp. 234–244, 2014.
- [63] Rick Houghton, *Emergency Characterization of unknown materials*. .
- [64] X. Chen, J. Schröder, S. Hauschild, S. Rosenfeldt, M. Dulle, and S. Förster, 'Simultaneous

- SAXS/WAXS/UV-Vis Study of the Nucleation and Growth of Nanoparticles: A Test of Classical Nucleation Theory', *Langmuir*, vol. 31, no. 42, pp. 11678–11691, 2015.
- [65] G. W. Luther and D. T. Rickard, 'Metal sulfide cluster complexes and their biogeochemical importance in the environment', *Journal of Nanoparticle Research*, vol. 7, no. 6, pp. 389–407, 2005.
- [66] Q. Yu and C. Y. Liu, 'Study of magic-size-cluster mediated formation of cds nanocrystals: Properties of the magic-size clusters and mechanism implication', *Journal of Physical Chemistry C*, vol. 113, no. 29, pp. 12766–12771, 2009.
- [67] A. Veamatahau *et al.*, 'Origin of surface trap states in CdS quantum dots: relationship between size dependent photoluminescence and sulfur vacancy trap states', *Phys. Chem. Chem. Phys.*, vol. 17, no. 4, pp. 2850–2858, 2015.
- [68] Y. Zou, D. Li, and D. Yang, 'Noninjection synthesis of CdS and alloyed CdS_xSe_{1-x} nanocrystals without nucleation initiators', *Nanoscale Research Letters*, vol. 5, no. 6, pp. 966–971, 2010.
- [69] D. F. Garcia-Gutierrez, L. P. Hernandez-Casillas, M. V. Cappellari, F. Fungo, E. Martínez-Guerra, and D. I. García-Gutiérrez, 'Influence of the Capping Ligand on the Band Gap and Electronic Levels of PbS Nanoparticles through Surface Atomistic Arrangement Determination', *ACS Omega*, vol. 3, no. 1, pp. 393–405, 2017.
- [70] R. Rossetti, J. L. Ellison, J. M. Gibson, and L. E. Brus, 'Size effects in the excited electronic states of small colloidal CdS crystallites', *The Journal of Chemical Physics*, vol. 80, no. 9, pp. 4464–4469, 1984.
- [71] W. Bu, Z. Chen, F. Chen, and J. Shi, 'Oleic acid/oleylamine cooperative-controlled crystallization mechanism for monodisperse tetragonal bipyramidal (MoO₄)₂ nanocrystals', *Journal of Physical Chemistry C*, vol. 113, no. 28, pp. 12176–12185, 2009.
- [72] N. Herron, J. C. Calabrese, W. E. Farneth, and Y. Wang, 'Crystal Structure and Optical Properties of Cd₃₂S₁₄(SC₆H₅)₃₆. DMF₄, a Cluster with a 15 Angstrom CdS Core', *Science*, vol. 259, no. 5100, pp. 1426–1428, 1993.
- [73] S. A. Bobrovnik, 'Determination the rate constants of some biexponential reactions', *Journal of Biochemical and Biophysical Methods*, vol. 42, no. 1–2, pp. 49–63, 2000.
- [74] '<https://www.precisionlabware.com/content/18-solvent-miscibility>' . .
- [75] X. Chen, J. Schröder, S. Hauschild, S. Rosenfeldt, M. Dulle, and S. Förster, 'Simultaneous SAXS/WAXS/UV-Vis Study of the Nucleation and Growth of Nanoparticles: A Test of Classical Nucleation Theory', *Langmuir*, vol. 31, no. 42, pp. 11678–11691, 2015.
-

- [76] J. L. Osborn, B. Lutz, E. Fu, P. Kauffman, D. Y. Stevens, and P. Yager, 'Microfluidics without pumps: reinventing the T-sensor and H-filter in paper networks', *Lab on a Chip*, vol. 10, no. 20, p. 2659, 2010.
- [77] O. Khani, H. R. Rajabi, M. H. Yousefi, A. A. Khosravi, M. Jannesari, and M. Shamsipur, 'Synthesis and characterizations of ultra-small ZnS and Zn(1-x)FexS quantum dots in aqueous media and spectroscopic study of their interactions with bovine serum albumin', *Spectrochimica Acta - Part A: Molecular and Biomolecular Spectroscopy*, vol. 79, no. 2, pp. 361–369, 2011.
- [78] R. Rossetti, R. Hull, J. M. Gibson, and L. E. Brus, 'Hybrid electronic properties between the molecular and solid state limits: Lead sulfide and silver halide crystallites', *The Journal of Chemical Physics*, vol. 83, no. 3, pp. 1406–1410, 1985.
- [79] K. Sooklal, B. S. Cullum, S. M. Angel, and C. J. Murphy, 'Photophysical Properties of ZnS Nanoclusters with Spatially Localized Mn²⁺', *The Journal of Physical Chemistry*, vol. 100, no. 11, pp. 4551–4555, 1996.
- [80] G. W. Luther, S. M. Theberge, and D. T. Rickard, 'Evidence for aqueous clusters as intermediates during zinc sulfide formation', *Geochimica et Cosmochimica Acta*, vol. 63, no. 19–20, pp. 3159–3169, 1999.
- [81] M. L. Steigerwald and L. E. Brus, 'Semiconductor Crystallites: A Class of Large Molecules', *Accounts of Chemical Research*, vol. 23, no. 6, pp. 183–188, 1990.
- [82] X. Wang, H. Xu, H. Liu, Z. A. Schelly, and S. Wu, 'Preparation and oscillation of absorption bands of ZnS clusters', *Nanotechnology*, vol. 18, no. 15, 2007.
- [83] S. K. Mehta, S. Kumar, S. Chaudhary, K. K. Bhasin, and M. Gradzielski, 'Evolution of ZnS nanoparticles via facile CTAB aqueous micellar solution route: A study on controlling parameters', *Nanoscale Research Letters*, vol. 4, no. 1, pp. 17–28, 2009.
- [84] H. Y. Jung *et al.*, 'Synthesis of quantum-sized cubic ZnS nanorods by the oriented attachment mechanism', *Journal of the American Chemical Society*, vol. 127, no. 15, pp. 5662–5670, 2005.
- [85] S. H. Choi, K. An, E. G. Kim, J. H. Yu, J. H. Kim, and T. Hyeon, 'Simple and generalized synthesis of semiconducting metal sulfide nanocrystals', *Advanced Functional Materials*, vol. 19, no. 10, pp. 1645–1649, 2009.
- [86] A. Tiwari, S. A. Khan, R. S. Kher, S. J. Dhoble, and A. L. S. Chandel, 'Synthesis, characterization and optical properties of polymer-based ZnS nanocomposites', *Luminescence*, vol. 31, no. 2, pp. 428–432, 2016.
- [87] Komal, P. Shikha, and T. S. Kang, 'Facile and green one pot synthesis of zinc sulphide
-

- quantum dots employing zinc-based ionic liquids and their photocatalytic activity', *New Journal of Chemistry*, vol. 41, no. 15, pp. 7407–7416, 2017.
- [88] Lev I. Berger, *Semiconductor Materials*. CRC Press, 1996.
- [89] S. I. Sadovnikov, A. A. Rempel, and A. I. Gusev, *Nanostructured Lead, Cadmium, and Silver Sulfides*, vol. 256. Cham: Springer International Publishing, 2018.
- [90] M. Askari and M. S. Ghamsari, 'A new colloidal technique for the synthesis of lead sulfide nanoparticles', *Scientia Iranica*, vol. 10, no. 3. pp. 357–360, 2003.
- [91] S. Chen, L. A. Truax, and J. M. Sommers, 'Alkanethiolate-protected PbS nanoclusters: Synthesis, spectroscopic and electrochemical studies', *Chemistry of Materials*, vol. 12, no. 12, pp. 3864–3870, 2000.
- [92] F. W. Wise, 'Lead salt quantum dots: The limit of strong quantum confinement', *Accounts of Chemical Research*, vol. 33, no. 11, pp. 773–780, 2000.
- [93] Y. Wang, A. Suna, W. Mahler, and R. Kasowski, 'PbS in polymers. From molecules to bulk solids', *The Journal of Chemical Physics*, vol. 87, no. 12, pp. 7315–7322, 1987.
- [94] K. Moller, T. Bein, N. Herron, W. Mahler, and Y. Wang, 'Encapsulation of lead sulfide molecular clusters into solid matrixes. Structural analysis with X-ray absorption spectroscopy', *Inorganic Chemistry*, vol. 28, no. 15, pp. 2914–2919, 1989.
- [95] C. Y. Yang and S. Rabii, 'Relativistic electronic structure of PbS and PbSe molecules', *J. Chem. Phys.*, vol. 69, no. 1978, p. 2497, 1978.
- [96] H. Y. Yang, Y. W. Zhao, Z. Y. Zhang, H. M. Xiong, and S. N. Yu, 'One-pot synthesis of water-dispersible Ag₂S quantum dots with bright fluorescent emission in the second near-infrared window', *Nanotechnology*, vol. 24, no. 5, 2013.
- [97] T. G. Schaaff and A. J. Rodinone, 'Preparation and Characterization of Silver Sulfide Nanocrystals Generated from Silver(I)-Thiolate Polymers', *The Journal of Physical Chemistry B*, vol. 107, no. 38, pp. 10416–10422, 2003.
- [98] K. I. Ozoemena and S. Chen, Eds., *Nanomaterials for Fuel Cell Catalysis*. Cham: Springer International Publishing, 2016.
- [99] J. Yang and H. Liu, *Metal-Based Composite Nanomaterials*. Cham: Springer International Publishing, 2015.
- [100] G. Calzaferri, D. Brühwiler, S. Glaus, D. Schürch, A. Currao, and C.- Bern, 'Quantum-Sized Silver, Silver Chloride and Silver Sulfide Clusters', *Luminescence*, pp. 59–62, 2000.
- [101] S. I. Sadovnikov and A. I. Gusev, 'Recent progress in nanostructured silver sulfide: from synthesis and nonstoichiometry to properties', *J. Mater. Chem. A*, vol. 5, no. 34, pp. 17676–17704, 2017.
-

- [102] P. Mulvaney and A. Henglein, 'Formation of unstabilized oligomeric silver clusters during the reduction of Ag⁺ ions in aqueous solution', vol. 168, no. 3, pp. 391–394, 1990.
- [103] W. Chen, J. M. Rehm, C. Meyers, M. I. Freedhoff, A. Marchetti, and G. McLendon, 'Luminescence properties of indirect bandgap semiconductors: Nanocrystals of silver bromide', *Molecular Crystals and Liquid Crystals Science and Technology. Section A. Molecular Crystals and Liquid Crystals*, vol. 252, no. 1, pp. 79–86, 1994.
- [104] N. M. Correa, H. Zhang, and Z. A. Schelly, 'Preparation of AgBr quantum dots via electroporation of vesicles', *Journal of the American Chemical Society*, vol. 122, no. 27, pp. 6432–6434, 2000.
- [105] M. Husein, E. Rodil, and J. H. Vera, 'Formation of silver bromide precipitate of nanoparticles in a single microemulsion utilizing the surfactant counterion', *Journal of Colloid and Interface Science*, vol. 273, no. 2, pp. 426–434, 2004.
- [106] H. Zhang and M. Mostafavi, 'UV-Absorption Observation of the Silver Bromide Growth from a Single Molecule to the Crystal in Solution', *The Journal of Physical Chemistry B*, vol. 101, no. 42, pp. 8443–8448, 1997.
- [107] T. Yamamoto *et al.*, 'The room-temperature superionic conductivity of silver iodide nanoparticles under pressure', *Journal of the American Chemical Society*, vol. 139, no. 4, pp. 1392–1395, 2017.
- [108] G. Burley, 'Polymorphism of silver iodide', *American Mineralogist*, vol. 48, no. 11–2, p. 1266, 1963.
- [109] L. . Strock, 'The crystal structure of high temperature iodine silver alpha-AgI', *Z. Phys. Chem-Abt B*, vol. 25, pp. 441–459, 1934.
- [110] S. Chen, T. Ida, and K. Kimura, 'Thiol-Derivatized AgI Nanoparticles: Synthesis , Characterization , and Optical Properties', vol. 5647, no. 98, pp. 6169–6176, 1998.
- [111] R. Makiura *et al.*, 'Size-controlled stabilization of the superionic phase to room temperature in polymer-coated AgI nanoparticles', *Nature Materials*, vol. 8, no. 6, pp. 476–480, 2009.
- [112] A. Henglein, M. Gutierrez, H. Weller, A. Fojtik, and J. Jirkovsky, 'Reactions and Fluorescence of AgI and AgI - Ag₂S Colloids', 1989.
- [113] I. Lj, I. A. Jankovi, M. Mitri, and J. M. Nedeljkovi, 'Growth and quantum confinement in AgI nanowires', vol. 61, pp. 3522–3525, 2007.
- [114] T. Kodaira, 'Incorporation of AgI clusters into the cages of zeolites LTA and FAU observed by optical spectra and X-ray diffraction patterns', no. February, pp. 499–503, 1999.
- [115] S. Shaker-Agjekandy and A. Habibi-Yangjeh, 'Facile one-pot method for preparation of AgI/ZnO nanocomposites as visible-light-driven photocatalysts with enhanced activities',
-

Materials Science in Semiconductor Processing, vol. 34, pp. 74–81, 2015.

- [116] Y.-G. Guo, Y.-S. Hu, J.-S. Lee, and J. Maier, ‘High-performance rechargeable all-solid-state silver battery based on superionic AgI nanoplates’, *Electrochemistry Communications*, vol. 8, no. 7, pp. 1179–1184, 2006.

Summary

Colloidal semiconductor nanomaterials are the subject of an extensive field of research with great interest in their wet-chemical synthesis and size-dependent properties. This research has led to much new and fundamental information about materials in the nano-size regime and has led to their use in industrial applications. However, the underlying formation processes of these nano-materials are still not completely understood. The synthesis of sufficiently stabilized nanocrystals, and their assembly into well-defined superstructures needs further investigation before the full potential of these materials can be exploited. In this dissertation, appropriate semiconductor nanomaterial systems were chosen to highlight size-related properties arising from quantum confinement effects and to demonstrate their formation process in real-time using in-situ and ex-situ characterization methods.

The first work describes the formation of CdTe-nanoclay nanocomposites using hot-injection synthesis of quantum dots in the presence of inorganic clay materials. The composite material features well-separated quantum dot arrays along an inorganic clay material framework. The solution pH during synthesis, the initial metal ion concentration, the ionic strength, and contact time of cadmium ions were all tuned, with the results suggesting preferred edge coverage on the 2:1 phyllosilicate materials. In general, the irreversible adsorption of cadmium ions arises from the high binding affinity of the divalent heavy metal cations and the high cation exchange capacity of nanoclay materials. The predominant and selective coverage along the edges finds its origin in the high sorption capacity on deprotonated hydroxyl groups under basic conditions. In the deprotonated form the active edge sites are able to remove efficiently cadmium ions from the reaction mixture at room temperature. The cadmium ions are not able to occupy lattice positions in nanoclays and therefore the subsequent injection of the telluride precursor induces well-separated and uniform CdTe quantum dot growth. The presence of organic ligands as well as the controlled deposition on nanoclay edges allows the stabilization of well-ordered quantum dot arrays. This first system was analysed by using UV-Vis spectroscopy and fluorescence microscopy to monitor size-related optical properties. Atomic Force Microscopy (AFM) and Transmission Electron Microscopy (TEM) were used to highlight the quantum dot attachment along the clay edges. The specific adsorption of the nanocrystals on the inorganic support material, the ease of fabrication of the construct, as well as the resulting optical features, may be of interest in the field of 'smart materials' towards applications in optoelectronic devices.

In a second work, a microfluidic setup was used for the first time to study the methylammonium-based perovskite formation by in-situ Small-Angle X-ray Scattering (SAXS) and in-situ UV-Vis spectroscopy. The $\text{CH}_3\text{NH}_3\text{PbBr}_3$ formation was performed in a quartz capillary where perovskite precursor salts diffuse into the anti-solvent toluene to induce the nanocrystal formation. The nanocrystals grew in the presence of stabilizing ligands via the 2D oriented attachment mechanism into highly crystalline nanosheets and 3D superstructures. This could be clearly highlighted by the red-shift in the absorption spectra reaching from zero-dimensional nanocrystals to the bulk materials. The SAXS scattering profile clearly demonstrates the beginning of the perovskite growth by the detection of spherical particles which grow into anisotropic nanoplatelets. The strongly pronounced structure peak factor is indicative of a highly-ordered 3D stacking structure.

The crystallinity, composition analysis and morphologies at different growth stages were investigated by Scanning Electron Microscopy (SEM) and Selected Area Electron Diffraction (SAED) Transmission Electron Microscopy (TEM).

The second approach for the $\text{CH}_3\text{NH}_3\text{PbBr}_3$ undertaken herein was the successful adaption of the diffusion-controlled soft-template method to a polymer-based microfluidic chip in combination with Confocal Laser Scanning Microscopy (CLSM). The fast and controlled mixing within the 3D focusing channels of the microfluidic chip enables emission detection from the early stages of the self-assembly process. The clearly defined solvent streams allow the calculation and control of the mixing point and solvent composition along the mixing channels. Therefore, the study provides insight not only into the self-assembly process but also on the time-scales of the rapid perovskite formation.

The large scale synthesis, the rapid synthesis in the microfluidic chip, and the slow interdiffusion experiment together elucidate the structural pathways starting from 0D nanocrystals, to 2D nanosheets, and finally resulting in 3D stacked assemblies of highly crystalline perovskite nanosheets.

In a third work, a novel, room temperature synthetic route to colloidal metal chalcogenide and metal halide nanoclusters was developed in organic solvents. For the wet-chemical synthesis of CdS, ZnS, PbS, Ag_2S , AgI and AgBr nanocrystals, the cationic reaction components were synthesized together with organic ligands for their introduction into organic solvents. The organic precursors show in general a similar structure with the halogen and sulfur anions stabilized by the large tetraoctylammonium cation to generate the corresponding organic precursor.

For the synthesis, the precursors were dissolved in cyclohexane to generate a highly supersaturated system. The addition of *n*-octylamine, together with the introduced stabilizing ligands allow a strong complexation and subsequent formation of nanoclusters at room temperature.

In-situ UV-Vis investigations were used to demonstrate the sequential growth of metal-based clusters of II-VI and IV-VI semiconductor materials by monitoring the excitonic transition energy of nanoclusters, which shows a strong blue-shift with decreasing nanocluster size. The systematic variation of the reaction parameters (e.g. reaction temperature, ligand system, precursor ratio and injection order) during monitoring highlighted the heterogeneous cluster growth and quantum-confined properties of the CdS model system. The clusters were characterized by Transmission Electron Microscopy (TEM) and showing sub-nanometer radii.

The classical nucleation model cannot account for formation processes which occur via stable nanoclusters with distinct structures in highly supersaturated systems. However, the sequential cluster growth process is explained by distinct stages of intermediates which show extraordinary thermodynamic stability according to the spectroscopic measurements.

Temporal analysis highlights the temperature-dependency in pseudo-first order reaction conditions. The compositions were analyzed by X-ray diffraction (XRD) and advanced electron microscopy techniques like Scanning Transmission Electron Microscopy in combination with Energy Dispersive X-ray Spectroscopy (STEM-EDS). On the basis of the results for CdS nanoclusters, we extended this general approach to a variety of metal-based clusters. Study of the nanocluster was also undertaken in microfluidic devices, opening new avenues for the detection of semiconductor nanomaterials. The developed microfluidic methodologies, the novel synthesis of highly stable nanoclusters, together with in-situ and ex-situ characterization techniques provides fundamental knowledge of nanoclusters formation important for fabrication of future nanodevices.

Zusammenfassung

Kolloidale Halbleiter-Nanomaterialien weisen ein umfangreiches Forschungsbiet auf, welches sowohl die nasschemische Herstellung als auch ihre vielversprechenden größenabhängigen Eigenschaften umfasst. Zahlreiche Materialien wurden bereits umfangreich untersucht, um fundamentale Informationen über den Größenbereich zu erhalten und mögliche Anwendungspotentiale auszuschöpfen. Jedoch ist die analytische Beschreibung der zugrundeliegenden Nukleations- und Wachstumsmechanismen bis heute noch nicht vollständig nachvollziehbar und verstanden. Diese Dissertation beschäftigt sich mit Halbleiter-Nanomaterialien und deren größenabhängigen optischen Eigenschaften, welche auf den Quantum Confinement Effekt zurückzuführen sind. Die Synthese von ausreichend stabilisierten Nanokristallen, die systematische Forschung an Quantum Dots, aber auch die strukturierte Anordnung der quantisierten Nanoteilchen soll demnach untersucht werden. Zur Strukturaufklärung wurde das Wachstumsverhalten in Echtzeit mittels in-situ und ex-situ Charakterisierungsmethoden dargestellt.

Das erste untersuchte System beschreibt die Herstellung von CdTe-Schichtsilikat Nanokomposite gemäß einer 'hot-injection' Synthese. Quantum Dots konnten somit in Anwesenheit von Schichtsilikaten erfolgreich hergestellt werden. Das Kompositmaterial vereint die herausragenden Eigenschaften beider Komponenten und ermöglicht die systematische Anreicherung von separierten Nanopartikeln entlang des anorganischen Matrixmaterials. Der pH-Wert während der Synthese, die vorhandene Konzentration an Metallionen, deren Ionenstärke und die Inkubationszeit von Cadmiumionen und Schichtsilikaten ermöglichen eine bevorzugte Anreicherung von CdTe Quantum Dots an den Kanten der 2:1 Phyllosilikate. Eine irreversible Anbindung wird durch die hohe Bindungsaffinität der divalenten Schwermetallkationen und der hohen Kationenaustauschkapazität des Natrium-Hektorits ermöglicht. Die selektive Anordnung entlang der Kanten wird durch eine Deprotonierung der Hydroxyl-Gruppen erreicht. Diese erfolgt unter basischen Bedingungen, wodurch aktive Hektorit-Kanten generiert werden um Cadmiumionen effektiv an sich zu binden. Die Adsorption der Ionen erfolgt im wässrigen Medium bei Raumtemperatur. Die Cadmiumionen sind aufgrund ihrer Größe nicht in der Lage die Gitterplätze des Schichtsilikates zu besetzen, wodurch eine nachfolgende Injektion des Tellurid-Precursors das Wachstum von separierten und gleichförmigen CdTe Quantum Dots induziert. Organischen Liganden und die kontrollierte Anbindung an Schichtsilikat-Kanten ermöglichen die Stabilisierung wohldefinierter Quantum Dot-Arrays. Die Charakterisierung der optischen Eigenschaften erfolgte mittel UV-Vis Spektroskopie

und Fluoreszenzmikroskopie. Raster-Kraft-Mikroskopie (Atomic Force Microscopy, AFM) und Transmissionselektronenmikroskopie (Transmission Electron Microscopy, TEM) bestätigten die selektive Anordnung der Quantum Dots entlang der Hektorit-Kanten. Die spezifische Adsorption der Nanopartikel am anorganischen Trägermaterial, die vergleichsweise einfache Herstellung der Nanokomposite sowie der Erhalt der optischen Eigenschaften von CdTe Nanopartikeln leisten einen großen Beitrag im Bereich der 'smart materials'. Diese Erkenntnis dient als Basis für optoelektronische Anwendungen.

Beim zweiten System, wurden mikrofluidische Systeme für die Synthese von methyllumonium-basierenden Perovskiten herangezogen. Das erste Mal dienten in-situ Röntgenkleinwinkelstreuung (Small-Angle X-ray Scattering, SAXS) und in-situ UV-Vis Spektroskopie zur Strukturaufklärung. Die $\text{CH}_3\text{NH}_3\text{PbBr}_3$ Synthese wurde hierzu in einer Quarzkapillare durchgeführt. Die Precursor-Salze können durch den geeigneten Aufbau in das Anti-Lösungsmittel Toluol diffundieren, wodurch das Nanokristallwachstum induziert wird. Das Wachstum wird durch stabilisierende Liganden gesteuert, welche eine orientierte Anlagerung in 2 Dimensionen ermöglicht. Diese Selbstorganisation führt zu hochkristallinen Nanoplättchen und 3-dimensionalen Überstrukturen. Der klare Rot-shift der Absorptionssignale weist deutlich auf eine Transformation von 0D Nanopartikeln zu bulk-Materialien hin. Mittels SAXS Streubildern kann das Perovskitwachstum eindeutig dargestellt werden. Zu Beginn werden sphärische Nanopartikel detektiert, welche zu anisotropen Nanoplättchen heranwachsen. Der stark ausgeprägte Strukturfaktor-Peak in den Streukurven ist Beleg für die Ausbildung von hochgeordneten 3-dimensionalen Stapel-Strukturen. Die hohe Kristallinität der Perovskite, die chemische Zusammensetzung, sowie die Morphologien in unterschiedlichen Wachstumsstadien konnten mittels Raster- und Transmissionselektronenmikroskopie (Scanning Electron Microscopy, SEM und Selected Area Electron Diffraction, SAED, Transmission Electron Microscopy, TEM) belegt werden. Der Untersuchung des $\text{CH}_3\text{NH}_3\text{PbBr}_3$ Perovskit Wachstums in einem polymerbasierende Mikrofluidik Chip geht eine erfolgreiche Adaption der diffusionskontrollierten Synthese voraus. Die weiteren Untersuchungen erfolgen in Kombination mit Konfokaler Laser Scanning Mikroskopie (Confocal Laser Scanning Microscopy, CLSM). Das rasche und kontrollierte Mischen im 3D fokussierten Chipkanal ermöglicht es, die Emission in den frühen Stadien der Selbstassemblierung zu detektieren. Die klar definierte Flussfokussierung lässt den Mischungspunkt und die Zusammensetzung entlang des Mikrofluidikkanals bestimmen und kontrollieren. Somit ermöglicht diese Studie einen Einblick in die zeitliche Abfolge der Perovskit-Synthese und den Selbstassemblierungsprozess. Die Synthese im großen Maßstab, die rasche Synthese im

Mikrofluidik Chip und das langsame Interdiffusions-Experiment in der Kapillare beschreiben die strukturelle Entwicklung beginnend bei 0D Nanokristallen, über 2D Nanoplättchen und die Ausbildung der 3D hochkristallinen Überstruktur.

Eine neuartige Raumtemperatur-Synthese von kolloidalen Metallchalcogenid- und Metallhalogenid-Nanoclustern wurde in organischen Lösungsmitteln entwickelt. Für die nasschemischen Synthesen von CdS, ZnS, PbS, Ag₂S, AgI und AgBr Nanokristallen wurden kationische Reaktionskomponenten zusammen mit organischen Liganden hergestellt. Somit gelang eine erfolgreiche Einführung in das organische Lösungsmittel. Der anionische Precursor weist eine ähnliche Struktur auf, bei der die Stabilisierung der Halogenid- und Schwefelanionen mittels quarternisierten Gegenionen erfolgt. Für die eigentliche Synthese werden die Precursor in Cyclohexan gelöst, um ein übersättigtes Reaktionsmedium zu generieren. Der Zusatz von *n*-Octylamin und die Anwesenheit der organischen Liganden ermöglicht eine Bildung und starke Komplexierung von Nanoclustern. In-situ UV-Vis spektroskopische Untersuchungen demonstrieren den sequentiellen Wachstumsprozess der II-VI und IV-VI metallbasierenden Halbleitermaterialien. Die exzitonische Übergangsenergie der Nanocluster zeigt mit abnehmender Partikelgröße eine Verschiebung zu niedrigeren Wellenlängen. Durch die systematische Variation der Reaktionsparameter (Reaktionstemperatur, Ligandensystem, Precursorverhältnis und Reihenfolge der Precursor etc.) konnte die Strukturentwicklung aufgezeichnet werden. Das heterogene Clusterwachstum sowie Confinement-Effekte wurden mit Hilfe des CdS Modellsystems zugänglich gemacht. TEM Messungen wurden herangezogen um die Dimensionen der Nanocluster im Subnanometerbereich zu ermitteln.

Im Gegensatz zur klassischen Nukleationstheorie kann der Bildungsprozess in übersättigten Systemen durch die Entstehung von stabilen Nanoclustern beschrieben werden. Das sequentielle Clusterwachstum ist durch ausgeprägte Intermediate gekennzeichnet, welche eine herausragende thermodynamische Stabilität aufweisen. Kinetische Untersuchungen an dem CdS System zeigen eindeutig einen temperaturabhängigen Wachstumsprozess (Reaktion pseudo-erster Ordnung). Die Analyse der chemischen Zusammensetzung erfolgte mittels Röntgendiffraktometrie (X-ray Diffraction, XRD) und fortgeschrittenen Elektronenmikroskopie-Techniken (Scanning Transmission Electron Microscopy in Kombination mit Energy Dispersive X-ray Spectroscopy (STEM-EDS)). Basierend auf der Syntheseroute von CdS Nanoclustern konnte die generelle Synthesevorschrift auf weitere Halbleitermaterialien und Mikrofluidik-Setups übertragen werden. Diese Kombination birgt neue Chancen für die Zukunft, um den Nukleations- und

Wachstumsprozess weiter zu analysieren. Die Entwicklungen basierend auf mikrofluidischen Systemen, die neuartige Nanocluster-Synthese in Kombination mit in-situ und ex-situ Charakterisierungsmethoden sowie Erkenntnisse dieser Arbeit sollen als Basis für fortgeschrittene Analysemethoden und für die Entwicklung zukunftsreicher industrieller Anwendungen dienen.

Declaration/(Eidesstattliche) Versicherungen und Erklärung

(§ 9 Satz 2 Nr. 3 PromO BayNAT)

Hiermit versichere ich eidesstattlich, dass ich die Arbeit selbstständig verfasst und keine anderen als die von mir angegebenen Quellen und Hilfsmittel benutzt habe (vgl. Art. 64 Abs 1 Satz 6 BayHSchG).

(§ 9 Satz 2 Nr. 3 PromO BayNAT)

Hiermit erkläre ich, dass ich die Dissertation nicht bereits zur Erlangung eines akademischen Grades eingereicht habe und dass ich nicht bereits diese oder eine gleichartige Doktorprüfung endgültig nicht bestanden habe.

(§ 9 Satz 2 Nr. 4 PromO BayNAT)

Hiermit erkläre ich, dass ich Hilfe von gewerblichen Promotionsberatern bzw. –vermittlern oder ähnlichen Dienstleistern weder bisher in Anspruch genommen habe noch künftig in Anspruch nehmen werde.

(§ 9 Satz 2 Nr. 7 PromO BayNAT)

Hiermit erkläre ich mein Einverständnis, dass die elektronische Fassung meiner Dissertation unter Wahrung meiner Urheberrechte und des Datenschutzes einer gesonderten Prüfung unterzogen werden kann.

(§ 9 Satz 2 Nr. 7 PromO BayNAT)

Hiermit erkläre ich mein Einverständnis, dass bei Verdacht wissenschaftlichen Fehlverhaltens Ermittlungen durch universitätsinterne Organe der wissenschaftlichen Selbstkontrolle stattfinden können.

Waischenfeld, 04.05.2018,

.....

Ort, Datum, Unterschrift